Ultraviolet auroral signatures of magnetospheric phenomena at Jupiter

Diego Moral Pombo, MSc

Faculty of Science and Technology

Lancaster University

A thesis submitted for the degree of

Doctor of Philosophy

April, 2025

Ultraviolet auroral signatures of magnetospheric phenomena at Jupiter

Diego Moral Pombo, MSc.

Faculty of Science and Technology, Lancaster University

This thesis is submitted for the degree of *Doctor of Philosophy.* April, 2025.

Abstract

Jupiter's magnetosphere is one of the most fascinating (and largest) bodies in our Solar System. Many of the physical mechanisms occurring in the Jovian plasma environment have an impact on the auroral emissions generated in its upper atmosphere, which we study with instruments like the imaging spectrograph onboard the Hubble Space Telescope (HST-STIS). This thesis uses images from STIS to study the equatorward aurorae in the context of other auroral emissions present, and their connection to different magnetospheric phenomena.

The first chapter outlines the key physical mechanisms driving auroral emissions, describing the Jovian magnetospheric structure and the more relevant dynamics of the plasma, such as the Dungey and Vasyliunas cycles, as well as examining auroras across different bodies in our Solar System for broader context. The second chapter details the instrumentation (HST-STIS imager and Juno's particle detectors), datasets and processing techniques utilised, including the custom algorithm developed to detect auroral emissions. Chapter three presents a comprehensive statistical study of the auroral emissions in Jupiter's Southern hemisphere, focusing on the secondary oval and the injection signatures and quantifying its emission frequencies and main characteristics to offer the most complete analysis to date. Chapter four adds an in-situ component, analyzing Juno's electron data from the JADE particle detector for the equatorward emissions region, and comparing them to the HST observations. The fifth chapter compiles results from three different studies, offering ultraviolet auroral context for Jovian X-ray emissions, its cusp region, and dipolarization front events. In the sixth and final chapter, the main results are synthesised, and some recommendations for expanding on the previous studies are provided.

Acknowledgements

First and foremost, I would like to thank Dr. Sarah Badman for her help, ideas, and kindness. I am very aware of the too often hostile academic environments and tough supervisors many doctoral researchers have to deal with, adding an extra burden to a strenuous task in its own right. Despite the remote working for the first couple of years and the rest of pandemic-related issues, I honestly think my PhD was as close to smooth sailing as one could expect given the circumstances (that is, of course, until Greenland's ice sheet got in the way!). On top of all the help and guidance, I can confidently claim that I would be more than happy to eventually become a researcher half as good, honest, and exemplary as her. I reckon that a PhD supervisor is ultimately the decisive factor that may make a researcher leave academia after their PhD for good or try fortune in this onerous career. In my case, I am very clear about the path that Sarah helped me choose. So, thank you for making me stick to science (be it on this planet or on another, more complicated but more fun, too).

I extend my gratitude to the rest of the Space and Planetary Physics Group of Lancaster University, who welcomed me with open arms from the very first moment and whose mere presence, knowledge, and overall good mood undoubtedly made this journey a pleasant one. To name just a few: Dr Licia Ray, for her smart ideas and unwavering interest in the project, Dr Jim Wild, particularly for his role in the delivery of this work, and Dr Joe Kinrade, for all the pints, the convos and the crash course on all things British (not English!). Thanks also to the rest of the folks at B504, those with whom I coincided and those with whom, for virological reasons, I did not. Without leaving Lancaster, a final mention must be made to all the other people I have crossed paths with, both in Physics and LEC, including Dr Mal MacMillan and his empathetic understanding of my situation during the final stage of the PhD, my mate Nick, and my diverse friends at Primrose Street (long live those *plovs*).

Gracias a mis padres, por la educación que me dieron y su fomento de mi interés por la ciencia, además de su inspiradora manera de entender el mundo. Y a mi hermano, referente en muchas cosas, incluyendo, cómo no, su visión de la ciencia. Todos ellos junto con el resto de mi familia, tanto la de sangre como la elegida, han sido un apoyo constante en la persecución de una carrera en la ciencia, a pesar de la distancia. Y gracias también a los y las colegas de La Laguna y la Complutense, que hicieron la Física mucho más llevadera entre cervezas, risas y constantes vacil*ada*s.

And last but definitely not least, Lara. Being able to share a life (British railways permitting), a common goal and even some estranged flatmates with the most clever person and best researcher on that side of the Clyde is a privilege I do not take for granted. I find it very helpful and reassuring that you are always one step ahead, *demon*strating what to do to succeed in academia without burning out.

Declaration

I, Diego Moral Pombo, declare that the work presented in this thesis titled "Ultraviolet auroral signatures of magnetospheric phenomena at Jupiter" is, to the best of my knowledge and belief, original and my own work. The material has not been submitted, either in whole or in part, for a degree at this, or any other university. This thesis does not exceed the maximum permitted word length of 80,000 words including appendices and footnotes, but excluding the bibliography. A rough estimate of the word count is: 38280

Diego Moral Pombo

Publications

The following publication has been generated while developing this thesis, and to an extent has guided the thesis into what it has become. The specific contributions of the author to that work are detailed in Section 5.1 of Chapter 5:

D. M. Weigt, C. M. Jackman, D. Moral Pombo, S. V. Badman, C. K. Louis, W. R. Dunn, S. C. McEntee, G. Branduardi-Raymont, D. Grodent, M. F. Vogt, C. Tao, G. R. Gladstone, R. P. Kraft, W. S. Kurth, and J. E. P. Connerney (2023). "Identifying the Variety of Jovian X-Ray Auroral Structures: Tying the Morphology of X-Ray Emissions to Associated Magnetospheric Dynamics". en. In: *Journal of Geophysical Research: Space Physics* 128.11. ISSN: 2169-9402. DOI: 10.1029/2023JA031656

Contents

List of Figures

List of Tables

List of Acronyms

- ADS: Auroral Dawn Storm
- CEC: Corotation Enforcement Currents
- CML: Central Meridian Longitude
- DAM: Decametric Emissions
- EMIC: ElectroMagnetic Ion Cyclotron
- ESA: European Space Agency
- EUV: Extreme Ultraviolet
- FAC: Field Aligned Currents
- FL: Field Lines
- FUV: Far Ultraviolet
- FWHM: Full Width at Half Maximum
- HOM: Hectometric Emissions
- HST: Hubble Space Telescope
- IFP: Io Footprint
- IMF: Interplanetary Magnetic Field
- IPT: Io Plasma Torus

- IR: Infrared
- JADE: Jovian Auroral Distributions Experiment
- JEDI: Jupiter Energetic Particle Detector Instrument
- JIRAM: Jovian Infrared Auroral Mapper
- KH: Kelvin-Helmholtz
- LT: Local Time
- MAB: Main Auroral Brightening
- MAMA: Multi-Anode Micro-channel Array
- ME/MO: Main Emission/Oval
- MHD: Magnetohydrodynamics
- NASA: National Aeronautics and Space Administration
- nIR: (near) Infrared
- NUV: Near Ultraviolet
- n-KOM: Narrowband Kilometric emissions
- PAD: Pitch Angle Distribution
- PJ: Perijove (of Juno's orbit)
- STIS: Space Telescope Imaging Spectrograph
- SW: Solar Wind
- UTC: Coordinated Universal Time
- UV: Ultraviolet
- UVS: Ultraviolet Spectrograph

And because we are alive, the universe must be said to be alive. We are its consciousness as well as our own. We rise out of the cosmos and we see its mesh of patterns, and it strikes us as beautiful. And that feeling is the most important thing in the universe - its culmination, like the color of the flower at first bloom on a wet morning.

Kim Stanley Robinson, *Green Mars*

–Aurora Borealis?! At this time of year, at this time of day, in this part of the country, localized entirely within your kitchen!?
–Yes.
–...May I see it?
–No.

Seymour Skinner and Superintendant Chalmers

Chapter 1

Introduction

Aurorae, or Northern lights, have fascinated humanity from the beginning of time. For millennia, different cultures have incorporated them into their own mythologies and conceived all kinds of explanations for them. For example, they have been interpreted as propitious signs for herring fishing (by Swedish fishermen), ethereal bridges to Valhalla (according to the Vikings) or even playfields for games between spirits using the skull of a walrus as a ball (among some Inuit tribes from Greenland). However, in the last century, science has unveiled to us the considerably more complex reality of the aurorae.

This initial chapter lays the groundwork for the rest of the thesis. First, it outlines the basic characteristics of the single particle dynamics, as well as the combination of most general physical mechanisms associated with the generation of the aurorae polaris, like the acceleration processes or the radial transport. Second, it depicts the main outlines that form the skeleton of the magnetohydrodynamics (MHD). Third, it describes the magnetic field and the structure of the magnetosphere of Jupiter, separating it into its inner, middle and outer regions. Fourth, it details the magnetospheric dynamics with specific attention to the Dungey and Vasyliunas cycles and the corotation enforcement currents theory. Fifth, it summarises the production of aurorae and its detections in other planetary bodies of our own Solar System for an ampler context. Sixth and finally, it addresses the morphology and dynamics of the main topic of this project: the mighty Jovian aurorae, with a focus on the UV.

1.1 Space Plasmas

This work is of an analytical nature and it relies heavily on the refined and validated conceptual framework developed after years of observations with innumerable instruments and missions. A succinct introduction to some of the foremost theoretical concepts necessary for the background of the present thesis will be presented now. They include the equations governing single-particle motions (e.g., relevant for precipitation of particles onto the ionosphere), the main processes of particle acceleration, the basic outlines of charge exchange and ionisation, and the radial transport of plasma (as a key player in its distribution across the magnetosphere).

1.1.1 Single particle motion

The trajectory of a single particle of mass m, subjected to a force ($\mathbf{F}$) as a function of time (t) and position (r) is determined by the first law of Newton, $m \cdot a = \mathbf{F}(r, t)$. In the case of an electromagnetic field (and in the absence or neglecting any other forces like the gravitational one), then we can define $\mathbf{F}_L$ as the Lorentz force:

$$\mathbf{F}_L = q(\mathbf{E} + \mathbf{v} \times \mathbf{B})$$

where q is the charge of the particle, $\mathbf{E}$ the electric field, $\mathbf{v}$ the velocity of the particle and $\mathbf{B}$ the magnetic flux density (or magnetic field). The problem scales very quickly in complexity when one realises that a plasma is by definition a mix of charged particles forming a (tenuous) gas, generating their own electromagnetic fields while moving. This effectively renders it impossible to solve the original equations with such a direct approach, and it is the problem that fuels the study of magnetohydrodynamics (MHD), introduced in the next section.

Still, we can consider some of the simplest cases of electric and magnetic fields to study the motion of an ideally isolated particle under those conditions. First, let us consider a constant and homogenous magnetic field **B** in a perpendicular direction to the particle's initial motion. In this case, the particle will start a circular motion with a specific angular frequency (Ω_C, called cyclotron frequency or gyrofrequency) and radius (ρ_C, Larmor radius or gyroradius):

$$\Omega_C = qB/m \qquad\qquad \rho_C = v_\perp/\Omega_C \tag{1.1}$$

If a velocity component parallel to the magnetic field direction is included in this motion, the circular motion becomes helical, with the parallel velocity unaltered by **B**, as shown in Figure 1.1a.

To add an extra layer of depth, we now add a uniform electric field, **E**, perpendicular to both the magnetic field and the particle's initial direction. The parallel motion of the particle will simply be given by the initial velocity (since **E** is perpendicular to v_0). However, as shown in Fig. 1.1b, the motion perpendicular to the field will consist of two terms: the gyromotion due to the magnetic field already considered, plus a constant drift ($\mathbf{E} \times \mathbf{B}$) motion of the guiding centre around which the particle gyrates, caused by the appearance of the electric field (first and second terms of Eq. 1.2, respectively). In the absence of other external forces, this drift does not generate currents in the plasma.

$$\mathbf{u}(t) = \mathbf{u}_{circ} + \mathbf{u}_E = \mathbf{u}_{circ} + \mathbf{E} \times \mathbf{B}/B^2 \tag{1.2}$$

The next level in complexity appears when the magnetic field is not homogeneous (Kivelson et al. 1995). In that case, two additional drifts must be considered when the particle feels changes in the force during a single gyration. If the magnetic field changes with the spatial position, there will be a gradient drift (described by Eq. 1.3). This gradient B drift refers to the increase of the field force in a particular direction, causing the Larmor radius to be variable along the orbit, and thus leading to a drift perpendicular to both the direction of the magnetic field and the direction of the gradient.

$$\mathbf{u}_{gradB} = \frac{1}{2}mv_{\perp}^{2}\frac{\mathbf{B}\times\nabla\mathbf{B}}{qB^{3}} \tag{1.3}$$

The second one is the curvature drift. This drift occurs when a particle whose guiding centre moving along a curved field line feels a centrifugal force. Its direction is perpendicular to both the direction of the magnetic field and the velocity of the guiding centre. It is described by the Equation 1.4, where R_c is the local curvature radius of the field, $\hat{\mathbf{b}}$ is the unit vector of the magnetic field, and $\hat{\mathbf{n}}$ another unit vector normal to it and pointing away from the centre of the curve:

$$\mathbf{u}_{curv} = \frac{mv_{\parallel}^{2}\mathbf{B}\times(\hat{\mathbf{b}}\cdot\nabla)\hat{\mathbf{b}}}{qB^{2}} = -\frac{mv_{\parallel}^{2}\mathbf{B}\times\hat{\mathbf{n}}}{R_{c}qB^{2}} \tag{1.4}$$

1.1.2 First adiabatic invariant and magnetic mirroring

The magnetic moment, μ, also known as the first adiabatic invariant, can be formulated as:

$$\mu = \frac{1}{2}mv_{\perp}^{2}/B \tag{1.5}$$

This means that it will not undergo changes while the parameters of the system, such as the field strength and direction, change slowly compared to the cyclotron period. Since the total energy must remain constant, as B increases, the perpendicular component of the velocity also increases, while the parallel decreases. This can be explained by looking at Faraday's law: the change of magnetic flux over the surface defined by the particle's gyration induces an electric field $E = -v_{\parallel}B_r$ directed along the direction of the gyromotion (for a positively charged particle). This will generate a force on the particle that will increase $v_{\perp}$. The conservation of the magnetic moment along the field together with the decrease in the velocity parallel to the field as described above imply that the particle will eventually turn around when the parallel velocity becomes 0, i.e., when the magnetic field strength becomes $B = \frac{1}{2}mv^{2}\mu$. When that happens, it is said that the particle is mirrored back.

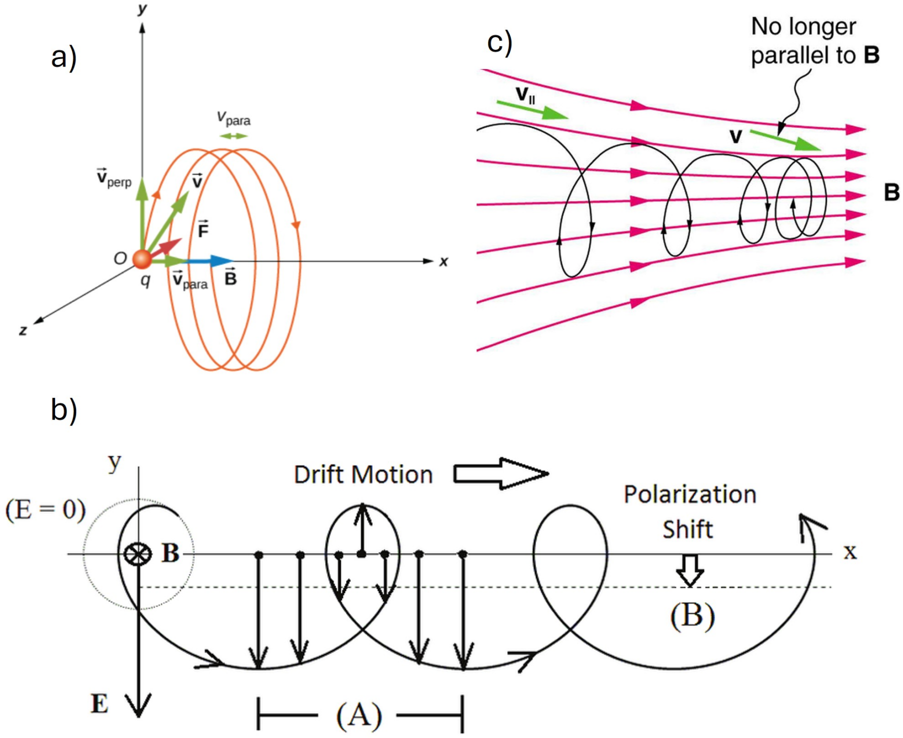

Figure 1.1: Charged particle motion under different conditions: a) A charged particle moving in a magnetic field. The velocity component perpendicular to **B** creates circular motion, while the component parallel to the field moves the particle along a straight line, resulting in a helical motion. b) The drifting motion of a gyrating charged particle in perpendicular **E** and **B** leads to a polarisation shift from the guiding-centre position (on the x-axis) to the averaged particle position (on the dotted horizontal line). If $\mathbf{E} = 0$ (no drift), the particle's gyromotion is along a circular orbit (grey). c) Motion of a gyrating charged particle in a magnetic field with an intensity gradient along a field line, eventually resulting in magnetic mirroring. Credit: Ling et al. (2018) & Brizard (2013).

If the mirroring happens on both ends of a magnetic field line, the particle is held in a "magnetic bottle". This phenomenon is highly important in the magnetosphere of a magnetised planet because it confines many of the plasma particles "bouncing" between the poles (see Fig. 1.1c). The periodicity of that "bouncing" in a symmetric bottle will define the second (or longitudinal) adiabatic invariant, whose actual form is beyond the scope of this analysis.

At this point, it is necessary introducing another crucial concept for this work. The **pitch angle** is the angular difference between the local magnetic field direction and the velocity vector of the particle, or, in other words, the arctangent of the ratio of perpendicular to parallel components of the velocity (Equation 1.6).

$$\tan \alpha = \frac{v_\perp}{v_\parallel} = \frac{v_{\perp 0}}{v_{\parallel 0}} \tag{1.6}$$

which, when combined with the energy conservation magnetic moment described in Equation 1.5, can be turned into Eq. 1.7, where α is the pitch angle, B is the magnetic field at the location of the particle, and α_0 and B_0, those same variables for the initial point in the bottle where the field strength is at a minimum.

$$\sin^2 \alpha = \frac{B}{B_0} \sin^2 \alpha_0 \tag{1.7}$$

The particles with a pitch angle α small enough (i.e. a direction close, or parallel, enough to the direction of the magnetic field line) will be considered to enter the so-called "loss cone". These particles will "escape" the magnetic bottle, and, in the case of the dipolar field of planet, then precipitate onto the planet's atmosphere. There, they can collide with the neutral particles and produce auroral emission via charge exchange or transfer collisions (more on the specifications of these mechanisms in section 1.6). This results in the formation of a loss cone in the previously isotropic particle distribution.

1.1.3 Ionisation and charge exchange

Photoionisation (the formation of an ion from the interaction between a photon and a neutral atom or molecule) and electron impact ($A+e^- \to A^+ + 2e^-$) are the two main mechanisms through which an atom or neutral molecule can get electrically charged. The third mechanism is particle attachment between small ions and neutrals, but it does not play a relevant role in magnetospheric plasmas. Since H and H_2 are the most abundant species in Jupiter's atmosphere, H^+ and H_2^+ are the most common ions generated through these mechanisms. H_2^+ however is highly reactive and rapidly can interact with H_2 neutrals to form H_3^+, to be lost later through electron dissociative recombination (Badman et al. 2015).

When the energised and accelerated electrons precipitate onto the atmosphere, they transfer their energy to the atmospheric particles via inelastic collisions. These collisions can ionise the neutral atoms or molecules in the atmosphere, and excite the electrons, and/or the vibro-rotational levels of the present molecules. This process is the ultimate cause of the auroral emissions, as explained later (see Section 1.6).

Besides the ionisation, there can be charge exchange (transfer of electrons) between ions, or between ions and neutrals, which can produce energetic neutral atoms (ENAs). The charge exchange processes between ions and neutral are particularly relevant in the context of Io and its continuous yet variable output of particles to its exosphere, first, and to the torus, eventually (Johnson et al. 1982, Dols et al. 2023).

1.2 Magnetohydrodynamics

As was already mentioned, the "single particle" picture is not enough to explain many of the characteristics of the plasma physics. On the other hand, the electromagnetic field intrinsic to a plasma differentiates it from the usual thermodynamical description of neutral gases. Hence the need for considering the plasma as a fluid and assessing some of the main physical properties that can be described under this MHD theory.

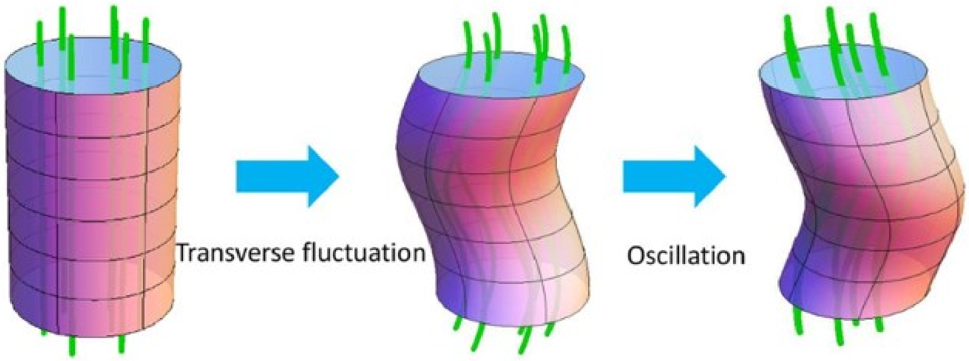

Figure 1.2: Transverse Alfvén wave propagating along the magnetic field (green) in a plasma (purple-red). The tension of the magnetic lines acts as a restoring force that tends to bring the flux tube back to the original position. Credit: Hattori et al. (2022).

1.2.1 Frozen-in Flux Theorem

Several fundamental assumptions are considered in the simplest description of MHD theory usually applied to space plasmas. First, that the spatial and temporal scales of the plasma are, respectively, larger and slower than the gyroradius and gyrofrequency (respectively) of the particles that conform it. Second, that the plasma is "collisionless" in the sense that the mean free paths of the particles are very large because the density is relatively low and, thus, the kinetic processes controlling energy and momentum exchange are not collisions.

Of the four Maxwell equations that sustain classical electrodynamics, Faraday's law (Equation 1.8) has the largest impact for the properties of space plasmas. Physically, it means that in a region of space in which there is a curl of the electric field $\mathbf{E}$ there is a temporally variable magnetic field.

$$\nabla \times \mathbf{E} = -\frac{\partial \mathbf{B}}{\partial t} \tag{1.8}$$

When combined with the $\mathbf{E} \times \mathbf{B}$ drift defined above, this implies that the plasma flow will be converging (or diverging), and that the associated magnetic flux will be transported into (or out of) the region, "attached" to the flow. This is what is called the **"frozen-in flux" theorem** (also known as Alfvén theorem). Physically, it means that a moving region of plasma carries its magnetic field with it, and if the region changes size or shape as it moves (i.e. there is non-zero divergence in the flow) the magnetic field inside of it is also changed in consequence. A visual representation of this theorem is shown in Figure 1.2.

The frozen-in flux theorem relies on the plasma's low resistivity (high conductivity), which implies magnetic field lines cannot diffuse through the plasma and allows them to remain "frozen" into the plasma flow. However, when there is significant diffusion within the plasma, this condition breaks down, and the frozen-in flux theorem is violated. When there is significant diffusion within the plasma, the frozen-in flux theorem is violated. For measuring the relevance of the diffusion, usually, a parameter known as magnetic Reynolds number (R_m) is introduced. Reynolds number accounts for the ratio between the non-diffusive motion (advection and induction) and the diffusion of the magnetic field (hence, it becomes low when diffusion is important).

The frozen-in flux theorem also stops being applicable in highly dynamic environments and/or at small spatial scales (compared to ion or electron characteristic lengths), where pressure gradient effects become important and the single-fluid MHD approximation breaks down. Additionally, when currents are generated from the different drifts in the species forming a plasma (Hall currents), the magnetic fields and all the particles in the plasma stop moving together and the particles with larger inertial scales (ions) will start deviating from the motion of the field lines, drifting as explained in the previous section.

1.2.2 Magnetic Reconnection

Reconnection is the main transport process for collisionless plasmas without the need for diffusion. It occurs when the frozen-in flux theorem breaks down, generating a considerably more complex picture that will only be summarised here qualitatively. Essentially, the reconnection occurs as a local rupture in the stability of a magnetic

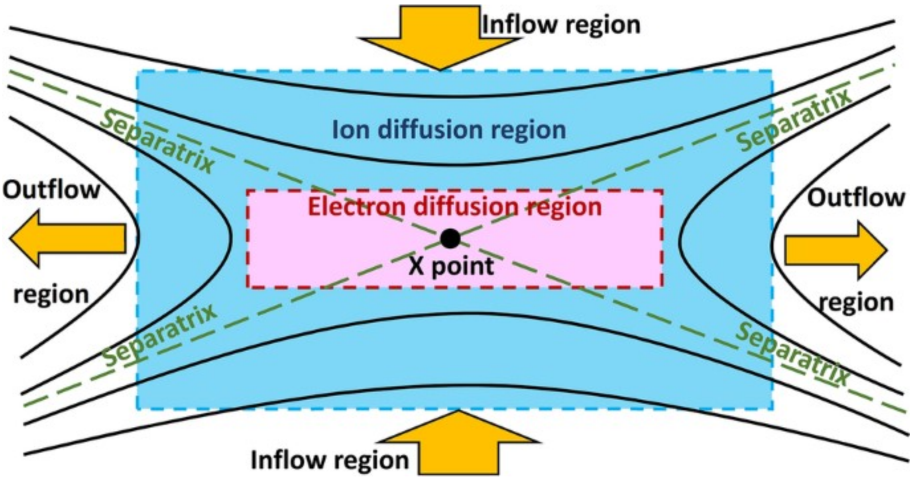

Figure 1.3: A sketch of different regions in a collisionless magnetic reconnection: X point (black dot), separatrices (green dashed lines), inflow region, outflow region, ion diffusion region (blue) and electron diffusion region (pink). Black solid lines indicate magnetic field lines and yellow arrows are for inflow and outflow velocities. In 3-D geometry, the X point becomes an X line or separator, and the separatrix line becomes surface. Credit: Lee et al. (2020).

field topology, i.e., when in regions with close antiparallel field lines, the magnetic field goes locally null and the field lines reconfigure. Figure 1.3 shows the different regions in which the magnetic reconnection configuration can be split: the X point (or line), inflow and outflow regions, the separatrix that divides them, and ion and electron diffusion regions.

Reconnection not only allows the reconfiguration of the magnetic field but also converts magnetic energy into thermal (heating) and kinetic energy (bulk plasma motions). Even though it can only occur in local regions of non-ideal MHD applicability, its consequences extend globally really quickly, affecting systems at a much larger scale than that of its original location. The two main models for magnetic reconnection are those proposed originally by Sweet and Parker, and Petschek (Kulsrud 2001).

In the case of the Earth's magnetosphere, the lines reconnecting are those from the interplanetary magnetic field (IMF) and the terrestrial magnetic field. In the

Dungey model (explained in Section 1.4), reconnection occurs along a single neutral line (X line) on the dayside magnetopause. The reconnected magnetic field lines flow antisunward, frozen in the plasma, toward the magnetotail lobes, where they reconnect along an X line in the equatorial plane of the magnetotail. The inward part of the reconnected field lines is convected earthward, returning to the dayside magnetosphere. The outward part of the reconnected field lines convect further in the antisunward direction and later becomes the IMF field lines. Observations and simulations of magnetic reconnections in the Earth and planetary magnetopause and magnetotail have been widely reported. As for the observational evidence of the reconnection, it was first detected in the terrestrial magnetosphere in the late 70s (Paschmann et al. 1979), and down the magnetotail by the WIND spacecraft (Øieroset et al. 2001), while it had been already been identified in the solar wind and corona (Stix 2002 and references therein).

The reconnection diffusion region is generally much smaller compared to the magnetosphere. The satellites more frequently record the by-products of the magnetic reconnection than the diffusion itself. The by-products, i.e., the bursty bulk flow, flux rope, plasmoid, etc., impact the magnetosphere at much larger scales, with the energised particles dispersing in a wide area.

Seeing from the magnetic signal, the large and rapid variations of the magnetic component that are normal to the current sheet are commonly treated as the representation of the magnetic reconnection. The dipolarization front, accompanied by the bursty bulk flow, displays a local enhancement in the magnetic component normal to the current sheet and a decrease in the magnetic component along the outflow direction (Yao et al. 2020).

1.2.3 Continuity Equations

The single-fluid mass continuity equation (that states the **conservation of mass** during the motion of the fluid) is found by mass-weighting the electron and ion equations and using the definitions of density (ρ) and ($\mathbf{u}$) to obtain:

$$\frac{\partial \rho}{\partial t} + \nabla \cdot (\rho \mathbf{u}) = m_i S_i \tag{1.9}$$

where m_i and S_i are the mass of the different components of the plasma. It is derived from the integrated Vlasov equation, which is, on its part, the Boltzmann equation with the collision term being neglected. From Equation 1.9, when multiplied by the electric charges, it is derived the **conservation of charge**:

$$\frac{d\rho_q}{dt} + \nabla \cdot \mathbf{j} = 0 \tag{1.10}$$

where ρ_q is the charge density [C/m^3], and $\mathbf{j}$ is the current density [A/m^2]. Finally, the equation of **conservation of momentum** (or fluid equation of motion), still ignoring collisions for simplicity (which eventually cancel one another for electrons and ions anyway), can be constructed by introducing an element called the total pressure tensor, $\mathbf{P}$, and the single fluid velocity, $\mathbf{v}$. For each of the species (ions and electrons), then we have, respectively:

$$\frac{\partial (n_i \mathbf{v}_i)}{\partial t} + \nabla \cdot (n_i \mathbf{v}_i \mathbf{v}_i) = -\frac{1}{m_i} \nabla \cdot \mathbf{P}_i + \frac{n_i e}{m_i}(\mathbf{E} + \mathbf{v}_i \times \mathbf{B}) \tag{1.11}$$

$$\frac{\partial (n_e \mathbf{v}_e)}{\partial t} + \nabla \cdot (n_e \mathbf{v}_e \mathbf{v}_e) = -\frac{1}{m_e} \nabla \cdot \mathbf{P}_e - \frac{n_e e}{m_e}(\mathbf{E} + \mathbf{v}_e \times \mathbf{B}) \tag{1.12}$$

If we add up those two equations, use the previously introduced ρ and $\mathbf{j}$ terms are introduced and move the mass term to the left-hand side of the equation, we obtain the final form of the momentum conservation equation:

$$\frac{\partial (nm\mathbf{v})}{\partial t} + \nabla \cdot (nm\mathbf{v}\mathbf{v}) = -\nabla \cdot \mathbf{P} + \rho \mathbf{E} + \mathbf{j} \times \mathbf{B} \tag{1.13}$$

1.2.4 Pressure and Plasma Beta

Finally, another crucial concept in the study of magnetohydrodynamics is the plasma beta. Plasma beta is defined as the ratio between the thermal and the magnetic pressure:

$$\beta = \frac{P}{P_{mag}} = \frac{nk_BT}{B^2/2\mu_0} \tag{1.14}$$

where the magnetic pressure (P_{mag}) is derived from the Lorentz force and is associated with the magnetic tension on a conducting MHD fluid, while the thermal pressure of the plasma (P) is defined in statistical mechanics as the product of the number density (n), the Boltzmann constant (k_B) and the temperature (T). Plasmas with a low β (<1), like those found in nuclear fusion reactors, will be dominated by the magnetic field, while plasmas with a high β (>1), such as the solar wind (away from the Sun), will be carried out by the particles in the plasma.

1.3 Morphology of the Jovian Magnetosphere

The Jovian magnetosphere is the largest single object in the Solar System and, accordingly, has a unique complexity, further enhanced by its fast rotation and the presence of an internal plasma source. Since the 1970s, several spacecraft (Pioneer 10 and 11, Voyager 1 and 2, Ulysses, Cassini, New Horizons and Juno) have flown through it and provided us with invaluable in-situ measurements taken by their many different instruments. The data provided by these missions, in conjunction with the development of plasma physics, MHD theory and better modelling, are the main ingredients for our current comprehension of the Jovian magnetosphere.

Regarding its composition, and besides electrons, in the Jovian magnetosphere, many species of ions have been observed by different spacecraft (Geiss et al. 1992): H^+, He^+, H_2^+, H_3^+, and many species of S and O, mostly of iogenic origin. Regarding its structure, and depending on the radial distance, the magnetosphere is usually divided into the inner, middle and outer parts. They are described below, right after a brief summary of the magnetic field topology.

1.3.1 Magnetic field structure

As the main engine driving its magnetosphere, Jupiter's unique and powerful magnetic field is necessarily worth being described, even if it is briefly. To first order, the Jovian magnetic field is, similar to the Earth one, dipolar, yet with significant contributions from the quadrupole and octupole moments (24% and 21% of the dipole, Acuña et al. 1976). However, the dipole axis of the magnetic field is tilted by about 10° with respect to the rotation axis of the planet and is oriented with its south polarity towards the south geographic pole (contrary to the case of the Earth). This dynamo is powered by the circulation of a conducting fluid in the outer core of the planet, which in the case of Jupiter's is metallic hydrogen (Smoluchowski 1971). The main peculiarity of this magnetic field, besides its sheer magnitude (with a dipole moment of around ∼18,000 times that of Earth, Olson et al. 2006) is the strong deviation from dipolarity that displays almost exclusively in its northern hemisphere. This unusual topology may be due to layering, either in density and/or electrical conductivity, as explained by Connerney et al. (2018).

The most complete and accurate models currently available for the Jovian internal magnetic field are JRM09 (Connerney et al. 2018) and JRM33 (Connerney et al. 2022). Their parameters were derived from the measurements taken by Juno during its first 9 and 33 orbits, respectively. These models are based on spherical harmonics (up to degree and order 10) and can be used to trace the location of a point in the equatorial plane of the magnetosphere to the ionosphere, as explained in greater detail in Section 2.4. An outline of the magnetic field configuration (and current systems) described by these models is shown in Figure 1.4. Figure 2.7a in the next Chapter shows the magnetic field magnitude (in Gauss) on the surface, in Cartesian coordinates.

They can be complemented by an external magnetic field component, such as the "flux equivalent" model by Vogt et al. (2011), to extend its validity range to the outer magnetosphere. This kind of model (such as the Con2020 utilised in this work) is based on the existence of the plasma magnetodisc, formed around 15-20 R_J from the material first expelled from Io and subsequently ionised (as described below). Due to the frozen-in-field property of the plasma, the magnetic field moves with it and also lags its rotation when the radial distance from the planet increases. This produces a spiral-shaped rotating flow (that can resemble the Parker spiral generated by the Sun, as shown by Fig. 1.4d, but with very different intrinsic properties and stretched by the solar wind pressure).

1.3.2 Inner magnetosphere (0-10 R_J)

In the innermost part of the magnetosphere, the quadrupole and octupole components of the magnetic field described above gain relevance (Acuña et al. 1976), but it is mostly a dipolar-like regime, with a particle population generally trapped in the magnetic field and showing a pancake-like distribution (with electrons maximum flux at around 90°, Tomás et al. 2004 and references therein). The presence of its moon Io dominates the inner part of the Jovian magnetosphere. Orbiting at 6 R_J, Io and the plasma torus produced by its continuous output of plasma play a crucial role in the general dynamics of the magnetosphere. Besides the key importance of this plasma torus as a plasma reservoir, described in more detail below, other remarkable structures within the inner magnetosphere are the "banana"-shaped sodium clouds (Thomas 1992), produced by atmospheric sputtering of this element by the ions on the IPT.

Io Plasma Torus

Voyager's in-situ and remote observations of Io and its vicinity showed that the moon is the primary source of plasma in Jupiter's magnetosphere, contributing around a tonne per second of material into it (compared to the estimated solar wind contribution of around 0.1 tonne/s). The material is mostly sulfur dioxide (SO_2), expelled through volcanoes into the moon's atmosphere through outbursts lasting a few days (Yoneda et al. 2010). From there, some of these exospheric, initially neutral, molecules, are then dissociated and ionised through different collisional and

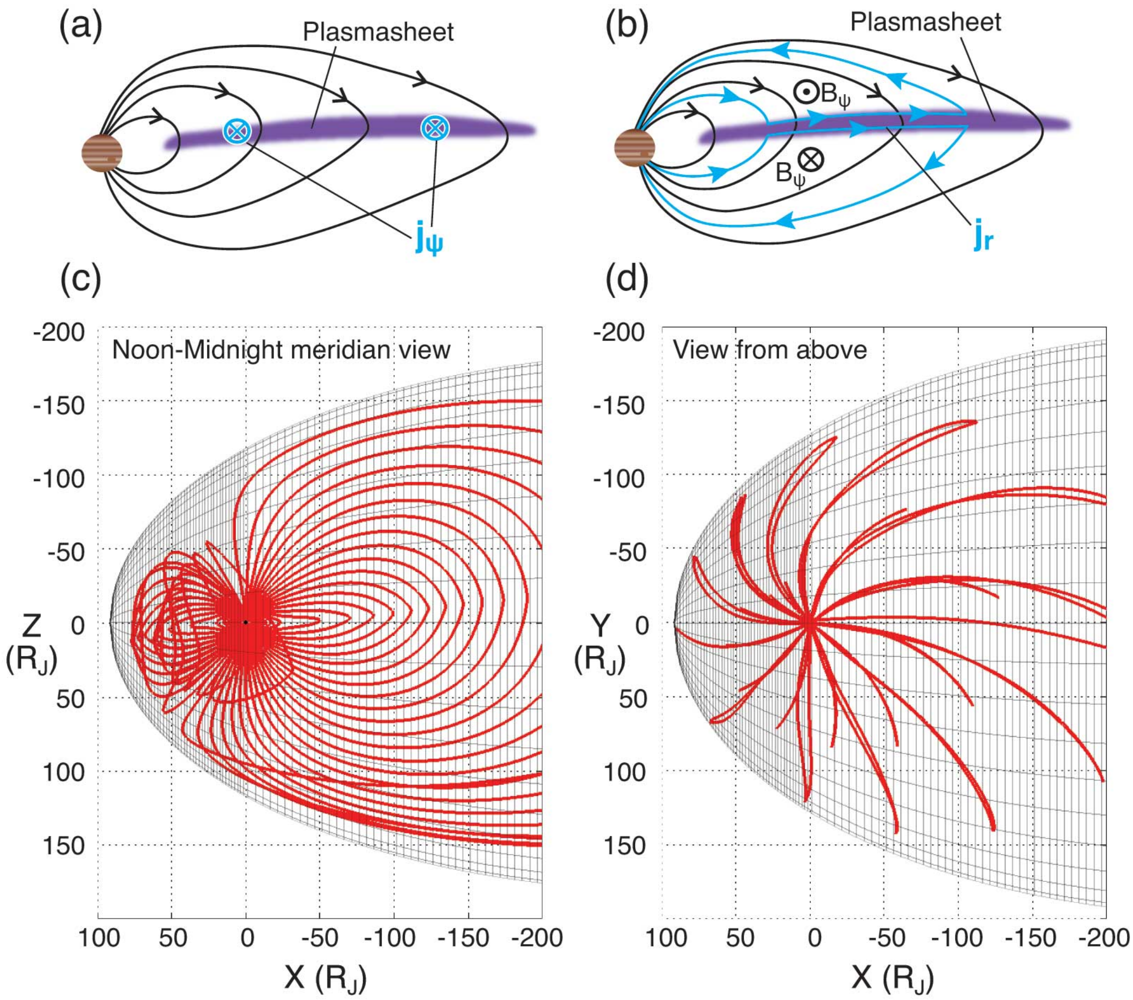

Figure 1.4: Magnetic field configuration and current systems in Jupiter's magnetosphere. The top diagrams show the (a) azimuthal and (b) radial current systems. The lower diagrams show the magnetic field configuration (c) in the noon-midnight meridian plane and (d) in the equatorial plane derived from in situ magnetic field measurements. Credit: Khurana et al. (2005).

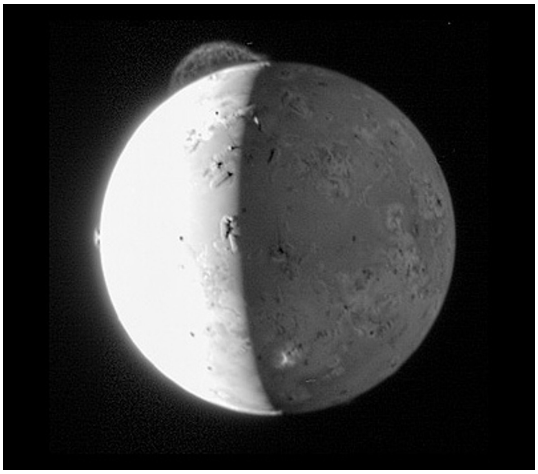

Figure 1.5: Plume erupting from Tvashtar volcano on Io (Spencer et al. 2007). Taken by the LORRI camera on New Horizons on February 28, 2007, from a distance of 2.5 million km. Credit: NASA.

ionospheric processes, e.g. sputtering or the jet of sodium, respectively (Thomas et al. 2023). This fresh plasma, thus composed mostly of various charged states of sulfur and oxygen, populates a torus region extending from about 5.2 R_J to 10 R_J (Bagenal et al. 1981), and with a total mass of ∼2 Mton.

The thermal electron gas in the torus is at a temperature of ∼200 eV. However, the torus features an inner cold zone with confined ions at ∼1 eV and an outer warm region where the more energised plasma diffuses under the influence of centrifugal force and interactions with Jupiter's plasmasheet. On the other hand, studies on volcanic plumes such as the spectacular Tvashtar plume (Fig. 1.5, Spencer et al. 2007) suggest an even more direct, yet not fully understood, impact on the Jovian aurorae by modulating its main emissions (Bonfond et al. 2012). However, the precise sequence and time scales of the effect of Io's volcanic activity on the auroral emissions are still a hot research topic in the field (Yoshikawa et al. 2017, Roth et al. 2024).

Radiation Belts

A combination of synchrotron emission analyses (Bolton et al. 2001), and in-situ investigations (like those carried out by Voyager 1, Galileo or Cassini) have progressively increased our understanding of Jupiter's radiation belts. These belts consist of relativistic electrons trapped in a near-dipolar, slightly offset, and tilted magnetic field. The belts form in Jupiter's inner magnetosphere due to plasma getting energised by electric fields as it diffuses inward. Ionospheric dynamo fields, produced by Jupiter's atmospheric motions, drive this radial diffusion (Brice et al. 1973), although it remains a question whether any other processes are energising the electrons.

More recently, Woodfield et al. (2014) have suggested that wave-particle interactions, and more specifically whistler mode chorus, may be the cause for the acceleration of the electrons that is required by the intense inner radiation belt (which peaks at $\sim$1.5 R_J, Pater et al. 2003). The origin of the particles populating these radiation belts, including the energetic neutral atoms that eventually become ionised, is probably further radially, though (Kollmann et al. 2021).

1.3.3 Middle magnetosphere (10-40 R_J)

The ring currents and the corotation breakdown region, mapping to the main emission described below, are both located in the middle magnetosphere. In this region, the iogenic plasma remains bound to the magnetic field, but its angular speed decreases as radial distance increases due to the conservation of angular momentum. The radial distance at which this occurs is called the corotation breakdown region, and it is thought to be a key element of the auroral emission in Jupiter, as explained in section 1.7.1. The deviation from corotation stems from two different physical phenomena. First, the finite conductivity of the plasma populating the ionospheric regions mapping to these parts of the magnetosphere (Hill 1979). Second, the waning of the equatorial magnetospheric field strength with radial distance, which due to the frozen-in field theorem brakes the plasma and make it subcorotate beyond a certain distance (Hill 2001, Cowley et al. 2001). More on this in the next section.

Magnetodisc, plasma and current sheets

When the first observations of Jupiter's magnetosphere were made by Pioneer 10, the term "magnetodisc" was introduced to describe the plasma confined near the magnetic equator because of the centrifugal forces on the corotating plasma in a rapidly rotating dipolar magnetic field (Connerney 1981, Khurana et al. 2004).

This disc can be considered to be axisymmetric around the dipolar magnetic field of the planet (at least until $\sim 20 - 30R_J$), rotating tilted with it (Achilleos 2018), as shown in Fig. 1.4a-b. The angular velocity gradient of the plasma mentioned above induces an equatorward Pedersen current, with the associated azimuthal $J \times B$ force maintaining partial corotation out to at least 60 R_J (Kane et al. 1995). In the middle magnetosphere, the azimuthal currents generate perturbation magnetic fields that become comparable to the planet's internal field beyond approximately 20 R_J. This deviation from the internal field is sometimes called the perturbation field and was first modelled by Connerney (1981), who used those characteristics of the disc to fit a magnetic field model to the measurements taken by the Voyager and Pioneer missions, and then by Caudal (1986). Its associated current system has been extensively studied for its responses to variations in mass outflow rate, ionospheric conductance, and solar wind pressure (Achilleos et al. 2015). The modelling of the magnetodisc is still a work in progress, e.g., Nichols et al. (2015), who has updated the original Caudal (1986) model of the Jovian magnetodisc to include the effects of anisotropic hot plasma pressure, which for example may explain latitudinal shifts in the location of the main emission. Connerney et al. (2020) proposed a magnetodisc model with a second current system, composed of outward radial currents that presumably mimic the outward transfer of angular momentum, which is the one used together with JRM33 in this work.

Jupiter's plasma reservoir, confined near the dipole magnetic equator, forms a thin sheet due to the mirror force's influence on gyrating particles on a non-uniform magnetic field (see top diagrams on Fig. 1.4). The current sheet location arises from a balance of centrifugal, thermal and electromagnetic forces. Therefore, its thickness is not constant, but rather increasingly modulated by changing plasma and field conditions further from the planet. Its thickness ranges between 3 and 15 R_J for dawn and dusk sectors of the outer magnetosphere, respectively (Khurana et al. 2004). This asymmetry results from dynamics consistent with the Vasyliunas cycle (Kivelson et al. 2005), caused by the unequal transport of returning flux from the magnetotail's plasmoids and the instability of the plasma field configuration on the nightside (Vogt et al. 2014).

The dipolar magnetic field approximation is no longer valid beyond ~20 R_J, and the magnetic field is strongly influenced by the ring current flowing azimuthally in the sheet (~30 MA between 10 and 20 R_J, Cravens 2004). This azimuthal current grows stronger further from the planet and develops a strong asymmetry in density between dayside (~88 MA) and nightside (~144 MA) in the middle magnetosphere, probably related to effects of the solar wind pressure (Khurana 2001).

The inner edge of the sheet lies near Io's orbit (~7.8 R_J). Between 10 R_J and 30 R_J, the vertical centre of the plasma sheet coincides with that of the dipole magnetic equatorial plane. This implies that Ganymede's trajectory intersects with the sheet on an orbital basis. The moon dives in and out of the plasma sheet, and these crossings create an asymmetry in its auroral emissions, by enhancing the brightness of the leading hemisphere when inside the plasma sheet (Saur et al. 2022, Greathouse et al. 2022). Beyond 30 R_J, the sheet is located more loosely between the centrifugal and magnetic dipole equators, and solar wind pressure starts affecting more strongly the sheet, especially in the magnetotail far from the planet (r>60 R_J), where the sheet "hinges" and becomes parallel to the solar wind flow (Khurana 1992).

1.3.4 Outer magnetosphere (>40 R_J)

The outer magnetosphere extends up to ~100 R_J on the dayside (with a very high variability depending on the solar wind conditions, Joy et al. 2002), while it virtually reaches Saturn's orbit on the nightside (>7000 R_J, or twice Jupiter's orbit). Several key structures are present in the outer magnetosphere: the lobes (regions of low plasma density and open magnetic field lines), the plasma sheet (already introduced, this higher-density region near the equatorial plane becomes flatter at these distances), and the boundaries between open and closed magnetic flux, with magnetic reconnection (see 1.2.2) processes facilitating energy transfer between these regions. More recent and precise measurements taken with Juno locate the magnetopause at dawn at 71-114 R_J and the bow shock at ~15-20 R_J beyond (Hospodarsky et al. 2017). The outer magnetosphere is the region where tail reconnection takes place, and it hosts the magnetotail current system, which connects the magnetodisc current to the magnetopause ones. It also harbours the poorly understood "cushion region", a ~20 R_J thick region embedded between the magnetodisc and the noon magnetopause with relatively emptied plasma flux tubes and an almost dipolar magnetic field (Went et al. 2011, Gershman et al. 2018).

Magnetotail

A magnetotail emerges towards the nightside of a magnetised body due to the pressure exerted on the body's magnetosphere by the solar wind and its consequent stretching. Its shape is determined by both viscous interaction and direct solar wind entry. As confirmed by the Voyager and Galileo spacecraft, Jupiter's magnetotail has a thin current sheet encircled by lobes. These lobes are regions devoid of plasma with a weakened magnetic field, and contain open flux connecting Jupiter and the interplanetary magnetic field (Behannon et al. 1981). This open magnetic flux however is not symmetrically distributed, occupying more the dawn side, which could be due to corotation-driven convection (Khurana et al. 2004).

Magnetic reconnection events have been long observed to take place in the magnetotail (Nishida 1983, Vogt et al. 2010), showing similar characteristics to the dipolarisation fronts detected in the terrestrial magnetotail (Kasahara et al. 2011) or the solar coronal mass ejections (Grodent et al. 2004). Plasmoids (coherent structures of plasma) associated with the Vasyliunas cycle (next section) have also been accounted for significant losses of plasma down the magnetotail, more likely to do so in a drizzle-like manner than in large-scale burst events (Bagenal 2007). Delamere et al. 2010 have suggested that the flanks of the tail are regions of mixing of material, where tailward iogenic material encounters incoming solar wind. X-lines (where anti-parallel plasma flows intersect) are suggested to locate beyond 80 R_J and up to 150-200 R_J downtail (Krupp et al. 2004). Figure 5.6a shows an example of X-line and plasmoid (Vogt et al. 2014).

Dawn-Dusk Asymmetry

The asymmetry in the distribution of the incoming open flux between dawn and dusk mentioned above is not the only one present in the outer magnetosphere. Kivelson et al. (2002) revealed that flux tubes are less stretched on Jupiter's dusk side due to Local Time variations of the normal field component (B_e). At $40-100R_J$ radial distance, B_e is nearly twice as strong on the dusk side than on the dawn side. Galileo's magnetic field observations show a thinner current sheet and different lobes on dawn and dusk sides, as already mentioned in the **Plasma and current sheet** part. This difference in the current sheet thickness can be attributed to an asymmetric distribution of open flux across the magnetotail (Krupp et al. 2001). This is supported by the observation of bi-directional streaming of particles on closed field lines on the dusk side (Krupp et al. 1997) and open regions on the dawn sector (Zhang et al. 2021). Corotation-driven convection may explain the flux distribution differences; observations of the ionospheric flow by Stallard et al. (2003) suggest the existence of a unique convection cell at dawn, but not at dusk (Delamere et al. 2010). The aforementioned difference in thickness for the dawn (thinner) and dusk (thickest) sectors of the plasma sheet is explained by the Vasyliunas cycle (Vogt et al. 2014): the plasma becomes unstable on the nightside and is accelerated down the tail; the emptied flux tubes keep rotating towards dawn and carried inwards via interchange motions; they refill at dayside through diffusion and keep the cycle going (Kivelson et al. 2005). Finally, Lorch et al. (2020) showed Local Time asymmetries extend to the radial and azimuthal currents up to at least 30 R_J, having a strong and often overlooked impact on the location of field-aligned currents. In general and related to many of these asymmetries, it is becoming increasingly clear that the solar wind may have a greater influence on many processes taking place in the Jovian magnetosphere than previously thought.

1.4 Dynamics of the Jovian magnetosphere

We already know that the plasma in the Jovian magnetosphere, generated by Io and propelled by the centrifugal force, essentially corotates. But that is only true up to a certain (radial) extent. Now, I will study more carefully the main guidelines and theoretical frameworks that explain the dynamics of the Jovian magnetosphere. I will start with the radial transport and the interchange instability, continue with the Dungey cycle, then transition to the Vasyliunas cycle, more relevant to Jupiter, and end with the arguments for (and some against) the corotation enforcement currents theory. Figure 1.6 depicts the Jovian magnetosphere (bottom left), as compared to those of Mercury, Earth and Saturn.

1.4.1 Radial transport and interchange instability

The radial transport of plasma involves energy changes describable through the conservation of adiabatic invariants (or adiabatic compression/expansion) within magnetic flux tubes. The radial transport of plasma acts as a main diffusion process in the inner and middle magnetosphere of Jupiter. However, the exact mechanism through which the plasma is transported radially is not clear yet and remains one of the biggest mysteries in the Jovian magnetosphere. The difference in the estimated transport time scales for this radial diffusion (tens of days for the thermal part of the plasma at $L>5.7$, and a few years for $L<5.7$, Richardson et al. 1980) suggests two different processes happening inwards and outwards. The outwardly directed centrifugal force can favour interchange instability, which is why this has been broadly considered one of the best candidates for the radial motion of plasma

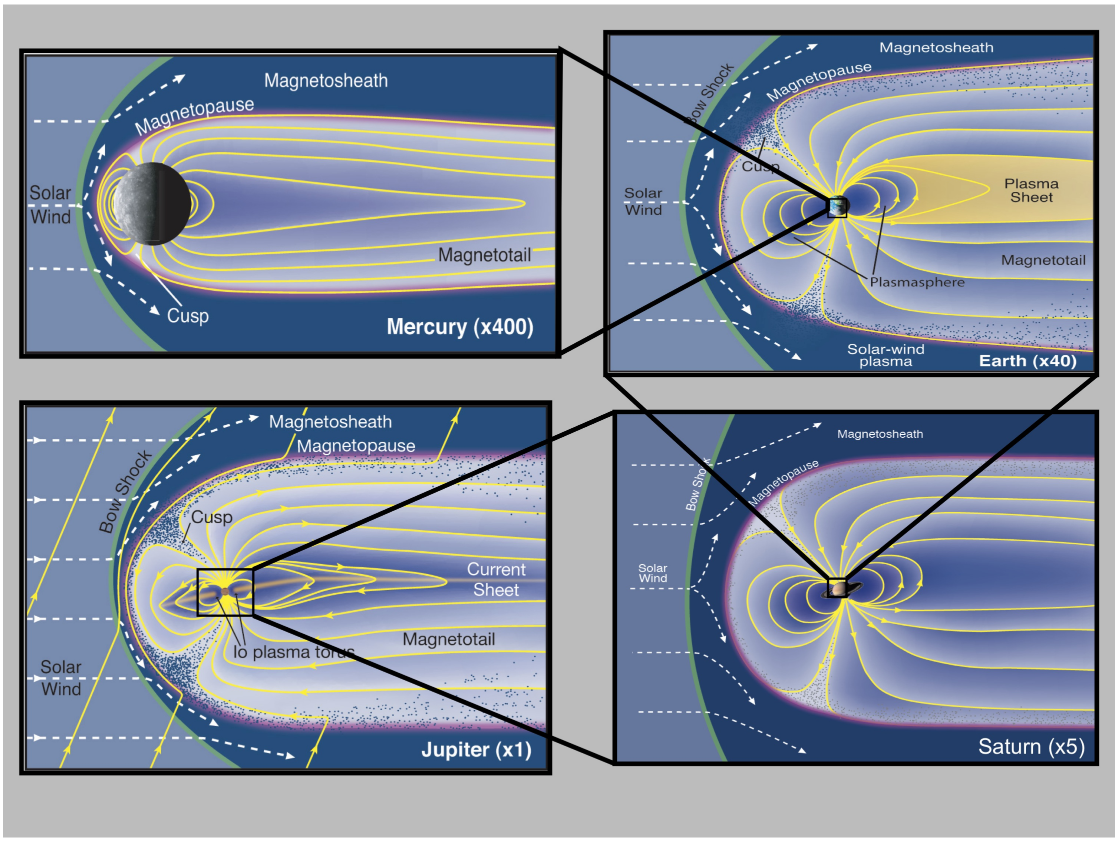

Figure 1.6: Comparison of different planetary magnetospheres in the Solar System: Mercury, Earth, Saturn, Jupiter. Credit Fran Bagenal and Steve Bartlett.

beyond the orbit of Io (Southwood et al. 1989).

The interchange, or flute, instability is a type of hydromagnetic instability which arises from a gradient of plasma pressure when it is aligned with a magnetic field. In that situation, the plasma moves to occupy the location of the empty flux tubes in order to conserve magnetic flux at the boundary, therefore without modifying the magnetic field configuration. This interaction is similar to the Rayleigh-Taylor one provoked by gravity, and like that one, it favours narrow interchange tubes in and out of the plasma gradient.

In the case of Jupiter, the constant outflow from Io creates a pressure and density gradient which, combined with the Jovian magnetic field structure, provides the conditions for this instability to occur. In particular, hot and underdense plasma flux tubes move radially inwards, swapping their location with the cold and denser plasma which was originally closer to Io. This interchange has been suggested to happen in two different scales: a smaller one close to the plasma torus edges (Kivelson et al. 1997), and a larger one further in the middle magnetosphere, where the hot plasma could have a reconnection origin (Mauk et al. 2002; Mitchell et al. 2015; Southwood et al. 1989).

1.4.2 Dungey cycle

The first of the two main mechanism theories which broadly explain the magnetospheric plasma dynamics and the origin of the aurorae is called the Dungey cycle, from the 1961 seminal paper in which it was first proposed (Dungey 1961), applied to the context of the Earth. According to this theory, the solar wind is the main driver of the aurorae. It does so via reconnection, first occurring at its dayside magnetopause, and then closing the cycle through the tail after dragging the open field lines in the anti-sunward direction. The circulation of plasma is thus driven by convection and "pushed" by the solar wind.

The Dungey model is an oversimplified view that does not account for additional processes such as viscous interaction at the magnetopause, quick variations in the solar wind (it is a steady-state model), ionospheric outflow, or wave-particle interactions. However, it still is the most essential model of an open magnetosphere. The concept of magnetic reconnection, happening both at dayside and nightside (down the tail), is the solution for the magnetic flux not to be lost entirely, and the key factor of this magnetospheric convection cycle. The observation of the modulation of the geomagnetic activity by the vertical (y) component of the IMF by Fairfield et al. (1966), as well as the distinct spectrum of electrons found on polar-cap lines, or the observation of magnetic reconnection (Paschmann et al. 1979, Burch et al. 2016) have all proved the validity of the Dungey cycle on Earth. Since its original steady-state model, however, subsequent refinements and extensions to the theory have been proposed. They have served to explain the variability of magnetospheric convection driven by the solar wind, which can be described by the expanding/contracting polar cap model (ECPC, Cowley et al.; Milan 1992; 2013). Regarding Jupiter, Badman et al. (2007) showed that the Dungey cycle may contribute a minority yet significant fraction of the transport of magnetic flux within the outer parts of the closed field regions (Figure 1.7 shows the Dungey cycle flows). Alternatively, viscous interaction between denser plasma inside the magnetosphere and tenuous plasma from the solar wind could intermittently open and close flux in small-scale structures on the flanks of the magnetosphere (Delamere et al. 2010).

1.4.3 Vasyliunas cycle

At Earth, the large-scale circulation of magnetospheric plasma is primarily driven by the solar wind through convection. Solar wind plays the leading role, acting as both the major source and the strongest influence on the magnetospheric plasma, as explained by the Dungey cycle. However, at Jupiter, the situation is more complex. While the solar wind still contributes in both energy and mass to the system (so the Dungey cycle still takes place to a limited extent, mainly in the outermost regions of the magnetosphere, Southwood et al. 2016), it is the internal source of Io, for the material, and the planet's rotation, for the energy, which is far more dominant.

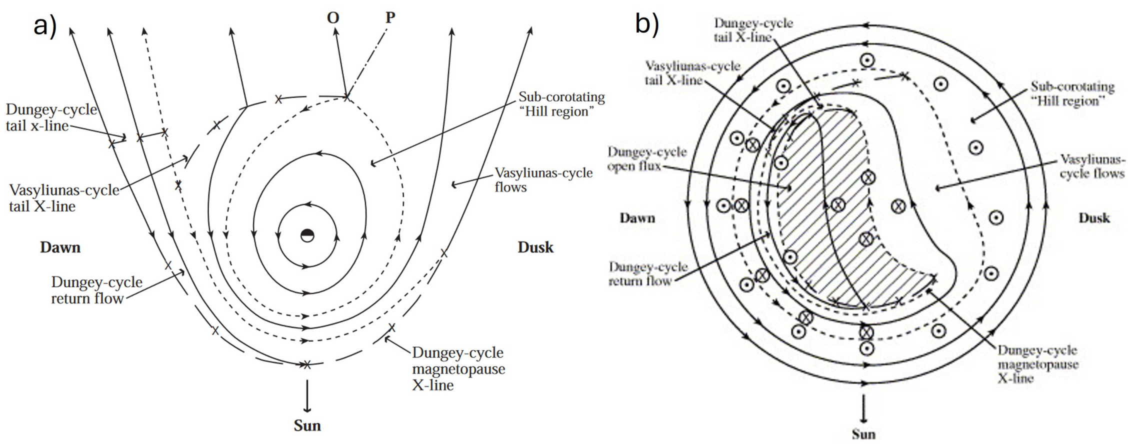

Figure 1.7: Sketch of the plasma flows a) in the jovian equatorial plane, and b) in the northern jovian ionosphere. Solid lines with arrows show plasma streamlines, while dashed lines with arrows separate different flow regions. Dashed lines with "X"s: X-type reconnection lines. Solid line with "O": the O-type line of the Vasyliunas-cycle plasmoid ejected downtail. Dot-dashed line marked "P": outer boundary of the plasmoid. Credit: Cowley et al. (2003).

The Vasyliunas cycle (Vasyliunas 1983) is the most relevant model to understand the dynamics of the Jovian magnetosphere. In this theory, radial diffusion is the main transport mechanism of plasma and energy within the magnetosphere (see Figure 1.7). Under-dense flux tubes move towards the planet, while denser ones move outward through unstable overturning interchange motions (Southwood et al. 1989). When plasma pressure equals magnetic field pressure, flux tubes expand radially, eventually leading to material loss via magnetic reconnection down the magnetotail only (and not the dayside magnetopause, like in the Dungey cycle). Another difference with the Dungey cycle is that this expansion of the flux tubes is not driven by the solar wind but by the centrifugal force caused by fast-rotating magnetospheres like the Jovian one.

From Voyager 1 and 2 back in the 70s, to the most recent Juno spacecraft, observations from multiple spacecraft missions have revealed reconnection events around different parts of the Jovian magnetosphere, supporting the validity of the Vasyliunas cyle. These reconnection events are usually identified as rapid changes in the magnetic field direction (or magnitude), often as dipolarisations of the field. The signatures of X-type magnetic reconnection down the tail predicted by the Vasyliunas cycle have been detected in Jupiter, by instruments onboard Galileo (Vogt et al. 2010) or Juno (Vogt et al. 2020), and in Saturn, by Cassini (Smith et al. 2016), while for example New Horizons detected evidence of discrete plasmoids (O-type reconnection) at distances as large as 2000 R_J (McComas et al. 2007). A periodicity of 2-3 days has been found in the frequency of reconnection burst events (Vogt et al. 2010, Krupp et al. 2015), which may be explained by the time needed for the emptied field lines to return to the planet (while sub-corotating) and re-start the mass loading cycle (Badman et al. 2015).

The corotation enforcement current theory

The corotation enforcement current (CEC) theory is the most commonly accepted theoretical framework for the explanation of the main emission in Jovian aurorae (Cowley et al. 2001, Southwood et al. 2001). The main idea is that the system of field-aligned upward currents coming from the middle magnetosphere plays a pivotal role in the transfer of momentum from the ionosphere to the plasma sheet. This momentum is carried radially outward within the sheet, where the $\mathbf{J} \times \mathbf{B}$ force acts as the driving mechanism, propelling the magnetospheric plasma toward corotation with the planet.

Models predict that field-aligned currents coupling the magnetosphere and the ionosphere reach their peak near the region where the system can no longer maintain full corotation with the planet, known as the corotation breakdown distance (Khurana et al. 2004). According to the Knight kinetic theory (Knight 1973, or its updated version by Ray et al. 2009), field-aligned potentials are expected to form around that region, accelerating electrons into the atmosphere, to provide the required current density and generate the aurorae by exciting the atmospheric particles, as explained in section 1.6. At the opposite end of this circuit, equatorward-flowing Pedersen currents close it, creating a $\mathbf{J} \times \mathbf{B}$ force opposite to the rotation

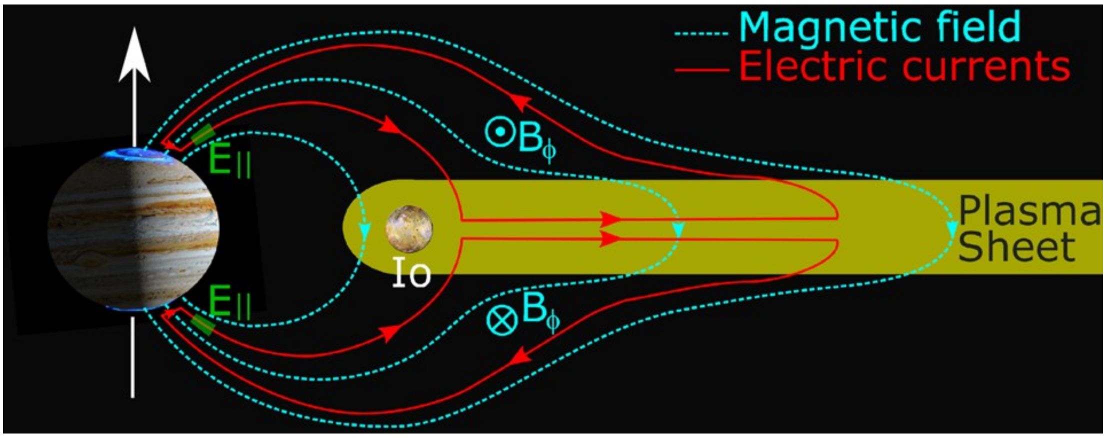

Figure 1.8: Classical scheme of the corotation enforcement currents model to explain the main auroral emissions at Jupiter (after Cowley et al. 2001). The dashed cyan lines represent the magnetic field, the solid red lines represent the electric currents, and the green lines are the electric fields accelerating the electrons into the aurora. Credit: Bonfond et al. (2020).

of the planet and that balances out the friction between the neutrals and the ions. This cycle is sketched in Fig. 1.8, and some examples of the currents participating in the system (including the ring current) are outlined in Fig. 1.9.

Having stated the corotation enforcement current theory, it is necessary to acknowledge that some authors like Bonfond et al. (2020) have argued that this is not a complete enough mechanism to explain the fundamental characteristics of the main emission. Their arguments are: the asymmetries found between dawn and dusk sides in both particle velocity measurements (Krupp et al. 2001) and brightness of the main emission (Bonfond et al. 2015); the unexpected observed anti-correlation between the intensity of the aurorae and the solar wind pressure (Nichols et al. 2007, Nichols et al. 2017); the brightness variations due to the loading and unloading of magnetic energy (Yao et al. 2020); the weakness and asymmetry between hemispheres of the field-aligned currents (Connerney et al. 2017); and, associated to the latter, the previously underestimated role of the stochastic acceleration to the detriment of quasi-static potentials as drivers of the main emission (Mauk et al. 2018). However, other studies still support the CEC theory, for example linking the

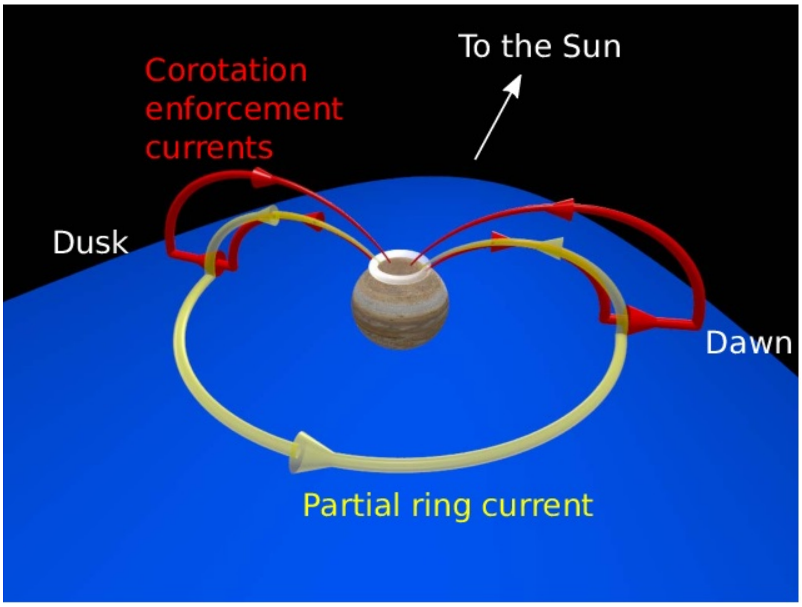

Figure 1.9: Scheme of the two current systems suggested to affect the main emission brightness (for the Northern hemisphere). The blue area represents the magnetosphere and the Sun is towards the top. The corotation enforcement current loops are present at all Local Times, albeit with varying intensity, but only the dawn and the dusk loops are shown. On the dusk side, the currents of the lower latitude field-aligned branches flow in the same direction, thus leading to a brighter aurora, while the currents on the dawn side flow in the opposite direction, leading to a dimmer aurora. Credit: Bonfond et al. (2015).

azimuthal component of the magnetic field with the auroral power (Nichols et al. 2022).

A proposal for a complete alternative to the corotation enforcement current theory is, however, non-existent as of today. In very broad terms, the current paradigm points toward a refinement of this theory, by considering and including in it the role of Local Time effects (as opposed to axisymmetric models), wave-particle interactions (as opposed to assuming steady-state currents), and the Poynting flux and Alfvén waves (including a deeper understanding of stochastic acceleration processes, as opposed to relying solely on the FACs to decipher the origin of the main emissions).

1.5 Planetary Aurorae

Aurorae are large-scale manifestations of electromagnetic radiation produced when particles in an atmosphere de-excite and emit photons. These emissions can occur in the visible spectrum, producing the captivating displays witnessed from Earth, or in other wavelengths, such as the UV range that this study will focus on. The energy necessary to ionise, excite, or dissociate the atmospheric atoms and molecules, and eventually produce the photons that form the aurorae, is provided by external particles arriving from the magnetosphere. These particles can reach the upper levels of the atmosphere through a myriad of processes, some of them mentioned in section 1.6.1. The aurorae can be seen as the signatures of the magnetospheric dynamics since they are closely linked to (and thus shed light on) a myriad of aspects such as the atmospheric and ionospheric compositions and structures, the energy balance, the plasma transport, the strength of the solar wind, or the magnetic field topology of a planet (Bhardwaj et al. 2000).

1.5.1 Aurorae in the Solar System bodies

Aurorae are not a treasure exclusive to the Earth. In fact, have been observed even outside of our Solar System (e.g., through both optical and radio spectroscopy of a brown dwarf, Hallinan et al. 2015). However, so far, it is in our planetary neighbourhood where we can find plenty of examples of different types of auroral emissions and the physical mechanisms producing them. As expected, the most interesting case for this thesis is the one of Jupiter, which is why it will be left for the end of this section (the physics behind its emissions have already been addressed and its auroral structure will be described in detail in the next section). Again, Figure 1.6 presented schematically the magnetospheres of Mercury, Earth, Saturn, and Jupiter, for comparison of their scales and structures.

The rocky planets

Mercury's lack of significant atmosphere prevents it from having strong aurorae. However, the small size of its magnetosphere (about 5% of that of Earth) combined with the intense solar wind it receives, makes it prone to fast reconfigurations following the above-explained Dungey cycle. This results in nightside fluorescence events caused by the precipitation of magnetospheric electrons, as observed in X-ray by MESSENGER spacecraft (Lindsay et al. 2016).

Venus does not have a strong enough magnetic field to create aurorae the way they are created on Earth. Nevertheless, it does display auroral emission from Oxygen lines bright enough to be detected in the UV (Gérard et al. 2008) and visible ranges (Slanger et al. 2006), as well as nightside airglow in the IR (Hueso et al. 2008). The 5577 Å Oxygen green emission line has also been detected, potentially caused by dayside photodissociation from strong solar flare photons and subsequent recombination from electrons precipitating from CMEs or dense solar wind streams, according to Gray et al. (2014). Furthermore, Zhang et al. (2012) showed signs of magnetotail reconnection despite it being a non-magnetised planet.

Similarly to Venus, **Mars** does not have an internal magnetic field (Acuna et

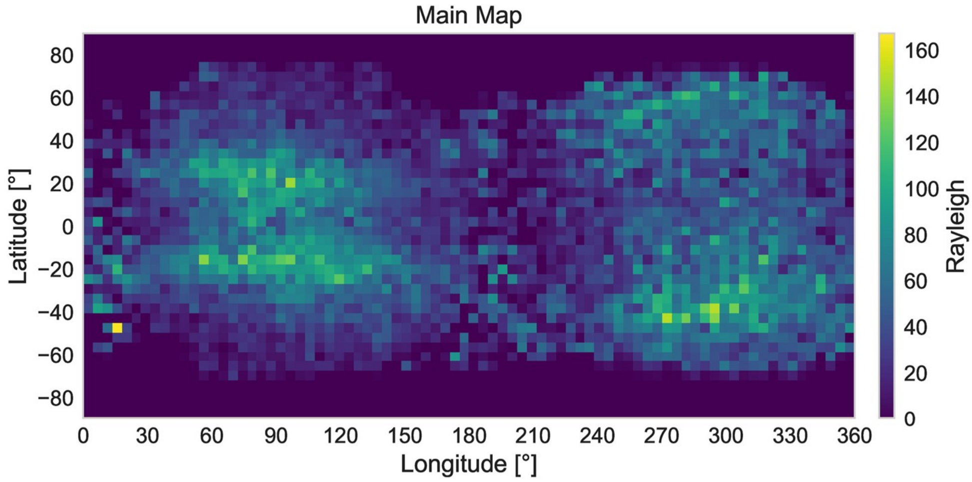

Figure 1.10: Brightness map of Oxygen 1,356 Å emission on Ganymede, incorporating 46 exposures from HST-STIS between 1998 and 2017, in Mercator projection. Credit: Marzok et al. (2022).

al. 1998), but it has proven to have up several different types of auroral precipitation. First, it displays some discrete, localised aurorae in regions where remnant crustal magnetic fields are found (Bertaux et al. 2005). Second, it also has a global diffuse aurora similar to that of Venus, detected on its nightside (Schneider et al. 2015). Third, a proton aurora occurring on the dayside has been recently detected by MAVEN spacecraft (Deighan et al. 2018). Finally, and more recently, some elongated, so-called sinuous auroras have also been detected at nightside, potentially linked to the IMF orientation and the electron energisation in the magnetotail current sheet (Lillis et al. 2024).

Although it is not a planet, it must be noted the case of the Galilean moon **Ganymede**, the only satellite known to have its own magnetic field, which is not too dissimilar to Mercury's. Auroral emission has been not only detected as FUV airglow emission (Hall et al. 1998) but also imaged by HST-STIS (Feldman et al. 2000, Marzok et al. 2022), as can be seen in Fig. 1.10. Saur et al. (2022) has suggested that this aurora is powered by stresses generated from the coupling between the moon's asymmetric magnetic field and the Jovian plasma sheet north and south of its magnetosphere.

Lastly, the **Earth** is the most studied body in our Solar System for obvious reasons, and the understanding of its aurorae has set the initial blueprint for the posterior auroral research in all the other planets. However, the auroral emissions on Earth are unique due to the combination of being the only rocky planet with a strong magnetic field, lacking an internal plasma source (such as the gas giants) and being considerably closer to the Sun, i.e., more affected by its wind of particles.

In a nutshell, Earth aurorae are ruled by the Dungey cycle described above. This mechanism drives strong currents around the magnetic field and energises plasma such that energetic, charged particles flow into the ionosphere above the poles and generate the auroral emissions, which often appear as a well-defined oval surrounding a devoid polar region above 70° to 75° in latitude. The dependence on the conditions of the solar wind (known as space weather) has a direct impact on the latitude and the brightness of the Earth's aurorae. The most dramatic example of this relationship takes place when a burst of plasma from the Sun reaches the Earth's magnetosphere, triggering magnetic storms that can affect satellites and communications, besides powering beautiful Northern and Southern lights in the upper atmosphere (Miller 2021, and references therein).

Saturn

Saturn is another example of magnificent auroral displays. This giant planet is peculiar because, as Cassini showed, it seems to combine both the Earthly and the Jovian mechanisms (solar wind-driven and with an internal plasma source, respectively) in a complex, and not yet fully understood, equilibrium (Mauk et al. 2009, Bradley et al. 2020). Its magnetosphere is rotationally dominated, but the main aurora is less constant than on Jupiter and seems to be heavily modulated by CIR and changes in the solar wind pressure. In other words, the main auroral oval at Saturn, like that on Earth, maps to the boundary between open and closed magnetic flux.

Analogously to Jupiter and Io, Saturn has its own internal source of plasma, which is its moon Enceladus. Through its cryogeysers, Enceladus loads the inner magnetosphere with ∼250 kg of water vapour and ice every second (Hansen et al. 2011, Ingersoll et al. 2011), from which a fraction of 17-38% will eventually become ionised (Jurac et al. 2005). That plasma outflow is balanced out by quasiperiodic magnetotail reconnection of the nightside magnetodisc (with very weak or non-existent dayside reconnection).

On top of that, there are a couple of significant features of the Kronian magnetosphere worth mentioning. The first is the almost perfect axisymmetry of its magnetic field, which surprisingly does not prevent the flapping of its current sheet with the rotation period of the planet (Arridge et al. 2008). And last but not least, the preponderant role of the neutral gas population, which is considerably greater than the one at Jupiter (Smith et al. 2010), and whose energetic component (ENAs) are formed around concentric tori around the planet (Kinrade et al. 2021).

The Ice Giants

The information we have about Uranus and Neptune is quite limited (which only adds to the existing reasons to send a spacecraft to at least one of them to explore it from up close). Their magnetospheres seem extremely complex to model due to the large angles between their rotation and magnetic axis, as well as their non-dipolarity. Most of the data we have available on them comes from the 1980s Voyager 2 flybys. The spacecraft detected auroral emission at radio and UV, but the latter has only been re-observed ever since then in Uranus, not in Neptune (Lamy 2020). The Uranian UV aurora showed stark seasonal variability due to the interaction between its magnetosphere and the solar wind (Lamy et al. 2017). (Near) IR aurorae has also been detected only in Uranus (Thomas et al. 2023), and according to Melin et al. (2019), the H_3^+ measurements from its upper atmosphere reveal a steady and puzzling cooling between, at least, 1993 and 2018.

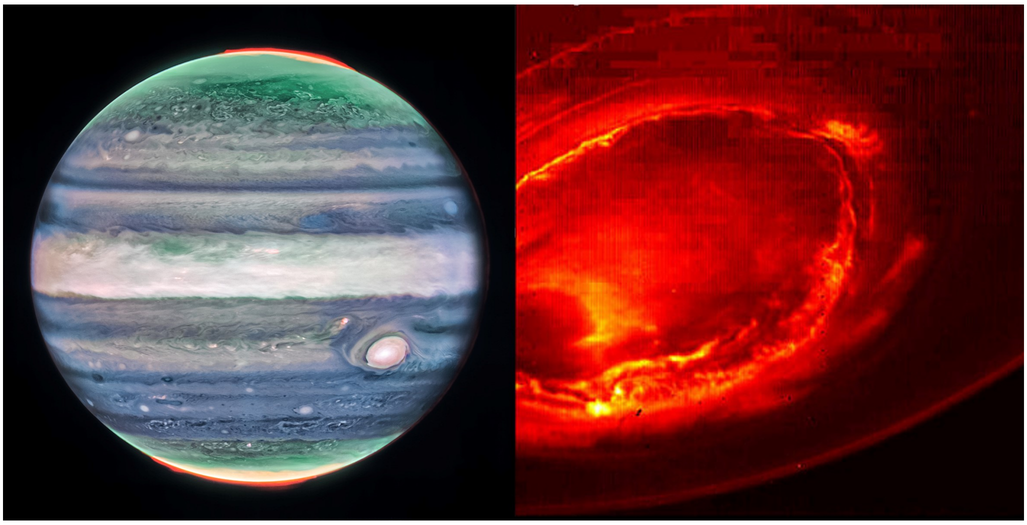

Figure 1.11: Left: IR image of Jupiter from James Webb Space Telescope's NIRCam (Near-Infrared Camera) showing aurorae, appearing in red above and below the polar regions. Credit: NASA, ESA, CSA, STScI, R. Hueso (EHU). Right: detailed image of Jupiter's southern IR aurora taken by the Juno JIRAM imager. Credit: Mura et al. (2017).

Jupiter

Dominated by the Vasyliunas cycle, Jupiter's magnetospheric dynamics has such a large scale that a myriad of processes influence it to different degrees. For example, although the Dungey cycle is not the dominant engine of the aurorae, the solar wind does have an impact on Local Time auroral distribution (Yao et al. 2022) and the electron energisation (Yao et al. 2019), among others.

Jupiter's aurorae have been observed in a good fraction of the electromagnetic spectrum. The first detections were made in **radio** signals by Burke and Franklin et al. (1956). Those first detections were in the 13.6m wavelength, but there is a very wide range of relevant bands in which Jupiter emits, from the hectometric (HOM) and decametric (DAM) emissions, correlated with the solar activity (and Io, in the case of a subtype of the DAM), to the narrowband kilometric (n-KOM) emissions, linked to internal dynamics.

The emission in **IR** from the H_3^+ in the upper atmosphere of the planet is another important auroral display that has been observed by several different instruments such as JWST-NIRCam (1.11, left) or Juno-JIRAM (right). The H_3^+ ions form from the ionisation of H_2 caused mainly by EUV radiation in the low-latitude regions and energetic precipitating electrons in the auroral regions. H_3^+ acts as a heat sink that radiatively cools the thermosphere (Lam et al. 1997, Bougher et al. 2005). This ability to re-radiate heat into space allows its use as a proxy for the cooling of the atmosphere (Johnson et al. 2018).

Although substantially weaker, the Galileo spacecraft took the first images of Jupiter's aurorae at **visible** wavelengths at the nightside of the Northern hemisphere in 1996 (Ingersoll et al. 1998; Vasavada et al. 1999). This emission is produced by dissociative excitation of molecular hydrogen due to the impact of energetic particles on the H_2.

Finally, soft **X-ray** emission has also been detected in the polar regions of the planet since 1983. In this case, the aurorae are caused by iogenic sulfur and oxygen ions precipitating onto the ionosphere, although many questions remain regarding the role of mechanisms such as outer magnetospheric EMIC waves (Yao et al. 2020; Yao et al. 2021) or dayside reconnection (Bunce 2004) as modulating factors of these emissions. Findings of hard X-ray emissions caused by electron bremsstrahlung radiation were also obtained with XMM-Newton in 2007 (Branduardi-Raymont et al. 2007). A more detailed description of the X-ray aurorae and its comparison with the UV emission is provided in its dedicated Section 5.1 of Chapter 5.

1.6 Auroral mechanisms

The energetic precipitating particles interact with the ones in the atmosphere through elastic scattering and inelastic collisions. These collisions can include ionisation, excitation, dissociation, or combinations thereof. In these interactions with the atmosphere, the particles lose energy and their pitch angles change. The proportion of energy lost in collisions with neutrals increases as the electron energy rises (Galand et al. 2011). Different wavelengths have different emission processes associated with their aurorae, and emissions in radio, UV, visible, IR, and X-ray have been detected in the Solar System.

1.6.1 Particle acceleration processes

Particles in a magnetic field can get accelerated from a wide range of physical processes, including shock waves, stochastic, electric fields/FACs, and reconnection (as it was first discovered on Earth's magnetosphere, Paschmann et al. 1979). But all these processes can be more widely categorised into two families: unidirectional and stochastic acceleration processes. Without entering into too much detail, this general classification is equivalent to the consideration between adiabatic (or quasiadiabatic) processes, and the non-adiabatic processes (i.e. whether they violate or not the first and second adiabatic invariants, Hill 1983). Finally, the specific process of pitch angle scattering is briefly considered.

Field aligned/Potential driven acceleration

Electric fields with a parallel component to another magnetic field (which can arise, for example, as a result of magnetic field reconnection, Vasyliunas 1975) can accelerate charged particles. This process is particularly significant in regions associated with Jupiter's aurorae, where strong electric potentials along the magnetic field lines accelerate electrons and ions. Since arriving at Jupiter, Juno has observed instances of field-aligned proton and electron beams, in both the upward and downward current regions (Ebert et al. 2017, Mauk et al. 2020). These field-aligned beams are identified by inverted-V structures in plasma data, which occur when particles accelerated by the potential drop gain a range of energies, forming a spectrum with a peak corresponding to the maximum potential drop.

These parallel potential drops have been observed to develop in an acceleration region between ~1.6 and 2.9 R_J over the polar caps (Clark et al. 2017), although their actual origin is relatively unknown. According to Mauk et al. (2017b), the downward energy flux from discrete acceleration is much less at Jupiter than that

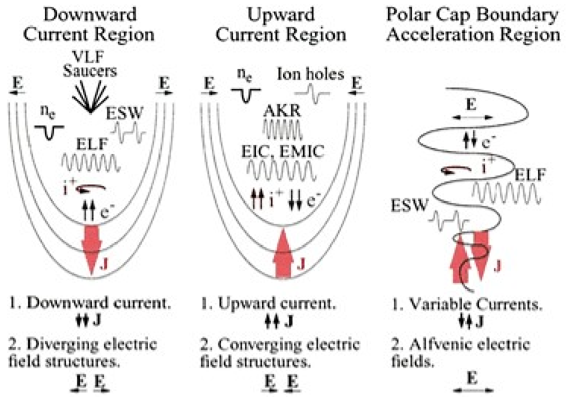

Figure 1.12: The three types of auroral zones based on experience from Earth: upward currents, downward currents and Alfvénic regions. Adapted from Carlson et al. (1998).

caused by broadband or stochastic processes (around ∼7%, Salveter et al. 2022). More on the regions associated with these two types of acceleration in Section 1.7.1 and in Figures 1.12, which presents a summarised version of the plasma properties that characterise the two regions, and 1.15 (for the Jovian main emission).

Stochastic/Broadband acceleration

Stochastic acceleration in the Jovian magnetosphere goes hand in hand with kinetic Alfvén waves (Saur et al. 2018). These waves cause both Landau damping (dominating around the inner magnetosphere) and cyclotron damping (more important beyond 30 R_J). These two mechanisms consist of the energy loss of the waves to particles in resonance with them. In the case of Landau, the resonance is between the velocity of the particles and the phase velocity of the wave, while cyclotron damping occurs when the gyrofrequency of the particles matches the frequency of the wave.

The resulting broadband bidirectional electron distributions have been observed above Jupiter's main oval and polar regions (Mauk et al. 2020). A spectrogram example of these distributions (transitioned from an inverted-V) is shown in Figure 1.13. Alfvén waves are also in the origins of the electrons precipitating to form

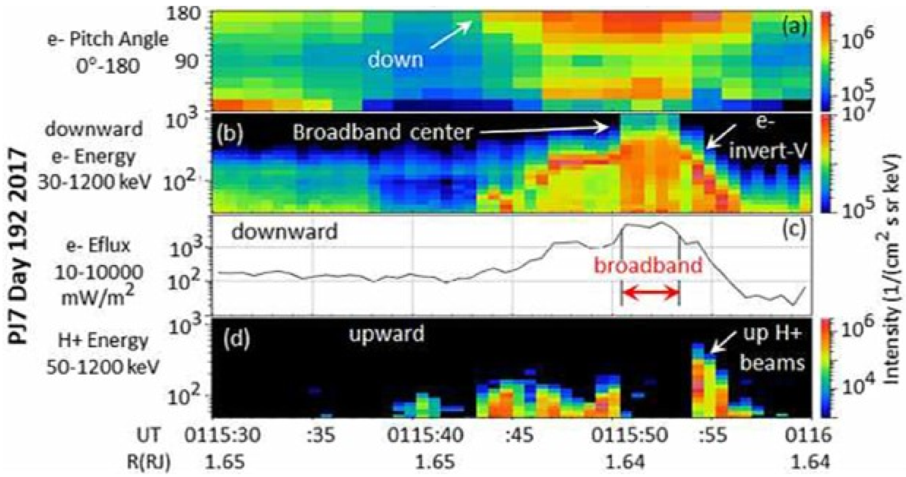

Figure 1.13: PJ-7 north example of the transition from an inverted-V distribution to a broadband distribution. (a) Electron pitch angle distributions. (b) Downward electron energy distributions. (c) Estimated downward electron energy fluxes. (d) Upward proton energy distributions. Credit: Mauk et al. (2020).

the moon footprints. In general, the role of stochastic acceleration seems to be increasing in importance in the Jovian magnetosphere (Allegrini et al. 2017). Since it often appears very close to regions of potential-driven acceleration, it has been suggested that some instabilities of strong potential-driven plasma may sometimes make it transition to broadband acceleration (Mauk et al. 2018).

It must be noted that there are other types of wave-particle interactions, such as the whistler-mode waves (Woodfield et al. 2014, Mauk et al. 2002) that can accelerate electrons and cause them to scatter.

The pitch angle scattering could be considered a third type of particle acceleration process but since it can also be provoked on its part by the two described above, it will not be considered as such. Scattering occurs when collisions make the pitch angle of an electron small enough that it falls within its loss cone, making the particle precipitate into the ionosphere. Electron pitch angle scattering is the culprit of Jupiter's diffuse emission (Li et al. 2017, Allegrini et al. 2017). Through this process, electron PADs would transition from normal pancake distributions (peaking in the direction perpendicular to the field) to a quasi-isotropic distribution (Tomás et al.

2004). The trigger of this scattering is still unknown, with the previously mentioned whistler-mode waves having been suggested as such (Mauk et al. 2002), supported by recent evidence from Juno measurements that show the violation of the adiabatic motion of the electrons between 2.5 and 7.2 R_J (Elliott et al. 2018).

1.6.2 Emission in UV

Due to the dataset used in this work, I am focusing on the UV range, although a more comprehensive and wide explanation for the giant planets across the entire spectrum is provided by Badman et al. (2015), and a brief summary of X-ray emissions is provided in section 5.1.

Jupiter's (like Saturn's) UV emissions mainly consist of H Lyman α and, mostly, H_2 Lyman and Werner bands. The strength of these bands is directly related to the excitation rates to the B and C states, respectively. Transitions from other excited states of H_2 (B', B", D, D') also contribute to EUV emission in the 80–120 nm range, to a smaller degree. UV auroral emissions at wavelengths below 130 nm and 120 nm are absorbed and modified by hydrocarbon molecules and H_2, respectively. The UV colour ratio, defined as the ratio of the intensity in a range with no hydrocarbon absorption (such as 155-162 nm) to that of an absorbed waveband (e.g. 123–130 nm), provides an estimate of the amount of hydrocarbons present above the emission altitudes. Because hydrocarbons are found at low altitudes, an increase in their column indicates either deeper penetration (i.e., higher energy) of the precipitating particles, or an increase in high-altitude hydrocarbon content due to changes in the local atmosphere (Livengood et al. 1990, Gérard et al. 2003).

For reference, the average energies of the precipitating electrons range from 1-2 keV for Io's footprint (Bonfond 2010) to characteristic energies of a few tens of keV for the polar region and the main emissions (Benmahi et al. 2024), with differences between the hemispheres, and reaching several hundred of keV in the acceleration regions. The colour ratios typically range between $\sim$3 (for the dark polar and equatorward emissions) and 5-10 (for the main oval) and up to 20 for the brightest emissions in the swirl region (Gérard et al. 2016, Greathouse et al. 2021,Benmahi et al. 2024). As for the relation between flux and energy, the conversion factor is usually based on electron transport models for which 1 mW/m^2 of electron precipitation, over a wide range of initial electron energies, gives rise to auroral intensities of ~10 kR (of Lyman and Werner H_2 band emissions, Gustin et al. 2004, and verified in Gustin et al. 2012).

Although they are not addressed in this thesis, the IR aurora exhibit a similar morphology to the UV emissions. Some differences between them include lower intensity for the moon footprints and injection signatures in the IR, or a stronger limb brightening in the IR, probably caused by a higher difference between the altitudes of the auroral emission and where the atmosphere becomes optically thick.

1.7 Morphology of the Jovian UV aurora

The structures that form the Jovian UV aurorae are usually split into three large regions. This classification is based on their different location but also responds to different generation mechanisms and degrees of variability. We are going to follow this framework from the brightest region, the main oval or main emission, to the polar regions, and then to the low latitude regions which are one of the main subjects of this thesis, and finishing with a final note on the energetic dawn storms.

1.7.1 Main emission

Like in most of the other planets that display aurorae, including the Earth, Jupiter's main emission is the brightest and most stable auroral structure in the planet. It is oval-shaped, with a relatively constant width and a location fixed in longitude for both hemispheres. In the South, it adopts an almost circular shape, more or less closed depending on the magnetospheric conditions. In the North, its shape is affected by some strong non-dipolar components of the magnetic field, including the northern magnetic anomaly, giving it its well-known kidney shape. Figure 1.14

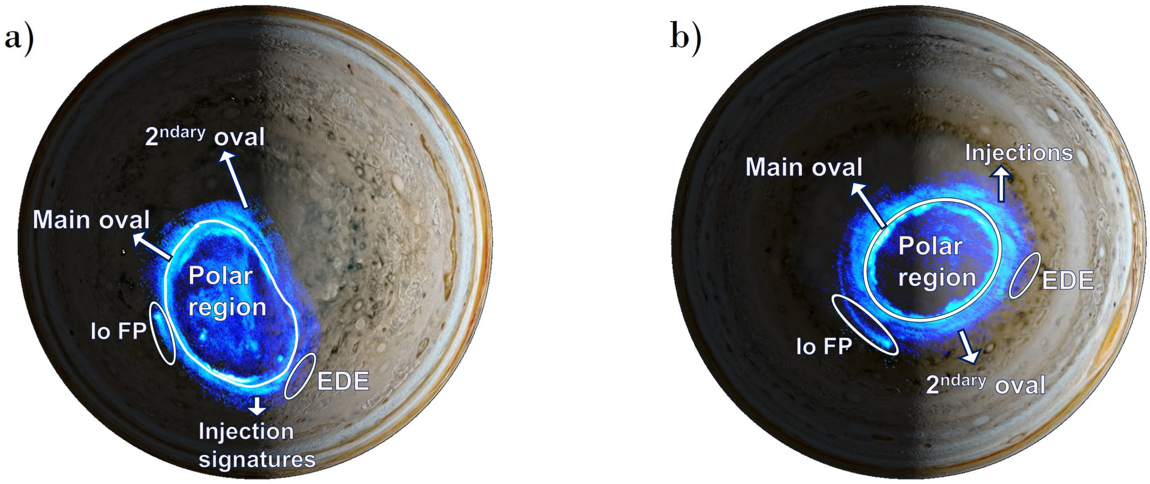

Figure 1.14: Juno UVS images from PJ3 superimposed on JunoCam images of Jupiter, with some of the main auroral features labelled. **a)** Northern hemisphere. **b)** Southern hemisphere. Credit: Bertrand Bonfond, Université de Liege.

shows the Jovian auroral emissions projected on both poles of the planet, as observed by Juno-UVS and displaying clearly the shapes of both main ovals (a) North; b) South).

In the case of Jupiter, the main emission is believed to be powered by the coupling current system associated with the breakdown of corotation in the middle magnetosphere, as explained in sections 1.3.3 and 1.4. Studying its structure in more detail, Mauk et al. (2020) have proposed a subdivision by latitude on three zones, each of them associated with different magnetospheric regions (see Fig. 1.15). The polarmost one (Zone II) would be powered by bidirectional broadband electron acceleration, with higher intensities in the upward directions. Secondly, there would be an intermediate zone (ZI) driven by downward electrons. These electrons would sometimes be broadband and sometimes accelerated by inverted Vs potentials, and they would have upward magnetic field-aligned currents associated. Finally and most equatorwardly, there would be the hot electron populations precipitating onto the atmosphere by wave-particle scattering.

Although the main oval is considered to be the most constant feature in the Jo-

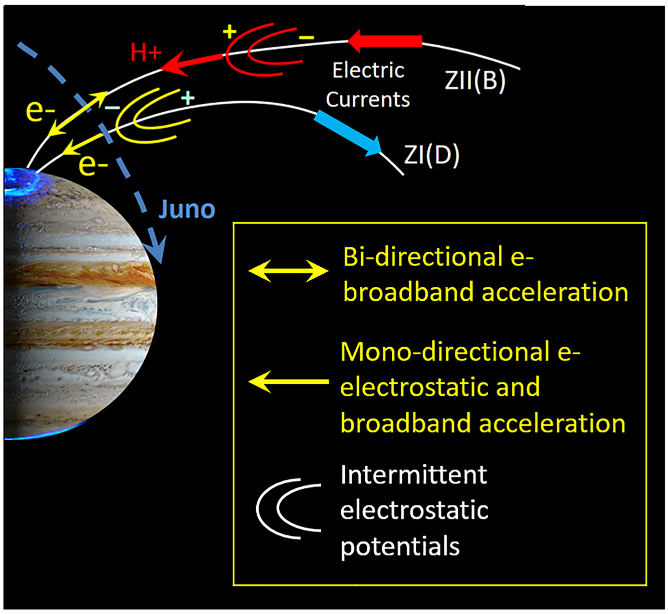

Figure 1.15: Schematic showing the two zones, Zone-I, or ZI(D) - downward, and Zone-II, or ZII(B) - bidirectional, and some of the characteristics of the phenomena occurring over Jupiter's main aurora. Credit: Mauk et al. (2020).

vian aurorae, it undergoes variability in timescales spanning from seconds to weeks. Badman et al. (2016) detected a 70% decrease in the emitted power, potentially caused either by an expansion of the magnetosphere or an increase in the inward transport of hot plasma. However and as stated before, the direct relations (or anticorrelations) with the state of the magnetosphere and the influence of the solar wind (Nichols et al. 2007), on one hand, and with changes in the mass loading from Io (Yoneda et al. 2010), on the other, are still a topic of hot debate within the community (check extensive review by Roth et al. 2024).

1.7.2 Polar region

The regions inside the main auroral ovals are extremely variable. Compared to the main emission, they usually look like a "hole" devoid of everlasting and powerful emissions, but they are often full of short-lived, bright flashes instead. These flashes take very different shapes and locations and are not distributed neither homogeneously nor randomly, which has in turn led to the division of the poles into three smaller subregions fixed in magnetic Local Time, with different physical processes associated with them (described next). These three regions are displayed in Figure 1.16 in different colours. This strong and quick variability unveils a close dependence on the magnetospheric conditions in the inner and middle magnetosphere. Besides, the open field lines within the polar cusps, and their potential auroral footprints, are thought to be hosted in this region (Pallier et al. 2004, Bunce 2004), although this is a topic of open discussion. Finally, reconnection events happening in the magnetotail had been proposed to sometimes display auroral signatures poleward of the main oval too (Grodent et al. 2004).

Active region

The active region is located poleward of the dusk sector of the main oval. This area hosts bright, very variable, localised transient flares. It has been suggested to be, if not directly controlled, at least modulated by the solar wind ram pressure (Pallier et al. 2001) and likely associated with IMF reconnection at dayside magnetopause (Grodent et al. 2003). Quasi-periodic (∼2 minute) flares have been observed in this region, mapping to the dayside outer magnetosphere (Bonfond et al. 2016), although they have displayed variability in their brightening even under quiet solar wind conditions.

Dark region

The dark region, poleward of the dawn sector of the main oval, has a crescent moon shape and it stretches parallel to the main oval. As its name suggests, it is a region almost totally devoid of UV auroral emissions, with the noticeable exception of some potential signatures of reconnection return flows (Gray et al. 2016). Recent studies (Dunn et al. 2020, Weigt et al. 2023) have shown that this region coincides almost exactly with an area inexplicably devoid of X-ray emission.

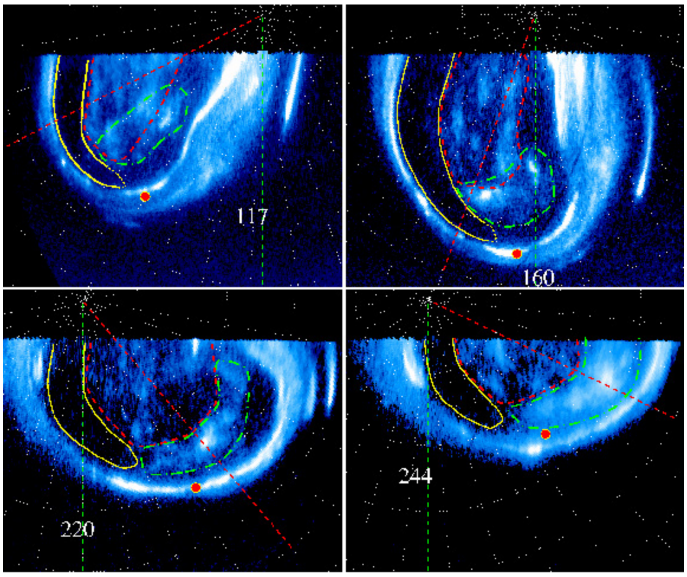

Figure 1.16: Jupiter's polar aurora from STIS UV images (top-North, bottom-South). Polar emission subregions outlined are the dark region (yellow, solid), the swirl region (red, dashed), and the active region (green, dot-dashed) at different CMLs (vertical green line). Credit: Grodent et al. (2001), Clarke et al. (2015).

Swirl region

The swirl region is constricted between the previous two, closest to the magnetic poles. It gets its name from the faint, patchy and short-lived flashes that appear frequently on it, moving turbulently. It accounts for about 50% of the total UV polar emission, and its location at the highest latitudes approximately coincides with the IR fixed polar region (Masters et al. 2021). Greathouse et al. 2021 has recently suggested that this region has a very strong dependence on the (solar) Local Time, which also anti-correlates with the intense upward moving electron beams detected by Bonfond et al. (2018) above it.

1.7.3 Equatorward emissions

The equatorward emissions are the least defined of the Jovian aurorae. A myriad of different features are tarred with the same brush under the concept of "low-latitude" or equatorward emissions. It is one of the main objectives of this thesis to try and shed some light on the different facets and mechanisms that fall under this term. They are described next, although some of them will be reviewed later on in considerably more detail. For context, they are labelled in Figure 1.14.

Moon footprints

The moon footprints are the most stable and brightest of the features appearing beyond the main emission. Of the Galilean moons, Callisto is the only one which does not show a bright footprint in UV, due to its larger orbital radius ($\sim 27R_J$), which causes the footprint to overlap with the main oval (Bhattacharyya et al. 2018). The visible footprints of the other three are the product of the interaction between the moons and the corotating plasma of the magnetodisc around Jupiter (Kivelson 2003). The specific mechanisms proposed for the generation of the auroral footprints involve either the downstream propagation of Alfvén waves along magnetic field lines or, for the specific case of Io, induced electric fields arising from the encounter between the slower fresh, iogenic plasma and the corotating one, not too dissimilar to a corotation breakdown system in miniature (Clarke et al. 2002).

Io and Ganymede footprints have structures themselves, showing a variable amount of aligned spots, often downstream of the moon longitude, caused by Alfvén waves accelerating electrons along the magnetic field lines and eventually causing auroral precipitation (Bonfond et al. 2013). Moirano et al. (2021) has studied the morphology of these footprints by using IR images from JIRAM, and suggests they may be caused by an ionospheric feedback instability (Atkinson 1970). The connection between the variabilities of the moon footprints' brightness and location with that of the main emission, as well as the changes in the strength of the current sheet, is not yet clear (Vogt et al. 2022).

Equatorial Diffuse Emissions

First addressed by Bhattacharya et al. (2001), Radioti et al. (2009) defined the equatorial diffuse emissions as the faint, non-localised emission appearing for broad ranges of longitude up to 10° equatorward of the main emission. This region maps to the Pitch Angle Distribution (PAD) boundary in both hemispheres, at least for certain sections of it, and potentially correlates with anisotropic injection events in others. In regions that do not align precisely with the PAD boundary, particularly in the Southern hemisphere, it is suggested that electron scattering by whistler waves (linked to anisotropic injection events), contributed to the observed phenomena (Li et al. 2017).

Injection signatures

Although this is not a canonical term, hereby I consider injection signatures the isolated, quasi-corotating, compact, auroral spots that appear equatorward of the main emission and are caused by the precipitation of energetic particles associated with the plasma motion in the middle magnetosphere (like those first detected by Mauk et al. 2002 and later defined by Dumont et al. 2014). These injection signatures are far from being completely understood. For instance, not all the plasma injections have an auroral counterpart, and so far the two main mechanisms proposed to produced these signatures have been indistinguishable (Haggerty et al. 2019). They are electron pitch angle scattering (as favoured by Dumont et al. 2018), and electric FACs flowing along the boundary of the injected hot plasma cloud (Kivelson et al. 1995).

Injections are not exclusive of low latitudes. Haggerty et al. (2019) have also reported injection signatures occurring at higher latitudes and including more frequent proton injections. That study, also suggests that magnetic gradients or discontinuities might exist at the boundary between injected and surrounding plasmas. This boundary-crossing could depend on differences in gyro-radii among particles, similar to the challenges observed in energetic particle escape across a magnetopause (Mauk et al. 2019). Over time, these magnetic gradients would diminish as particles disperse, potentially leading to the initial trapping and subsequent release of particles within the injection region, which would explain certain time delays observed between the injection events and their auroral responses.

Secondary oval

The secondary oval is the denomination received by the arc fragments that appear parallel to the main emission, often either at the dawn and/or dusk sectors, located between the footprints of Europa and Ganymede (Grodent et al. 2003). Its brightness and variability timescales differentiate this feature from both the EDE and the injection signatures described above (Tomás et al. 2004). The spatial coincidence between the ionospheric footprints of the PAD boundary and the secondary oval suggests a physical connection between the two. The source of the secondary oval would in that case be the whistler mode waves existing in that particular region of the magnetosphere (Woodfield et al. 2013), which scatter the electrons into a field-aligned distribution (Bhattacharya et al. 2001).

If not directly caused by them, it has been observed that the secondary oval brightness is enhanced after large plasma injections (Gray et al. 2017). According to that study, the reason was the double role of the plasma injections as both temperature anisotropies and particle sources to enhance electron scattering and thus the secondary oval brightness.

The secondary oval is not present at all times, and it is actually fairly elusive and hard to predict. The specific statistics of its frequency, location and relationship with the different states of the magnetosphere comprise one of the central topics of this thesis and therefore will be discussed in greater detail in Chapter 4.

Dawn storms

Due to their relative frequency and suspected connection with plasma injection signatures (Gray et al. 2016, Grodent et al. 2018, Yao et al. 2020), the transient auroral phenomena known as dawn storms are worth being addressed. Dawn storms appear as strong thickening and brightening of the dawn sector of the main emission in one or both hemispheres (Fig. 1.17), typically lasting for one or two hours and reaching peak intensities of 3 MR. They do not corotate like most of the other features, but lag behind ($\geq$30%) and often remain fixed at that dawn sector from which their name derives. Like Earth substorms, to which they have been thought of as analogues (Bonfond et al. 2021), they seem to be associated with reconnection (Kimura et al. 2017) and dipolarisation events (Yao et al. 2020).

The sequence of observation for an average dawn storm would be: the appearance of a relatively bright midnight arc, followed by a series of spots separated $\sim$1000 km poleward of it, followed by a midnight main emission brightening and broadening, often forming regularly spaced beads. Then the arc bifurcates with one branch moving poleward and the other remaining still. The void fills progressively as the arcs broaden in latitude. A longitudinal gap often forms as well while the whole feature accelerates toward corotation. Finally, everything dims and the equatorward part ends up as patches, which, according to Bonfond et al. (2021), could correspond to examples of hot plasma injection signatures. Yao et al. (2020) have also linked both features, suggesting dawnside reconnection as the physical driver for dawn storms and the subsequent dipolarisation producing the auroral injection signatures.

However, much is still unknown about dawn storms. Rutala et al. (2022) showed the prevalence of subcorotation in nearly half the auroral features detected in the dawn sector (35-65%), even when they were not as bright as to be considered dawn storms. This would point towards a shared physical mechanism behind both features: an increase in the ionospheric conductance (due to solar EUV) which would allow dawn to host higher FACs and would only be a minor correction to the traditional cororation-enforcement model. Ebert et al. (2021), on his part, presented evidence of bidirectional electrons, whistler-mode waves and broadband kilometric radio emissions simultaneous to an HST-observed dawn storm, all of them mechanisms already previously linked to other magnetospheric processes such as interchange events, plasma injections and tail reconnection.

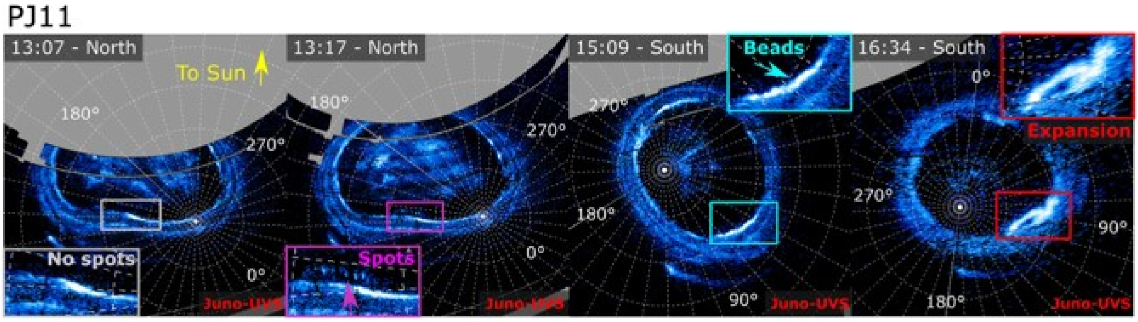

Figure 1.17: Polar projection of the development of a dawn storm, based on observations acquired by Juno-UVS and HST-STIS during the PJ11 and PJ6. On PJ11, the event was preceded by the progressive appearance of a set of transient spots poleward of the main emission. Two hours later, the dawn storm itself started as an enhancement of the main emission in the form of beads before the arc began to fork and expand, both latitudinally and longitudinally. Credit: Bonfond et al. (2021)

Summary

In summary, this chapter has provided an overview of the fundamental concepts and mechanisms underlying the plasma physics in order to introduce dynamics of Jupiter's magnetosphere and its auroral emissions. It began by exploring the single-particle motion in electromagnetic fields and the complexities of MHD, discussing the frozen-in flux theorem, magnetic reconnection, and the continuity equations that govern plasma behaviour. The morphology and the dynamics of Jupiter's magnetosphere were detailed, presenting the Dungey and Vasyliunas cycles, and introducing the corotation enforcement current theory as a key mechanism for auroral emissions. After showcasing the different ways auroral emissions occur across the Solar System, there is a description of the different physical mechanisms that give rise to the aurora, both field aligned and stochastic acceleration, with a special focus on the UV window. Finally, the chapter returns to the diverse auroral morphologies observed on Jupiter. It separates them into the main auroral oval, polar regions, and equatorward emissions, including moon footprints, equatorial diffuse emissions, injection signatures, and the secondary oval.

Chapter 2

Data and Instrumentation

In this chapter, the spacecraft instrumentation used in this thesis will be described, which comprises the Space Telescope Imaging Spectrograph (STIS) of HST and the JADE and JEDI particle detectors on board the Juno spacecraft, as well as their datasets and the reduction processes applied to make the data and images useful for scientific analysis. A description of the automatic detection algorithm developed for the equatorward emissions is also provided. Lastly, the procedures of connecting Jupiter's ionosphere and magnetosphere through the mapping of its magnetic field lines are explained as well.

2.1 Hubble Space Telescope - STIS

The Space Telescope Imaging Spectrograph (STIS) is a multi-capabilities instrument on board Hubble Space Telescope, where was installed in 1997 (Woodgate et al. 1998). It provides spatially resolved spectroscopy from 1150 to 10300 Å at medium spectral resolution (R$\sim 500 - 17,000$), high spatial resolution échelle spectroscopy (R$\sim 30,000 - 110,000$), solar-blind imaging and high-time resolution photon tagging in the UV, optical direct and coronagraphic imaging, and high signal-to-noise ratio spectra in the near-ultraviolet (NUV), optical, and near-infrared (NIR).

For this thesis, the detector of interest is the solar-blind, FUV camera MAMA.

MAMA is a 1024 x 1024px detector with an angular pixel size of 0.0246", a 25" x 25" field-of-view, and a Point Spread Function of 0.08" at full width at half maximum, which uses a SrF_2 filter which lets the detector operate between 1250 and 1900 Å, avoiding the intense Ly-α line at 1215 Å.

2.1.1 Reduction pipeline

During this PhD, I made an early attempt to develop a reduction and processing pipeline in Python from the existing IDL code. Ultimately, though, Dr Jonathan Nichols' version was utilised as the core and foundation for the reduction of the STIS images utilised. This pipeline is, in essence, a Python translation of the original Boston University one (Clarke et al. 2009, Nichols et al. 2009), with some improvements that will be briefly discussed next, among the general functioning of the pipeline.

The data processing pipeline takes the original raw images and corrects them for several well-known artefacts, some general and others more specific to the detector. The first reduction steps include correcting for dark current (counts caused by the thermal excitation of electrons in the detector), flat field (inhomogeneities in the pixel-to-pixel sensitivity), and geometric distortion (applying a polynomial for the detector accounting for differences of around one pixel across the detector, Walsh et al. 2001). The size of the images is then modified to display Jupiter at a standard distance of 4.2 AU in order to facilitate the comparison between visits.

The next stage in the reduction process is the subtraction of the background emission to separate the aurorae. Background emissions have two main sources: the geocorona (scattered light from the Earth's upper atmosphere) and Jupiter's planetary disc emissions (produced by both dayglow emissions and solar light reflections). The former is easier to remove, since it just uses sampling from "clear" parts of the image to obtain an average value, typically of a few counts per pixel per observation. The latter one is more complex and requires adjusting the planetary disc and centre, considering the limb darkening, as explained below.

Subtraction of the disc background contribution

One of the points of the pipeline that demanded more effort and which has been improved and fine-tuned repeatedly is the determination of the planetary centre location. The method consists of a first automatised limb-fitting function and a subsequent manual adjustment. Originally designed for Saturn by Adem Saglam (2004), the method consists of modelling the edge of the planet with a parametric step function. A rectangle containing a section of the limb without auroral emissions is automatically selected and every row of pixels is then fitted with the step function. Once all the step points have been detected, they are on their part fitted to an ellipsoid representing the planetary disc.

From there, improvements developed and explained by Nichols et al. (2009) and Clarke et al. (2009) have subsequently been added to the original procedure. After that initial approximation to the planetary centre is done by fitting a contour ellipse to the disc of the planet, and a mask is applied to the aurora to avoid its interference with the limb determination. Then, the limb position is refined by scanning the disc boundary as approximated by the initial ellipse. The limb point is defined as the inflexion point of the radial profile, and the image is rotated to align the tangent line to the Y-axis. Then, a two-part function is fitted to the profile (a 2nd-degree polynomial for the disc, and a decreasing exponential for the transition from the disc to the background brightness). The inflexion point is searched within the exponential domain. This method is particularly helpful for low signal-to-noise STIS data.

As an additional step, the band structure of Jupiter, although not very bright in UV, is used to perform a final correction on the orientation angle of the planet. Particularly, the transition between the polar dark region and the first bright band is utilised for this.

Finally, the surface brightness variations across planetary disc due to the limb darkening are modelled using a modified Minnaert function (eq. 2.1) to account for the reflected sunlight, with coefficients A, B, C and D varying between the sunlit and terminator sides, I/F is the reflectivity (intensity by incident solar flux), and μ

and μ_0 the cosines of the observation and solar zenith angles, respectively (Vincent 2000, West et al. 1995).

$$\mathbf{ln}(\mu I/F) = A + B\mathbf{ln}(\mu\mu_0) + C\mathbf{ln}(\mu\mu_0)^2 + D\mathbf{ln}(\mu\mu_0)^3 \tag{2.1}$$

This modelling requires images without auroral emissions, achieved by combining multiple images where auroras are masked in different sectors (e.g., one image in which the auroral emissions are concentrated on the dawn side and the other in which they appear at dusk). The assembled "disc-only" image is then used to fit the Minnaert coefficients for different latitudinal bands. A synthetic background disc is thus generated for each image, allowing the isolation of auroral emissions by subtracting this modelled disc from the original image.

Unit conversion

The conversion from counts per second to flux (kiloRayleigh) emitted from H_2 over the full wavelength range 700-1800 Å is done by following the procedure described by Gustin et al. (2012). Assuming a colour ratio of 2.5, this implies a factor of 1 kR = 4523 counts/s for the SrF_2 filter.

To find the energy flux from the observed brightness in a pixel (in kR), the brightness is multiplied by 10^9 to convert it to incident photons per second (Gustin et al. 2012). Regarding the energy-flux conversion, it is used the aforementioned factor of 10 kR of auroral intensity produced by $\sim$1 mW/m^2 of precipitating electron flux (verified in Gustin et al. 2012).

Image projection

Once reduced, the images are projected onto a planetocentric System-III grid assuming an auroral emission height of 1 bar pressure level of an oblate spheroid with radii corresponding to 240 km above the 1 bar level (the assumed altitude at which the UV auroral emissions are produced, according to Vasavada et al. 1999 and Grodent et al. 2001), with a resolution of 0.25° per image pixel in both latitudinal and

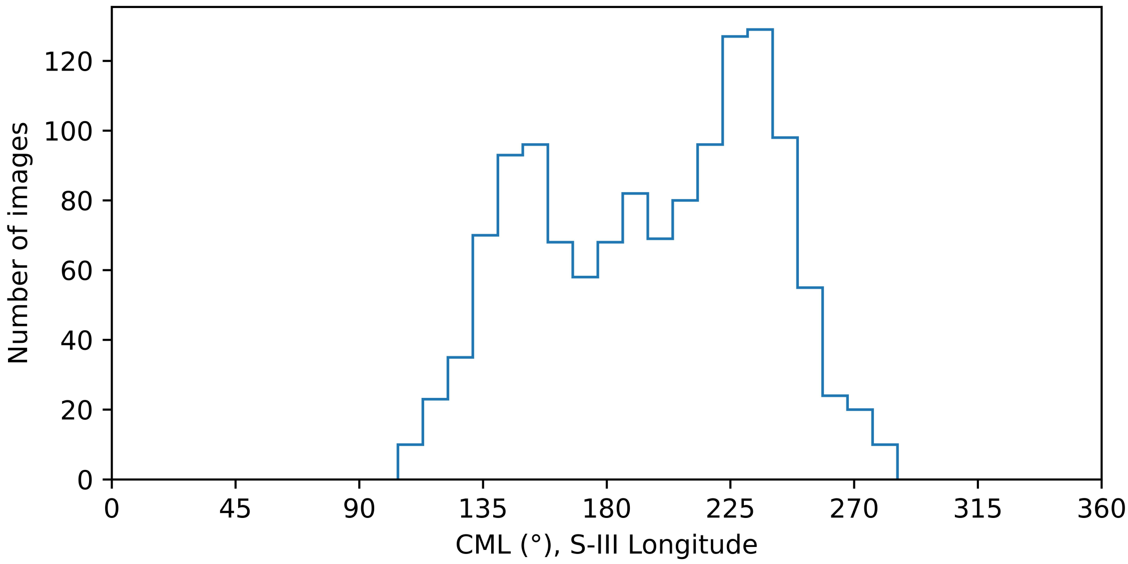

Figure 2.1: Histogram showing the distribution of the CML of the Southern visits used in this work.

longitudinal directions, which corresponds to a distance on the surface of around 250-300 km (considering a Jovian radius of 71,492 km) for the sub-observer point.

It must be noted that there is a noticeable stretching of the emission near the limb due to the geometry of the system, making the location of the auroral emission near the edges less accurate. This will be duly considered when analysing the auroral images, and in particular when applying the automatic detection algorithm (section 2.2: **Refinement of the algorithm**).

2.1.2 HST dataset

The geometry of the Sun-Jupiter-Earth system (since HST orbits our planet with a 96-min period) imposes some restrictions on the visibility of Jupiter. In brief, the night side of Jupiter is not visible to HST (although it is to Juno). The Central Meridian Longitude (CML) is the longitude subtended by the Earth observer to the planet, measured in a planetary rotation frame (System III longitude), i.e., the meridian of the sub-Earth point. The distribution of the CMLs (i.e., which longitudes of Jupiter are being observed) during the multiple studied HST observation

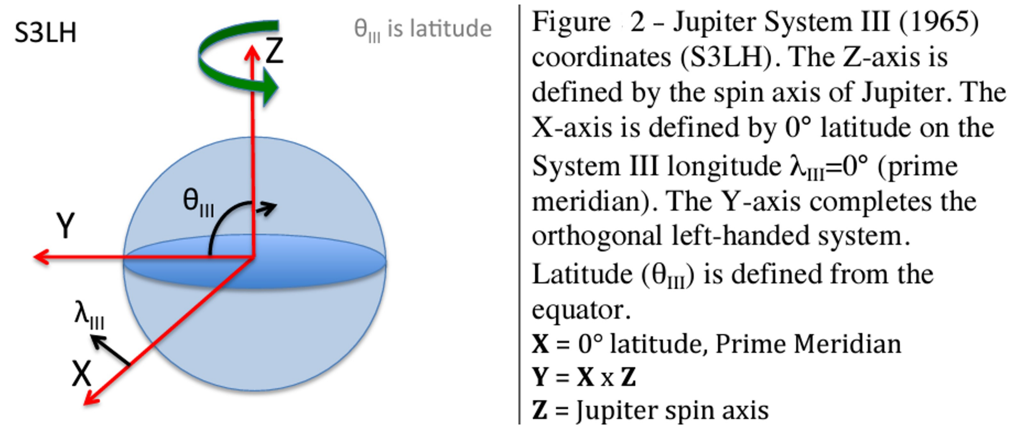

Figure 2.2: Left-handed S-III longitude scheme, taken from Jupiter Coordinate Systems (Bagenal et al. 2016).

campaigns is far from being random or uniform, as can be seen in the histogram shown in Figure 2.1. The reason for this non-uniformity is the significant tilt of the magnetic dipole relative to the spin axis in the northern hemisphere. Therefore, when the dipole points away from the observer, a very small portion of the aurora is visible (the rest is hidden behind the limb). This results in a visibility bias toward certain S-III longitudes (centred around 180° for the South, as can be seen in Fig. 2.1), and an overall unequal coverage of different regions of the aurora in both hemispheres (with very little to no images at all covering the 0° longitude for the South, for example).

As a clarification regarding the left-handed S-III frame of reference shown in Figure 2.2: if an auroral feature is fixed in longitude (like, approximately, the main emission), it means it corotates with the planet. On the other hand, if it is fixed in local time (e.g. the small transient structure located around 14 hours LT found by Palmaerts et al. 2014), it will not rotate with the planet and in the images it will look like it lags behind, fixed in the same "sector" of the field of view. Features moving faster than the planet in the same direction (super-rotating) will seem to move to lower longitudes in the System-III while sub-corotating features will move to higher values of S-III longitude. In this work, unless stated otherwise, the chosen reference system is the left-handed S-III longitude with the Southern images looked at "through" the planet (not from below; i.e., with the longitude increasing clockwise).

A final explanatory note on the conversion between S-III longitudes and Local Times used frequently in Chapter 3: The terms dayside, nightside, noon, midnight, (post-)dawn, and (pre-)dusk are intentionally ambiguous because a first-degree approximation has been made by equalling the subsolar and the sub-Earth points on Jupiter when utilising those Local Time sectors. This approximation takes into account that the maximum angle observed from Jupiter between the Sun and the Earth is 10.9°, and the average one is 0° due to the geometry of the system and the observational constraints of HST-STIS. However, it implies that effectively those aforementioned concepts, and their LT associated, are taken as seen from HST (the Earth), instead of their actual meanings which should refer to the Sun. The small difference between the two concepts (<0.7 hours in Local Time in the worst-case scenario) has no implication in the interpretation of the results obtained in that chapter (i.e., a feature located in the pre-dusk sector is still there, independently of whether the actual, Sun-referenced local time, or our "Earth-derived" Local Time, are used).

2.2 Automatic auroral feature detection algorithm

The automatic detection algorithm is the tool developed to locate and evaluate quantitatively the frequency and main parameters of the more recurrent and brighter auroral features of the Southern hemisphere. Next, the way the algorithm was created, refined and applied to the datasets is described thoroughly.

Several varied feature detection algorithms have been proposed and utilised in the past by different studies, including Bader et al. (2019) and Gray et al. (2017). The latter, which analysed the residuals after subtracting a Gaussian curve from the main emission, is the conceptual predecessor of the algorithm presented here. In short, the main differences between these two studies are: the size of the sample to which the algorithms have been applied (56 visits of the Southern hemisphere instead of 6 images of the North, in the case of the Gray study), the nature of the fitting functions (a compound model of Lorentzian curves in this case, vs. the analysis of residuals after subtracting a Gaussian curve to the main emission in the previous study) and the additional physical parameters obtained in this case (e.g., the width or the intensities of the different auroral emissions).

The fitting model

The model selected for the algorithm consists of a composition of successive Lorentzian curves, constrained to different latitudinal ranges. The Lorentzian profiles were chosen on a purely empirical basis, after trying and comparing the results with different types of curves, such as Gaussian or Voigt. They are described by Equation 2.2:

$$f(x) = \frac{A\gamma^2}{\gamma^2 + (x - x_0)^2} \tag{2.2}$$

where A is the amplitude of the peak, x_0 is its position, and γ is half of the given Full Width at Half Maximum. An estimation of its associated propagated error would be:

$$\begin{aligned}
\Delta f(x) &= \sqrt{\left(\frac{\partial f(x)}{\partial A}\Delta A\right)^2 + \left(\frac{\partial f(x)}{\partial x}\Delta x\right)^2 + \left(\frac{\partial f(x)}{\partial x_0}\Delta x_0\right)^2 + \left(\frac{\partial f(x)}{\partial \gamma}\Delta \gamma\right)^2} \\
&\approx \sqrt{\left(\frac{f(x)}{A}\Delta A\right)^2 + 2\cdot\left(\frac{2A\gamma(x - x_0)}{((x - x_0)^2 + \gamma^2)^2}\Delta x\right)^2 + \left(\frac{2f(x)(x - x_0)}{\gamma}\Delta \gamma\right)^2}
\end{aligned} \tag{2.3}$$

The pre-defined latitudinal ranges correspond to different types of auroral emissions, and vary with longitude due to the fact that the main oval is not perfectly centered around the geographical pole. Figure 2.3 shows a latitudinal profile with its corresponding full set of Lorentzians. On the uppermost part of the plot, the domains for these curves are displayed in different colours (some of them overlapping): blue for the main emission, red for the equatorward emissions, and orange for the Io footprint. Additionally, a seventh-order polynomial is applied to the polarmost latitudes to fit the quickly variable flashes, arcs and spots appearing in that polar region (in purple). The final compound function is shown in green.

Before its application to the data, this compound model was customised to improve its performance, by defining initial conditions and limits for each curve, while maintaining as many freedom degrees as possible to avoid overfitting. The values for both the initial conditions and the limits for the curves are obtained from a combination of previous literature (Grodent et al. 2003, Hess et al. 2011, Vogt et al. 2011) and preliminary analysis of the sample. These conditions include values for the amplitude of the peaks and their latitude. A lower limit is imposed on the minimum amplitude for the curves to be fitted (below, the auroral emission is considered too dim, and therefore negligible). Two latitudinal boundaries are defined for each curve, allowing overlap between the curves if required for the most optimal fitting. The latitudinal ranges are 10° for the main emission curve (starting at a preliminary latitude taken from reference oval by Vogt et al. 2011), 8° for the Io footprint curve (shaded in orange in Fig. 2.3, taken from the reference values by Hess et al. 2011), and a variable amount that considers the proximity between those two emissions for the secondary curve. The Io footprint curve is not always attempted to be fitted: only when the location of the moon footprint from the ephemerides falls within a certain range of longitudes, which include not only the "head" of the footprint but also its tail.

Refinement of the algorithm

The main objective of the detection algorithm was to provide us with a systematic, objective, and repeatable way of locating and getting the intensities of some of the most important Jovian auroral features, i.e. the main oval, the equatorward emissions, and Io's footprint. To achieve this, the fitting model explained in the previous subsection was iteratively tested, tweaked and expanded to improve its accuracy.

The starting point for the model was the reference location of the Southern main

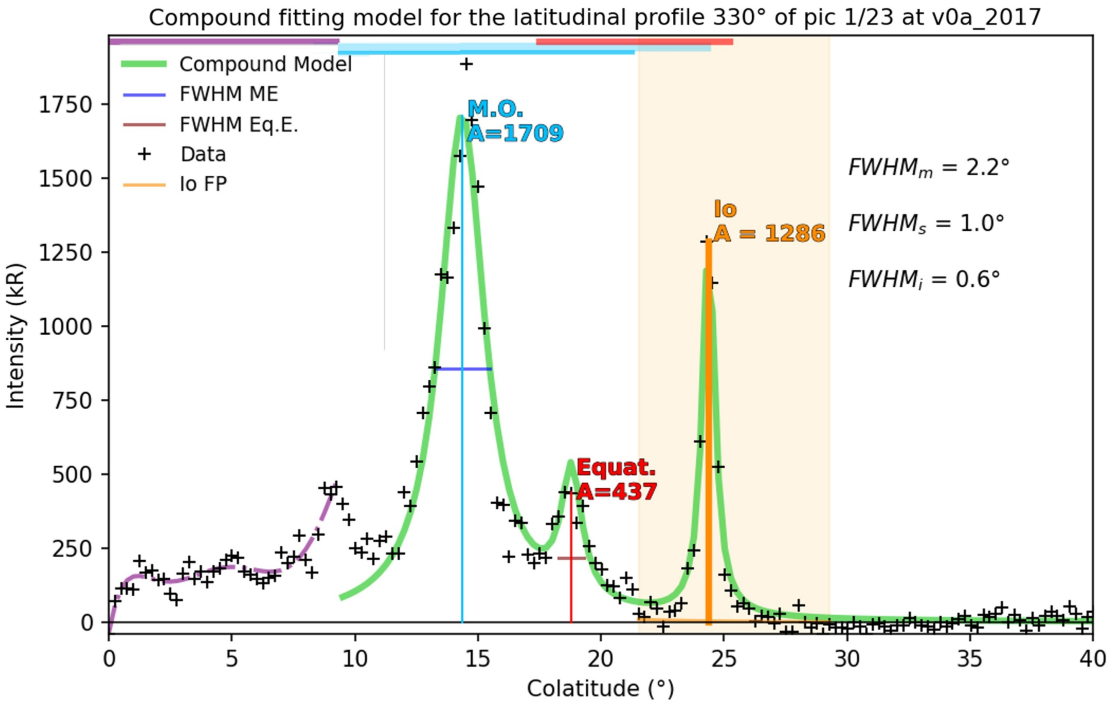

Figure 2.3: Lorentzian curves of the algorithm fitting the latitudinal profile of intensity along meridian 330° of the first image from visit od8k0a (campaign 16634, Grodent et al. 2018).

oval provided by Vogt et al. (2011), as well as the location of the moon footprints mapped by Hess et al. (2011). From those, only Io was finally considered, as Europa and Ganymede were discarded after verifying their footprints were not discernible in most of the analysed HST visits. As explained above, those initial locations for the position of the main emission were not considered as fixed in the model, but only as the initial values around which the model was allowed to fit the curves for the main oval and the Io footprint, respectively.

The wide range of auroral morphologies, discussed in depth in Chapter 3, prevented the model from being equally effective for all the images analysed. Because of that, after applying the model to all the visits of our analysed sample, an additional set of filters was applied to the output results. The selection of a particular set of filters involved a trial-and-error approach to strike a balance between allowing the algorithm maximum flexibility and constraining it to "sensible" values. This method ensured that the automated detection remained aligned with the visual identification of auroral features, optimising the algorithm's accuracy without over-restricting its sensitivity to the wide variability in the data.

1. **Latitude filter**: the main considerations regarding the latitude of the different features were applied when designing the algorithm, as explained above. However, a final filter discards the profiles whose "equatorward emission" curve peak was found at a more equatorward location than that of the Io footprint curve peak (if such one had been fitted in that profile).

2. **Curve parameters filter**: in order to reject the dimmest (and therefore more unreliable) profiles for fitting the curves, an additional filter was applied as a minimum threshold of 250 kR for the amplitude of the fitted Lorentzian curves. This 250 kR value was selected empirically: it was a value high enough to make sure emissions detected by the algorithm were bright enough, but sufficiently low to pick up not only the main oval but also the dimmer equatorward emissions.

3. **Z-score filter**: an extra filter was used to exclude outliers using a Z-score parameter. Z-score, or standard score, is a statistical value corresponding to the amount of σ deviations above or below the mean of a population. Curves with (absolute) Z-score values > 3 for the latitude of their peak were discarded. This equals all the peaks whose latitude fell outside a 3-σ range measured from the mean latitude of the curve at that specific S-III longitude.

4. **Edges filter**: as it was explained in the **Image projection** part of the section 2.1.1, the distortion of the STIS images towards the limb of the planet, due to the imperfect polar projection of the images, makes those regions near the edges of the contour of the disc stretched along the line of sight. To account for this, a margin of 3° taken from the limits of the image is removed from the final results. This effectively avoids those problematic parts and excludes them from the calculation of the reference ovals and the subsequent analysis.

2.3 Juno spacecraft

NASA spacecraft Juno (Fig. 2.4) was launched in 2011 and entered orbit around Jupiter in July 2016. It is part of the New Frontiers program, which aims at diverse and ambitious solar system exploration goals such as approaching Pluto and other even further objects (New Horizons), retrieving a soil sample from an asteroid (Osiris-REx) or flying a rotorcraft on Saturn's moon Titan (Dragonfly). The mission's objectives include studying the planet's origin, evolution, internal composition, atmosphere, magnetosphere, moons, and the study of the poles (also due to its highly eccentric polar orbits, designed to avoid the most extreme regions of radiation in the magnetosphere).

Since its arrival at Jupiter, Juno has kept providing scientists with invaluable images, spectra and in situ data from its wide range of instruments. The set of tools aboard the spacecraft includes a magnetometer, a microwave radiometer, a gravity experiment, an auroral mapper (JIRAM), a UV imaging spectrograph (UVS), a

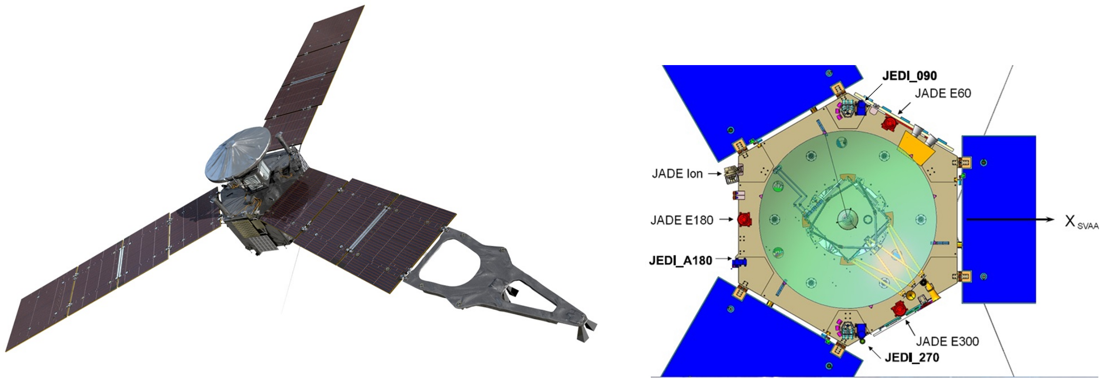

Figure 2.4: Left: Juno spacecraft. **Right**: JADE and JEDI installation locations, including JADE-I, the three JADE-E, and the three JEDI sensors). Credit: NASA.

radio and plasma waves experiment (Waves), a visible light camera (JunoCam) and two particles detectors (JADE and JEDI), which are the ones of foremost importance in this work (Fig. 2.4).

2.3.1 JADE

The Jovian Auroral Distributions Experiment (JADE) is a particle detector providing *in situ* measurements of electrons and ions from the different regions of the magnetosphere crossed by the spacecraft (detailed information about it in McComas et al. 2013). It is comprised of three identical electron sensors (JADE-Es) and one ion detector (JADE-I), each of which provides energy and angular resolution within a certain range: the electron detectors have an energy range between 0.1 and 95 keV, while the energy range for the ions is between 0.01 and 46.2 keV.

The three electron sensors are located at equidistant positions around the spacecraft body, providing full electron pitch angle coverage depending on orientation with respect to the background field. Each of them covers 120° in azimuth (Juno's spin plane) and has deflectors that track the magnetic field direction up to 35° in elevation when in high-rate science mode. The magnetic field measurements are provided every second by the companion magnetometer instrument also on board (MAG, Connerney et al. 2017), and they are used to calculate the deflection angles (whose angular resolution is ~7.5° in azimuth and ~2–5.5° in elevation).

Measuring the flux as a function of energy and angle relative to the continuously tracked magnetic field vector is enough to determine the pitch angle of the detected electrons. In high-rate science (such as the 1-second resolution mostly used in this work), JADE-E adjusts the deflector voltage to measure electrons travelling along the magnetic field line. These electrons impact a specific anode in one of the JADE-E sensors, while the neighbouring anodes measure flux away from the magnetic field vector, allowing for the reconstruction of the pitch-angle distribution, which has a resolution of 7.5°.

2.3.2 JEDI

The Jupiter Energetic Particle Detector Instrument (JEDI, Mauk et al. 2017) on board of Juno, whose energy range extends from ~25 to 800 keV (for electrons). It is a similar and complementary instrument to JADE for the more energetic particles. As such, JEDI also offers time-of-flight information about the energy of the particles it detects (although with a lower resolution than JADE), as well as a measurement of the pitch angle (with a variable resolution depending essentially on the part of the orbit Juno is in). Like its low-energy companion, JEDI is made up of three independent detectors, each of which has six telescopes arranged in a ~160° fan. The configuration of these three instruments (JEDI-90 or J90, J180, and J270) is also shown in Fig. 2.4.

If the estimation for the loss cone angle presented in Eq. 2.5 is compared to JEDI's angular resolution, a maximum value of ~3.5 R_J is obtained. Beyond that distance, JEDI's field of view is larger than the loss cone and thus the resolution of smaller angles is impossible. Besides these differences in the specifications (mainly: the angular and energy resolutions, and the rate of measurements), the process of reduction and utilisation of JEDI data is essentially the same as the one for JADE.

2.3.3 JADE and JEDI datasets

This work only uses JADE-E data as the ion dynamics were not of primary interest. The JADE data used for this study were the JNO-J/SW-JAD-5-CALIBRATED-V1.0 dataset until DOY 94 of 2021, and JNO-J/SW-JAD-1-CALIBRATED-V1.0 for dates after that. Both may be obtained from the Planetary Data System (PDS) at http://pds.nasa.gov/. Most of the data analysed belongs to intervals with the highest possible time resolution (1-s when possible, 30-s or 120-s when not). Unfortunately, it should be noted that one of the JADE-E sensors (E300) was rendered unusable, and so only $240° \times 70°$ field of views were available for this work. With the other two sensors (E060 and E180) working, JADE-E achieves full pitch angle coverage for approximately one-third of every $\sim$ 30-s spacecraft spin period but always covers at least 120°, including either the upward or downward magnetic field-aligned direction.

JADE-E datasets have been fully calibrated in sensitivity, converted into units of DEF, and with pitch angles, until April 4th, 2021. For dates after that, the data is calibrated in energy but the pitch angles are not publicly available as of the date of the submission of this thesis. An *ad hoc* conversion was applied to the datasets in order to obtain the fluxes. However, the lack of data about the sensitivity corrections implied that the numerical values obtained for the precipitating electron energy flux for those dates were not reliable enough. Once the more recent data corrected in sensitivity is published, the analysis will be extended to the present.

An example of the JADE-E dataset produced and utilised in this work is shown in Figure 2.5. It shows samples of 0.1–100 keV electron observations from JADE-E in Jupiter's Southern region during an interval when the instrument was taking measurements in high-rate science mode (full energy coverage every second). Top to bottom, the spectrogram shows the energy-time differential intensity over certain pitch angle directions (with a variable limit, depending on the distance of the spacecraft to the planet), and the pitch angle distributions associated (with its colour bar showing again differential energy flux) for a certain part of its trajectory. In the

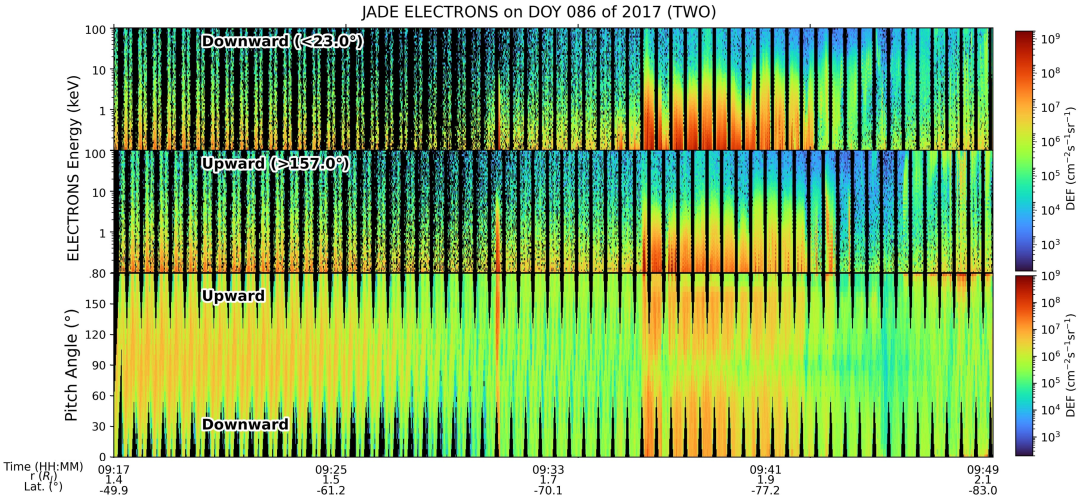

Figure 2.5: Top: Energy-time differential energy flux spectrograms of upward and downward 0.1–100 keV electrons observed along a 40-min interval of Juno's trajectory during PJ-05 (between 08:00 and 08:38 UT of DOY 86, 2017). **Bottom**: Pitch angle-time differential energy flux spectrograms of the electrons for the same interval.

bottom of the figure (as it will be shown in all of the ones in Chapter 4), are the times when the observations were collected, along with Juno's radial distance to the planet and its latitude.

Calculation of the precipitating electrons energy flux

The energy flux of the electrons is calculated by integrating the product of the particle intensity and the electron energy along each energy step in the instrument (see Clark et al. 2018 and Mauk et al. 2017), thus turning the integral into a discrete sum, as shown by Eq. 2.4:

$$EEF = \pi \cdot \sum_i (DEF_i \cdot \Delta E_i) \tag{2.4}$$

where π is the area-projected-weighted size of the loss cone (in steradians and assuming it is full at the top of the ionosphere), i is the energy step for the instrument, DEF_i is the differential energy flux of i averaged over the pitch angle (i.e., the product of the particle intensity and the central energy of each bin, in cm$^{-2}\cdot$

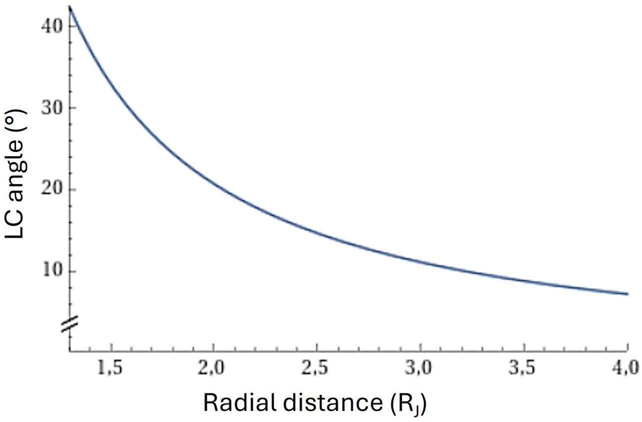

Figure 2.6: Loss cone angle (in °) relative to the radial distance of Juno.

s^{-1} · sr^{-1}), and ΔE_i is the width of the energy passband (in keV; obtained from Muñoz Jr et al. 2022). The energy flux is given in units of mW· m^2. In this work, all the final flux values presented are taken every second, so no averaging or summing over longer intervals has been performed.

$$\alpha_{LossCone} = \arcsin\sqrt{\frac{1}{R^3}} \tag{2.5}$$

The limits of the loss cone angle can be estimated (within a 30% uncertainty) by using Equation 2.5, assuming magnetic moment conservation and magnetic field strength as $B \sim 1/R^3$, as described by Mauk et al. (2017c). The curve described by that equation is shown in Figure 2.6. This will give the upper limits below which the direction of the particles measured in Chapter 4 will be included in the integration. The rest of the angles will be discarded in order to separate the particles moving upward or downward the magnetic field line and calculate their corresponding upward and downward energy fluxes that will eventually generate the auroral emissions.

2.4 Mapping Juno location to the ionosphere

The mapping between the auroral features on the ionosphere and their magnetospheric source region has to be made in the first place has a double objective in this thesis. First, it helps us locate the radial distances on the equatorial plane at which

Variable Name	Description	Default Value (and Units)
mu_i_div2__current_parameter_nT	$\mu_0 I_0/2$, azimuthal current sheet field parameter	139.6 nT
i_rho__radial_current_MA	I_ρ, radial current term from Connerney et al. (2020) (set this to zero to turn radial currents off as in Connerney et al. (1981)	16.7 MA
r0__inner_rj	R_0, inner edge of Con2020 current disk	7.8 R_J
r1__outer_rj	R_1, outer edge of Con2020 current disk	51.4 R_J
d__cs_half_thickness_rj	D, current sheet half thickness	3.6 R_J
xt__cs_tilt_degs	ϑ_D, tilt angle of current sheet normal	9.3 degrees
xp__cs_rhs_azimuthal_angle_of_tilt_degs	φ_D, azimuthal angle of the tilt of the current sheet normal sheet tilt	155.8 degrees (right handed)
error_check	1 to check that inputs are valid (Default), or set to 0 to skip input checks (faster) not a Con2020 model parameter	1
CartesianIn *(Python only)*	Input is expected in Cartesian co-ords if True, or Spherical co-ords if False.	True
CartesianOut *(Python only)*	Output B is given in Cartesian co-ords if True, or Spherical co-ords if False.	True

Table 2.1: Con2020 model code default parameters. Credit: Wilson et al. (2023).

the physical mechanisms behind some of the auroral features described in the next chapters. Secondly, the reversed mapping is pursued to discern which intervals from the Juno dataset to study in detail.

For this, a combination of an internal magnetic field model, JRM33 (Connerney et al. 2022), plus an additional term based on the magnetodisc component of the magnetic field is used (Connerney et al. 2020). The JRM33 model is based on measurements taken during the first 33 orbits of Juno around Jupiter. It is an update to the JRM09 internal magnetic field model (based on the first 9 orbits, Connerney et al. 2018), which in turn is the Juno version of the older VIP4 and VIPAL (Hess et al. 2011) models based on Voyager and Pioneer spacecraft measurements of the magnetic field. All of these models express the internal field through spherical harmonic expansions, with the values of the coefficients and the order of the expansion differing among them. On the other hand, Con2020, the external field source model, provides the magnetic field due to the magnetodisc located near Jupiter's magnetic equator.

The JupiterMag Python module (based on the *libjupitermag* code thoroughly

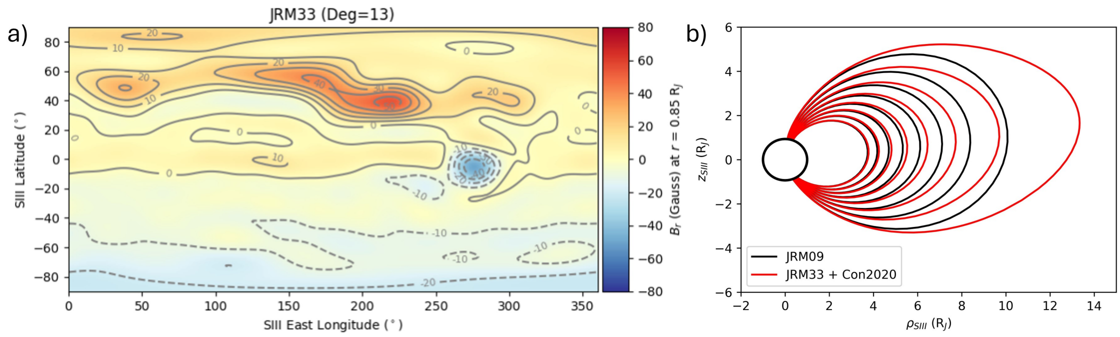

Figure 2.7: a) A map of the radial component of the JRM33 degree 13 magnetic field model at $r_c = 0.85$ R$_J$ in S-III (East) coordinates (0.85 R$_J$ is the assumed dynamo core radius). Credit: Wilson et al. (2023). **b)** Comparison on the ρ-Z plane of the traces for the JRM09 model (black) and the updated JRM33 with the Con2020 external component contribution (red).

explained by Wilson et al. 2023) has been used to implement this combination of magnetic fields to obtain the field line tracing. This tracing consists of the linking via the field lines obtained from the magnetic field models of a location in the inner or middle magnetosphere (e.g., that of Juno) to its footprint on the ionosphere (see Figure 2.7a), or, oppositely, from a point on the ionosphere to its radial distance in the magnetosphere (Fig. 2.7b). The Python community code (version 1.0.11, James et al. 2023) was used for the JRM33 order 13 interior field model and the Con2020 external field (Provan et al. 2023), ran in hybrid mode with the default parameters (shown in Table 2.1). Figure 2.7 b) shows the difference between the field lines traced using the internal field model JRM33 with (red) and without (black) the external component of Con2020.

Chapter 3

Statistical Overview of the Main and Equatorward Emissions

3.1 Introduction

This chapter will focus on the structure, location and frequency of the equatorward emissions, with a special emphasis on the elusive and poorly understood auroral feature known as secondary oval. The theoretical concepts explaining these emissions have already been introduced in Section 1.7.3. To better comprehend the causes, dynamics and appearance of the secondary oval, a statistical study as complete as possible of the low-latitude emissions in the Southern hemisphere of Jupiter has been accomplished. I have focused on the simpler, less-distorted, Southern hemisphere, but most of the conclusions derived from this hemisphere can be generalised to its Northern counterpart, as will be duly justified.

Characterising quantitatively the secondary oval was the main reason for the development of the automatic detection algorithm, described in Section 2.2. In this chapter, the results obtained from its application to a set of 56 HST visits are presented. These 56 visits correspond to 2240 minutes ($\sim$37.3 hours) of observations of the Southern hemisphere from Juno mission-era campaigns between 2016 and 2022, making this the most complete study of the Southern hemisphere so far.

SIII longitude	**Colatitude**	**SIII longitude**	**Colatitude**
0	17.4 ± 2.0	...	...
10	18.1 ± 1.9	210	6.0 ± 1.7
20	19.0 ± 1.8	220	6.1 ± 1.9
30	19.9 ± 1.9	230	6.4 ± 1.9
40	20.5 ± 1.9	240	6.9 ± 2.0
50	21.0 ± 2.0	250	7.4 ± 2.0
60	21.0 ± 2.0	260	8.0 ± 2.0
70	20.2 ± 2.0	270	8.6 ± 1.9
80	19.0 ± 2.0	280	9.5 ± 1.8
90	17.2 ± 2.0	290	10.2 ± 1.8
100	14.8 ± 2.0	300	11.3 ± 1.7
110	12.7 ± 1.9	310	12.5 ± 1.6
120	11.0 ± 2.0	320	13.6 ± 1.5
130	9.5 ± 1.9	330	14.8 ± 1.4
140	8.5 ± 1.8	340	15.7 ± 1.4
150	7.7 ± 1.9	350	16.5 ± 1.4
160	7.2 ± 1.8		

Table 3.1: Colatitude of the Southern main oval of the Jovian aurorae (± the half width at half maximum).

These results encompass the location (both in longitude, local time and colatitude) and frequency (number of detections divided by the number of profiles) of the equatorward emissions. They also include the study of the behaviour of the main emission, including, for the first time, a complete analysis of its variable width, as well as a breakdown of the intensities of these emissions, proxied by the amplitude of the algorithm fitted curves. The differences and similarities in the behaviour of the auroral emissions when separating the observations by the morphological families defined by Grodent et al. (2018) are also addressed. Finally, it must be noted that the algorithm also provided fitting results for the location of the footprint of the moon Io but its study falls beyond the scope of this project, albeit they may be interesting to analyse in further campaigns.

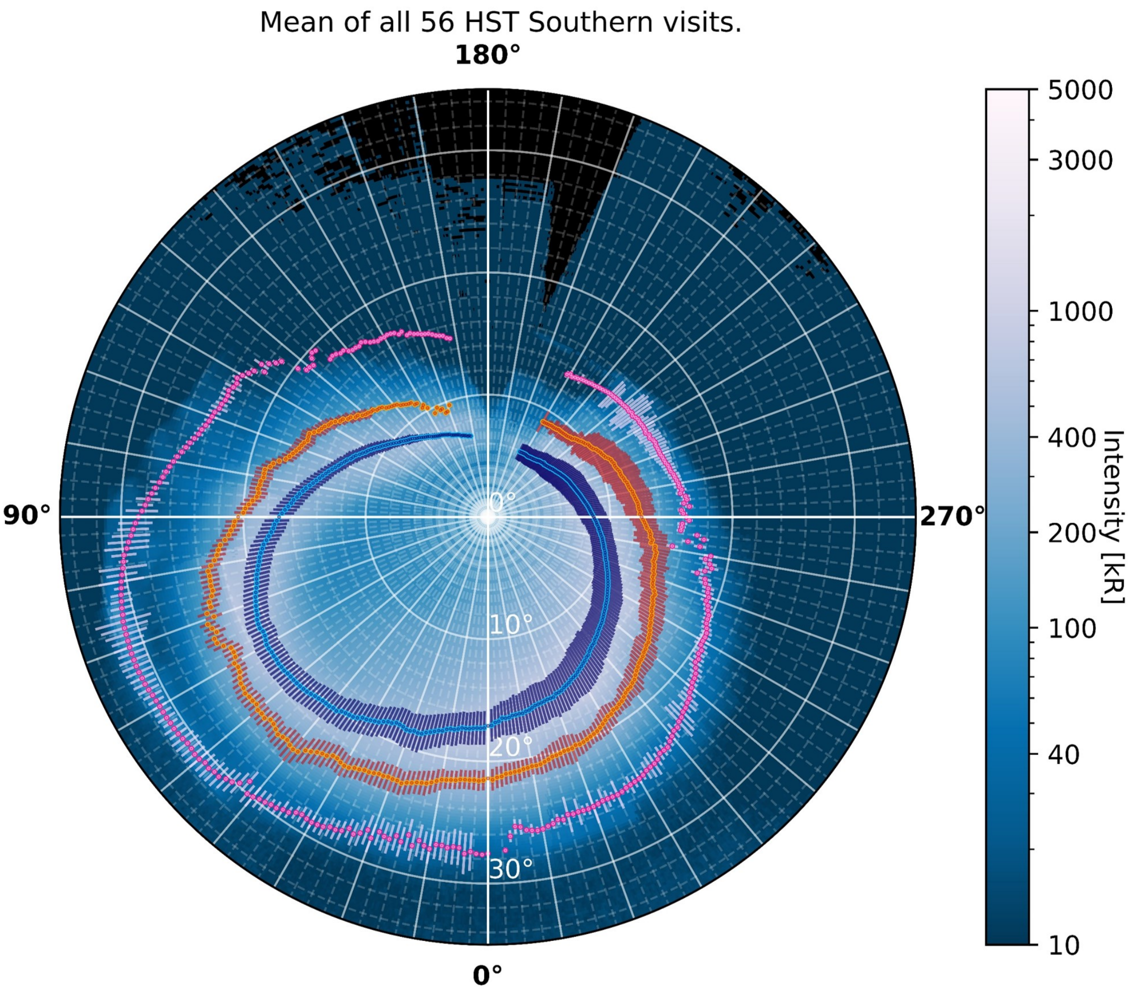

Figure 3.1: Projected image of the mean intensity of the 56 Southern visits studied, with the location of the average location of the peaks corresponding to the main oval (blue), the equatorward emissions (orange) and the Io footprint (pink), including their error bars associated. The error bars have been calculated as the average FWHM of the Lorentzian curves fitting the intensity profiles (in the case of the main emission) and as the standard deviation of the colatitude of every peak for each longitude value (in the other two cases).

3.2 Location of auroral features

This statistical study aims at constraining the location, in latitude and longitude/local time at which the secondary oval forms. Latitudinally, the detection algorithm provides an x_0 value for the centre of the Lorentzian curve, which, after some validation and further processing, will be considered the centre of the equatorward emission (sometimes arguably the secondary oval), and it usually coincides with the brightest peak between the main emission and Io footprint. Analogously, the amplitude parameters of the curves fitting the auroral emissions are considered proxies for their intensities. And finally, the width of the main emission is estimated from the full width at half maximum of the same curve. As a note, the width of the equatorward emissions and Io footprint is not estimated using this method due to the higher constraints imposed on those curves, as well as their lower intensities and smaller samples.

The large size of the original sample (more than 200,000 latitudinal profiles to be fitted) is, simultaneously, one of the main strengths of this analysis, and a challenge that did not allow for the algorithm to be equally reliable in all the visits and longitudes. This is why much effort has been put into the validity, repeatability, and statistics of the analysis made out of the raw results obtained from the detection algorithm. The subsequent filtering, via sigma deviations, minimum brightness and sample size thresholds helped avoid this issue by refining the dataset to be exploited next, as it was described in Section 2.2.

The average main, equatorward and Io footprint emission locations for the 56 visits analysed are shown in Fig. 3.1. The auroral image underlying the points corresponds to the average of all visits. The longitudes for which points are missing are due to either lack of CML coverage (i.e. the region around 180° always being on the nightside as seen from HST) or the fitting algorithm not performing (due to lack of strong enough emissions). The error bars of the main oval are the mean FWHM for every latitudinal profile, while those for the equatorward emissions and Io footprint correspond to the standard deviation of their latitudes.

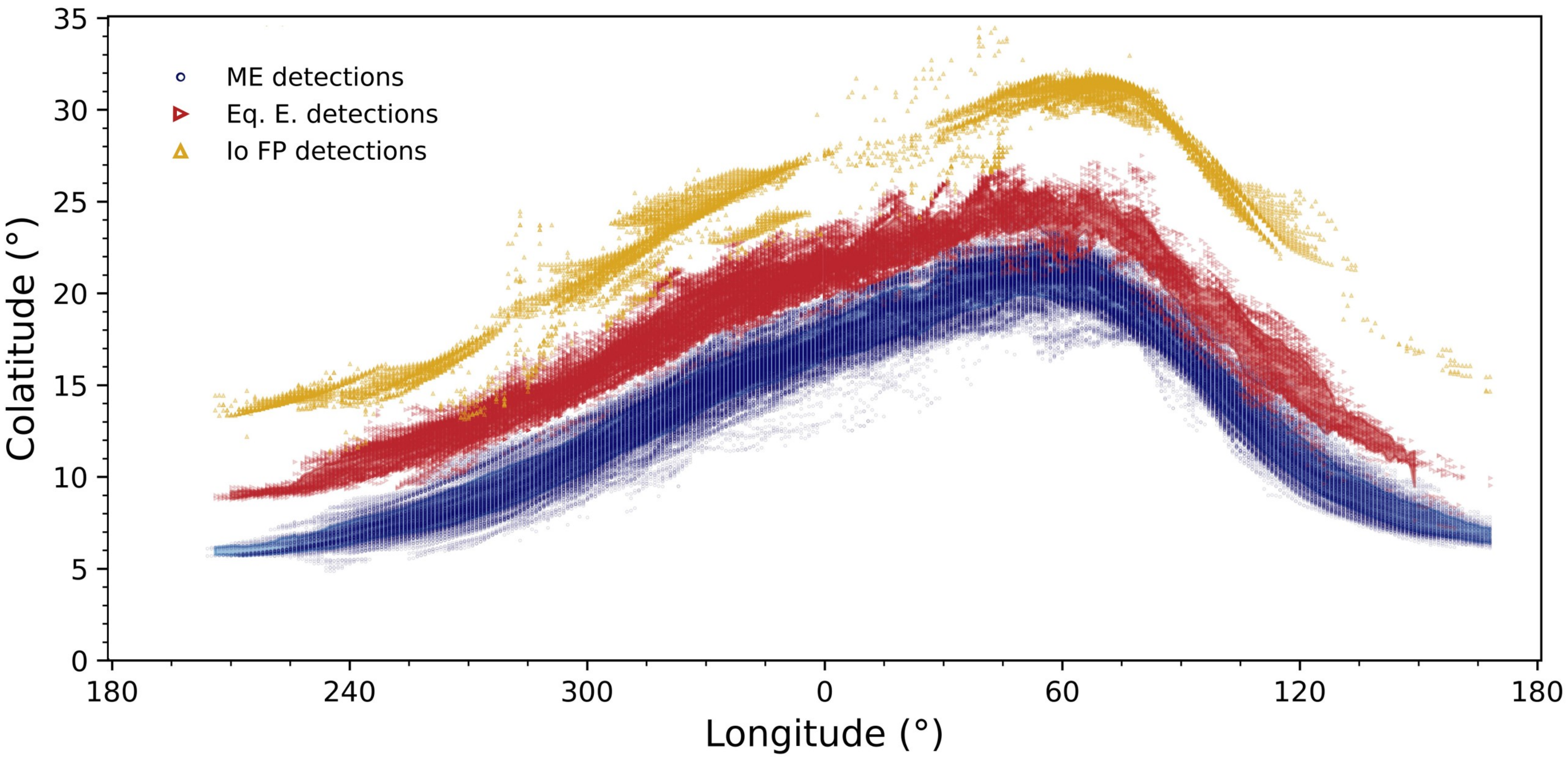

Figure 3.2: Location of all the fitted peaks corresponding to the main oval (blue), the equatorward emissions (red) and the Io footprint (yellow) for the Southern Jovian aurorae. The average location for every longitude, including their error bars (within a deviation of 1σ) is also shown for the main and equatorward emissions.

3.3 Statistical results

The clouds of points in Fig. 3.2 show the location (longitude and colatitude) of all the peaks of the Lorentzian curves fitted to both the main emission (blue), the equatorward emission (red) and Io footprint (green), by System-III longitude. All the ovals are concentric, as expected, appearing at minimum latitudes around 60° in longitude. As explained in Section 2.2, the gap around 180° (and the shifting of the data along the horizontal axis) is due to the lack of visibility for all CML values. The average separation between the equatorward and the main emissions is about 4°, and about 9° between the main emission and Io footprint. Table 3.1 provides the numerical values of colatitude for every 10° of S-III longitude (1° resolution data is available on the Table A.1 in Appendix A).

I have also used the mapping tool described in Section 2.4 to find the radial distances in the equatorial plane corresponding to the field lines whose ionospheric footprint falls on the locations of our studied emissions. Figure 3.3 shows the results for both reference ovals, the main one (in black) and the equatorward one (in red). I used the JRM33 model (Connerney et al. 2022) in combination with the external field component provided by Con2020 (Connerney et al. 2020). The resulting equatorial radial distances for the equatorward emissions span from 10 to 20 R_J (close to the 10-17 R_J given by Tomás et al. 2004).

This does not imply that the sources in the magnetosphere of some of these equatorward features detected must be always in that region since only the average location of the emissions was mapped, without considering their width (which is especially large at times when features like the secondary oval or injection signatures are present). When comparing these values to the semi-major axis of the orbits of the Galilean moons, the source for the equatorward emissions is found further than Io's orbit (5.9 R_J) and up to slightly more than Ganymede's (15 R_J). Regarding the main emission, its source is located at slightly further distances than previously estimated Vogt et al. (2011), if we use our reference oval. However, Grodent et al. (2003a) already showed that the main oval is not expected to map to a constant

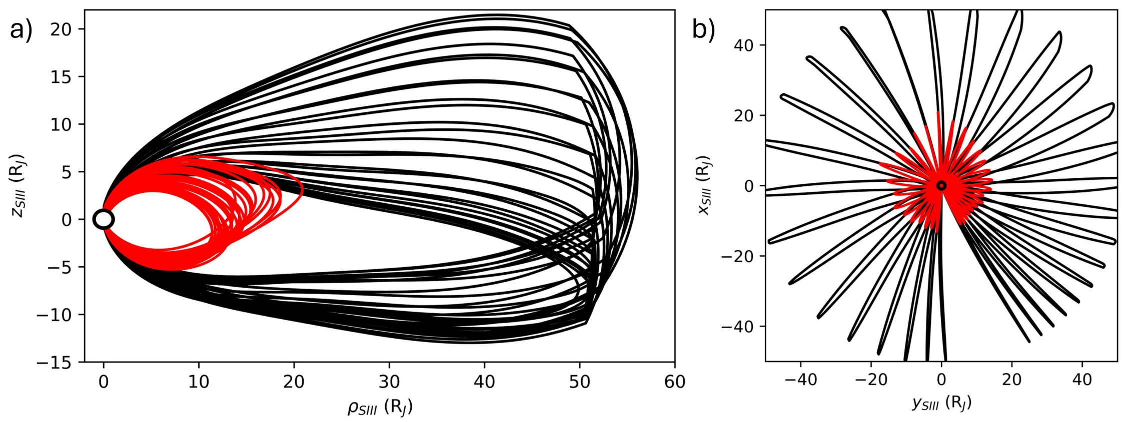

Figure 3.3: Magnetic field traces of the locations for the main emission (black) and equatorward emissions (red). Left figure, **a)**, shows the radial distance and Z coordinate of the locations in the magnetosphere, while **b)** shows their X and Y coordinates (all in left-handed S-III longitude system and using models JRM33 with Con2020).

radial distance, and if our estimations of width of the oval are included in the mapping, the range of radial distances encompasses a good fraction of the middle to outer magnetosphere (30-70 R$_J$).

Below follows a detailed analysis of the results provided by the detection algorithm. For the sake of clarity, it has been split into the different physical magnitudes involved: longitude and local time (and their role on both the frequency and the intensity of the emissions), width of the main oval, and temporal evolution of the features. Last, a general dissection by morphological families is presented, before moving on to the final discussion and summary.

3.3.1 Longitudinal location

The histogram in Fig. 3.4 (a) shows the binned frequency of detections by longitude of both the main and the equatorward emission concerning the total amount of intensity profiles the algorithm was applied to. In this case, the distribution of the main oval detection mostly follows that of the CMLs of the studied visits. This simply means that the main emission is found equally frequently across all longitudes,

(a) Longitude

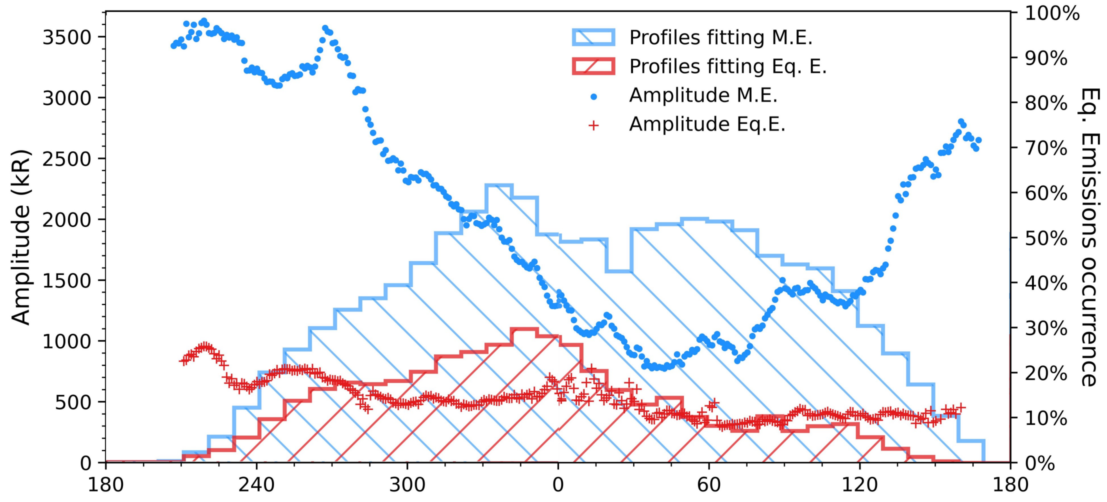

(b) Local Time

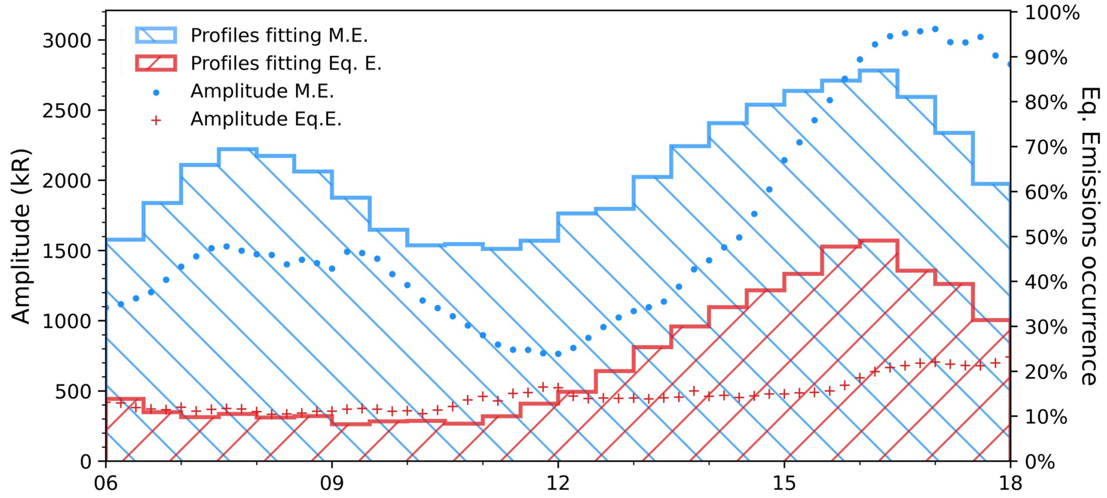

Figure 3.4: Median amplitude of the peaks corresponding to the main (blue circles) and equatorward (red crosses) emissions per **a)** S-III longitude and **b)** Local Time. The blue histogram displays the frequency of detected peaks for the main emission, while the red histogram shows the frequency of equatorward emission detections.

and it is only modulated by the angle of observation from HST (as expected). However, a more interesting result can be extracted for the equatorward emissions, which show a significant tendency to appear more often in the S-III longitudes between 240° and 360° than in the 0°-120° interval.

In the same Fig. 3.4 (a), the median amplitudes of the peaks of the fitted curves in the algorithm have been overplotted. As explained in Section 2.2, the amplitudes can be considered a good proxy for the intensities (and have the same units of kiloRayleighs). The blue points represent the median values for the main oval, while the red crosses do the same for the equatorward emissions. This shows that not only the frequency of the detections is higher for the longitude interval 200-360°, but also that the emissions are on average much brighter in those longitudes. This effect is more noticeable for the main emission (for which the median amplitude is up to 3 times brighter around 240° than around 60°) but also occurs in the equatorward emissions (65% brighter in the 200-360° interval than in the 45-160° interval).

3.3.2 Local time dependence

Analogously to the figure separating the detections by longitude, the histogram in Figure 3.4 (b) shows the binned frequency of detections by local time. The detections for the main emission (in blue) are relatively uniform, with an average of two out of three detections for all the profiles, as detailed in Table 3.4. The pre-dusk sector is the one showing a more distinctive main oval (more than 80% of detections around 16h LT), and it decays significantly in the pre-noon sector (between 09-12h LT). This coincides with the well-known gap in the main oval described by Radioti et al. (2008a). The frequency of detections for the equatorward emissions (in red) shows a higher dependence on the local time. The results have been summarised in Table 3.4, which proves that the algorithm detects equatorward emissions almost four times more often at the pre-dusk sector (between 15-18h LT) than at the post-dawn sector (06-09h). Table 3.3, in turn, shows the averaged values for their amplitude, separated by morphological families and local-time sectors.

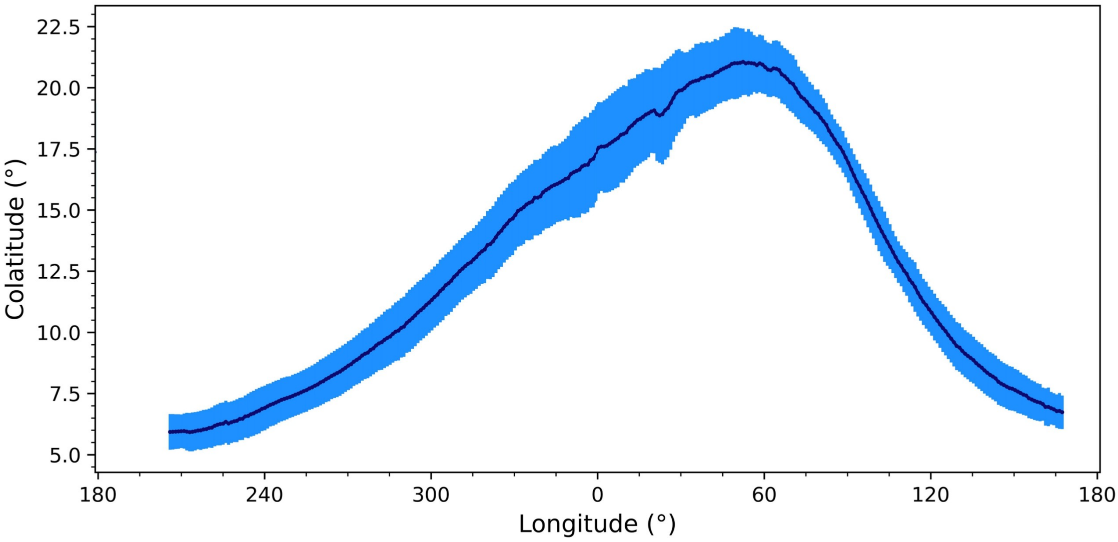

Figure 3.5: In blue, full width at half maximum of the Lorentzian curve fitting the main emission by left-handed S-III longitude. The average colatitude of the main emission is shown by a black line.

Figure 3.4 (b) also shows the median value for the amplitude of both peaks (main emission, in blue, and equatorward emission, in red) for every latitudinal profile. Both emissions are more intense in the pre-dusk sector than at noon and post-dawn. This difference is more dramatic for the main emission, which reaches median peak intensities of 2.7 MR around 16h LT, while it stays between 1-2 MR in the morning sector and shows a dip in the amplitudes right before noon. The variability in the equatorward emissions is not as stark as in the main oval, but they do show an increase of almost 70% from the pre-dusk sector compared to the post-dawn sector. Contrary to the main emission there is no dip but a slight increase in the median intensity around 12h LT, which can be explained by the recurring appearance of bright injection signatures in that region.

3.3.3 Width of the Southern Main Emission

Determining the width of the main emission is challenging due to the high variability of the power, location, and morphology of the auroral emissions. In the past, values for the width have either been estimated globally (Ingersoll et al. 1998, Cowley et al. 2001, who provided a value for the average width of 1°), or calculated for specific cases such as the narrowest morphologies (Grodent et al. 2003) or certain unusual features like general brightening or dawn storms (Yao et al. 2022).

The algorithm utilised for this chapter was not designed for calculating the width of the main emission as its main priority. However, considering the way it fits the latitudinal profiles to curves, and after empirically checking its correct functioning, it is concluded that the results obtained from it can be considered upper limits for the average main oval. The results are shown in Fig. 3.1 as the error bars/width of the projected main emission, and in Cartesian coordinates in Fig. 3.5. The mean value for the FWHM across all longitudes is 2.35° ± 0.72°. For the local times, there is not a large difference between the post-dawn (1.97°) and the pre-dusk sectors (2.14°), but the main oval (or at the very least the curves fitting it) around noon get substantially wider (2.79°).

This increase in the FWHM correlates with the smaller amplitude in the same sector shown in Fig. 3.4. In that sense, its interpretation can be twofold: physically, it shows wider emissions in that sector, but it can also be caused by the poorer fitting in the locations closer to noon, linked again to the presence of both the discontinuity (Radioti et al. 2008, Chané et al. 2013) and the injection signatures (Mauk et al. 1999, Mauk et al. 2002).

As a final note, the explanation for considering the values for the width of the main emission as an upper limit is due to the PSF of the instrument, which, when convoluted with the Lorentzian curve of the fitting, enlarges the observed FWHM of the emissions. This observed width is hence the quadratic sum of the real width and the latitudinal spread caused by the PSF, $\Delta\theta_{obs} = \sqrt{\Delta\theta^2_{real} + \Delta\theta^2_{PSF}}$. The latitudinal spread of the PSF ($\Delta\theta_{PSF}$) depends on the distance between the observer (HST) and Jupiter, the local time, and the difference between the latitude of the aurora and the sub-Earth point, being maximum for the noon and minimum for the dawn and dusk edges. After doing these calculations for an average distance to

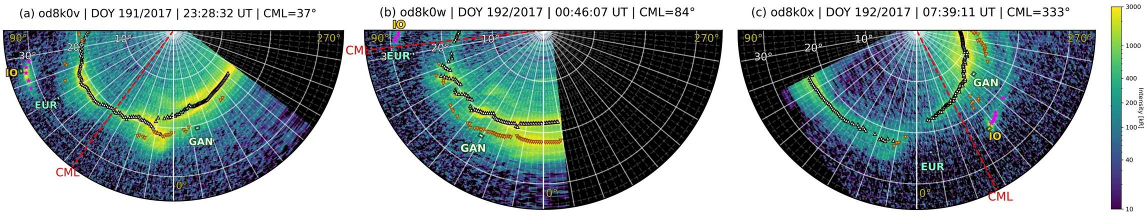

Figure 3.6: Images from three consecutive HST visits from the Observation Campaign 14634 (Grodent et al. 2018), showing the temporal evolution of the injection signatures. Overplotted to the images appear the location of the algorithm peaks for the main emission (black and white), the equatorward emissions (orange) and the Io footprint (fuchsia).

Jupiter of $7.14 \cdot 10^8$ km (4.88 AU), I obtained that the PSF of the instrument spreads between 0.25° and 0.9° for the edges and noon, respectively, and the total impact on the widths ranges between 2-15% lower than the observed values.

3.3.4 Temporal variability of the auroral emissions

The duration of the HST visits (around ∼40 minutes per visit) imposes restrictions on the conclusions that can be derived regarding the lifetimes and temporal variability of the different auroral emissions studied in this chapter. However, the emissions sometimes do exhibit variations within the length of the visits, and on some occasions, multiple consecutive HST observations allow for the analysis during a larger time interval.

As a paradigmatic example of the constraints and estimations we can make about the timescales regarding these emissions, Figure 3.6 shows three images taken in two consecutive HST orbits (od8k0v and od8k0w, separated by 90') and another visit six hours later (od8k0x). The first two show very similar auroral injection signatures near the 0° longitude and 22° colatitude (indicated in orange in the figure, under the black and white main emission) , while, by the time of the third visit, those features have dimmed (are barely picked out by the algorithm), but are still visible. The next visit, which observed the planet three Earth days after the first one, did not show any of these emissions. However, later in that same series of observations (visits od8k0z, od8k1b and od8k1c) an elongated secondary oval arc was detected at dusk and lasted for, as a minimum, an entire Jovian rotation.

Based on our analysis (albeit mainly qualitative, and obtained from a limited number of cases such as the example explained above), some conclusions can be drawn. The first is that there have been no observations of the secondary oval either forming or appearing. This, combined with the time passed between close HST visits in which this feature appears, suggests a minimum lifetime of around 3 hours (which corresponds to the interval between two visits of HST taken during two consecutive orbits, ∼90', plus the duration of the two visits, ∼80'). However, since the oval is often visible in the same locations for several days, the typical duration of this feature is surely much longer, on the scale of one to several Jupiter rotations. It must be noted that the only previous estimations of the lifetime of the secondary oval were done by Gray et al. (2017), which found an example of the oval surviving for at least 28 hours.

The second conclusion reinforces the interpretation made by Dumont et al. (2014) and Dumont et al. (2018). They stated that the auroral injection signatures generally have lifetimes of 5-10 hours, i.e. between half and an entire Jupiter rotation, and timescales for significant brightness variations of ∼8 minutes. These values are within the same range as the ones found in our studied cases, although a more detailed analysis would require distinguishing quantitatively between injection signatures and secondary oval (e.g. using their different shapes as a way for the algorithm to discern between them). In general, I find that the equatorward emissions are not particularly variable on timescales shorter than a single visit, although the injection signatures show more rapid changes than the secondary oval.

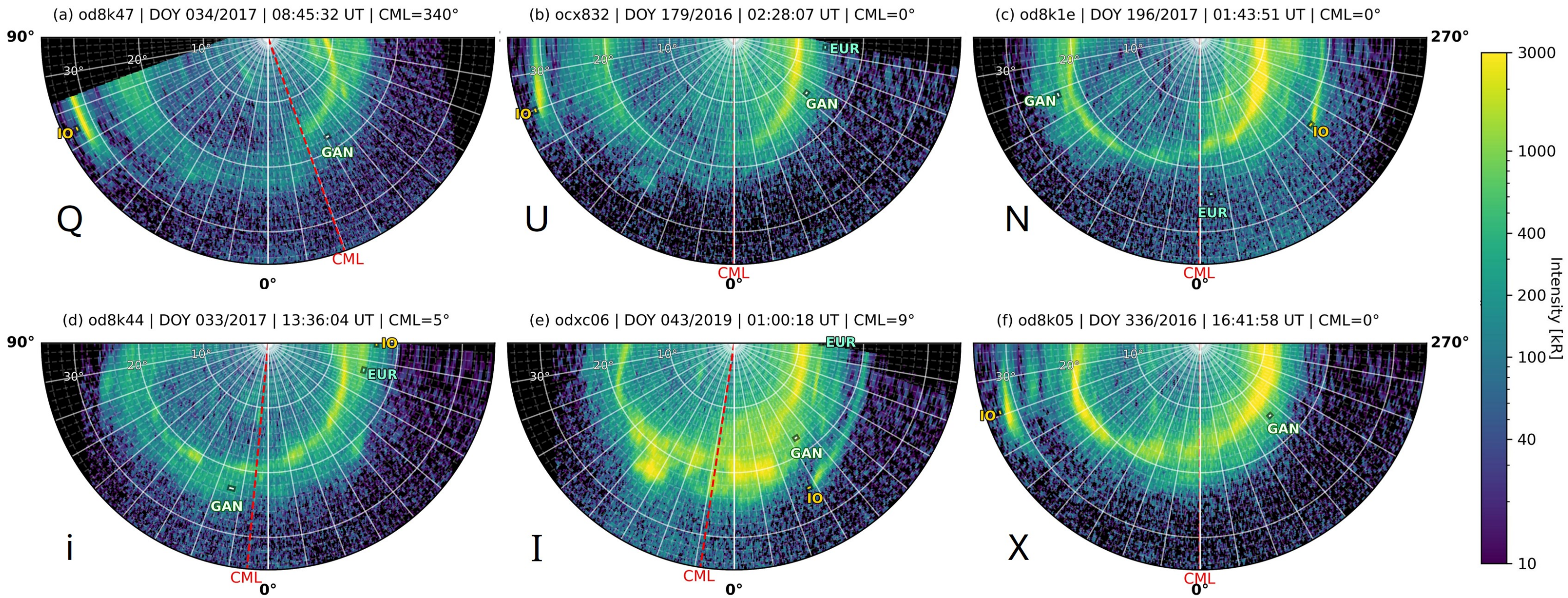

Figure 3.7: Six polar projected images of the Jovian Southern aurorae from the studied sample. Each of them is a visit showcasing one of the six morphological families as defined by Grodent et al. (2018). Top row, left to right: **a)** "Quiet", **b)** "Unsettled", **c)** "Narrow"; bottom row, left to right: **d)** "moderate injection", **e)** "strong Injection", **f)** "eXternal perturbation". The CML for each image is indicated in red and the images are shown in left-handed S-III longitude, looking "through" the planet. The locations for the moon footprints have been taken from Hess et al. (2011).

3.3.5 Relation with the auroral morphological families

Definition of the families

Grodent et al. (2018) classified 118 HST images, taken during Juno perijoves 3 to 7 (from November 2016 up to July 2017), into six new definitions of "UV auroral families" to help provide a simplified description of the complex dynamics observed in the UV auroral emissions. Although this classification is purely visual and is not exempt from its own issues (some of them mentioned below), in this work I decided to use it and characterise the newer visits based on it. These auroral family definitions are summarised as follows, and examples for every visit for the Southern hemisphere are shown in Figure 3.7:

1. ***Q*** **("Quiet")**: very low total auroral power (<1 TW) in a more expanded and broader main oval. No (or very dim and diffuse) equatorward auroral emissions.

2. ***N*** **("Narrow")**: very narrow, continuous and expanded main oval, with average auroral power and low to moderate polar activity.

3. ***U*** **("Unsettled")**: the intermediate stage between *Q* and *N*. Moderate intensity of the emissions. Main oval relatively wide but fainter at dawn and narrower in the afternoon and dusk sectors.

4. ***I*** **("Strong injections")**: strong enhancements at the noon sector (∼140-170° S-III longitude for the North, ∼40-100° for the South), equatorward of the main emission (usually corresponding to noon in local time). Associated with a corner-shaped feature towards the afternoon sector (visible in the Northern hemisphere only).

5. ***i*** **("Moderate injections")**: very similar morphology to *I* with an overall lower brightness of the equatorial auroral (and no corner feature for the North). This family has been interpreted as an early/late stage of *I*.

6. ***X*** **("eXternal perturbations")**: very strong and contracted main emission, enhanced at dawn and dusk. The polar region exhibits bright, pulsing patches and arcs parallel to ME. This type of family has been linked with magnetospheric responses to changes in the interplanetary medium (e.g. compressions).

Results of the algorithm

Next, the most significant results of each of the families will be discussed. Tables 3.3 and 3.4 summarise respectively the results of the algorithm for the amplitude and frequency of the detections by sectors, before and after separating the visits into the different morphological families described above.

- ***Q*:** one of the validation checkpoints used to confirm the well functioning of the algorithm is the fact that the frequency of the detections decays considerably for the visits tagged as "quiet" across all sectors and for both the main and equatorward peaks. This is particularly noticeable in the dawn sector (a quarter of the average fraction of detections). The median amplitude, as shown in Table 3.3, is also lower overall but specifically in the post-dawn sector of the main oval. Finally, another result in agreement with the expected morphology of this family is the relatively expanded main emission (Grodent et al. 2018), almost a degree equatorward with respect to the average location at the post-dawn and pre-dusk sectors. However, it must be noted the relatively small size of the Q family sample, with only 5 visits.

- ***U*:** the most remarkable result that the 17 "unsettled" visits yield is the very low frequency of detections at the noon sector, both for the main and the equatorward emissions, concurrent with a decrease in the intensity. This result coincides with the discontinuity in the main oval (Radioti et al. 2008) that appears especially frequently in this family.

- ***N*:** the "narrow" family includes 8 visits in this sample and, as expected, is the family that differs the least from the average location of the ovals, since it comprises the cases where the main emission is most clearly displayed and it does not include particularly abnormal features such as bright secondary emissions. The only statistically significant deviation of this family with respect to the average is a relatively brighter than usual main oval at dusk.

- ***I*:** the frequency of equatorward emission detections is increased during the stronger injection events, as expected. The relative enhancement of secondary emissions in both frequency and amplitude is stronger at pre-dusk and, especially, noon (the usual local times of the secondary oval and the injection signatures, respectively). This is in agreement with the brightening events associated with previous injections signatures detected by measuring the auroral power emitted (Kimura et al. 2015, Gray et al. 2016, Haggerty et al. 2019).

- ***i* and *X*:** similar to *I*, but less remarkable differences overall. There is an exception in the notable difference between *I* and *X* for the equatorward emissions at the dawn side, though, which can be linked respectively to the ADS (Auroral Dawn Storms) and MAB (Main Auroral Brightening) types of events defined by Yao et al. (2022). As a side note, it must be reminded that the distinction between these two families and the *I* family is very tenuous for the Southern hemisphere. This is due to two factors: the fact that the families were initially defined for the North, and the differences between them are subtler in the South (e.g., there is no presence of the corner-shaped feature which characterises the *X* family in any of the Southern visits). Regarding the amplitude, though, there is a difference in the intensity of the main emission, with that of the *X* family being consistently higher than the *i* group for all local times.

As a general comment, it is worth pointing out that our distribution of visits by families, i.e. the fraction of each family to the total amount, is very similar to the results in the original Grodent et al. (2018) definition (even though more than half

Sector	Average	Q	U	N	I	i	X
# visits:	56	5	17	8	10	12	4
			Main emission				
All	0.0 ± 1.1	0.8 ± 0.9	0.3 ± 1.1	0.2 ± 0.9	-0.4 ± 1.1	-0.3 ± 1.2	-0.1 ± 1.1
Noon	-0.5 ± 1.1	0.5 ± 1.0	-0.3 ± 1.1	-0.1 ± 0.7	-0.9 ± 1.2	-0.8 ± 1.0	-1.2 ± 1.1
Dusk	0.2 ± 1.0	0.8 ± 0.8	0.4 ± 0.9	0.1 ± 0.9	-0.1 ± 1.0	-0.3 ± 1.0	0.0 ± 0.9
Dawn	0.4 ± 1.1	1.3 ± 1.0	0.5 ± 1.2	0.7 ± 1.1	-0.1 ± 0.9	0.3 ± 1.0	0.6 ± 0.6
			Equatorward emission				
All	0.0 ± 1.0	0.1 ± 1.0	0.0 ± 1.1	-0.1 ± 0.9	0.0 ± 1.0	0.1 ± 1.0	-0.2 ± 1.1
Noon	0.0 ± 1.1	0.8 ± 1.3	-0.2 ± 1.2	0.2 ± 0.8	-0.2 ± 0.9	0.1 ± 1.0	-0.4 ± 1.1
Dusk	0.1 ± 0.9	-0.1 ± 0.6	0.2 ± 0.8	-0.1 ± 0.8	0.3 ± 0.9	0.1 ± 1.0	0.0 ± 0.7
Dawn	-0.1 ± 1.3	-0.6 ± 0.9	-0.2 ± 1.4	0.0 ± 1.5	-0.1 ± 1.3	0.1 ± 1.0	-0.2 ± 1.7

Table 3.2: Deviation in degrees from the average colatitude of the Main Emission (top) and Equatorward emission (bottom), by morphological family (and total average).

of these visits had not been categorised previously). However, the lack of striking differences in the parameters between the families is not particularly surprising, albeit raises some doubts about the applicability of the classification. The reasons that explain this lack of variability between families are:

1. **Lack of homogeneous sampling**: due to the unequal CML coverage, the longitudes close to 180° get relatively few (or no) fitting profiles compared to the 0° ones.

2. **Small number of families**: which results in each family having a relatively large number of cases with respect to the total visits. Thus, each family has a strong impact on the average ("reference") result, preventing major differences between the average of a particular family and the reference.

3. **The diversity in the aurorae:** beyond the different families, across the 56 visits different peculiar features are found for whose the fitting algorithm is not optimised and tend to fail more than with the more "canonical" families. These

Sector	Average	Q	U	N	I	i	X
				Main emission			
All	1640 ± 1710	1612 ± 1030	1640 ± 1640	1660 ± 1620	1650 ± 1860	1520 ± 1900	2500 ± 1500
Noon	920 ± 930	860 ± 360	700 ± 500	690 ± 550	950 ± 790	1060 ± 1240	1900 ± 1500
Dusk	2810 ± 1500	2680 ± 740	3100 ± 1630	3940 ± 1370	2180 ± 1150	2210 ± 1500	4240 ± 900
Dawn	1450 ± 2160	380 ± 130	850 ± 1100	1630 ± 1580	1990 ± 2670	1330 ± 2900	1620 ± 930
				Equatorward emission			
All	520 ± 780	440 ± 160	460 ± 420	470 ± 320	770 ± 1080	470 ± 820	530 ± 420
Noon	460 ± 640	320 ± 110	310 ± 260	310 ± 130	1120 ± 780	430 ± 200	460 ± 290
Dusk	610 ± 460	550 ± 140	620 ± 360	610 ± 300	670 ± 670	590 ± 270	630 ± 240
Dawn	370 ± 1140	310 ± 100	380 ± 280	390 ± 200	540 ± 2870	350 ± 1170	340 ± 160

Table 3.3: Mean amplitude in kR of the peak for the Main emission (top) and Equatorward emission (bottom), by morphological family (and total average).

features include dawn storms (Clarke et al. 2009), polar spots or flashes (Pallier et al. 2001, Bonfond et al. 2016), broad brightening of the dusk sector (Bonfond et al. 2015), or even the occasional appearances of Europa and Ganymede footprints, whose intensity is very hard if not nearly impossible to predict.

4. **The ambiguity** in the definition of the morphological families. First, because they are catalogued on a visual basis, based on a series of features that rarely appear simultaneously and clearly. Second, because the basis for their descriptions is the aurorae in the Northern hemisphere, and the application of the features that determine them is sometimes not directly applicable to the Southern morphology. Nonetheless, the fact that our fractions (all from Southern visits) are very similar to the original ones (which were a mix of North and South) indicates that the categorisation is consistent.

3.4 Summary and discussion

I have compiled the largest sample of FUV images of the Southern Jovian hemisphere so far and applied an automatic detection algorithm to identify and locate

Sector	Average	Q	U	N	I	i	X
Main emission							
All	**66%**	43%	56%	77%	69%	75%	90%
Noon	**53%**	31%	28%	68%	65%	72%	90%
Dusk	**79%**	78%	82%	75%	64%	85%	87%
Dawn	**63%**	17%	58%	76%	73%	64%	85%
Equatorward emission							
All	**26%**	16%	22%	23%	38%	25%	28%
Noon	**17%**	12%	6%	12%	34%	21%	31%
Dusk	**46%**	29%	42%	39%	69%	47%	38%
Dawn	**12%**	5%	16%	14%	7%	10%	13%

Table 3.4: Frequency of detections of the Main and Equatorward emissions by morphological family (and total average).

the most noteworthy auroral features in them, including the main oval, the equatorward features and the footprint of the moon Io. The statistical results obtained from this algorithm confirm the suspected dependence on local time of the both the main and the equatorward emissions, particularly of the feature known as the secondary oval (Gray et al. 2017, Grodent et al. 2003, Tomás et al. 2004). Next, we list the main results split by the variables they refer to:

- **Location of the emissions:** This analysis exposes a differential behaviour dependent on the S-III longitude. In particular, the equatorward emissions appear more often in the South at the 240-360° range than at any other. Latitudinally, the equatorward emissions are mostly found to be constrained between the main emission and the auroral footprint of Europa, with a greater dispersion around noon. This dispersion is explained by the injection signatures appearing in a vaster latitude range than the secondary oval. Finally, the results of the detections exhibit moderately different behaviours when split by auroral morphological families Grodent et al. (2008), as shown in the Tables.

- **Intensity:** The average intensity of the emissions, provided by the amplitude of the curves fitted to the latitudinal profiles, was found to show a strong dependence on both local time and longitude, independently of the frequency of the emissions or the type of emission considered (main and equatorward). The **main emission** shows a dip around noon, and it reaches its maximum intensities (near 3 MR) in the sector immediately before dusk, being between two and three times brighter there than in the post-dawn sector (which is consistent with Bonfond et al. 2015). It remains unknown where exactly it would start decaying within the night sector.

The fact that the Southern hemisphere has a more symmetric and less disturbed topology than the North suggests that it is a more reliable indicator of the distribution of field-aligned currents linked to the main emission. Thus, this strong dawn-dusk asymmetry in the brightness of the main emission would coincide with that found for the electric current configuration by Khurana (2001), while it mismatches the prediction made by Ray et al. (2014) of higher auroral energy flux at dawn. Even more interestingly, this enhancement at dusk would be explained by a dusk-dawn asymmetry in the inward-directed field-aligned currents, like the one recently found by Provan et al. (2024). Although that study focused on the outer magnetosphere, there is evidence that suggests that said configuration would explain the brighter dusk sector as an ultimate consequence of the plasma outflow asymmetry imposed by magnetospheric confinement by the solar wind flow (Cowley et al. 2003).

The **equatorward emissions** behave slightly differently and show no dip around 12h LT. They increase fairly constantly from dawn to dusk, where they reach intensities/amplitudes of around 700 kR on average. As for the S-III longitudes, the main oval and the equatorward emissions both reach their maximum intensities around 240° (which often corresponds to the pre-dusk sector), and the main one particularly falls unexpectedly between 0 and 90°.

- **Extension and width of the main auroral oval:** Opposite to its intensity, the width of the main auroral oval (represented by the FWHM of the curve) shows no significant difference between the post-dawn and the pre-dusk sectors, i.e. the oval is brighter, but not broader at dusk. This differs from the classical view (albeit based mainly on Northern images) of the main emission being narrower at dawn Palmaerts et al. 2024. The equatorward emissions are, in contrast, not only brighter but also more common around and before dusk, as could be inferred from Tables 3.3 and 3.4. Regarding the relation between the width of the main emission and the S-III longitude (shown in Figure 3.5), the oval is wider closer to 0° and narrows towards 180° (despite the limited coverage around the latter). More importantly, our result shows a broader main emission (2.35°) than the previous value of 1° (Cowley et al. 2001). As for its extension, our average locations for the main emission are between 0.5-1.5°, and 1.5-3° poleward of the existing Southern reference ovals provided by Bonfond et al. (2012) and Grodent et al. (2003a), respectively.

- **Temporal evolution of the equatorward emissions:** Due to the discontinuous coverage (gaps in the sampling) and the short length of the HST visits relative to the duration of these features, it is almost unfeasible to obtain some numbers for the lifetimes of these auroral features. However, based on the few close-in-time cases available, a lower limit of ∼3 hours is proposed for the secondary oval, with a typical duration of one to several Jovian rotations (in the order of tens of hours). Similarly, and as had already been indicated by Dumont et al. (2014) and Bonfond et al. (2012), the injection signatures seemingly display a slightly shorter duration of between half and one Jovian rotation.

Chapter 4

Dual Observations of the Equatorward Emissions

Chapter 3 explored in a statistical way the different auroral emissions present in the Southern hemisphere, studied using remote sensing data from HST-STIS. This chapter adds a new dimension to that study by analysing what is happening in situ in certain parts of the inner and middle magnetosphere for times close or simultaneous to HST observations of the FUV aurorae. To do that, I will use two instruments on board the Juno spacecraft: the particle detectors JADE and JEDI, whose functioning and capabilities have been explained in Section 2.3.

More specifically, the following sections describe our results for the particle detections during times when Juno was crossing the region of the magnetosphere mapping to auroral features in the ionosphere of special interest for this work: the equatorward emissions region. Therefore, in this Chapter, I focus on comparing how the in-situ particle data obtained from Juno compare with the observed auroral emissions at the footprint of the spacecraft (with HST).

4.1 Introduction

Since Juno reached the orbit of Jupiter in July 2016, the continuous stream of data from its varied set of instruments has been invaluable to comprehend better the physical mechanisms ruling the Jovian magnetosphere. Among others, it has provided us with a much better depiction of the Jovian magnetic field, including its anomaly on the Northern hemisphere (Moore et al. 2018, Connerney et al. 2017), it has proved the relationship between the brightness of the main emission and the radial current causing the enforcement corotation current (Allegrini et al. 2017, Nichols et al. 2022), and it has found inverted-V structures in downward electric current regions, demonstrating the existence of field-aligned potentials above the polar regions (Clark et al. 2017, Mauk et al. 2020).

Regarding specifically the auroral emissions beyond the main oval, several previous studies have also used Juno to study their origins and connections to the magnetosphere. The convection-driven hot plasma injections in the magnetosphere have been linked unambiguously to their ionospheric signatures (Nichols et al. 2023), with pitch angle scattering being suggested as the mechanism most likely to generate them (Dumont et al. 2018). However, there is not a straightforward correspondence between the injections and their footprints, particularly when their origin is at further radial distances, and thus their aurorae at higher latitudes on the planet (Haggerty et al. 2019).

A recent, extensive study by Palmaerts et al. (2024), combined images from HST-STIS and Juno-UVS with particular interest on the main emission, but also showcasing different auroral structures inside and outside of it, such as polar flares (Bonfond et al. 2011, dawn storms (Kimura et al. 2015), bridges (Greathouse et al. 2021), or moon footprints (Gérard et al.; Moirano et al. 2005; 2021). Nevertheless, there has not yet been a complete and combined effort to study the different outer emissions with conjugate HST and in-situ Juno observations.

The Juno dataset has been described in detail in section 2.3.3, along with the calculation of the precipitating energy flux, and the description of the mapping

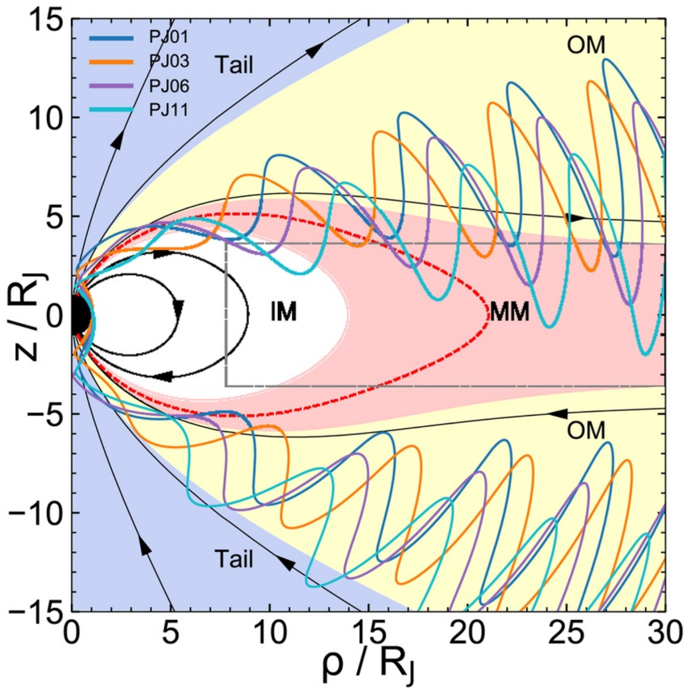

Figure 4.1: Diagram showing the evolution of Juno's near-periapsis trajectory between PJs 01 and 11 in a magnetic meridian plane. Arrowed black lines show field lines corresponding to the JRM09 model. The black dashed rectangle represents the magnetodisc. The inner (IM), middle (MM), outer magnetosphere (OM), and tail field line regions are shaded white, red, yellow, and blue, respectively, with the red dashed line showing the position of the peak L-MIC model upward field-aligned current density. Credit: Kamran et al. (2022).

between the location of the spacecraft and the region on the ionosphere. As can be seen in figure 4.1, the highly eccentric orbits of Juno allow it to cross very different magnetic field line domains. They correspond to different radial distances in the magnetosphere and different associated regions on the ionosphere: from very far distances down the magnetotail (corresponding to polarmost locations on the upper atmosphere) to very close North-to-South crossings (mapping to equatorward regions in the aurorae). Due to this orbital configuration, these closer parts of the orbit, close to the perijoves, are the ones studied in the four case studies analysed. Next, the complete set of case studies is introduced and presented in detail, before ending with some concluding remarks.

4.2 Juno crossing the equatorward emissions

In Chapter 3, I studied the equatorward emissions of the Jovian aurora, including the feature known as the secondary oval. I have identified at least three case studies in which Jupiter was being observed by HST while Juno was crossing the magnetospheric region mapping to the secondary oval. The first one happened during perijove (PJ) 3 and it corresponds to visit 44 of observation campaign 14634, DOY 33 of 2017. The second one happened at PJ-5 (visits 70 and 71 of observation campaign 14634, DOY 86 of 2017), and it was studied already by Ebert et al. (2019), but with a focus on the poleward emissions. The third one corresponds to PJ-21, and it is close, although not completely simultaneous, to visits 38 and 39 of the observation campaign 15638 (DOY 201 and 202 of 2019).

The procedure through which these particular cases were selected and analysed is as follows: all these HST visits display interesting and varied auroral emissions (Case #1: injections family; Case #2: unsettled/strong injections; Case #3: narrow, with secondary oval). Then, the trajectory of Juno was mapped to the ionosphere using the magnetic field models explained in Section 2.4, to confirm the times in which the spacecraft crossed the equatorward emissions region. Finally, those intervals for JADE-E data are analysed, searching for specific structures in both the spectrum

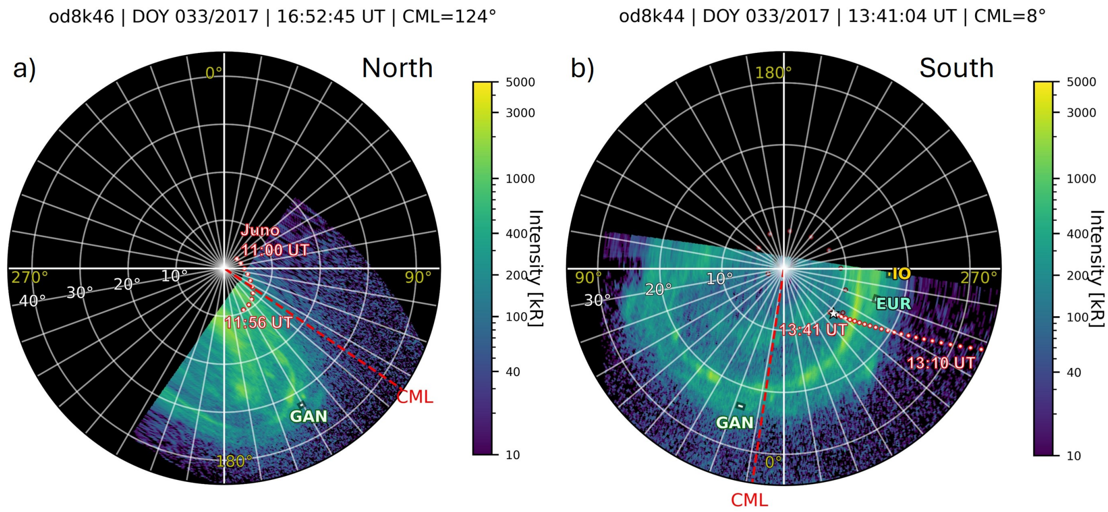

Figure 4.2: HST-STIS images during Case #1: od8k46 **(a)** and od8k44 **(b)**. White points with red edge indicate Juno's trajectory during the visit 5h before the first case (between 11:00 and 11:56 shown every five minutes), and during the visit in the second case (every minute), based on the JRM33+Con2020 magnetic field model. CML (red dotted line), Io, Europa, and Ganymede footprints are indicated too.

and the energy flux that correspond to the equatorward emissions.

4.2.1 Case #1 (calibrated): 033/2017

Case #1 consists of visits od8k44 (Southern hemisphere) and od8k46 (Northern hemisphere), and the simultaneous JADE observations during PJ-3, (day 33/2017). The auroral emission and Juno mapping for these visits are shown in Figure 4.2 (in white circles with a red edge, and a white star with black edge for the specific time-stamp of the image shown).The morphology of this case is typical of the moderate injections family as defined by Grodent et al. (2018), i.e., a relatively dim main oval accompanied by widespread injection signatures equatorward of it, diffuse and not too bright (up to 1 MR), and including the presence of a secondary oval in the afternoon sector in od8k46.

On the other hand, Figure 4.3 shows the corresponding data from JADE-E for the time intervals of those visits. They include the spectrograms (top panel), pitch angle distributions (middle), and electron energy fluxes (bottom), separated by pitch angle in the electrons precipitating within 15° and 30° of the magnetic field line, and the ones detected in the same ranges of angles but in the opposite direction. The selection of the angles for the loss cone, in this and the rest of the case studies, is given by the Equation 2.5, explained in Chapter 2 (from Mauk et al. 2017).

In the first visit (od8k44, Figure 4.2a, and the JADE-E data in Fig. 4.3, right-hand side) it can be seen the clearest example of Juno perpendicularly crossing the equatorward emission at dusk, right before traversing the main emission. That main oval can be used to get an accurate time-stamp for the secondary emission crossing and distinguish its spectral and energy flux signatures. There is a slight offset of a couple of minutes between the mapping and the spectrum, evidenced by the peak at 13:38 in the latter (downward red arrow in Fig. 4.3b). This corresponds to the encounter with the field lines mapping to the main emission, which, according to the mapping, occurs at 13:36. Taking this bright feature as a reference, it can be argued that the equatorward emissions, in an intermediate state between diffuse and a well-delineated arc-shaped feature in this case, are associated with a series of increasingly brighter injections of downward and upward electrons up to energies of ~10 keV, easy to appreciate in the energy flux (bottom panel, reaching values of up to 300 mW/m^2).

This particular interval was already studied by Mauk et al. (2020), which focused on the main emission, with its differentiated structure, from the JEDI perspective. The proposed separation between Zone-I (of downward electrons) and Zone-II (with bidirectional electrons) is also clearly observed in the electron energy flux obtained from this JADE-E data, as shown in the bottom panel of the right-hand side of Fig. 4.3, where the strongest flux comes from downward electrons first, and from upward electrons after 13:39 (marked by an upward red arrow). For comparison, the precipitating energy flux in the main emission ranges between 10-5000 mW/m^2 (here it is between 50-4000 mW/m^2).

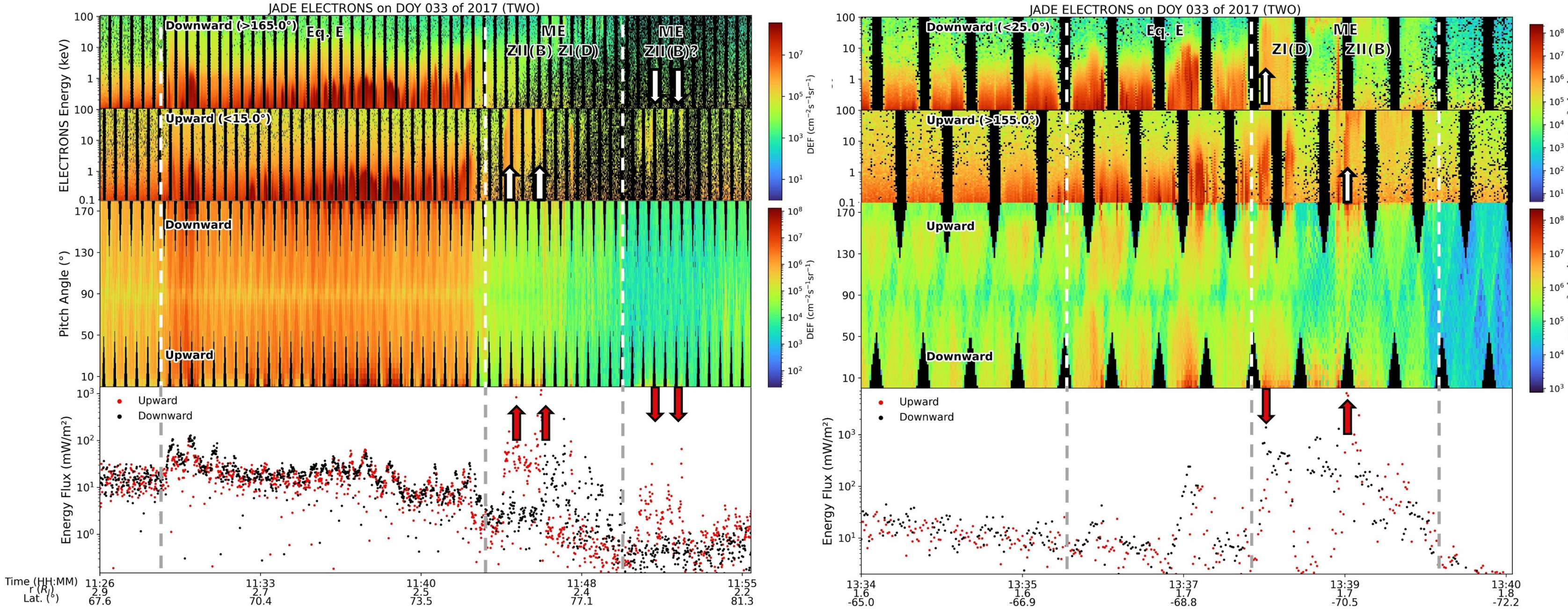

Figure 4.3: JADE-E data for Case #1. **Top:** Energy-time differential energy flux spectrograms of upward and downward 0.1–100 keV electrons observed along Juno's trajectories shown in Fig. 4.2a (**left**, between 11:26 and 11:56 UT), and b (**right**, between 13:34 and 13:41). Center: Pitch angle-time differential energy flux spectrograms for 0.1–100 keV electrons. **Bottom:** Upward (red) and downward (black) energy fluxes of 0.1–100 keV electrons.

Before the HST visit od8k44, there is another case of crossing of the main emission, but this time during an interval with no simultaneous HST evidence. When exploring the JADE-E data for that crossing, similar signatures to the ones just described above have been found, which point to the presence of equatorward emissions below the main oval. Although there is no conjugate HST evidence to confirm them when looking at the auroral region mapping to the traversed magnetospheric sector ~5 hours later (visit od8k46, Fig. 4.2a), there is significant auroral emission in the area. Taking into account the average lifetimes of these emissions (explored in Chapter 3), it is very likely that the emissions were already there around the time of the analysed Juno data. The JADE-E data for that earlier crossing is presented on the left-hand side of Figure 4.3. In it, the emission appears again as a series of periodic peaks, stronger for the downward electrons than for the upward ones. For the main emission, though, it must be noted that its structure appears inverted in this case, with ZI(D) after the ZII(B), with seemingly two late peaks of upward electrons at 11:51 and 11:52. The estimated loss cone is narrower in this case (15°), due to the larger radial distance of the spacecraft.

Figure 4.4 presents the JEDI-E particle data corresponding to these two intervals. JEDI lacks the angular resolution of JADE, and that is why the pitch angle has been split more simply between the electrons coming from "ahead" (<90°) and those coming from the "back" (>90°). Despite that lack of finer angular resolution, the intervals where the main oval is crossed (around 11:46 in a), 13:39 in b), indicated by white arrows) are sharply differentiated, including the separation between zones of downward and upward electron flux just explained above. However, the equatorward emission is less distinctive than the main emission and its signature on the JADE-E data (particularly on the bottom visit, where Juno was in the Southern hemisphere). The reason for this is that the energies of the electrons responsible for this auroral emission are usually lower than those causing the main emission (below ~30 keV, as pointed out by Allegrini et al. 2020). This is another source of discrepancy between the origins of both auroral emissions, which will be discussed later in this chapter.

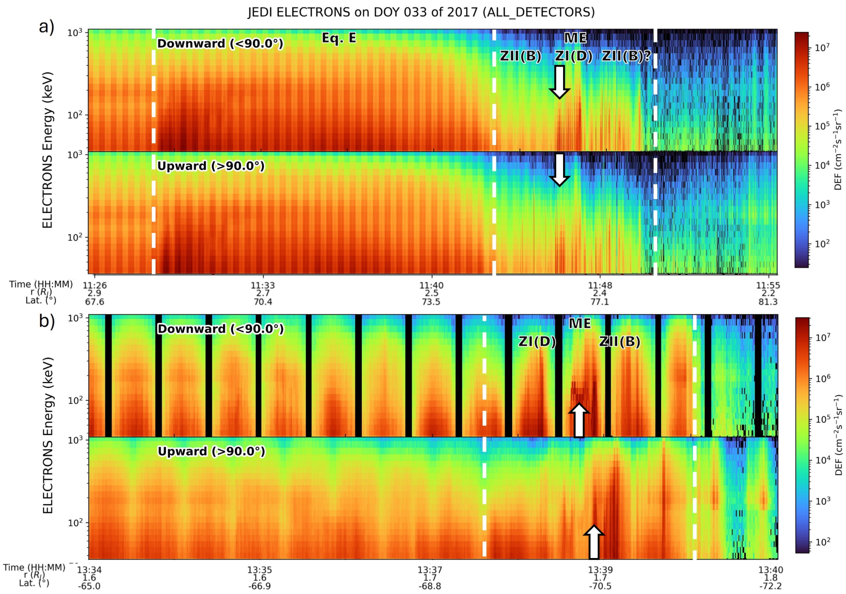

Figure 4.4: JEDI-E data for Case #1. Energy-time differential energy flux spectrograms of upward and downward 30–1000 keV electrons observed along Juno's trajectories shown in Fig. 4.2a (top, between 11:26 and 11:56 UT), and b (bottom, between 13:34 and 13:41), averaged over the three JEDI-E detectors.

4.2.2 Case #2 (calibrated): 086/2017

The two visits comprising Case Study #2 (od8k70 and od8k71) appear in Figure 4.5, including the footprint of Juno's part of the orbit simultaneous to the HST observations (between 8:04 and 8:40 UT for the Northern hemisphere, and between 9:35 and 10:15 for the Southern). The footprint is indicated in white circles with a red edge and a white star with black edge for the specific time of the image. The auroral morphologies are not very good examples of any families in particular but could be associated with injections and the unsettled case, respectively. The most relevant features for this study are: the stretched, arc-like equatorward emission parallel to the main oval around 150-180°in the North image (left), and the bright, diffuse equatorward emission between Io's footprint and the bright dusk flank of the main oval in the South (right). The magnetospheric regions mapping to these two sectors are traversed by Juno during PJ-5. Analogously to Case #1, the Figure 4.6 presents the corresponding spectrograms, pitch angle distributions, and electron

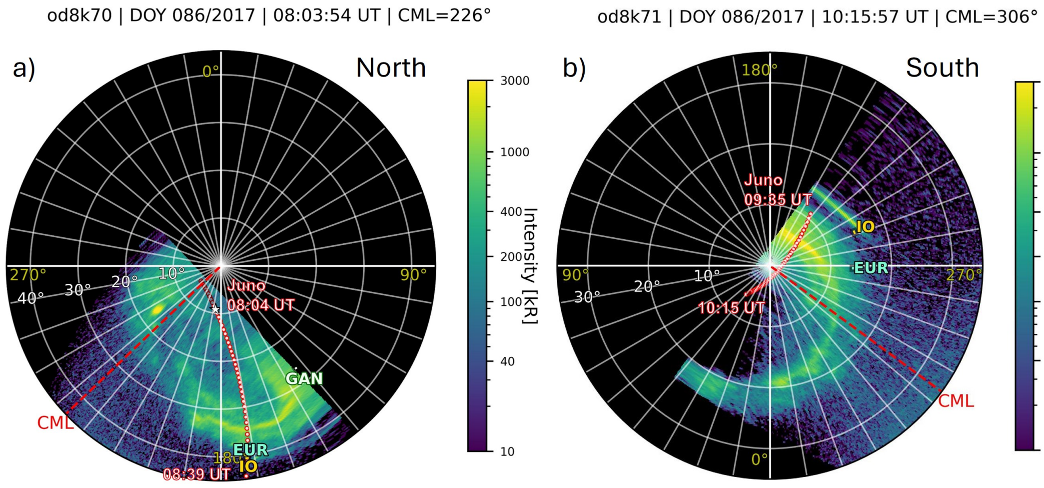

Figure 4.5: HST-STIS images during Case #2: od8k70 **(a)** and od8k71 **(b)**. White points with red edge indicate Juno's trajectory during the visit, based on the JRM33+Con2020 magnetic field model (one white point for every minute, grey points indicate 5 minutes before the start of the visit).

energy fluxes (separated by a 23° pitch angle) obtained from JADE-E for the time intervals of those two HST visits, respectively.

As it was shown by Ebert et al. (2019), the mapped trajectory of the spacecraft and peaks in the spectrogram-derived fluxes show a great concordance. Especially remarkable are the detected maxima in the energy flux corresponding to the crossing of the main emission and the Io footprint, which agree in time and thus serve as validation for the magnetic field model used for the mapping (JRM09, in that case). The main emission is characterised by bidirectional fluxes of up to 10 keV, occasionally reaching hundreds of keV for narrow features, partly provided by inverted-V configurations, but mostly broadband (Mauk et al. 2017, Ebert et al. 2017). The IFP is identified as a narrow beam of downward electrons at similar energies (∼10 keV, Frank et al. 1999, Hess et al. 2010, Hue et al. 2023), with lower energies for its tail (1-2 keV, Bonfond et al. 2009) and shown by the yellow downward arrow in Fig. 4.6). The equatorward emission is the region embedded between these two (not poleward of the main oval) and is generally characterised by ∼1-3 keV electrons, mainly in the downward direction. It shows an interesting saw-like pattern with sudden increases and decreases in the precipitating flux (marked by the red arrows), as if the spacecraft was crossing discrete flux tubes.The downgoing energy flux is 20 mW/m^2, an order of magnitude lower than the peaks associated with the main emission. In this work, I am particularly interested in new calculations of these fluxes for cases where brighter auroral features are found in this region (right-hand side of 4.6).

Ebert et al. (2021) and Bonfond et al. (2021) have both identified two dawn storm-like events occurring around 4:00 and 7:30 UT, right before the HST-STIS visits. The remnants of the latter dawn storm seem to be more discernible in the v71 images (Southern hemisphere, Fig.4.5b), as a very discontinuous main oval arc in the dawn sector. Allegrini et al. (2020) studied in detail the energy flux for the main emission across several Juno PJs, including this one.

As a side note, it must be said that penetrating relativistic particles can cause a detectable impact on the spectrograms (Becker et al. 2017, Gérard et al. 2019). This penetrating radiation caused by spurious particles with energies above the instrument range typically appears as vertical lines saturating the measurements across the entire energy range (Ebert et al. 2019). Some examples of this penetrating radiation are visible in Fig. 4.6 before 08:18 and 08:25, and at 9:30 (indicated with blue arrows), although in general, for this case and the rest in this chapter, the datasets seem relatively free of this artefact.

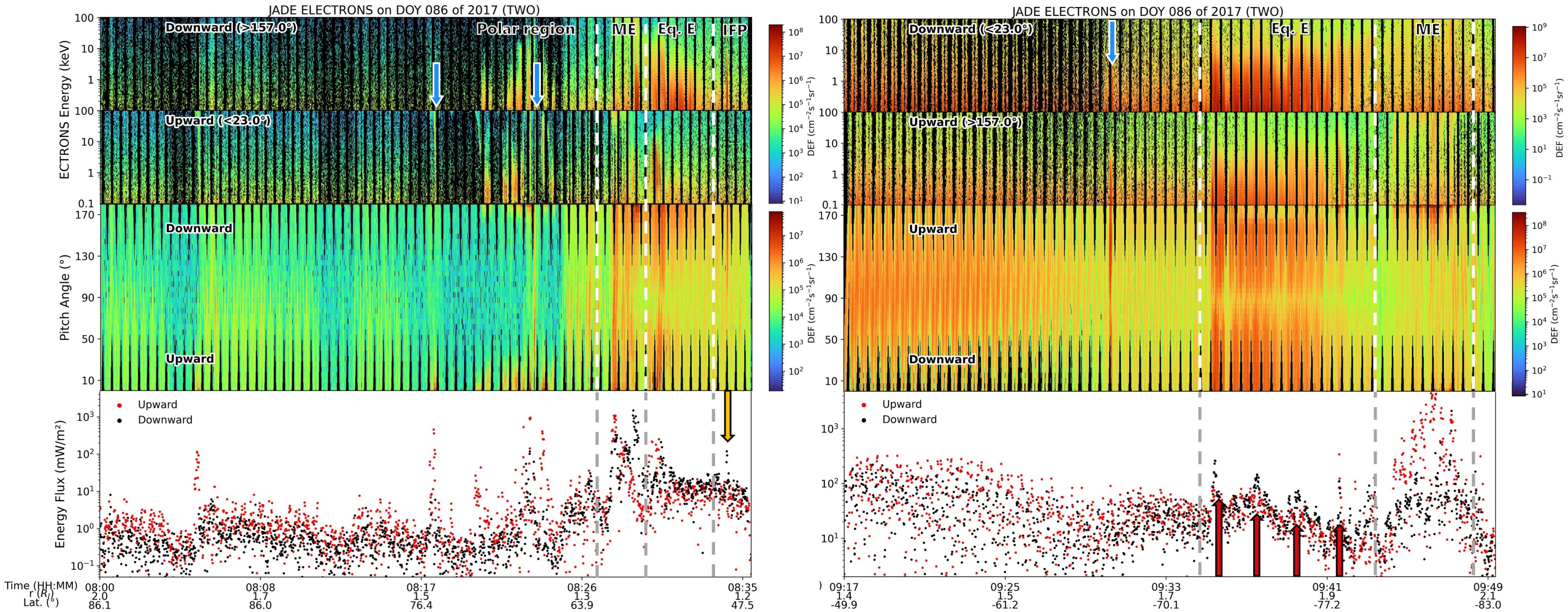

Figure 4.6: JADE-E data for Case #2. **Top:** Energy-time differential energy flux spectrograms of upward and downward 0.1–100 keV electrons observed along Juno's trajectories shown in Fig. 4.5a (**left**, between 08:00 and 08:36 UT), and b (**right**, between 09:17 and 09:50). Center: Pitch angle-time differential energy flux spectrograms for 0.1–100 keV electrons. **Bottom:** Upward (red) and downward (black) energy fluxes of 0.1–100 keV electrons. Blue arrows indicate penetrating radiation, yellow arrow indicates crossing of the Io footprint, and red arrows show the saw-like pattern in flux.

4.2.3 Case #3 (calibrated): 200-201/2019

Unlike the others, Case #3 is not comprised of simultaneous HST and Juno data. It consists of HST visits odxc38 (Southern hemisphere) and odxc39 (Northern hemisphere), along with the corresponding JADE measurements from PJ-21, days 201 and 202/2019. The auroral emission and Juno mapping close (but not simultaneous) to these visits are shown in Figure 4.7 in white circles with a red edge. The auroral morphology of this case is peculiar since it resembles that of the "narrow" family but with a quite clear secondary oval in the pre-dusk sector (and noon, in the visit odxc39). In the first visit (left) Juno's footprint overlaps with this secondary oval almost perfectly, while in the second one (right), the mapping of the spacecraft traverses this oval right before the main emission. This stark difference in the angle at which Juno crosses the secondary oval is patent in the difference in the JADE-E data analysed next.

The Juno trajectories correspond to the times of the observed JADE-E datasets∼2 hours after and ∼6 hours before the HST visits odxc38 and odxc39, respectively. The JADE-E spectrograms (top panel), pitch angle distributions (middle), and electron energy fluxes (bottom) are displayed in Figure 4.8, separating the data by pitch angle into electrons precipitating within 23° of the magnetic field line and those detected in the same range of angles but in the opposite direction.

Although this visit does not include conjugate data, its inclusion as another case study stems is doubly justified: first, due to the proximity of these HST observations to PJ-21 (occurring at 04:03 UTC of 202/2019), and second, due to the two distinct crossings of a long-lasting secondary oval in the dusk sector of the Northern hemisphere (no HST images available for the South). In the first visit, odxc38, the mapped footprint of Juno is moving alongside the equatorward region at dusk (Fig. 4.7a), while in the second one, Juno crossed the secondary oval around 03:30 (Fig. 4.7b), only half an hour before PJ-21 (at 4:02). The JADE-E data associated with the latter (Fig. 4.8, right-hand side, red upward arrows) shows a structure similar tothe one seen in Fig. 4.6, i.e., a series of increasingly strong peaks in the en-

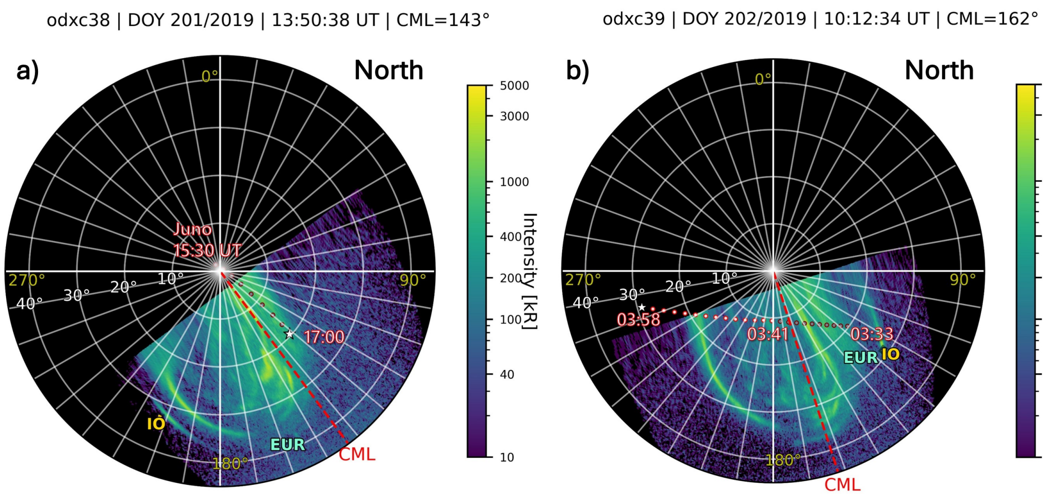

Figure 4.7: HST-STIS images during Case #3: odxc38 **(a)** and odxc39 **(b)**. Juno's trajectory is plotted in red, based on the JRM33+Con2020 magnetic field model. In a), its position between 15:33 and 17:00 UTC (201/2019); in b) between 03:33 and 03:58 UTC (202/2019). CML (red dotted line), Io, Europa, and Ganymede footprints are indicated as well.

ergy flux (10-300 mW/m^2 in both directions) before reaching its maximum (~5000 mW/m^2) when crossing the main emission at 03:37. There is an unexpected dip in the downward energy flux right after 03:34 (yellow downward arrow), especially considering the close radial distance of the spacecraft, which explains the wide choice of 45° for the width of the loss cone). This upward turn in the precipitating flux is characteristic of the polar cap regions (the swirl region, specifically, for more energetic electrons, Paranicas et al. 2018), where it has been linked to the presence of inverted-V structures (Clark et al. 2017). Although it has also been associated with the so-called Zone-II of the main emission (Mauk et al. 2020), the lack of a dominant downward accelerated electron population supports the idea that these precipitating particles map to a region different (lower in latitude) than the main oval.

The JADE-E data for the first visit (Fig. 4.8, left-hand side) is less characteristic of the secondary oval. I attribute its more uniform appearance to the fact that Juno is not transitioning between different regions (like the main and the polar regions), which is always useful as a comparison for the behaviour of the fluxes and geographical reference. Instead, the spacecraft has been located for a long period in an area mapping to the equatorward emissions (i.e., "running in parallel" to the auroral arc), thus showing a very homogeneous spectrum and smaller range in the energy flux (although with values in the expected range for the secondary oval and a similar "saw-like" profile). The mapping of the spacecraft is also less reliable than in the other visit, due to the spacecraft orbiting at a larger distance ($\sim$13 R$_J$ vs. 1.5 R$_J$), while it gets closer to the PJ, and the counterpart auroral emissions may have changed (e.g. the equatorward emission may have faded), which is impossible to know since there is no simultaneous HST images. Although the pitch angle distributions were also analysed for this interval, there is very little difference in the amount of energy flux of the electrons moving in both directions relative to the field lines, no matter the angle for the loss cone selected (at this radial distance, that upper limit for the loss cone would be smaller than the angular resolution of the instrument)

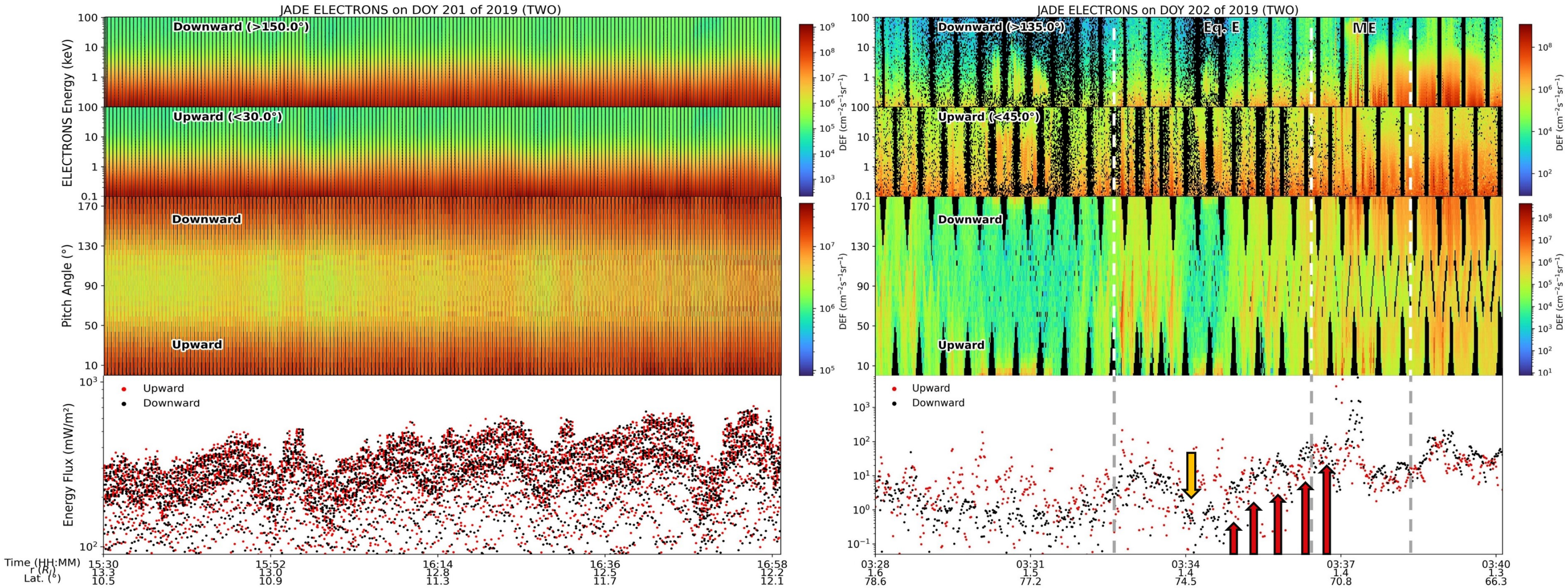

Figure 4.8: JADE-E data for Case #3. **Top:** Energy-time differential energy flux spectrograms of upward and downward 0.1–100 keV electrons observed along Juno's trajectories shown in Fig. 4.7a (**left**, between 15:30 and 17:00 UT), and b (**right**, between 03:28 and 03:41). Center: Pitch angle-time differential energy flux spectrograms for 0.1–100 keV electrons. **Bottom:** Upward (red) and downward (black) energy fluxes of 0.1–100 keV electrons. Yellow arrow shows unexpected dip in downward flux, and red arrows again show the saw-like pattern.

4.3 Comparison with injections and main oval crossings

The auroral footprints of injections of hot plasma moving planetwards, probably caused by pitch angle scattering (Dumont et al. 2014, Dumont et al. 2018), are some of the most studied types of emissions in the equatorward region. Since they are generated in adjacent and sometimes even overlapping regions of the ionosphere, it seems logical to do a quick comparison between the fluxes and spectra associated with the injections and the distinct secondary oval type covered in this chapter.

The study of energetic particle injections above the Jovian ionosphere provides context and information about the auroral emissions detected below, and vice versa. However, as Haggerty et al. (2019) proved by using JEDI data for the polar regions, there is no straightforward correspondence between the in-situ injection events and the aurorae, despite the progressive improvement in the modelling (and mapping) of the magnetic field lines. The main reason for this discrepancy is the uncertain lifetimes of the injections, which depend on its part on the lifetimes of the electron populations (Dumont et al. 2018). More recently, Nichols et al. 2023 has used JEDI data to successfully link the injections and their auroral footprints.

The most remarkable feature of the electron spectrum corresponding to those injections was the existence of several energy bursts approximately matching the location and timing of the auroral patches. That study estimated the precipitating electron energy flux (within a loss cone of 20°), yielding a value of ∼100-300 mW/m^2 (see Figure 4.9), and showing evidence of flux tube interchange during that interval (in the shape of alternating intervals of cold (few hundred eV) and hot (1-10 keV) plasma between ∼07:30 hr and ∼11:00 hr. As explained by Nichols et al. (2023), even if not necessarily causally related, this radial interchange is a proxy for ongoing magnetospheric convection, which is consistent with the production of inward injections of hot plasma.Even though it was hard to link to the individual spots, the precipitating electron energy flux value observed is enough to explain the auroral

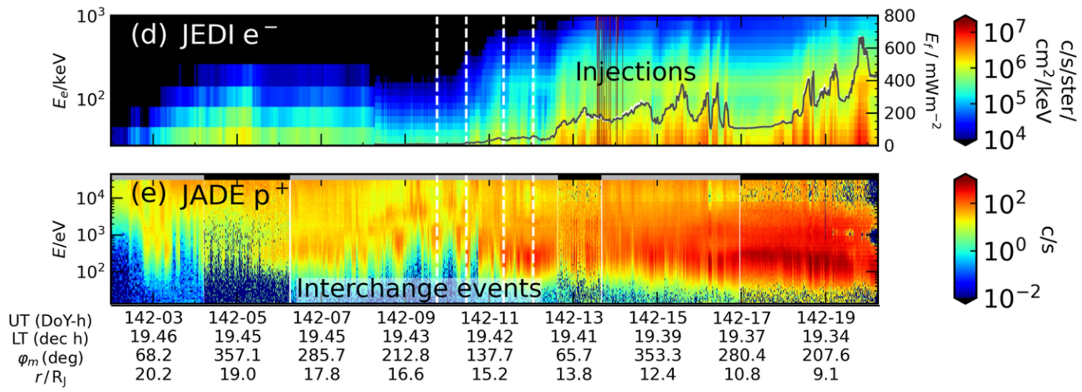

Figure 4.9: Case study d) JEDI electron energy spectra along with the anti-field-aligned energy flux, in mW/m^2 (black line overimposed). e) JADE proton energy spectra. Dashed lines correspond to two intervals with HST coverage. In panel (e) the grey and black bars at the top indicate intervals of low-resolution and high-resolution data, respectively. Credit: Nichols et al. (2023).

powers observed simultaneously by HST.

Compared to our studies from previous campaigns, the secondary oval shows values ranging from a few to up to 500 mW/m^2 (a peak of 1200 mW/m^2 is found at 20:23 of Fig. 4.6, but its spectrum seems that of penetrating radiation, making it an unreliable value). However, the secondary oval does not seem to be associated with a constant and linear increase in the energy flux. Instead, these maximum values appear as isolated, higher peaks, usually (but not always) happening simultaneously for both downward and upward electrons. A structure that seems to appear frequently across all these case studies is a "saw"-like feature: a quasi-periodic series of increasingly high peaks that appear when the spacecraft crosses the region moving from lower to higher latitudes. This feature is displayed considerably more clearly (showing a wider range in the flux variability) when Juno traverses the equatorward emission nearly perpendicularly than when it "accompanies" it for a longer period, as it does in the visit odxc38 in Case #3 (left-hand side of Fig. 4.7).

Despite the differences shown, as Gray et al. (2017) proved, the close relation between the secondary auroral oval and the injections implies some common ground regarding the origin of both the secondary oval and the “bead”-shaped auroral features (associated with injections; not to be confused with the beads linked to pre-substorms at the Earth, Gallardo-Lacourt et al. 2014). Thus, the main difference between the secondary oval and the spot-like injection signatures may reside in the physical mechanism accelerating the electrons along the field lines: with pitch-angle scattering for the former (Dumont et al. 2018), and some other kind of wave-particle interaction playing that role for the latter.

Besides comparing these emissions with the injection signatures, it is also worth observingtheir differences with respect to the main emission. As it has been mentioned already, the main emission’s signature in the spectra is characterised by higher energies, mostly dominated by broadband distributions (Mauk et al. 2017). This is opposed to the pre-Juno expectation of the more relevant role of inverted-V acceleration events, by analogy to the Earth (Amm et al. 2002, Paschmann et al. 2002). However, these inverted-V profiles, or parallel electric potentials, strongly accelerate particles downward in the polar region (Clark et al. 2017). If the present equatorward case studies are included (with no signature of inverted-V structures) in the cross-latitudinal picture, it could be conjectured that these field-aligned potentials become more important as we get closer to the poles, and become gradually more negligible towards the equator. For this equatorward emission, the broadband processes seem to be the most relevant acceleration mechanisms, but it remains to be explored in more depth the characteristics of the more energetic electrons (in the JEDI range), as well as the protons and heavy ions distributions (JADE-I).

Turning our attention to the differences in the pitch-angle distributions between these types of emission, those typical of the main oval (Mauk et al. 2017, Mauk et al. 2020) have been considerably more studied than those of injections (Haggerty et al. 2019). However, a similar trend is observed for the width of the beams, as the main emission and, even more, the polar cap regions show narrow beamsthat cannot be resolved by the JEDI angular resolution, and that are even more extreme for the ions. While the downward electrons slightly dominated the equatorward

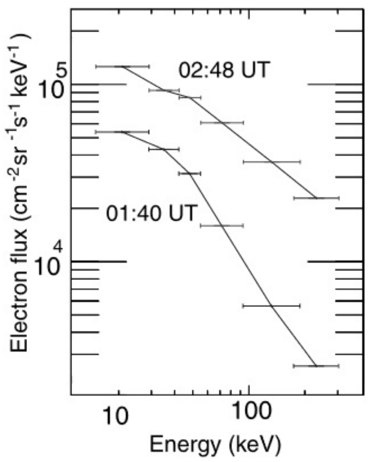

Figure 4.10: Galileo EPD electron energy spectra at the energy range of 15-304 keV, during an injection event on 263/1997. It comprises intervals of minimum (01:40 UT) and maximum (02:48 UT) energy flux measured along the PAD boundary found for the diffuse emission. Credit: Radioti et al. (2009).

region according to Allegrini et al. (2020), and the pitch angle distributions showed a partially emptied upward loss cone (a sign of a "diffuse aurora"), it stems from these case studies than when the secondary oval (or simply an enhanced equatorward emission) is present, the distributions become more energetic, increasing across all pitch angles (see Fig. 4.3-left or Fig. 4.6-right), but showing a wide variability (sometimes relatively isotropic, sometimes showing empty loss cones).

This relatively complex behaviour of the secondary oval is in agreement with its mapping to the transitional region of the pitch-angle distribution (PAD) boundary (Gray et al. 2017), beyond which electrons start to scatter and precipitate guided through field-aligned currents. This enhanced flux across a broad PAD is also consistent with the wave-particle interactions and the triggering of pitch angle scattering suggested by Tomás et al. (2004b), Radioti (2006), and others, as the main mechanisms that originate auroral emissions such as the secondary oval (Gray et al. 2017) or transient injection signatures (Mauk et al. 2002).

Finally, another study worth mentioning, because it showed an estimation of electron fluxes (and its corresponding auroral brightness) for this region, was the

Case	Date	HST visit	Hem.	Family	UT (Juno)	Juno long.	Juno lat.	R_J	Max. LC$^+$	EE Intensity	Energy flux	Dominant flux$^\oplus$
#1	033/2017	od8k46	N	inj^	11:26 - 11:56	80 - 150°	68°- 81°	2.9 - 2.2	15°	~1000 kR	1 - 1000 mW/m^2	Bidirectional
-	033/2017	od8k44	S	inj	13:34 - 13:41	~300°	65°- 72°	1.6 - 1.8	25°	~500 kR	10 - 3000 mW/m^2	Downward
#2	086/2017	od8k70	N	U	08:00 - 08:36	~170°	86°- 47°	2.0 - 1.2	23°	~1000 kR	1 - 2000 mW/m^2	Bidirectional
-	086/2017	od8k71	S	inj	09:17 - 09:50	~230°	50°- 83°	1.4 - 2.1	23°	~2000 kR	10 - 3000 mW/m^2	Bidirectional
#3	201/2019	odxc38	N	N^	15:30 - 17:00	~140°	10°- 12°	13 - 12	30°*	~1500 kR	100 - 500 mW/m^2	Bidirectional
-	202/2019	odxc39	N	N^	03:28 - 03:41	120 - 180°	79°- 66°	1.6 - 1.3	45°	~1000 kR	1 - 3000 mW/m^2	Upward

Table 4.1: Summary of characteristics of the Juno JADE-E case studies and their corresponding HST visits. ^ including secondary oval; $^\oplus$ direction of the energy flux during the corresponding equatorward emission; $^+$ maximum loss cone angle; * the angle selected was 30°, but at that radial distance it would be ~1-2°.

work on the equatorial diffuse emission (EDE) by Radioti et al. (2008b). Figure 4.10, taken from it, shows the energy flux calculated from the electron energy spectra measured along the PAD boundary. The energy precipitation flux is found to range between 1.2 and 7.2 mW/m^2, corresponding to an auroral brightness of 12-72 kR (assuming that 1 mW/m^2 of injected electrons corresponds to FUV emission of 10 kR, Grodent et al. 2001). These values agree with the measured ones at the ionospheric counterpart of the boundary (50 kR in the North, 15 kR in the South) and the general EDE region (40–100 kR in the North, 10–40 kR in the South). However, these ranges of both fluxes and brightness are considerably below the ones found in our case studies, depicting an intermediate state of the ionosphere between totally quiet and undergoing high particle precipitation.

4.4 Summary and conclusions

The case studies on the secondary oval presented in this chapter are a limited yet useful source of information that proves that the secondary oval has a plasma source with distinct spectral signature. Table 4.1 summarises the main characteristics of these case studies, including the dates of the HST visits, the times of the Juno crossings studied, the location of Juno (in left-handed S-III longitude, latitude, and radial distance), the maximum loss cone angle, the rough intensity of the equatorward auroral emissions traversed, the range in energy flux measured by JADE-E (both downward and upward), and the dominant direction of the precipitating energy flux during the equatorward emission region, if there is any. Next, the main findings from these observations are summarised:

- Despite mapping to the same PAD region, this auroral feature does show different characteristics in the particles causing it than those of the equatorial diffuse emission (Radioti et al. 2008) or the injection signatures, to which the secondary oval had been linked in the past via a temporal association between them and the brightening of the secondary oval (Gray et al. 2017). Here, these emissions are considered separately.

- Similar electron energy fluxes were observed in both upward and downward directions across all case studies, with slight directional preferences in some visits. Larger up-going electron fluxes than down-going fluxes have been found on field lines connected to auroral emissions in Jupiter's polar region (Ebert et al. 2017, Mauk et al. 2017), like in the case of fixed polar bright spots (Haewsantati et al. 2023).

- In the case of these lower-latitude emissions, the initial expectation was to find larger downward electron energy fluxes dominating, at least in the clearest examples of the secondary oval (Allegrini et al. 2020). This has not been the case, having found relatively similar fluxes for both directions across all the case studies (slightly larger in the downward direction for visit od8k44, and the upward direction for visit odxc39). In that regard, the precipitation of the equatorward emission would therefore be closer to that of the bidirectional region of the main emission, or Zone-II, defined by Mauk et al. (2020).

- A novel and puzzling "saw-like" feature has been found consistently in the electron energy flux in both directions, becoming particularly notable when Juno crossed the secondary oval at approximately perpendicular angles and when the auroral emission was brighter in those latitudes.

- The intensity of the secondary auroral oval correlates with changes in electron distribution in magnetospheric regions mapping to equatorward latitudes.

- The lack of direct correlation between downward energy flux and auroral emission has already been pointed out for other types of auroral features. Similarly to what Haggerty et al. (2019) proved for the polar injection footprints, Nichols et al. (2023) showed that the injection auroral signatures, although associated with the motion of plasma, do not reflect in an immediate way the variation in the field-aligned energy fluxes calculated.

The observations demonstrate a clear connection between the intensity of the secondary auroral oval and electron distribution changes in the corresponding magnetospheric regions, even if the relationship isn't always straightforward.

Chapter 5

UV Auroral Counterpart of Different Magnetospheric Processes

Understanding the relationship between the complex magnetospheric dynamics and the resulting auroras provides valuable insight into the fundamental processes governing Jupiter's magnetosphere. This chapter explores the auroral counterparts to different regions and phenomena within it. This investigation synthesises findings from three distinct studies.

Firstly, I study the correlation between X-ray and UV auroral emissions, as presented in Weigt et al. (2023). This connection is essential for a better understanding of the multi-wavelength nature of Jovian auroras and the different energetic processes that contribute to their formation. Secondly, I investigate the processes occurring in the Jovian magnetospheric cusp region and their implications for its auroral signatures. The cusp region, where solar wind particles have direct access to the magnetosphere, plays a crucial role in the energy transfer processes that drive auroral emissions (Bunce 2004). Third and finally, I focus on the response of Jupiter's auroras to dipolarisation front events in the magnetotail, based on the statistical study conducted by Blöcker et al. (2023). Dipolarisation fronts are rapid reconfigurations of the magnetic field structure in the magnetotail which lead to significant ion intensity variations and are pivotal in understanding the transient processes within the magnetosphere. By linking these events to auroral responses, we enhance our understanding of how large-scale magnetospheric reconfigurations influence auroral dynamics.

5.1 X-ray emissions

This section summarises a study done in collaboration with Dr Weigt, Dr Caitriona Jackman et al., that resulted in the publication of Weigt et al. (2023). This study stems from a previous one (Weigt et al. 2021) that aimed at cataloguing X-ray northern auroral emissions and studying their potential drivers, finding that they show a large variability with only a very small number of pervasive "hot spots". In the more recent study, I provided the UV context for the new catalogue of Chandra observations (also contrasted with Waves and magnetometer data from Juno) using HST images.

5.1.1 Introduction

The X-ray emission from Jupiter can be seen as even more complex than its UV counterpart, given the wide range of energies it covers. It is broadly divided into the hard X-ray emission (appearing generally along the same region as the UV main oval) and the soft X-ray (more concentrated in the polar region). The X-ray emission was initially predicted from the FUV auroral intensities and spectral characteristics, using those to calculate the X-ray bremsstrahlung fluxes expected by the spacecraft Ulysses (Waite Jr. et al. 1992). More recently, an examination of combined Chandra X-ray and HST FUV observations of the Jovian aurora by Branduardi-Raymont et al. (2008) revealed a spatial coincidence in their origin, and even suggested a shared population of energetic electrons driving both (hard) X-ray and FUV emissions. As for the soft X-ray emission originating from ion precipitation, it is predominantly found over the UV polar and swirl regions, sometimes coincident with polar flashes detected in the UV (Elsner et al. 2005, Dunn et al. 2022b).

The connection between the X-ray emission and the UV emission has been further studied more recently by Wibisono et al. (2021) (focusing on the dawn storms), Dunn et al. (2022)b (for the dark polar region), and Dunn et al. (2020b) (including radio and solar wind measurements), among others. This overlap in the spatial distribution of the higher-energy X-ray and lower-energy UV auroras suggests that, if not the same, related magnetospheric acceleration processes are responsible for the full spectrum of energies powering the particles that generate these distinct auroral phenomena. Understanding the details of these particle acceleration mechanisms is crucial for elucidating the coupling between Jupiter's magnetosphere and ionosphere/atmosphere. A comprehensive review of the X-ray emissions in the Jovian system can be found in Dunn (2022)a.

5.1.2 Chandra X-ray Observatory

The Chandra X-ray Observatory (CXO, more commonly referred to as simply Chandra) has been NASA's X-ray telescope since its launch in 1999. Chandra's much greater angular resolution than its predecessors (FWHM$\simeq$0.4") allows it to provide detailed images of X-ray sources within our Solar System and beyond (Wilkes et al. 2019). Chandra orbits the Earth with a period of $\sim$64 hours, and its high eccentricity lets the telescope spend 85% of its orbit outside of the Van Allen belts, resulting in $\sim$55 hours of uninterrupted, useful observation time per orbit.

The instrument onboard Chandra utilised in this study is the High-Resolution Camera (HRC-I), plus some complementary data from Juno's magnetometer (MAG, Connerney et al. 2017) and Waves instrument (radio and plasma waves, Kurth et al. 2017). In the case of Jupiter observations, its photons lie in the lowest energy range detectable by Chandra, which prevents any potential spectral study (or distinction between different generation mechanisms). Chandra data also requires to perform a re-tracking of the photons to the planetary disk, as explained by Weigt et al. (2020),

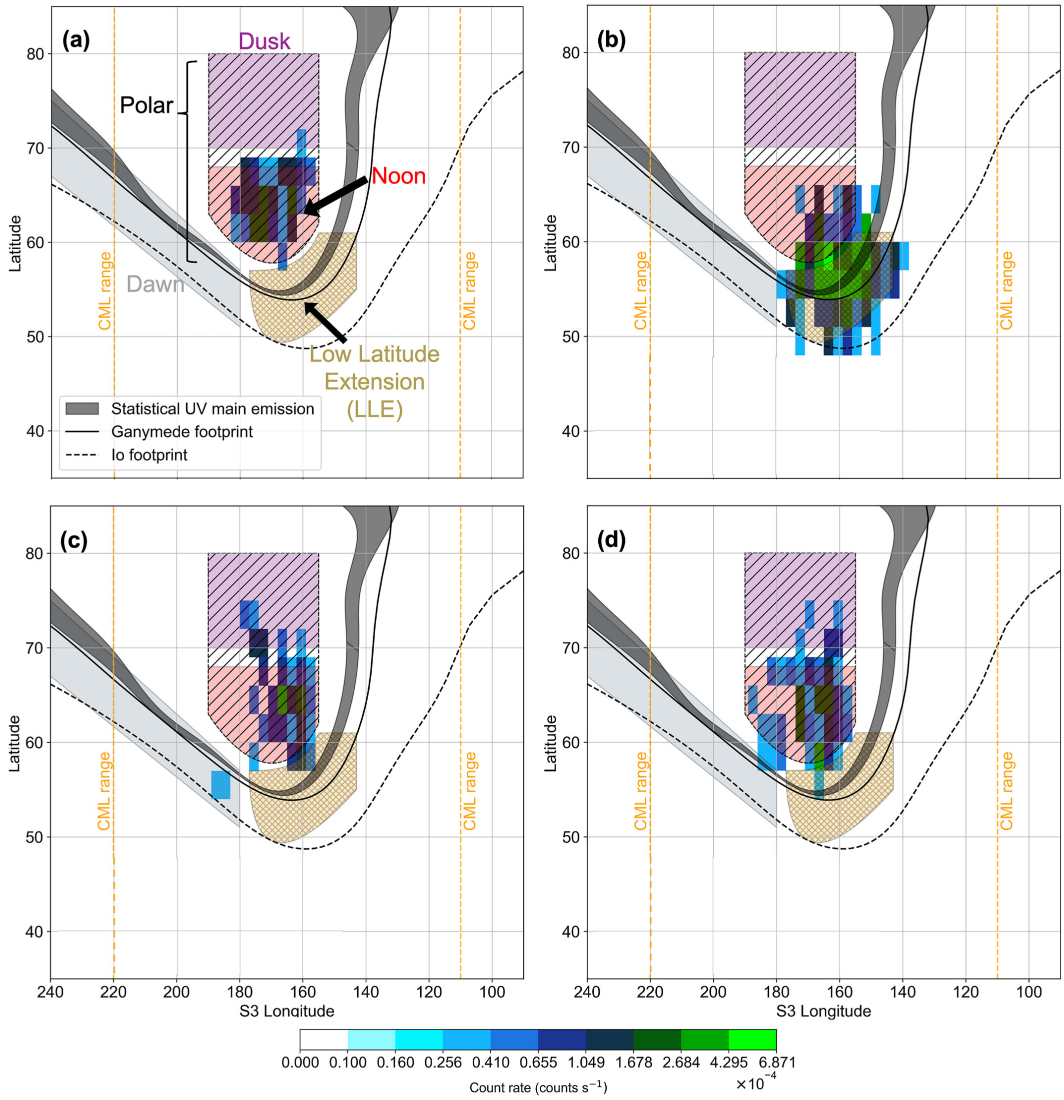

Figure 5.1: Cartesian plots of the X-ray mapping for 4 example Chandra observations from Weigt et al. (2023): **(a)** DOY 33/2017, all auroral emissions are within the polar region; **(b)** DOY 252/2019, where the auroral emissions are shifted equatorward, and two cases linked to UV *X* family during **(c)** a confirmed compression event (169/2017) and **(d)** a potential compression event (DOY 91/2018) during a Juno perigee (unknown magnetospheric state). The location of the X-ray auroral structures is: red-noon; purple-dusk; grey-dawn; gold-LLE; striped-polar. The statistical UV main emission (dark grey shading; Bonfond et al. 2017), and the footprints of Io (black-dashed line) and Ganymede (solid black line) are overplotted (Connerney et al. 2020, 2022).

and some additional corrections to account for the time-dependent degradation of the instrument (McEntee 2021). This Chandra dataset comprises 17 observations from the Juno-era, between 2016 and 2019, 14 of which had near-simultaneous HST-STIS data (± 1 day).

5.1.3 Conjugate X-ray and UV analysis

My main contribution to this study was the reduction and classification of the HST visits to obtain the behaviour of the UV auroral emissions for the coincident times with the observations of Chandra, as described in Table B.1 (in Appendix B). The initial idea consisted of using the five regions (called X-ray auroral families) predefined by Weigt et al. (2023) to analyse and compare the behaviour of the UV auroras in them. These regions, or families, were defined based on their different physics and X-ray emissions displayed, in an analogy to the UV families defined by Grodent et al. (2018). Figure 5.1 shows a selection of four examples of different X-ray auroral morphologies with emissions: (a) concentrated in the polar region, (b) having shifted equatorward, and (c)-(d) corresponding to magnetospheric compressions/UV *X* family. In these plots, the defined divisions of the X-ray emission are shown: X-ray dusk (purple), dawn (grey), Low-Latitude Extension region at the equatorward noon (LLE; gold), and the polar region comprising the first two (striped). Their UV counterpart is shown in Figure 5.2, which includes some of the simultaneous HST-STIS images (the rest are in Figures B.1 and B.2 of Appendix B). The same regions as Fig. 5.1 are overplotted in the polar projection (with left-handed S-III longitude, as usual).

5.1.4 Results and discussion

I now directly compare the X-ray and the UV emissions described by Weigt et al. (2021). The more extreme cases of X-ray emissions occur in the dusk and LLE regions. The X-ray dusk is associated with magnetotail reconnection, which is responsible for episodes of enhanced auroral power in the region (Kasahara et al.

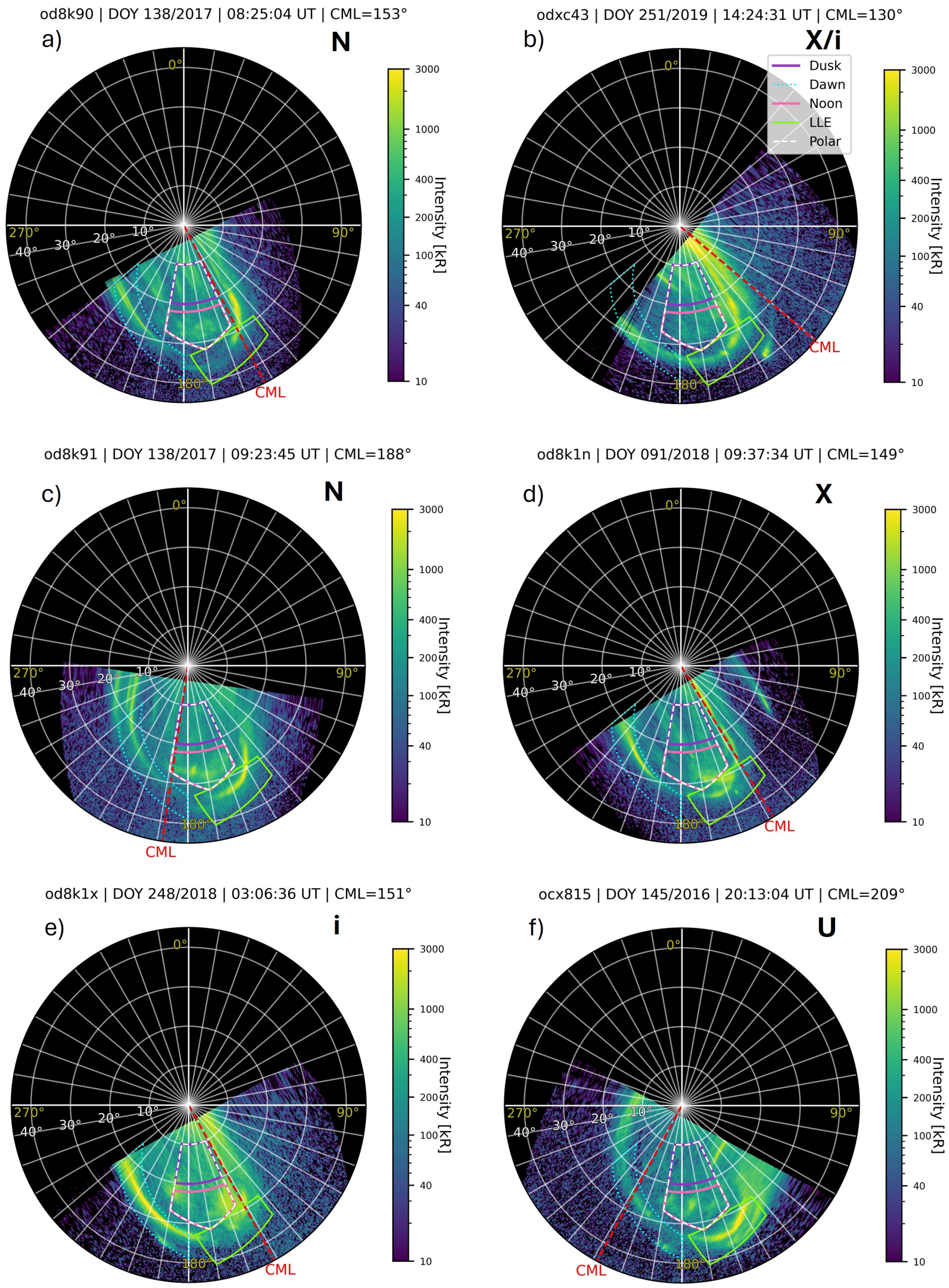

Figure 5.2: Polar images of 6 HST-STIS visits of the Northern hemisphere simultaneous to Chandra X-ray observations: **a)** od8k90 (Narrow family); **b)** odxc43 (eXternal pert./injections); **c)** od8k91 (Narrow); **d)** od8k1n (eXternal pert.); **e)** od8k1x (injections); **f)** ocx815 (Unsettled). Legend for the regions is in the top right.

2013). Meanwhile, the LLE region is linked to hot plasma injections from the middle magnetosphere, which often present auroral signatures in the UV (Gray et al. 2017, Dumont et al. 2018). The distributions of the auroral X-ray photons detected within each defined region and split by each Chandra observation are shown as a stacked bar chart in Figure 5.3 (from Weigt et al. 2023). On one hand, “P” corresponds to four Chandra observations (18301 - shown in Fig. 5.2a, 20002, 18679 and 18680) that had almost all their X-ray emission originated in the noon region. Two of the three HST visits simultaneous to these cases presented morphologies compatible with injections (i).

On the other hand, the “L” letter identifies the observations with a high population of photons (10%) coming from the LLE region. Opposite to the “P”-labelled cases, many of the UV visits corresponding to these low-latitude X-ray emissions are either quiet (Q) or unsettled (U) morphologies (see B.1). This association with different morphological families for the polar (“P”) and low-latitude (“L”) cases may suggest that the LLE region is linked to activity in Jupiter’s middle magnetosphere, independent of solar wind conditions (and potentially involving the flux tubes connected to Ganymede and Io, due to their proximity to this region, Nulsen et al. 2020).

Along the same lines, an association is proposed between some of the X-ray cases and compressions or perturbations of the magnetosphere that may trigger injection events. For instance, cases b) 22151and d) 18678 of both Figs. 5.2 and 5.1 show observations with different characteristics. As mentioned above, case b) shows an example of the X-ray emissions concentrated in lower latitudes (“L”). In the meantime, the UV emission corresponds to the external perturbations (X) morphological family and its noon region is devoid of emission. However, in case d) (intermediate between“L” and “P”) - most X-ray emissions are found in the noon polar region (pink), and its corresponding UV image displays another case of the X family (or maybe i), this time with brighter emission at the noon region. This significant difference between the origin of the X-ray emissions (while the UV

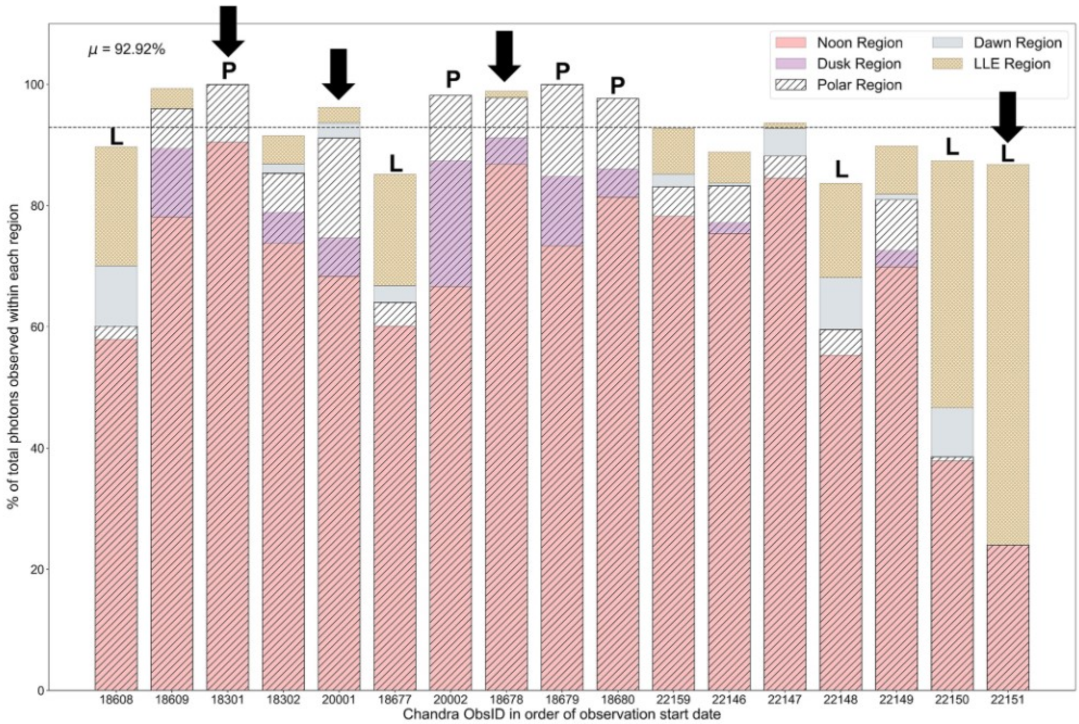

Figure 5.3: Stacked bar chart showing the distribution of all X-ray auroral emissions in each structure across the Juno-era Chandra observations. “P” and “L” indicate “fully polar” or “low latitude” emissions respectively, while the arrows indicate the four cases displayed in Fig. 5.1 (whose same colours are used to label the different families: red-noon; purple-dusk; grey-dawn; gold-LLE; striped-polar). Credit: Weigt et al. (2023).

remains relatively similar, corresponding to the same family and showing similar values for the intensity of the main emission), suggests a certain degree of decoupling between the two. Still, the X-ray distributions may serve as a precursor or follower of magnetospheric phenomena like these injections, as well as a proxy for the local solar wind conditions, as the three observations of fully polar X-ray emissions (ObsID 18301, 20001, 18680) coincided with a predicted solar wind compression and/or produced UV auroral emissions associated with the UV X or i families.

Nevertheless, it must be noted that no clear link was found between the different populations and the solar wind dynamic pressure, predicted from the combination of Juno's MAG and Waves data with the Tao et al. (2005) 1-D MHD propagation model. This could indicate that the solar wind affects multiple regions at the same time, or that the emission in the LLE region is not directly correlated with the compressions (although it may lag behind if they are triggered or followed by plasma injections, as proposed). However, the solar wind observations and propagation model have not been studied in this thesis. The last, more general conclusion to be extracted from Fig. 5.3, is the wide variety in the origins of X-ray emissions detected by Chandra, and the need for more contextual information (ideally in situ) to further comprehend the triggering of the common or different drivers triggering the auroral emissions.

5.2 Cusp region

5.2.1 Introduction

The cusp regions of a magnetosphere are the areas near the poles of a planet where the magnetic field lines are open to the solar wind. This would allow the magnetosheath plasma to penetrate very deep into the magnetosphere, even reaching the ionosphere. These regions are of particular interest due to the myriad of processes occurring within them (detailed for example in Bunce 2004), and their spatial concurrence with some of the X-ray studies discussed above (e.g., ROSAT detections by Waite Jr. et al. 1994). In Earth's magnetosphere, the cusp region is located near the polar regions, where the magnetic field lines are open and can reconnect directly with the IMF field carried by the solar wind. The polar caps are thus relatively dark, due to the low energy flux provided by the extremely low-density plasma populating these open field lines. In Saturn, short-lived poleward cusp spots appear associated with southward-oriented solar wind and lobe reconnection (Bunce et al. 2005, Gérard et al. 2005), although magnetopause reconnection can take place at a wide range of locations, each mapping to different auroral regions (Badman et al. 2013), and under very different solar wind conditions (Jasinski et al. 2016).

Moving on to Jupiter, two studies conducted by Pallier et al. (2001) (for the North) and Pallier et al. (2004) (for the South), found a patchy UV emission located slightly poleward of the noon sector of the main oval (in both hemispheres), which was identified as the potential signature of the dayside cusp. However, the lack of follow-up observations, consistent detections of corresponding auroral emissions, and specific investigations about the dayside magnetopause made this issue remain unclear (Cowley 1993). Bunce (2004) also pointed at the likely connection of the UV emission and the main X-ray hotspot, and developed two conceptual flow models ("fast" and "slow") to predict the resulting auroral emissions. More recently, Hue et al. (2021) identified some circular, expanding polar emissions with an origin consistent with dayside reconnection.

However, and as it also happens in Saturn (Bunce et al. 2005), neither the observed emissions in that "cusp" region nor the so-called "polar flare" aurora (Gérard et al. 2003, Grodent et al. 2003) can be directly caused by the precipitation of "cusp" plasma, due to the significant difference in energy levels and auroral intensities involved. The UV spectra show electron and proton energies around 100 keV (Pallier et al. 2004), far exceeding those of magnetosheath particles. Similarly, X-ray auroras require the presence of heavily charged ions like O^{5+}/O^{7+} for charge-exchange reactions, but their densities and fluxes in both the solar wind and the outer magnetosphere are insufficient (Cravens et al. 2003). Thus, if the auroral phenomena are indeed linked to the cusp, additional processes accelerating the magnetospheric plasma must occur (probably linked to the pulsed reconnection at the dayside magnetopause driving the flows and currents, Bunce 2004).

5.2.2 Recent evidence of the magnetospheric cusp

The lack of data about the specific characteristics of the cusp regions has limited so far the possibility of exploring accurately their auroral counterparts. However, a recent study by Xu et al. (2024) has pinpointed the cusp region in the dusk flank of the magnetosphere by using magnetometer, plasma, and waves measurements from the Juno spacecraft. By using a combination of already known criteria for identifying the cusp (i.e., presence of magnetosheath-like electron distributions inside the magnetopause at high latitudes, ion dispersion, and whistler-mode auroral hiss waves), as well as its location, they detected two cusp-like structures at the pre- and post- dusk sectors, respectively. In both cases, Juno was orbiting on the dusk flank above the Southern pole. This differs from most previous identifications of the cusp region, usually connected to the dayside magnetopause.

Figure 5.4 displays the areas corresponding to the magnetospheric regions with different magnetic field configurations (i.e., open to IMF, open to the far magnetotail, closed). The information about the magnetospheric topology and information about the expected solar wind is then included using the MHD simulation results from Zhang et al. (2021). The trajectory of the spacecraft footprint would cross the open magnetic field region near the dusk side when the cusp is detected in the particles and waves data. By utilising the same models (JRM33 + Connerney2020) for the mapping used extensively across this thesis (and explained in section 2.4), Xu et al. (2024) defined the region on the ionosphere corresponding to these detected magnetospheric cusps.

Considering those footprints of the cusp region (as shown in Fig. 5.4, right) as the areas on which the auroral emissions are to be studied, I analysed the full archive of HST visits looking for observations simultaneous to (or shortly after)

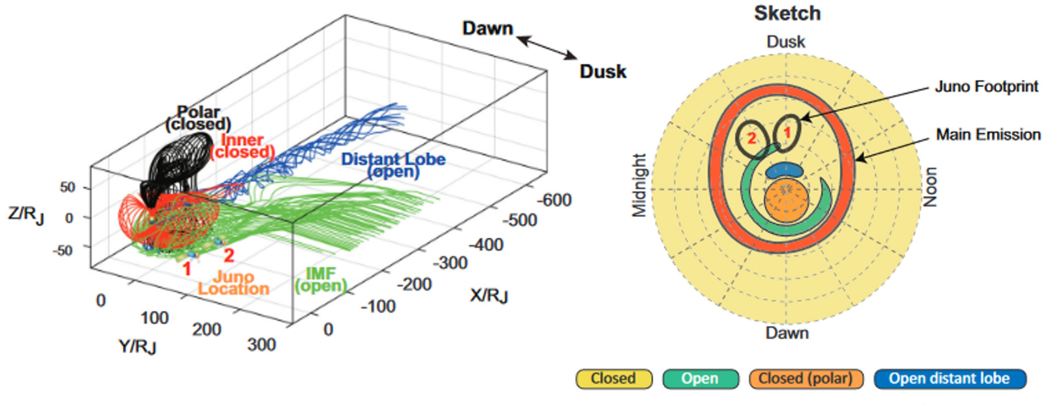

Figure 5.4: Left: Jupiter's global magnetospheric topology and open-field configuration based on Zhang et al. (2021). Green lines are created by magnetopause reconnection and modulated by the solar wind, while blue lines originate from a specific part in the dusk region and map to the further magnetotail. Labels 1 and 2 indicate Juno positions during different cases in the study. **Right:** Diagram of the footprint distribution corresponding to the open and closed magnetic field regions in magnetic coordinates in the southern hemisphere. Credit: Xu et al. (2024).

the 6 cusp cases presented in the Supplementary Information of Xu et al. (2024). Unfortunately, none of the cases (dated 2022 and 2023) have HST data available for those dates. Despite this lack of simultaneity between the two datasets, which prevented obtaining direct auroral counterparts to these cusp detections, I first study the location, and then the brightness detected within the region delimited by them.

5.2.3 Discussion

Location

The top of Figure 5.5 shows the mapping of Juno while crossing the cusp regions overlaid on top of the HST visits (a-North, b-South) closest in time to the studied cases (oeow20 and oeow04, respectively). The background auroral images serve as simple examples to showcase some typical emissions in the ionospheric regions mapping to the cusp in both hemispheres. The 6 cases all have different colours (the two from 279/2022 are considered together as Case #2). The first thing to notice is that all the cases detected map to very similar, almost overlapping, areas. Furthermore, when comparing the mapping of the cusp regions by Xu et al. (ibid.) (top) with the spot features shown by Pallier et al. (2004) (bottom), I found that the latter appear at slightly lower latitudes than the former ($\leq$1-2° for the Northern hemisphere, and $\sim$1-6° for the Southern one).

Another relevant result from this comparison of the mapping and the auroral emission is the coincidence of the footprint of the cusp region with the boundary between the dark and the swirl polar regions. If we compare the footprint with Figure 1.16, we can see that for both hemispheres, but particularly for the Southern one, both the footprint and the cusp detections shown in Fig. 5.5 overlap with this boundary , as it can be seen when comparing the top and bottom images (Southern hemisphere is flipped horizontally due to different systems of reference being selected). Interestingly, there is less (yet some) overlap with the boundary between the active and swirl subregions, although this usually hosts the polar "flares" first described by Waite et al. (2001), and seen relatively often in the active region. The flares have been initially speculated to be directly influenced by the solar wind (Grodent 2015, but their time scales and location connect them to bursty reconnection (flux transfer events, Walker et al. 1985) in the dayside magnetopause (Bonfond et al. 2016). This would prove them as cusp-related auroral features. However, the auroral features that may be a more direct consequence of the cusp region, without mapping specifically to the dayside magnetopause, are the bright spots found all along the edge of the swirl region (Haewsantati et al. 2021). Their scattered distribution, particularly in the Southern hemisphere, across a wide range of local times prevented them from being linked to noon-facing (Earth-like) cusp. But if a more complex, helical magnetic field topology, such as the one described by Zhang et al. (2021) (shown in Fig. 5.4a) is considered, these bright spots could in fact be the auroral signatures of the cusp region found by Xu et al. (2024). Their association with field-aligned currents and relatively fixed position in S-III longitude (Haewsantati et al. 2023) suggests a relatively stable source in the outer magnetosphere, compatible

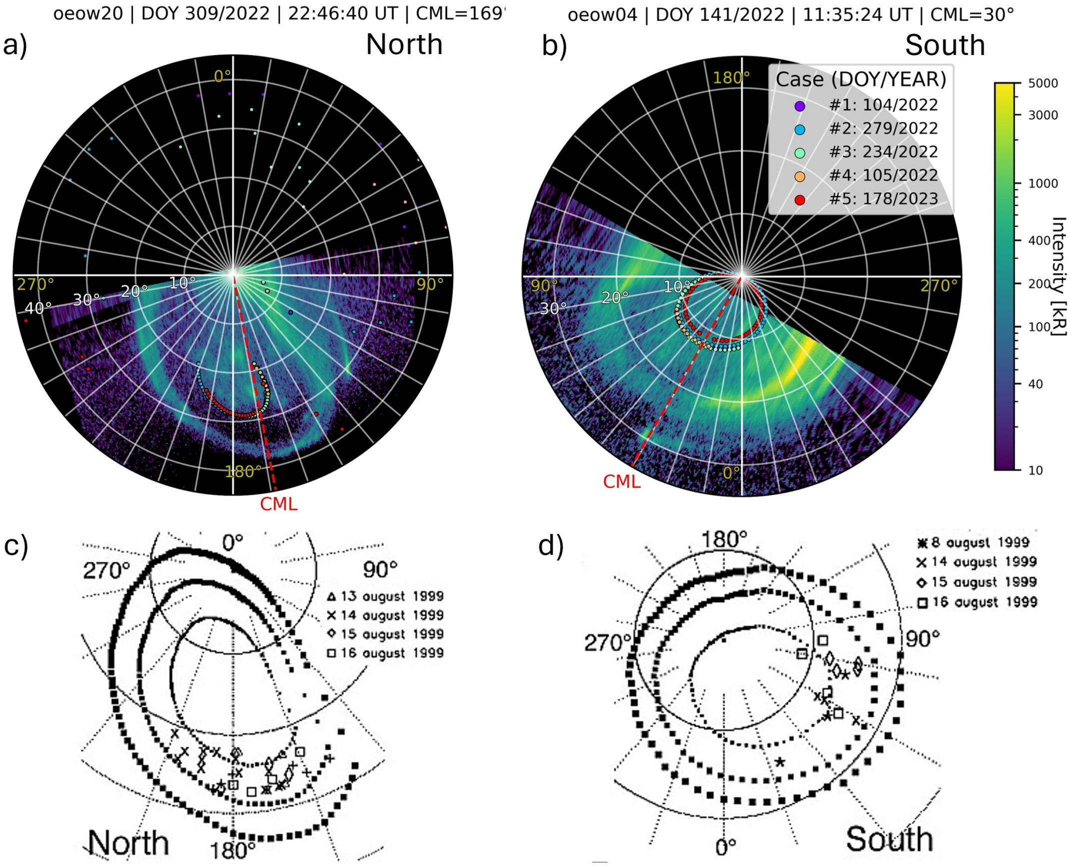

Figure 5.5: HST-STIS visits **a)** oeow20, 309/2022, N; **b)** oeow04, 141/2022, S; with the mapping of the 6 cusp detections by Xu et al. (2024) overlaid in different colours. **c)** and **d)** Polar maps of the N & S spots from the August 8–16, 1999 images. Dotted curves represent different reference ovals. The HST-STIS images are presented in LH S-III longitude, but looking up from below the planet in the Southern hemisphere (unlike those presented here). After Pallier et al. (2004).

with the polar cusp.

To conclude, regarding the location: it must be noted that Juno was in Southern latitudes when crossing the cusp region, so the mapping is more reliable for this hemisphere. A much larger difference is found in the local time of the cusp regions in these two cases: noon (11-13 LT) for Pallier et al. (2004), and dusk in the case of Xu et al. (2024). However, the slight discrepancy in latitude and the larger one in local time should be expected, given that Pallier et al. (2004) could not provide the location in the magnetosphere of their auroral spots, and simply mentioned as potential origins magnetic reconnection either in the tail or dayside magnetopause, or flux transfer events.

Brightness

Having addressed the location of the cusp footprints, the brightness of these regions is measured across different HST visits next, and compared to this and other previous identifications of cusp-like features. The cusp spots found by Pallier et al. (2001) and Pallier et al. (2004) are bright and variable, reaching up to 1 MR in both hemispheres. An extreme case of polar "flare" studied by Waite et al. (2001) (potentially related to access of "cusp plasma") reached 40 MR during only 70s. Bunce (2004) results range, depending on the flow model selected, from ∼22-84 kR for the closed side of the boundary, and ∼1.2-3 kR for the open/magnetosheath part. It must be remembered, though, that for these older cases, the unit conversion from counts to intensity was performed using different values than for the more recent observations such as the ones presented here. Finally, the circular spots observed by Hue et al. (2021) showed brightness values of up to ∼140 kR.

The range of values for the brightness across this varied set of features, in consequence, spans from very few kR to MR. The values obtained for the region from this analysis show a clear asymmetry between the hemispheres, caused by the much higher frequency of polar flashes in the North than in the Southern hemisphere, in the specific area mapping to the cusp. On average, the values for both hemispheres are around 100 kR for the "quiet" (featureless) auroral state. However, more than 95% of the North HST visits analysed displayed at least one flash with brightness >1 MR in the region during the duration of the visit ($\sim$40'). Sometimes, these flashes continued for most, or even the entirety, of the visit, or more than one appeared within a single visit. For comparison, in the South, this kind of event only appears in <15% of the visits, and in $\sim$50% of the total visits the studied region does not surpass a few hundred kR (with considerably dimmer, or directly no brightening, in the area delimited by Fig. 5.5b). This relatively low emission from the Southern polar region was already seen in the reference average emission in Fig. 3.1.

This hemispheric asymmetry is partly explained by the bias in the observation geometry of HST. The angle of observation of the planet leaves the region of interest near the edge of the nightside in the South, while it sits in the middle of the elongated auroral oval in the North. However, the difference in brightness (and frequency of the polar flashes) is too remarkable to be due only to this effect. This absence of polar emissions in the South was already reported by Gérard et al. (2013), albeit based on a much smaller sample. Haewsantati et al. (2023) also showed a higher brightness for the auroral bright spots found in the North (PJ-3) than in the South (PJ-15 and PJ-33). The underlying cause of the asymmetry in the emission between the two hemispheres has yet to be determined, although it may be partly explained if there were near-planet polar reconnection as proposed by Masters et al. (2021), associated with the more complex Northern pole.

5.3 Auroral emissions associated with dipolarisation fronts

5.3.1 Introduction

Dipolarisation fronts (DFs) are sharp magnetic boundaries characterised by a strong and steep increase of the "vertical" magnetic field component B_z, associated with

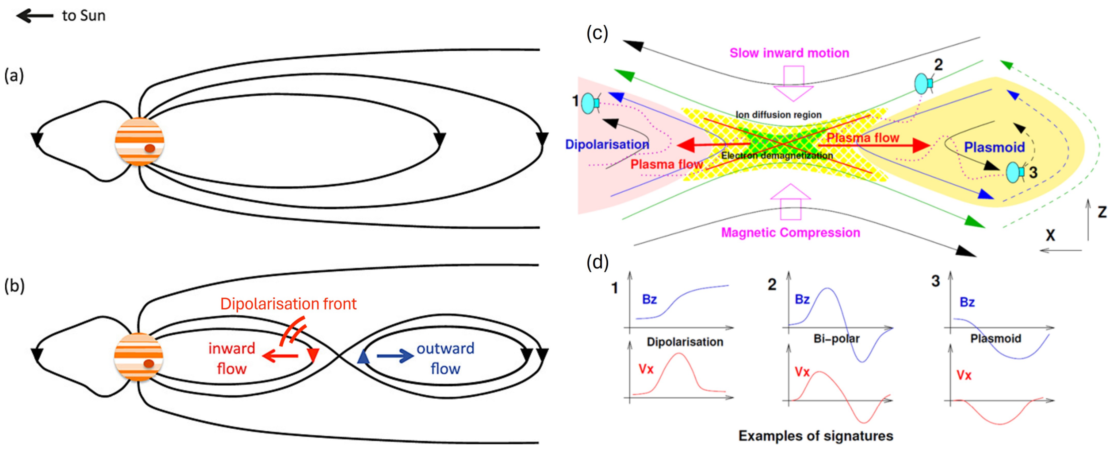

Figure 5.6: Reconnection in the Jovian magnetotail, in a meridional view. **(a)** Initial field configuration (mostly radial direction, except near the current sheet). **(b)** Field configuration during reconnection (including dipolarisation front). After Vogt et al. (2014). **(c)** More detailed standard model of the 2D reconnection (adapted to the tail configuration). **(d)** Magnetotail signatures of reconnection in different locations of the spacecraft with respect to the reconnection site. Credit: Louarn et al. (2015).

enhanced current density (Sitnov 2009) and quick changes in the magnetotail plasma characteristics (e.g. drops in pressure, density, and speed). These turnings in the magnetic field are thought to be associated with reconnection processes produced in the magnetotail, both on Earth (Huang 2002) and Jupiter (Kronberg et al. 2005). A schematic of the dipolarisation process can be seen in Figure 5.6, with the DF moving planetwards. DFs were first discovered on Earth by ESA's Cluster mission (Nakamura et al. 2001) and later described in better detail using NASA's THEMIS spacecraft (Runov et al. 2009, Fu et al. 2020).

Signatures of DFs have also been identified in the magnetospheres of Mercury (Sundberg et al. 2012), Saturn (Jackman et al. 2015, Xu et al. 2021), and Jupiter, (Kasahara et al. 2011, Kronberg et al. 2012). In them, the DFs have been found to play a relevant role in driving the previously discussed hot plasma injections, as well as accelerating ions (Artemyev et al. 2013). In the framework proposed by Yao et al. (2020), magnetic dipolarisation is triggered by reconnection in the dawn flank of the magnetosphere. Alternatively (or complementarily), perturbations of the current sheet, e.g. via interchange or ballooning instabilities (Panov et al. 2012, Mitchell et al. 2015, Achilleos et al. 2015), could also give rise to these front-like magnetic field structures. Whichever its origin, after its formation, the DF corotates and powers plasma injections planetward, eventually producing auroral signatures in a broad range of local times and during several hours (Figure 5.6d, Louarn et al. 2015).

5.3.2 Observations

In this section, I use the list of DF events identified by Blöcker et al. (2023) using ion data obtained with Juno to perform a comprehensive survey of the status of the auroral emissions in the time intervals subsequent to the detections. The location of this set of 87 DF events is presented in Figure 5.7. Jackman et al. (2013) did a similar study on the auroral counterpart of the DF events detected at Saturn's magnetotail with Cassini data, and they found some discrete auroral spots appearing often at the post-midnight sector. However, and like this study in Jupiter, their conclusions are limited by the lack of simultaneous coverage of the aurorae and the DF detections in the tail.

After studying the times of the 87 DF events identified in Fig. 5.7, a total number of 17 HST visits were found to occur shortly after at least one DF event between 2017 and 2019. The time range considered for creating this list spans from 0.1 hours to 10 hours (approx. one Jovian rotation) after the DF event. This interval is justified given the distance at which the DF events are detected by Juno and the ion flow speed ($\sim$400 km/s) estimated by Kasahara et al. (2011). No images prior to the events were considered, because any observable effects on the auroral emissions would not yet be detectable then, due to the time needed for the disturbances to propagate and interact with the ionosphere.

Those 17 visits were analysed in the search of particular auroral features that may serve as signatures of the DF events (or the plasma injections provoked by

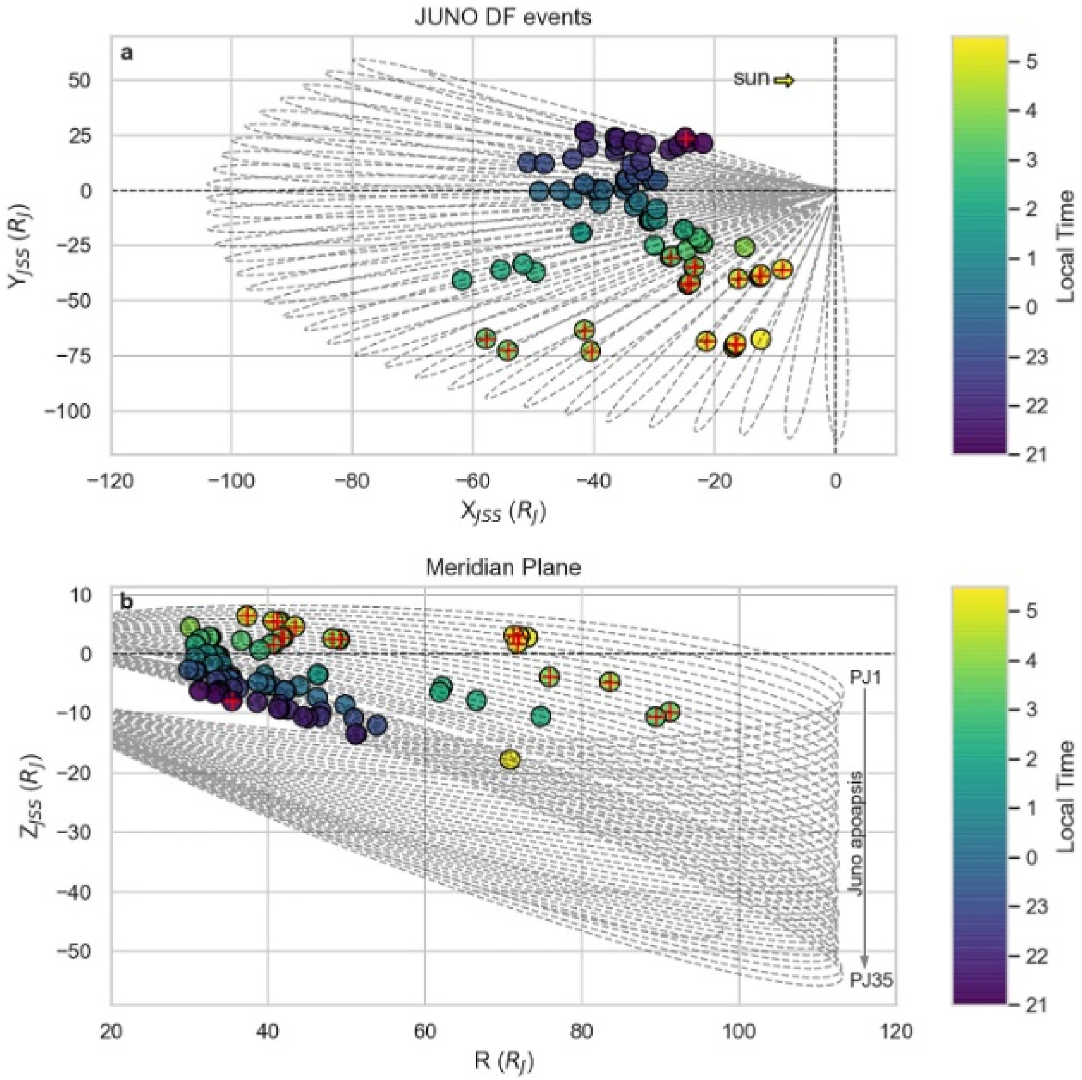

Figure 5.7: a) Juno's 35 orbits (grey dashed lines) and locations of Juno during the 87 identified dipolarisation front (DF) events in the MAG data (coloured circles) in the Jupiter De-Spun Sun (JSS) coordinates. The sun is to the right. The colorbar of the circles gives information on the local time of each event. **b)** As in panel a) but in the meridian plane view. The crosses inside the circles indicate an additional decrease in the energy spectral index. Credit: Blöcker et al. (2023).

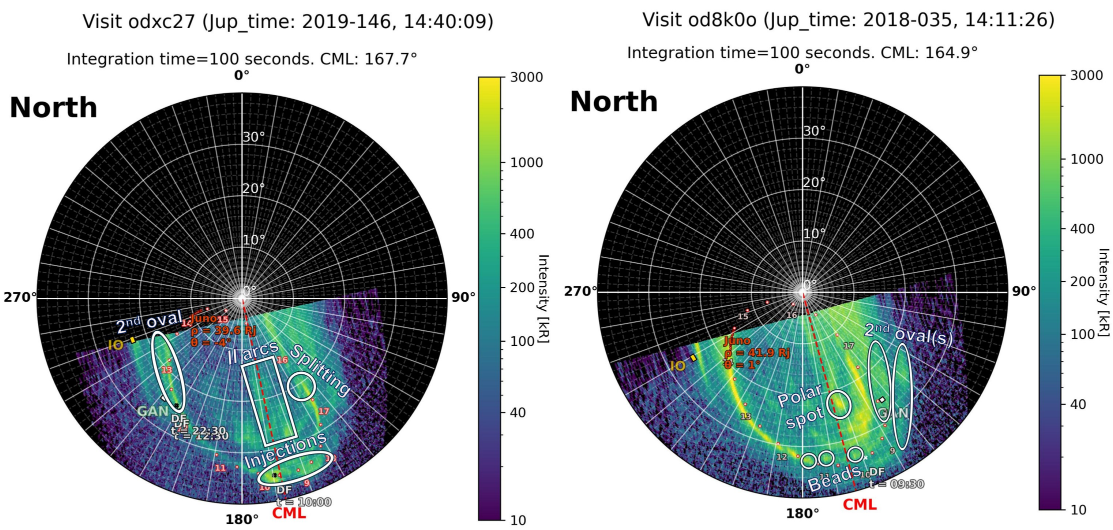

Figure 5.8: Two examples of HST images (visits odxc27 and od8k0o, highlighted in Table 5.1), showcasing the auroral features detected in this study, as well as the footprints mapping to the Juno location around (in red) and during the respective DF event detections (in white). **Left:** splitting (of the main oval arc), parallel polar arcs, injection signatures, secondary oval (at dawn). **Right:** polar bright spot, azimuthally separated beads, secondary ovals (at dusk; two in this case).

them). These features include isolated, bright spots poleward of the main emission (Pallier et al. 2001, Haewsantati et al. 2021), splitting of the main emission arc (Guo et al. 2021, Palmaerts et al. 2024), azimuthally separated beads as signs of ballooning/interchange instability (Panov et al. 2019, Hwang et al. 2011), injection signatures at the noon sector (Mauk et al. 2002, Dumont et al. 2014), parallel arcs appearing in the polar region (Pallier et al. 2001, Grodent et al. 2003), and secondary oval arcs, either at the post-dawn or pre-dusk sectors (Gray et al. 2017).

5.3.3 Results

The results of this study are summarised in Table 5.1, which presents all the individual visits analysed and their detected auroral features (indicated with an "X" symbol). The main takeaway results appear in the second to last row, where the frequencies for each of the auroral features are shown. The last row shows those same values for the full set of HST visits spanning between 2017 and 2022. This set comprises a total number of 72 visits, which gives a more general picture of the average frequencies of these auroral features and allows the comparison with the "post-DF" observations.

The differences between the "post-DF" and the overall observations are evident, with the former showing a higher frequency of detected features across all categories than the latter. Specifically, the injection signatures at noon and the presence of the secondary oval are the auroral emissions with larger increases (around a factor of x2). The presence of beads has a smaller total frequency, but a similar proportional increase than those, proving that this feature is surely associated with DF events in Jupiter similar to how it has been shown for the Earth (at nightside) by Hwang et al. (2011).

These discrepancies suggest that the auroral activity shortly after the DF events detected by Juno is more intense in general. Moreover, the increases in frequency for some of the auroral features (those associated with injections in particular) reinforce the idea that they are generated, or triggered, by dipolarisation or reconnection

DF date (DOY/year)	HST visit	Δt (hours)	Spot	//	PP	Inj.	2^{nd} oval	Beads	Family
30-31/2017	od8k38	+6/+8				X	X	X	I
136/2017	od8k88	+5		X	X	X	X	X	i/I
136/2017	od8k0t	+11	X		X		X		U
35/2018	od8k0o	+5	X				X	X	i/X
142/2018	od8k1o	+5	X			?	?		U
200/2019	odxc37	+6.5	X	X		X			N/i
253/2019	odxc46	+4				?	X	?	X
253/2019	odxc47	+7	X			X			i/I
24/2017	od8k30	+1/+8.5	X		X	X	X	X	I
24/2017	od8k31	+2.5/+10				X	X	X	I
27/2017	od8k34	+5/+8/+10	X	X	X	X	X	X	N/i
79/2017	od8k58	+4.5	X		X		X		N/i
194/2018	od8k1u	+1.5/+5	X	X					U/N
195/2018	od8k1m	simultaneous	X	X	X		X		U
146/2019	odxc27	+3/+5.5		X	X	X	X		i
146/2019	odxc24	+9			X	X			N
147/2019	odxc26	+9		X				X	N
# of cases		Mean: +5.4h	9	7	7	11	10	4	-
% in DF visits			**64%**	**50%**	**50%**	**79%**	**71%**	**29%**	-
% overall			**50%**	**34%**	**41%**	**37%**	**32%**	**14%**	-

Table 5.1: Auroral features identified for each of the HST visits analysed corresponding to the DF events found by Blöcker et al. (2023). Highlighted: the two visits shown in Fig. 5.8. Δt: hours passed between the DF event (or events) and the HST visit; Spot: polar bright spot; //: splitting of main oval; PP: parallel polar arcs; Inj: injection signatures; 2^{nd} oval: secondary oval; Beads: azimuthally separated beads. Family: morphological family of the visit.

(Kronberg et al. 2005, Yao et al. 2020), with the DF events acting as key players in the acceleration of particles planetward (Jackman et al. 2013, Xu et al. 2022). Additionally, it was noted that no sign of dawn storms was detected in any of the visits. This result (although stemming from a limited sample) is rather intriguing because it would imply that the origin of dawn storms (possibly analogous to Earth substorms, Bonfond et al. 2021) may not be directly associated with dipolarisation (Kronberg et al. 2008). The idea of the dawn storms being powered mainly by reconnection was already proposed by Yao et al. (2020), but then the question of the actual link between the reconnection processes and the DF events remains (Nakamura et al. 2002).

Besides the different auroral features studied hereby, Figure 5.8 also shows the ionospheric mapping to the corresponding DF events (from Blöcker et al. 2023) of those HST visits, with the UT time of their detection by Juno. Related to this, it is important to acknowledge, as mentioned above, that the mapping of auroral features signalling DF events is subject to large uncertainties, both in terms of their precise location (especially in terms of local time, Jackman et al. 2013) and the specific temporal intervals during which these features are expected to be detectable on the ionosphere. This uncertainty may modulate the observed differences between the sub-sample and the overall results, but it does not compromise the main conclusions.

Chapter 6

Summary and Future Work

In the previous Chapters I have identified the secondary oval appearing equatorward of the main emission in the Jovian aurorae in a statistical way, studied particle data from its corresponding magnetospheric region (using Juno's JADE instrument), and provided UV auroral context for different physical processes (X-ray emission, dipolarization front events) and regions (magnetospheric cusp region). In this last chapter, the main findings of this thesis are reported and summarised, and then I propose several ideas for expanding the work presented hereby. Some of them are more specific and detailed, and others more ambitious in nature and consequently less elaborate, but all of them are feasible (albeit in different timescales) and can be carried out in a straightforward way based on the foundations established within this work.

6.1 Summary

An in-depth state-of-the-art review of the morphology and dynamics of the Jovian magnetosphere has been presented in Chapter 1, after the description of some fundamental plasma physics concepts. Then, the main mechanisms producing the auroral emissions are addressed, along with a depiction of the main aurorae detected across the bodies of the Solar System. Finally, the characteristics of the different regions and features of the Jovian UV aurora are reported. Chapter 2 thoroughly described the methods and datasets utilised in this thesis (HST-STIS, Juno JADE-E and JEDI), including the functioning of the developed auroral emissions detection algorithm.

The first data chapter, Chapter 3, compiles the largest sample of FUV images of Jupiter's Southern hemisphere to date, applying an algorithm to automatically detect the main auroral oval, the equatorward emissions, and the Io footprint. Statistical analysis reveals that the main oval is consistently detected across all local times and S-III longitudes (except for the pre-noon discontinuity). However, the equatorward emissions show a distinct preference for S-III longitudes between 240° and 360° and occur approximately four times more frequently in the pre-dusk sector than in the post-dawn region. This local time asymmetry is also reflected in their intensity, with both emissions being significantly brighter in the pre-dusk sector. Specifically, the main oval reaches up to 3 MR before dusk, which is two to three times higher than post-dawn values. The secondary oval reaches its peak intensity around dusk, with amplitudes averaging 700 kR.

The width of the main auroral oval is generally consistent across different sectors, challenging previous findings that suggested the oval narrows at dawn. The study identifies an upper limit for the width of the main emission of 2.35°. As for the equatorward emissions, they appear towards lower latitudes around the noon sector (which was expected due to the detection of injection signatures there). Comparing both auroral emissions and separating them by morphological families also reveals some differences, particularly in the behaviour of the equatorward features (e.g. more frequent and brighter for the *I* family, especially at dusk and noon; less frequent for *Q*). Finally, although an accurate estimation of the temporal evolution of the secondary oval is hindered by the duration of the HST visits and the lack of distinction with the injection signatures, a lifetime estimate of one to several Jovian rotations is proposed.

In Chapter 4, I study the in-situ component of Juno as a complementary tool to the observations analysed in the previous chapter and the literature, to obtain a more complete picture of the equatorward emissions and, in particular, the precipitating particles that cause them. To do so, data from the JADE electron detector is retrieved for three case studies during which the spacecraft crossed the equatorward emissions region.

The electron energy flux associated with the secondary oval is found to reach values of up to 500 mW/m^2 but does not seem particularly associated with downward electrons. Instead, it shows a characteristic "saw-like" pattern in the flux, happening for both downward and upward electrons, with periodic peaks occurring as Juno crosses the region. This spectral feature is clearer when Juno moves perpendicularly to the equatorward emission than when it moves along with the region. I also look at the differences between the secondary oval and other auroral features whose precipitating particles have been studied in the past, such as the main emission, the injection signatures or the equatorial diffuse emission (Radioti et al. 2008). Their different energy and pitch angle distributions are compared, and I find no evidence of inverted-V potentials for the secondary oval, and often (but not always) isotropic enhancements of the energy of the particles. This relatively complex behaviour of the flux causing this emission both reinforces its connection to the PAD boundary (Gray et al. 2017) and the pitch-angle scattering as the dominant mechanism originating it.

Chapter 5 is a compilation of three different studies, whose common denominator is the analysis of UV auroral emissions as context for different phenomena occurring in the Jovian environment. The first of the three studies is a conjugate analysis of X-ray and UV emissions using Chandra and HST data, focusing on our contribution to the work published by Weigt et al. (2023). The comparison of these two types of emission reveals that the rarer X-ray events in the low latitudes (LLE region) seem linked to UV morphological families (and thus, magnetospheric processes) different than the more usual polar emissions. HST observations show that cases with the former often correspond to Q or U morphologies. Alternatively, the polar emissions suggest a closer dependence on the compressed or perturbed states of the magnetosphere (given their X or injection-like features). The wide variety among the X-ray distributions and their UV auroral counterparts implies a) the existence of different drivers responsible for the former; and b) that the solar wind influence on the X-ray emission is complex and indirect, although a combination of X-ray and UV morphologies could be used as a proxy for the magnetospheric conditions.

The second study focuses on the cusp region in the Jovian aurora. This region, expected near the poles of Jupiter corresponds to the open magnetic field lines that allow the entrance of solar wind plasma deep into the magnetosphere to reach the ionosphere. Previous studies initially linked patchy UV emissions poleward of the noon sector to the dayside cusp (Pallier et al. 2001, 2004, Bunce 2004), but new evidence from Juno data (Xu et al. 2024) has identified two cusp-like structures in the dusk flank of the Southern magnetosphere. Although no simultaneous HST data were available to confirm these findings, I still carry out a comparison of the auroral counterparts in these regions and compare their characteristics to the previous cusp-related auroral features.

I explore both the location (sitting along the boundary between the swirl and dark polar regions) and the brightness of the ionospheric region delimited by the mapping in Xu et al. (2024). Based on those results, it is proposed that the most likely feature associated with the cusp regions may be the bright auroral spots found by Haewsantati et al. (2021). Although their correspondence with noon (Earth-like) cusp processes was discarded (Haewsantati et al. 2023), they could still map to the cusp following a more complex and twisted magnetic field topology, as proposed by Zhang et al. (2021). Finally, our intensity analysis exhibits a clear asymmetry in the studied region between the Northern and Southern hemispheres. While polar flashes are much more frequent in the North (and thus the overall intensity is higher), such features are much rarer and dimmer in the South. This discrepancy reflects inherent differences in the behaviour of open-field regions between the two hemispheres.

The third and final part of this chapter is dedicated to the search and classification of UV auroral features after a list of DF events detected by Blöcker et al. (2023). With a rather limited sample, I have shown at least empirical evidence of the connection between the DF events and several of the auroral features associated with plasma injections, i.e., the spots around noon and the secondary oval. The noticeable and generalised increase in the frequency of most auroral features suggests dipolarisation front events may act as triggers in the acceleration of particles that end up precipitating on the ionosphere (Jackman et al. 2013, Xu et al. 2022).

Using HST-STIS images and a qualitative approach in all three cases, the auroral counterpart to different magnetospheric processes (X-ray emission and DF events) and regions (cusp) have been investigated. Although the three sections were investigated independently, they are all connected: some of the most important X-ray emissions coincide spatially with some of the previously suspected regions corresponding to the cusps; although it was not its main focus, the cusp study by Xu et al. (2024) showed the ionospheric region mapping to an open field lines lobe corresponding to the further magnetotail, where the DF events have their origin; and finally, the three of them (the LLE region for X-rays, the “cusp plasma”, and the DF events) are linked by the process of magnetic reconnection.

6.2 Future work

For the study presented in Chapter 3, future work will include expanding the sample to include both older HST observation campaigns (which have not been done so far because their reduction process differs from the ones shown here) and, all other future campaigns (such as the upcoming HST observation campaign led by Dr Nichols and concurrent with JWST images). In general, the most straightforward and natural next step for this work is doing an equivalent study for the Northern hemisphere, adapting the algorithm to do so. At the same time, the classification of the aurorae by morphological families as described by Grodent et al. (2018), although useful, has proven to be a subjective matter due to its visual inspection foundation. Ideally, automating the detection of certain key features, which could be those defined

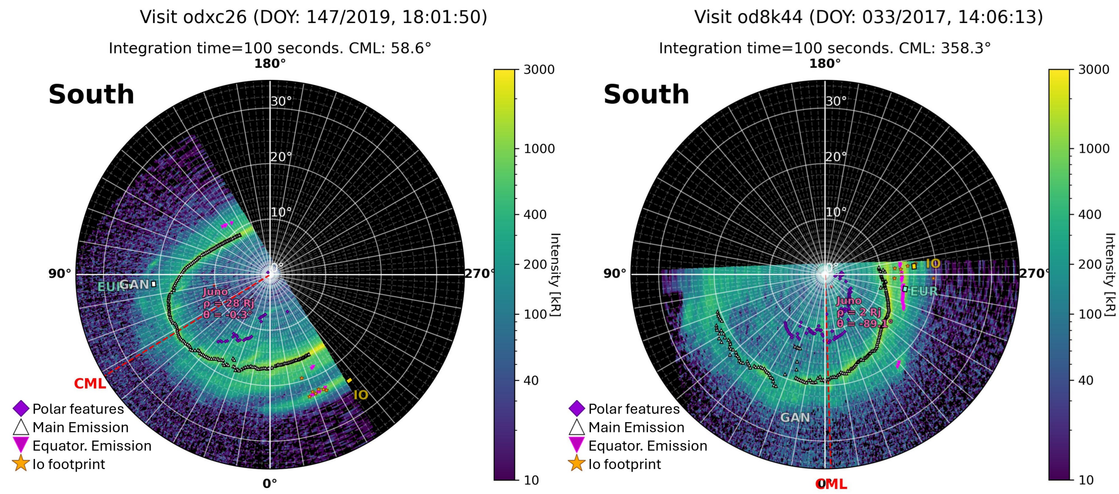

Figure 6.1: Two images from visits odxc26 and od8k44 from HST Observation Campaigns GO-15638 (Palmaerts et al. 2024) and GO-14634 (Grodent et al. 2018), showing an early attempt of the algorithm at fitting very fast polar flashes (in purple diamonds), as well as the discussed main oval, equatorward emissions, and Io footprint.

already for the different families, such as the continuity and brightness of the main oval, the existence of injection signatures, the overall power emitted by the aurorae, or the behaviour of the polar region, among others; would make the classification of the Jovian aurorae a more reliable resource to use as context or in combination with other data of magnetospheric, ionospheric, or atmospheric origin.

Finally, having demonstrated the potential of applying the automatic detection algorithm to identify the equatorward and main emissions with high precision, this method could be extended to other auroral features. Particularly, to Europa and Ganymede footprints (and their tails), and the polar flashes, arcs, and bright spots appearing and disappearing inside the main oval. The latter was attempted (see Figure 6.1), but the fitting of the polar features was ultimately discarded for lack of consistency across visits and for worsening the accuracy of the rest of the emissions. However, the systematic tracking of these features could allow for a better understanding of the particle precipitation originating them, as well as an improved database for comparing their characteristics with respect to the rest of the auroral emissions (e.g. frequency of the polar flashes or length of the Io footprint tail for the different auroral families). This may imply an independent fitting for the polar region, using a high-degree polynomial or other function that would allow for the detection of multiple simultaneous features.

Chapter 4 was based on Juno-JADE data and, thus, the nature of the trajectory of the spacecraft puts some constraints on both the availability of the data and the regions studied, added to the relatively sparse image acquisition by HST. Therefore, I suggest that possible avenues to build upon the work in this thesis would include incorporating images from the UVS imager onboard Juno to extend the sample of simultaneous datasets, as well as investigating the particle detector measurements from the JEDI instrument more in-depth. This could extend the investigation of the properties of the precipitating electrons producing the equatorward emission to higher energies. Additionally, for those (relatively rare) regions in which its angular resolution is enough to resolve the loss cone, some adjustments could be made to estimate new energy flux values derived from JEDI, to compare with the ones shown in this thesis from JADE. Lastly, the JADE results for the protons and heavy ions could be incorporated into the electron analysis. Their relevance has been addressed by studies of the injections (Haggerty et al. 2019), which could serve as a benchmark to compare new potential particle detections associated with the secondary oval instead. Finally, advanced machine-learning techniques could be integrated to analyze vast datasets from missions like Juno. Machine learning algorithms could identify subtle patterns and correlations between auroral emissions and magnetospheric events that may be overlooked by traditional analysis methods. For example, this approach could uncover new relationships between compressions/rarefactions of the magnetosphere and different auroral morphologies, and enhance predictive models of auroral activity for further comparison with UV images.

As for the final results chapter, several ideas could be developed based on those outlined in Chapter 5. First, the connection between the UV and X-ray emissions should be further analysed, considering a multi-wavelength perspective in all Jovian auroral studies (and, ideally, including local magnetic field and/or solar wind infor-

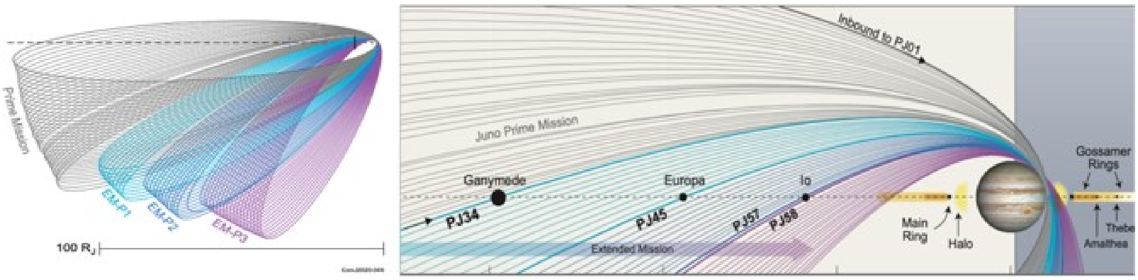

Figure 6.2: Juno's orbits from its prime mission (grey) to the 42 orbits of its extended mission (blue and purple). Left: The Juno orbit petal has been evolving due to the oblateness of Jupiter, such that perijove is moving north and apojove is moving south. Right: the extended mission phase includes flybys of the moons Ganymede, Europa, and Io. Credit: NASA/JPL-Caltech/SwRI.

mation). Relatedly, a further study similar to that of Weigt et al. (2023) for the Southern polar region would allow detailed comparisons between both hemispheres and shed some light on their seemingly independent behaviours (Dunn et al. 2017). If enough Chandra observations were taken, analogous X-ray regions could be defined for the South, using the main oval and the Io and Ganymede footprints as references. Lastly, the focus could be shifted to some of the other X-ray morphologies defined in that paper, like the comparison between the dawn and polar region, or even some yet to be defined (e.g. separating the equatorward or main emission by local time and comparing them).

Secondly, the cusp region study will benefit from the evolution of the Juno's orbits during the extended mission (currently in progress and up to September 2025). As the spacecraft changes its trajectory and it shifts its perijoves northward (see Figure 6.2), it will provide a closer "view" of the polar region, including the cusp region found by Xu et al. (2024). Performing a quantitative and systematic study on the auroral powers emitted by that region, the precipitating energy fluxes mapping to it, and the derived intensities from them would be very valuable.

Should coincident cusp region detections and remote observations become available (either with HST or other telescopes like the Chandra X-ray Observatory), the comparison of the characteristics of the auroral emissions (e.g. power, precipitating energy flux, and intensity) to the ranges obtained by Bunce (2004) would further refine our understanding of the cusp region, allow for the validation of the flow models, and constraining of their parameters. Furthermore, with more coverage of the pitch angle distributions, the precipitating energy fluxes could be estimated (in the same way as it has been done in Chapter 4) and compared to the auroral emissions. In conclusion, more cases of cusp region detections could open the possibility of studying the cusp-associated auroral signatures in "real-time".

Third and finally, Juno's extended mission will also unveil more information about the ionospheric counterpart of the furthest regions of the magnetosphere, including the magnetotail. Hence, more DF events are expected to be detected by the spacecraft, increasing the number of cases that can be studied in parallel with HST or other telescopes, in UV or other wavelengths. This will allow performing a statistical study of the DF events, similarly to what Jackman et al. (2013) did for Saturn.

In conclusion, analyzing auroral emissions as a response to various magnetospheric processes is crucial for advancing our understanding of Jupiter's complex magnetosphere. This thesis has underscored the importance of such studies, highlighting how auroral observations provide valuable insights into the dynamic interactions and energy transfer processes within the magnetosphere and into the ionosphere. By examining their auroral counterparts, we can better comprehend the underlying physical mechanisms driving these spectacular displays and their broader implications for planetary magnetospheres (including those affecting the Earth).

Appendix A

Additional Tables

SIII	Colatitude			SIII	Colatitude			SIII	Colatitude		
0	17.4	±	2.0	108	13.1	±	0.8	252	7.5	±	0.9
1	17.6	±	1.9	109	12.9	±	0.8	253	7.6	±	0.9
2	17.6	±	1.8	110	12.7	±	0.8	254	7.6	±	0.9
3	17.6	±	1.9	111	12.6	±	0.9	255	7.7	±	0.9
4	17.7	±	1.9	112	12.4	±	0.9	256	7.7	±	0.9
5	17.7	±	2.0	113	12.2	±	0.9	257	7.8	±	0.9
6	17.8	±	2.0	114	12.0	±	1.0	258	7.8	±	0.9
7	17.9	±	2.0	115	11.9	±	1.0	259	7.9	±	0.9
8	18.0	±	2.0	116	11.6	±	1.0	260	8.0	±	0.9
9	18.1	±	2.0	117	11.5	±	1.0	261	8.0	±	0.9
10	18.1	±	2.0	118	11.3	±	0.9	262	8.1	±	0.9
11	18.2	±	1.9	119	11.1	±	1.0	263	8.1	±	1.0
12	18.4	±	2.0	120	11.0	±	0.9	264	8.2	±	0.9
13	18.5	±	1.9	121	10.8	±	0.9	265	8.3	±	1.0
14	18.6	±	1.8	122	10.7	±	0.9	266	8.3	±	1.0
15	18.7	±	1.9	123	10.5	±	0.9	267	8.4	±	1.0
16	18.7	±	1.8	124	10.4	±	1.0	268	8.5	±	1.0
17	18.8	±	1.8	125	10.2	±	1.0	269	8.6	±	1.0
18	18.9	±	1.9	126	10.1	±	1.0	270	8.6	±	1.0
19	19.0	±	1.8	127	9.9	±	1.0	271	8.7	±	1.0
20	19.0	±	1.7	128	9.8	±	1.0	272	8.8	±	1.0
21	19.1	±	1.7	129	9.6	±	1.0	273	8.9	±	1.0
22	18.9	±	1.9	130	9.5	±	1.0	274	9.0	±	1.0
23	18.9	±	1.9	131	9.4	±	1.0	275	9.1	±	1.0
24	18.9	±	2.0	132	9.3	±	1.0	276	9.1	±	1.0
25	19.1	±	2.0	133	9.2	±	1.0	277	9.2	±	1.0
26	19.2	±	2.0	134	9.1	±	1.0	278	9.3	±	1.1
27	19.4	±	1.9	135	9.0	±	1.0	279	9.4	±	1.1

Table A.1 continued from previous page

28	19.6	±	1.8	136	8.9	±	1.0	280	9.5	±	1.1
29	19.8	±	1.8	137	8.8	±	0.9	281	9.6	±	1.1
30	19.9	±	1.7	138	8.7	±	1.0	282	9.6	±	1.1
31	19.9	±	1.6	139	8.6	±	1.0	283	9.7	±	1.2
32	20.0	±	1.5	140	8.5	±	0.9	284	9.8	±	1.2
33	20.1	±	1.4	141	8.4	±	0.9	285	9.8	±	1.2
34	20.2	±	1.4	142	8.3	±	0.9	286	9.9	±	1.2
35	20.3	±	1.4	143	8.2	±	0.9	287	10.0	±	1.2
36	20.3	±	1.5	144	8.2	±	0.9	288	10.1	±	1.2
37	20.3	±	1.5	145	8.0	±	0.9	289	10.2	±	1.2
38	20.4	±	1.5	146	7.9	±	0.9	290	10.2	±	1.2
39	20.4	±	1.4	147	7.9	±	0.9	291	10.4	±	1.2
40	20.5	±	1.4	148	7.8	±	0.9	292	10.5	±	1.3
41	20.5	±	1.4	149	7.8	±	0.9	293	10.6	±	1.3
42	20.5	±	1.4	150	7.7	±	0.9	294	10.7	±	1.3
43	20.6	±	1.4	151	7.7	±	0.9	295	10.8	±	1.3
44	20.7	±	1.3	152	7.6	±	0.9	296	10.9	±	1.2
45	20.7	±	1.4	153	7.6	±	0.8	297	11.0	±	1.2
46	20.8	±	1.3	154	7.5	±	0.8	298	11.1	±	1.3
47	20.9	±	1.4	155	7.4	±	0.8	299	11.2	±	1.2
48	20.9	±	1.4	156	7.3	±	0.8	300	11.3	±	1.3
49	21.0	±	1.4	157	7.3	±	0.8	301	11.5	±	1.2
50	21.0	±	1.5	158	7.2	±	0.8	302	11.6	±	1.3
51	21.0	±	1.5	159	7.2	±	0.8	303	11.7	±	1.3
52	21.0	±	1.4	160	7.2	±	0.8	304	11.8	±	1.3
53	21.1	±	1.4	161	7.1	±	0.7	305	11.9	±	1.3
54	21.0	±	1.3	162	7.0	±	0.8	306	12.0	±	1.3
55	21.0	±	1.4	163	7.0	±	0.8	307	12.1	±	1.3
56	21.0	±	1.3	164	6.9	±	0.7	308	12.3	±	1.3
57	21.0	±	1.2	165	6.9	±	0.7	309	12.4	±	1.3
58	20.9	±	1.2	166	6.8	±	0.7	310	12.5	±	1.3
59	21.0	±	1.2	167	6.8	±	0.7	311	12.6	±	1.3
60	21.0	±	1.2	168	6.8	±	0.7	312	12.7	±	1.3
61	20.9	±	1.1		...			313	12.8	±	1.3
62	20.8	±	1.1	206	5.9	±	0.7	314	12.9	±	1.3
63	20.7	±	1.1	207	5.9	±	0.7	315	13.0	±	1.3
64	20.8	±	1.1	208	6.0	±	0.7	316	13.1	±	1.3
65	20.8	±	1.2	209	6.0	±	0.7	317	13.2	±	1.3
66	20.7	±	1.2	210	6.0	±	0.7	318	13.3	±	1.3
67	20.6	±	1.2	211	6.0	±	0.7	319	13.4	±	1.4
68	20.5	±	1.1	212	5.9	±	0.8	320	13.6	±	1.4
69	20.4	±	1.2	213	5.9	±	0.8	321	13.6	±	1.4
70	20.2	±	1.2	214	5.9	±	0.8	322	13.7	±	1.5
71	20.2	±	1.2	215	6.0	±	0.8	323	13.9	±	1.5

Table A.1 continued from previous page

72	20.0	±	1.2	216	6.0	±	0.8	324	14.1	±	1.5
73	19.8	±	1.1	217	6.0	±	0.8	325	14.2	±	1.5
74	19.6	±	1.1	218	6.0	±	0.8	326	14.3	±	1.5
75	19.6	±	1.0	219	6.1	±	0.8	327	14.5	±	1.5
76	19.4	±	1.0	220	6.1	±	0.8	328	14.6	±	1.5
77	19.3	±	1.0	221	6.1	±	0.8	329	14.7	±	1.5
78	19.2	±	1.0	222	6.2	±	0.8	330	14.8	±	1.4
79	19.0	±	0.9	223	6.2	±	0.8	331	15.0	±	1.5
80	19.0	±	1.0	224	6.3	±	0.9	332	15.0	±	1.5
81	18.8	±	0.9	225	6.3	±	0.9	333	15.1	±	1.5
82	18.6	±	0.9	226	6.3	±	0.9	334	15.2	±	1.5
83	18.5	±	0.9	227	6.3	±	0.9	335	15.3	±	1.5
84	18.3	±	0.9	228	6.3	±	0.8	336	15.4	±	1.5
85	18.1	±	0.8	229	6.4	±	0.8	337	15.5	±	1.5
86	17.9	±	0.8	230	6.4	±	0.9	338	15.5	±	1.5
87	17.7	±	0.8	231	6.5	±	0.9	339	15.6	±	1.5
88	17.6	±	0.8	232	6.5	±	0.9	340	15.7	±	1.6
89	17.4	±	0.8	233	6.6	±	0.9	341	15.8	±	1.6
90	17.2	±	0.8	234	6.6	±	0.9	342	15.9	±	1.6
91	17.0	±	0.8	235	6.7	±	0.9	343	16.0	±	1.6
92	16.7	±	0.9	236	6.7	±	0.9	344	16.0	±	1.6
93	16.4	±	0.9	237	6.8	±	0.9	345	16.1	±	1.6
94	16.2	±	0.9	238	6.8	±	0.9	346	16.1	±	1.6
95	16.0	±	0.9	239	6.9	±	0.9	347	16.2	±	1.6
96	15.8	±	0.9	240	6.9	±	0.9	348	16.3	±	1.6
97	15.6	±	1.0	241	7.0	±	0.9	349	16.3	±	1.7
98	15.3	±	1.0	242	7.0	±	0.9	350	16.5	±	1.8
99	15.1	±	1.0	243	7.1	±	0.9	351	16.6	±	1.9
100	14.8	±	1.0	244	7.1	±	0.9	352	16.6	±	1.9
101	14.6	±	1.0	245	7.2	±	0.9	353	16.7	±	1.9
102	14.4	±	1.0	246	7.3	±	0.9	354	16.8	±	1.9
103	14.2	±	1.0	247	7.3	±	0.9	355	16.8	±	2.0
104	13.9	±	1.0	248	7.3	±	0.9	356	16.9	±	1.9
105	13.7	±	1.0	249	7.4	±	0.9	357	17.0	±	1.9
106	13.5	±	0.9	250	7.4	±	0.9	358	17.1	±	2.0
107	13.3	±	0.9	251	7.5	±	0.9	359	17.3	±	2.0

Table A.1: Colatitude of the Southern main oval of the Jovian aurorae (± the half width at half maximum).

Appendix B

Additional HST visits simultaneous to CXO data

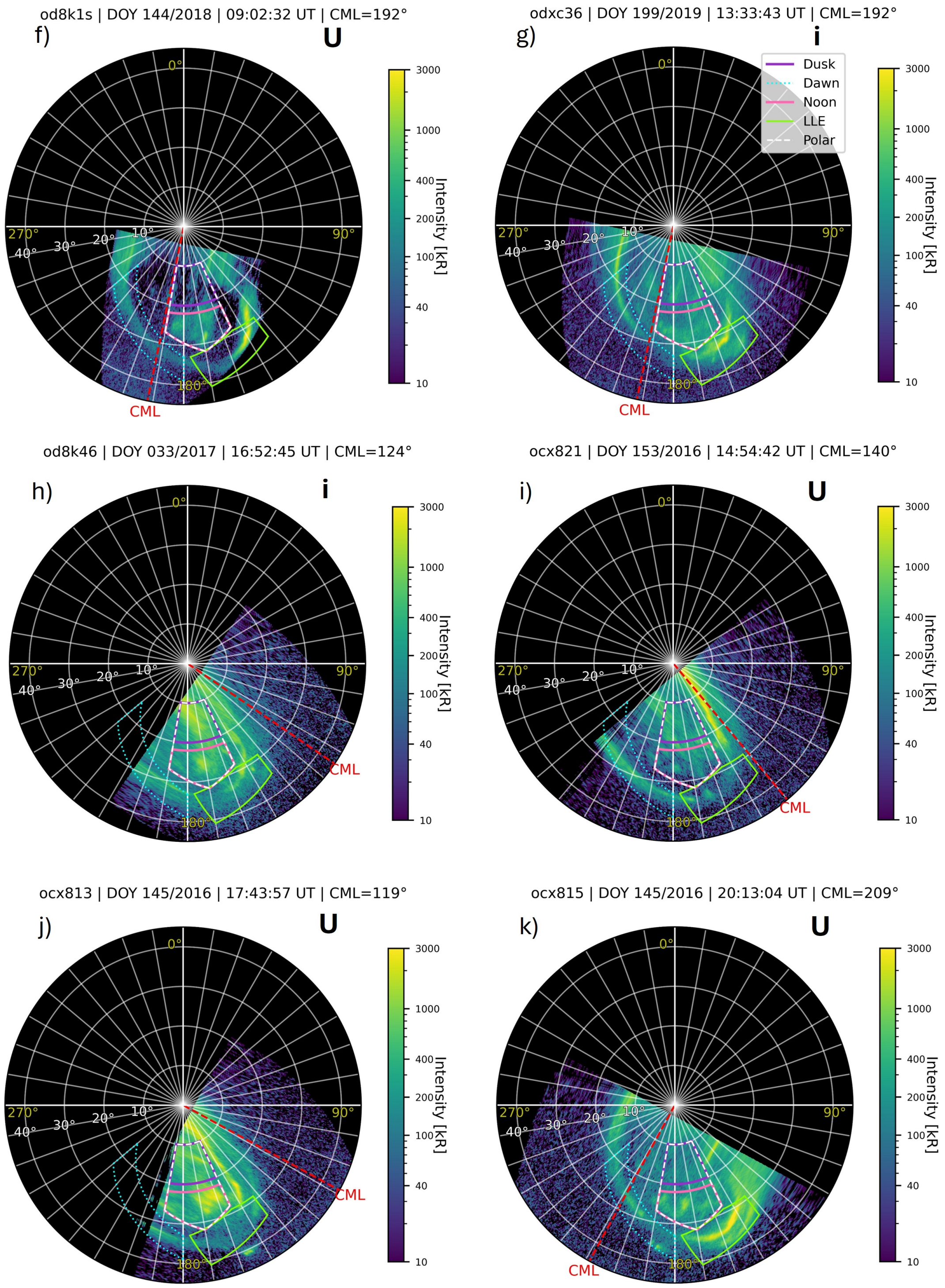

Figure B.1: Polar images of 6 HST-STIS visits of the Northern hemisphere simultaneous to Chandra X-ray observations. f) od8k1s (U family); g) odxc36 (i family); h) od8k46 (i family); i) od8k21 (U family); j) ocx813 (U family); k) ocx815 (U family).

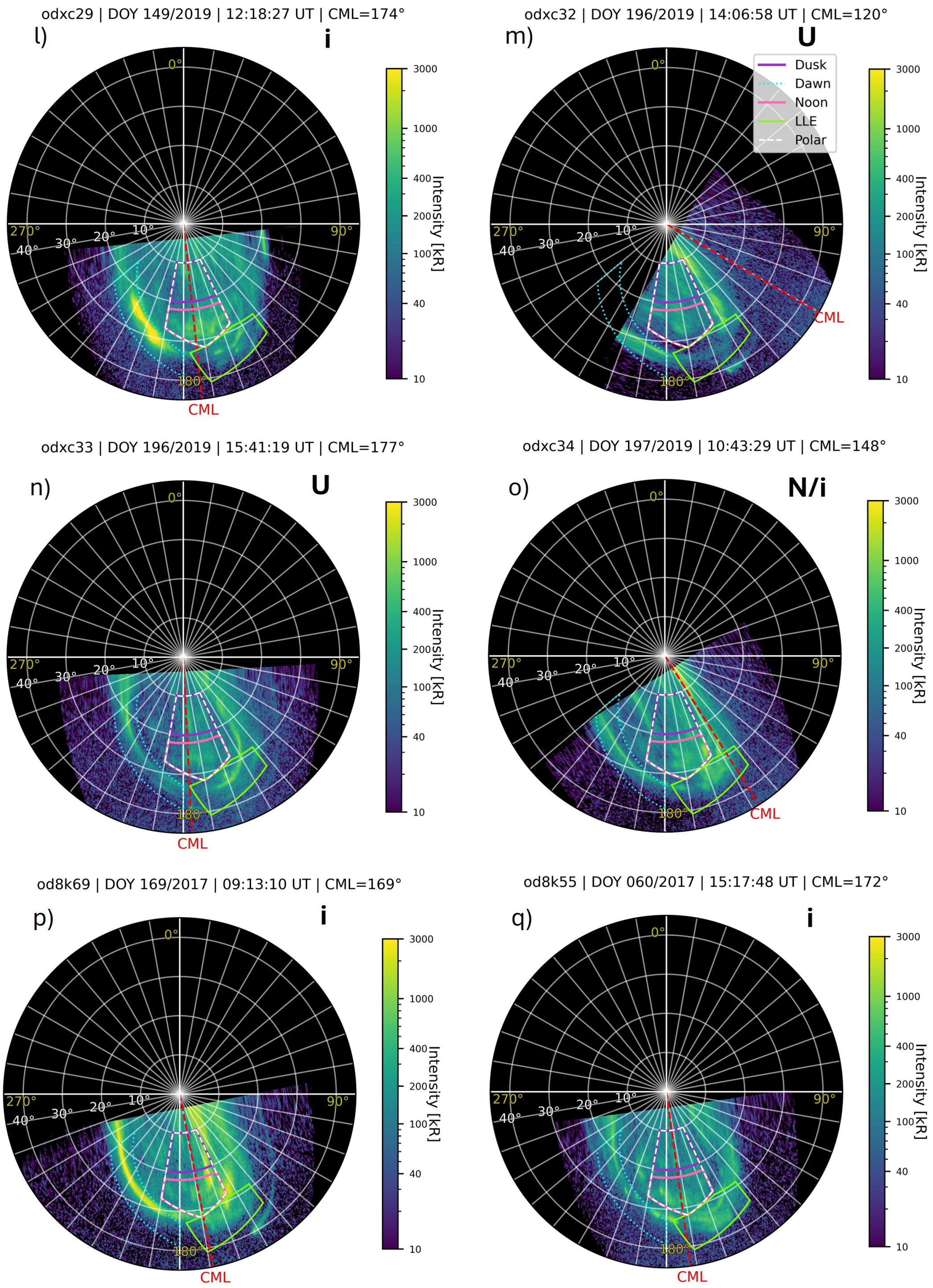

Figure B.2: Polar images of 6 HST-STIS visits of the Northern hemisphere simultaneous to Chandra X-ray observations. l) odxc29 (i family); m) odxc32 (U family); n) odxc33 (U family); o) odxc34 (N/i family); p) od8k69 (X/i family); q) od8k55 (i family).

Table 1
Table of Concurrent Chandra and Hubble Space Telescope (HST) Observations Throughout the Juno Era

Observation start date (dd/mm/yyyy)	Chandra ObsID	Observation interval (Juno time; light corrected)		HST UV northern auroral family[a]			Mean solar wind[b] P_{dyn} (nPa)	Max solar wind[b] P_{dyn} (nPa)	Mean Jupiter-Sun-Earth angle[b] (°)
		Chandra	HST	G18[c]	This study	D22[d]			
24/05/2016	18608	09:39–20:41	17:03–17:47	–	U	Q/N	0.006	0.007	~57.7
			20:14–20:58	–	U	U			
01/06/2016	18609	10:47–21:49	14:13–14:57	–	U	Q/N	0.138	0.309	~64.6
			17:24–18:08	–	U	Q/N			
02/02/2017	18301	09:14–18:19	16:17–16:57	–	i	i	0.009	0.015	~−79.9
28/02 (Chandra); 01/03/2017 (HST)[e]	20000[e]	11:58–07:34	14:37–15:16	i	i	–	0.019	0.024	~−53.3
18/05–19/05/2017	18302	23:48–10:10	04:27–05:07	N	N	N	0.052	0.148	~19.2
			06:03–06:43	N	N	N			
18/06/2017[e]	**20001**[e]	**17:55–04:06**	**08:31–09:13**	**X**	**i**	–	**0.090**	**0.230**	**~47.9**
06/08/2017[f]	20002[f]	01:07–10:50	–	–	–	–	0.015	0.024	~99.0
01/04/2018	**18678**	**09:59–21:06**	**09:59–10:17**	–	**X**	–	**0.116**	**0.275**	**~−58.4**
23/05–24/05/2018	18679	23:22–10:21	09:02–09:32	–	U	Q	0.049	0.115	~−3.6
06/09/2018	**18680**	**19:50–06:56**	**04:22–05:02**	–	**i**	**X**	**0.056**	**0.086**	**~97.0**
29/05/2019	22159	02:50–12:34	12:18–12:56	–	i	–	0.014	0.019	~−32.5
15/07/2019	22148	12:21–19:13	14:06–14:44	–	U	N	0.068	0.115	~10.5
			15:41–16:17	–	U	Q			
16/07/2019	22149	08:07–15:00	10:43–11:21	–	N/i	N	0.057	0.096	~11.3
18/07/2019[e]	22150[e]	19:40–01:32	14:10–14:49	–	i	–	0.012	0.018	~13.9
08/09/2019	**22151**	**08:01–14:46**	**14:24–15:02**	–	**X/i**	–	**0.262**	**0.879**	**~64.0**

Note. Date and time of each observation, identified UV auroral families from current literature using the G18 definition and predicted solar wind dynamic pressure from the Tao et al. (2005) model with average Jupiter-Sun-Earth angle are shown. Bold entries highlight observations associated with possible eXternal perturbation (X) structures linked with potential compression events as confirmed by Yao et al. (2022). Solar wind parameters determined over a 2 days window centered on the Chandra observation to account for propagation errors within Tao et al. (2005) model. Each Chandra observation is labeled with a unique Observation ID (ObsID).

[a]UV families as described in Grodent et al. (2018). [b]Predicted values from Tao et al. (2005) model over 2 days window centered on Chandra observation. [c]UV families identified from Grodent et al. (2018) (G18). [d]UV families identified from Dunn et al. (2022) (D22). [e]Observations not concurrent but occurred ±1 day from Chandra interval. [f]Inferred compression from Juno data, no HST data.

Table B.1

Bibliography

Achilleos, N. (2018). “The Nature of Jupiter’s Magnetodisk Current System”. en. In: 1st ed., pp. 127–138. DOI: 10.1002/9781119324522.ch8.

Achilleos, Nicholas, Nicolas André, Xochitl Blanco-Cano, Pontus C. Brandt, et al. (2015). “Transport of Mass, Momentum and Energy in Planetary Magnetodisc Regions”. en. In: *Space Science Reviews* 187.1, pp. 229–299. DOI: 10.1007/s11214-014-0086-y.

Acuna, Mario H., J. E. P. Connerney, P. Wasilewski, R.P. Lin, et al. (1998). “Magnetic Field and Plasma Observations at Mars: Initial Results of the Mars Global Surveyor Mission”. en. In: 279.5359. DOI: 10.1126/science.279.5357.1676.

Acuña, Mario H. and Norman F. Ness (1976). “The main magnetic field of Jupiter”. en. In: *Journal of Geophysical Research (1896-1977)* 81.16, pp. 2917–2922. DOI: 10.1029/JA081i016p02917.

Allegrini, F., F. Bagenal, S. Bolton, J. Connerney, et al. (2017). “Electron beams and loss cones in the auroral regions of Jupiter”. en. In: *Geophysical Research Letters* 44.14, pp. 7131–7139. DOI: 10.1002/2017GL073180.

Allegrini, F., B. Mauk, G. Clark, G. R. Gladstone, et al. (2020). “Energy Flux and Characteristic Energy of Electrons Over Jupiter’s Main Auroral Emission”. en. In: *Journal of Geophysical Research: Space Physics* 125.4, e2019JA027693. DOI: 10.1029/2019JA027693.

Amm, O., Joachim Birn, J. Bonnell, and J.E. Borovsky (2002). “Chapter 4 - In Situ Measurements in the Auroral Plasma”. en. In: *Space Science Reviews* 103.1, pp. 93–208. DOI: 10.1023/A:1023082700768.

Arridge, C. S., K. K. Khurana, C. T. Russell, D. J. Southwood, et al. (2008). "Warping of Saturn's magnetospheric and magnetotail current sheets". en. In: *Journal of Geophysical Research: Space Physics* 113.A8. DOI: 10.1029/2007JA012963.

Artemyev, A. V., S. Kasahara, A. Y. Ukhorskiy, and M. Fujimoto (2013). "Acceleration of ions in the Jupiter magnetotail: Particle resonant interaction with dipolarization fronts". In: *Planetary and Space Science* 82-83, pp. 134–148. DOI: 10.1016/j.pss.2013.04.013.

Atkinson, G. (1970). "Auroral arcs: Result of the interaction of a dynamic magnetosphere with the ionosphere". en. In: *Journal of Geophysical Research (1896-1977)* 75.25, pp. 4746–4755. DOI: 10.1029/JA075i025p04746.

Bader, A., S.v. Badman, J. Kinrade, S.w.h. Cowley, et al. (2019). "Modulations of Saturn's UV Auroral Oval Location by Planetary Period Oscillations". en. In: *Journal of Geophysical Research: Space Physics* 124.2, pp. 952–970. DOI: 10.1029/2018JA026117.

Badman, S. V., B. Bonfond, M. Fujimoto, R. L. Gray, et al. (2016). "Weakening of Jupiter's main auroral emission during January 2014". en. In: *Geophysical Research Letters* 43.3, pp. 988–997. DOI: 10.1002/2015GL067366.

Badman, S. V. and S. W. H. Cowley (2007). "Significance of Dungey-cycle flows in Jupiter's and Saturn's magnetospheres, and their identification on closed equatorial field lines". English. In: *Annales Geophysicae* 25.4, pp. 941–951. DOI: 10.5194/angeo-25-941-2007.

Badman, S.v., A. Masters, H. Hasegawa, M. Fujimoto, et al. (2013). "Bursty magnetic reconnection at Saturn's magnetopause". en. In: *Geophysical Research Letters* 40.6, pp. 1027–1031. DOI: 10.1002/grl.50199.

Badman, Sarah V., Graziella Branduardi-Raymont, Marina Galand, Sébastien L. G. Hess, et al. (2015). "Auroral Processes at the Giant Planets: Energy Deposition, Emission Mechanisms, Morphology and Spectra". en. In: *Space Science Reviews* 187.1-4, pp. 99–179. DOI: 10.1007/s11214-014-0042-x.

Bagenal, F. and R. J. Wilson (2016). *Jupiter Coordinate Systems*.

Bagenal, Fran (2007). “The magnetosphere of Jupiter: Coupling the equator to the poles”. en. In: *Journal of Atmospheric and Solar-Terrestrial Physics* 69.3, pp. 387–402. DOI: 10.1016/j.jastp.2006.08.012.

Bagenal, Fran and James D. Sullivan (1981). “Direct plasma measurements in the Io torus and inner magnetosphere of Jupiter”. en. In: *Journal of Geophysical Research: Space Physics* 86.A10, pp. 8447–8466. DOI: 10.1029/JA086iA10p08447.

Becker, Heidi N., Daniel Santos-Costa, John L. Jørgensen, Troelz Denver, et al. (2017). “Observations of MeV electrons in Jupiter’s innermost radiation belts and polar regions by the Juno radiation monitoring investigation: Perijoves 1 and 3”. en. In: *Geophysical Research Letters* 44.10, pp. 4481–4488. DOI: 10.1002/2017GL073091.

Behannon, K. W., L. F. Burlaga, and N. F. Ness (1981). “The Jovian magnetotail and its current sheet”. en. In: *Journal of Geophysical Research: Space Physics* 86.A10, pp. 8385–8401. DOI: 10.1029/JA086iA10p08385.

Benmahi, B., B. Bonfond, B. Benne, D. Grodent, et al. (2024). “Energy mapping of Jupiter’s auroral electrons from Juno/UVS data using a new H $_2$ UV emission model”. en. In: *Astronomy & Astrophysics* 685, A26. DOI: 10.1051/0004-6361/202348634.

Bertaux, Jean-Loup, François Leblanc, Olivier Witasse, Eric Quemerais, et al. (2005). “Discovery of an aurora on Mars”. en. In: *Nature* 435.7043, pp. 790–794. DOI: 10.1038/nature03603.

Bhardwaj, Anil and G. Randallˆ Gladstone (2000). “Auroras on Saturn, Uranus, and Neptune”. en. In: *Advances in Space Research* 26.10, pp. 1551–1558. DOI: 10.1016/S0273-1177(00)00096-X.

Bhattacharya, B., R. M. Thorne, and D. J. Williams (2001). “On the energy source for diffuse Jovian auroral emissivity”. en. In: *Geophysical Research Letters* 28.14, pp. 2751–2754. DOI: 10.1029/2000GL012616.

Bhattacharyya, Dolon, John T. Clarke, Jordan Montgomery, Bertrand Bonfond, et al. (2018). “Evidence for Auroral Emissions From Callisto’s Footprint in HST UV

Images". en. In: *Journal of Geophysical Research: Space Physics* 123.1, pp. 364–373. DOI: 10.1002/2017JA024791.

Blöcker, A., E. A. Kronberg, E. E. Grigorenko, E. Roussos, et al. (2023). "Dipolarization Fronts in the Jovian Magnetotail: Statistical Survey of Ion Intensity Variations Using Juno Observations". en. In: *Journal of Geophysical Research: Space Physics* 128.4, e2023JA031312. DOI: 10.1029/2023JA031312.

Bolton, Scott J., Steven M. Levin, Samuel L. Gulkis, Michael J. Klein, et al. (2001). "Divine-Garrett Model and Jovian synchrotron emission". en. In: *Geophysical Research Letters* 28.5, pp. 907–910. DOI: 10.1029/2000GL012071.

Bonfond, B. (2010). "The 3-D extent of the Io UV footprint on Jupiter". en. In: *Journal of Geophysical Research: Space Physics* 115.A9. DOI: 10.1029/2010JA015475.

Bonfond, B., G. R. Gladstone, D. Grodent, J.-C. Gérard, et al. (2018). "Bar Code Events in the Juno-UVS Data: Signature 10 MeV Electron Microbursts at Jupiter". en. In: *Geophysical Research Letters* 45.22, pp. 12, 108–12, 115. DOI: 10.1029/2018GL080490.

Bonfond, B., D. Grodent, S. V. Badman, J.-C. Gérard, et al. (2016). "Dynamics of the flares in the active polar region of Jupiter". en. In: *Geophysical Research Letters* 43.23, pp. 11, 963–11, 970. DOI: 10.1002/2016GL071757.

Bonfond, B., D. Grodent, J.-C. Gérard, T. Stallard, et al. (2012). "Auroral evidence of Io's control over the magnetosphere of Jupiter". en. In: *Geophysical Research Letters* 39.1. DOI: 10.1029/2011GL050253.

Bonfond, B., D. Grodent, J.-C. Gérard, A. Radioti, et al. (2009). "The Io UV footprint: Location, inter-spot distances and tail vertical extent". en. In: *Journal of Geophysical Research: Space Physics* 114.A7, 2009JA014312. DOI: 10.1029/2009JA014312.

Bonfond, B., J. Gustin, J.-C. Gérard, D. Grodent, et al. (2015). "The far-ultraviolet main auroral emission at Jupiter – Part 1: Dawn–dusk brightness asymmetries". en. In: *Annales Geophysicae* 33.10, pp. 1203–1209. DOI: 10.5194/angeo-33-1203-2015.

Bonfond, B., S. Hess, F. Bagenal, J.-C. Gérard, et al. (2013). "The multiple spots of the Ganymede auroral footprint". en. In: *Geophysical Research Letters* 40.19, pp. 4977–4981. DOI: 10.1002/grl.50989.

Bonfond, B., J. Saur, D. Grodent, S. V. Badman, et al. (2017). "The tails of the satellite auroral footprints at Jupiter". en. In: *Journal of Geophysical Research: Space Physics* 122.8, pp. 7985–7996. DOI: 10.1002/2017JA024370.

Bonfond, B., M. F. Vogt, J.-C. Gérard, D. Grodent, et al. (2011). "Quasi-periodic polar flares at Jupiter: A signature of pulsed dayside reconnections?" en. In: *Geophysical Research Letters* 38.2. DOI: 10.1029/2010GL045981.

Bonfond, B., Z. H. Yao, G. R. Gladstone, D. Grodent, et al. (2021). "Are Dawn Storms Jupiter's Auroral Substorms?" en. In: *AGU Advances* 2.1, e2020AV000275. DOI: https://doi.org/10.1029/2020AV000275.

Bonfond, Bertrand, Zhonghua Yao, and Denis Grodent (2020). "Six pieces of evidence against the corotation enforcement theory to explain the main aurora at Jupiter". en. In: *arXiv:2005.05938 [astro-ph, physics:physics]*.

Bougher, S. W., J. H. Waite Jr., T. Majeed, and G. R. Gladstone (2005). "Jupiter Thermospheric General Circulation Model (JTGCM): Global structure and dynamics driven by auroral and Joule heating". en. In: *Journal of Geophysical Research: Planets* 110.E4. DOI: 10.1029/2003JE002230.

Bradley, T. J., S. W. H. Cowley, E. J. Bunce, H. Melin, et al. (2020). "Saturn's Nightside Dynamics During Cassini's F Ring and Proximal Orbits: Response to Solar Wind and Planetary Period Oscillation Modulations". en. In: *Journal of Geophysical Research: Space Physics* 125.9, e2020JA027907. DOI: https://doi.org/10.1029/2020JA027907.

Branduardi-Raymont, G., A. Bhardwaj, R. F. Elsner, G. R. Gladstone, et al. (2007). "A study of Jupiter's aurorae with *XMM-Newton*". en. In: *Astronomy & Astrophysics* 463.2, pp. 761–774. DOI: 10.1051/0004-6361:20066406.

Branduardi-Raymont, G., R. F. Elsner, M. Galand, D. Grodent, et al. (2008). "Spectral morphology of the X-ray emission from Jupiter's aurorae". en. In: *Journal of Geophysical Research: Space Physics* 113.A2. DOI: 10.1029/2007JA012600.

Brice, Neil and Thomas R. Mcdonough (1973). "Jupiter's radiation belts". In: *Icarus* 18.2, pp. 206–219. DOI: 10.1016/0019-1035(73)90204-2.

Brizard, Alain J. (2013). "Beyond linear gyrocenter polarization in gyrokinetic theory". In: *Physics of Plasmas* 20.9, p. 092309. DOI: 10.1063/1.4823716.

Bunce, E. J. (2004). "Jovian cusp processes: Implications for the polar aurora". en. In: *Journal of Geophysical Research* 109.A9, A09S13. DOI: 10.1029/2003JA010280.

Bunce, E. J., S. W. H. Cowley, and S. E. Milan (2005). "Interplanetary magnetic field control of Saturn's polar cusp aurora". English. In: *Annales Geophysicae* 23.4, pp. 1405–1431. DOI: 10.5194/angeo-23-1405-2005.

Burch, J. L. and T. D. Phan (2016). "Magnetic reconnection at the dayside magnetopause: Advances with MMS". en. In: *Geophysical Research Letters* 43.16, pp. 8327–8338. DOI: 10.1002/2016GL069787.

Carlson, C. W., R. F. Pfaff, and J. G. Watzin (1998). "The Fast Auroral SnapshoT (FAST) Mission". en. In: *Geophysical Research Letters* 25.12, pp. 2013–2016. DOI: 10.1029/98GL01592.

Caudal, Gérard (1986). "A self-consistent model of Jupiter's magnetodisc including the effects of centrifugal force and pressure". en. In: *Journal of Geophysical Research: Space Physics* 91.A4, pp. 4201–4221. DOI: 10.1029/JA091iA04p04201.

Chané, E., J. Saur, and S. Poedts (2013). "Modeling Jupiter's magnetosphere: Influence of the internal sources". en. In: *Journal of Geophysical Research: Space Physics* 118.5, pp. 2157–2172. DOI: 10.1002/jgra.50258.

Clark, G., B. H. Mauk, D. Haggerty, C. Paranicas, et al. (2017). "Energetic particle signatures of magnetic field-aligned potentials over Jupiter's polar regions". en. In: *Geophysical Research Letters* 44.17, pp. 8703–8711. DOI: 10.1002/2017GL074366.

Clark, G., C. Tao, B. H. Mauk, J. Nichols, et al. (2018). "Precipitating Electron Energy Flux and Characteristic Energies in Jupiter's Main Auroral Region as Measured by Juno/JEDI". en. In: *Journal of Geophysical Research: Space Physics* 123.9, pp. 7554–7567. DOI: 10.1029/2018JA025639.

Clarke, J. T., J. Ajello, G. Ballester, L. Ben Jaffel, et al. (2002). "Ultraviolet emissions from the magnetic footprints of Io, Ganymede and Europa on Jupiter". en. In: *Nature* 415.6875, pp. 997–1000. DOI: 10.1038/415997a.

Clarke, J. T., Denis Grodent, S. W. H. Cowley, E. J. Bunce, et al. (2015). "Jupiter's Aurora". en. In: p. 32.

Clarke, J. T., J. Nichols, J.-C. Gérard, D. Grodent, et al. (2009). "Response of Jupiter's and Saturn's auroral activity to the solar wind". en. In: *Journal of Geophysical Research: Space Physics* 114.A5. DOI: 10.1029/2008JA013694.

Connerney, J. E. P. (1981). "The magnetic field of Jupiter: A generalized inverse approach". en. In: *Journal of Geophysical Research: Space Physics* 86.A9, pp. 7679–7693. DOI: 10.1029/JA086iA09p07679.

Connerney, J. E. P., M. Benn, J. B. Bjarno, T. Denver, et al. (2017). "The Juno Magnetic Field Investigation". en. In: *Space Science Reviews* 213.1-4, pp. 39–138. DOI: 10.1007/s11214-017-0334-z.

Connerney, J. E. P., S. Kotsiaros, R. J. Oliversen, J. R. Espley, et al. (2018). "A New Model of Jupiter's Magnetic Field From Juno's First Nine Orbits". en. In: *Geophysical Research Letters* 45.6, pp. 2590–2596. DOI: 10.1002/2018GL077312.

Connerney, J. E. P., S. Timmins, M. Herceg, and J. L. Joergensen (2020). "A Jovian Magnetodisc Model for the Juno Era". en. In: *Journal of Geophysical Research: Space Physics* 125.10, e2020JA028138. DOI: 10.1029/2020JA028138.

Connerney, J. E. P., S. Timmins, R. J. Oliversen, J. R. Espley, et al. (2022). "A New Model of Jupiter's Magnetic Field at the Completion of Juno's Prime Mission". en. In: *Journal of Geophysical Research: Planets* 127.2, e2021JE007055. DOI: 10.1029/2021JE007055.

Cowley, S. W. H. (1993). "The Magnetosphere and Its Interaction with the Solar Wind and with the Ionosphere". In: vol. 245. NATO ASI Series, pp. 147–181.

Cowley, S. W. H., E. J. Bunce, T. S. Stallard, and S. Miller (2003). "Jupiter's polar ionospheric flows: Theoretical interpretation". en. In: *Geophysical Research Letters* 30.5. DOI: https://doi.org/10.1029/2002GL016030.

Cowley, S. W. H. and M. Lockwood (1992). "Excitation and decay of solar wind-driven flows in the magnetosphere-ionosphere system". In: *Annales Geophysicae* 10, pp. 103–115.

Cowley, S.W.H. and E.J. Bunce (2001). "Origin of the main auroral oval in Jupiter's coupled magnetosphere–ionosphere system". en. In: *Planetary and Space Science* 49.10-11, pp. 1067–1088. DOI: 10.1016/S0032-0633(00)00167-7.

Cravens, T. E., J. H. Waite, T. I. Gombosi, N. Lugaz, et al. (2003). "Implications of Jovian X-ray emission for magnetosphere-ionosphere coupling". en. In: *Journal of Geophysical Research: Space Physics* 108.A12. DOI: 10.1029/2003JA010050.

Cravens, Thomas (2004). "Physics of Solar System Plasmas". In: *Physics of Solar System Plasmas, by Thomas E. Cravens, pp. 495. ISBN 0521611946. Cambridge, UK: Cambridge University Press, November 2004.* -1. DOI: 10.1017/CBO9780511529467.

Deighan, J., S. K. Jain, M. S. Chaffin, X. Fang, et al. (2018). "Discovery of a proton aurora at Mars". en. In: *Nature Astronomy* 2.10, pp. 802–807. DOI: 10.1038/s41550-018-0538-5.

Delamere, P. A. and F. Bagenal (2010). "Solar wind interaction with Jupiter's magnetosphere". en. In: *Journal of Geophysical Research: Space Physics* 115.A10. DOI: 10.1029/2010JA015347.

Dols, V. and R.E. Johnson (2023). "Ion-molecule charge exchange in Io's extended atmosphere: Velocity dependence". en. In: *Icarus* 392, p. 115365. DOI: 10.1016/j.icarus.2022.115365.

Dumont, M., D. Grodent, A. Radioti, B. Bonfond, et al. (2014). "Jupiter's equatorward auroral features: Possible signatures of magnetospheric injections". en. In: *Journal of Geophysical Research: Space Physics* 119.12, pp. 10, 068–10, 077. DOI: https://doi.org/10.1002/2014JA020527.

Dumont, M., D. Grodent, A. Radioti, B. Bonfond, et al. (2018). "Evolution of the Auroral Signatures of Jupiter's Magnetospheric Injections". en. In: *Journal of Geophysical Research: Space Physics* 123.10, pp. 8489–8501. DOI: 10.1029/2018JA025708.

Dungey, J. W. (1961). "Interplanetary Magnetic Field and the Auroral Zones". en. In: *Physical Review Letters* 6.2, pp. 47–48. DOI: 10.1103/PhysRevLett.6.47.

Dunn, W. R. (2022). "X-Ray Emissions from the Jovian System". en. In: pp. 1–56. DOI: 10.1007/978-981-16-4544-0_73-1.

Dunn, W. R., G. Branduardi-Raymont, L. C. Ray, C. M. Jackman, et al. (2017). "The independent pulsations of Jupiter's northern and southern X-ray auroras". en. In: *Nature Astronomy* 1.11, pp. 758–764. DOI: 10.1038/s41550-017-0262-6.

Dunn, W. R., G. Branduardi-Raymont, V. Carter-Cortez, A. Campbell, et al. (2020a). "Jupiter's X-ray Emission During the 2007 Solar Minimum". en. In: *Journal of Geophysical Research: Space Physics* 125.6, e2019JA027219. DOI: https://doi.org/10.1029/2019JA027219.

Dunn, W. R., R. Gray, A. D. Wibisono, L. Lamy, et al. (2020b). "Comparisons Between Jupiter's X-ray, UV and Radio Emissions and In-Situ Solar Wind Measurements During 2007". en. In: *Journal of Geophysical Research: Space Physics* 125.6, e2019JA027222. DOI: https://doi.org/10.1029/2019JA027222.

Dunn, W. R., D. M. Weigt, D. Grodent, Z. H. Yao, et al. (2022). "Jupiter's X-Ray and UV Dark Polar Region". en. In: *Geophysical Research Letters* 49.11, e2021GL097390. DOI: 10.1029/2021GL097390.

Ebert, R. W., F. Allegrini, F. Bagenal, S. J. Bolton, et al. (2017). "Spatial Distribution and Properties of 0.1–100 keV Electrons in Jupiter's Polar Auroral Region". en. In: *Geophysical Research Letters* 44.18, pp. 9199–9207. DOI: 10.1002/2017GL075106.

Ebert, R. W., T. K. Greathouse, G. Clark, F. Allegrini, et al. (2019). "Comparing Electron Energetics and UV Brightness in Jupiter's Northern Polar Region During Juno Perijove 5". en. In: *Geophysical Research Letters* 46.1, pp. 19–27. DOI: 10.1029/2018GL081129.

Ebert, R. W., T. K. Greathouse, G. Clark, V. Hue, et al. (2021). "Simultaneous UV Images and High-Latitude Particle and Field Measurements During an Auroral Dawn Storm at Jupiter". en. In: *Journal of Geophysical Research: Space Physics* 126.12, e2021JA029679. DOI: 10.1029/2021JA029679.

Elliott, S. S., D. A. Gurnett, W. S. Kurth, G. Clark, et al. (2018). "Pitch Angle Scattering of Upgoing Electron Beams in Jupiter's Polar Regions by Whistler Mode Waves". en. In: *Geophysical Research Letters* 45.3, pp. 1246–1252. DOI: 10.1002/2017GL076878.

Elsner, R. F., N. Lugaz, J. H. Waite Jr., T. E. Cravens, et al. (2005). "Simultaneous Chandra X ray, Hubble Space Telescope ultraviolet, and Ulysses radio observations of Jupiter's aurora". en. In: *Journal of Geophysical Research: Space Physics* 110.A1. DOI: 10.1029/2004JA010717.

Fairfield, D. H. and L. J. Cahill (1966). "Transition region magnetic field and polar magnetic disturbances". en. In: *Journal of Geophysical Research* 71.1, pp. 155–169. DOI: 10.1029/JZ071i001p00155.

Feldman, Paul D., Melissa A. McGrath, Darrell F. Strobel, H. Warren Moos, et al. (2000). "*HST* /STIS Ultraviolet Imaging of Polar Aurora on Ganymede". en. In: *The Astrophysical Journal* 535.2, pp. 1085–1090. DOI: 10.1086/308889.

Frank, L. A. and W. R. Paterson (1999). "Intense electron beams observed at Io with the Galileo spacecraft". en. In: *Journal of Geophysical Research: Space Physics* 104.A12, pp. 28657–28669. DOI: 10.1029/1999JA900402.

Franklin, K. L. and B. F. Burke (1956). "Radio observations of Jupiter." In: *The Astronomical Journal* 61, p. 177. DOI: 10.1086/107310.

Fu, Huishan, Elena E. Grigorenko, Christine Gabrielse, Chengming Liu, et al. (2020). "Magnetotail dipolarization fronts and particle acceleration: A review". en. In: *Science China Earth Sciences* 63.2, pp. 235–256. DOI: 10.1007/s11430-019-9551-y.

Galand, Marina, Luke Moore, Ingo Mueller-Wodarg, Michael Mendillo, et al. (2011). "Response of Saturn's auroral ionosphere to electron precipitation: Electron density, electron temperature, and electrical conductivity". en. In: *Journal of Geophysical Research: Space Physics* 116.A9. DOI: 10.1029/2010JA016412.

Gallardo-Lacourt, Bea, Y. Nishimura, L. R. Lyons, J. M. Ruohoniemi, et al. (2014). "Ionospheric flow structures associated with auroral beading at substorm auroral onset". en. In: *Journal of Geophysical Research: Space Physics* 119.11, pp. 9150–9159. DOI: 10.1002/2014JA020298.

Geiss, J., G. Gloeckler, H. Balsiger, L. A. Fisk, et al. (1992). "Plasma Composition in Jupiter's Magnetosphere: Initial Results from the Solar Wind Ion Composition Spectrometer". eng. In: *Science (New York, N.Y.)* 257.5076, pp. 1535–1539. DOI: 10.1126/science.257.5076.1535.

Gérard, J. -C., B. Bonfond, D. Grodent, and A. Radioti (2016). "The color ratio-intensity relation in the Jovian aurora: Hubble observations of auroral components". In: *Planetary and Space Science* 131, pp. 14–23. DOI: 10.1016/j.pss.2016.06.004.

Gérard, J.-C., B. Bonfond, B. H. Mauk, G. R. Gladstone, et al. (2019). "Contemporaneous Observations of Jovian Energetic Auroral Electrons and Ultraviolet Emissions by the Juno Spacecraft". en. In: *Journal of Geophysical Research: Space Physics* 124.11, pp. 8298–8317. DOI: 10.1029/2019JA026862.

Gérard, J.-C., D. Grodent, A. Radioti, B. Bonfond, et al. (2013). "Hubble observations of Jupiter's north–south conjugate ultraviolet aurora". en. In: *Icarus* 226.2, pp. 1559–1567. DOI: 10.1016/j.icarus.2013.08.017.

Gérard, J.-C., J. Gustin, D. Grodent, J. T. Clarke, et al. (2003). "Spectral observations of transient features in the FUV Jovian polar aurora". en. In: *Journal of Geophysical Research: Space Physics* 108.A8. DOI: 10.1029/2003JA009901.

Gérard, J.-C., B. Hubert, V.I. Shematovich, D.V. Bisikalo, et al. (2008). "The Venus ultraviolet oxygen dayglow and aurora: Model comparison with observations".

en. In: *Planetary and Space Science* 56.3-4, pp. 542–552. DOI: 10.1016/j.pss.2007.11.008.

Gérard, Jean-Claude, Emma J. Bunce, Denis Grodent, Stanley W. H. Cowley, et al. (2005). “Signature of Saturn’s auroral cusp: Simultaneous Hubble Space Telescope FUV observations and upstream solar wind monitoring”. en. In: *Journal of Geophysical Research: Space Physics* 110.A11. DOI: 10.1029/2005JA011094.

Gershman, Daniel J., Gina A. DiBraccio, John E. P. Connerney, Fran Bagenal, et al. (2018). “Juno Constraints on the Formation of Jupiter’s Magnetospheric Cushion Region”. en. In: *Geophysical Research Letters* 45.18, pp. 9427–9434. DOI: 10.1029/2018GL079118.

Gray, C.L., N.J. Chanover, T.G. Slanger, and K. Molaverdikhani (2014). “The effect of solar flares, coronal mass ejections, and solar wind streams on Venus’ 5577Å oxygen green line”. en. In: *Icarus* 233, pp. 342–347. DOI: 10.1016/j.icarus.2014.01.029.

Gray, R. L., S. V. Badman, B. Bonfond, T. Kimura, et al. (2016). “Auroral evidence of radial transport at Jupiter during January 2014”. en. In: *Journal of Geophysical Research: Space Physics* 121.10, pp. 9972–9984. DOI: https://doi.org/10.1002/2016JA023007.

Gray, R. L., S. V. Badman, E. E. Woodfield, and C. Tao (2017). “Characterization of Jupiter’s secondary auroral oval and its response to hot plasma injections”. en. In: *Journal of Geophysical Research: Space Physics* 122.6, pp. 6415–6429. DOI: 10.1002/2017JA024214.

Greathouse, T. K., G. R. Gladstone, P. M. Molyneux, M. H. Versteeg, et al. (2022). “UVS Observations of Ganymede’s Aurora During Juno Orbits 34 and 35”. en. In: *Geophysical Research Letters* 49.23, e2022GL099794. DOI: 10.1029/2022GL099794.

Greathouse, Thomas, Randy Gladstone, Maarten Versteeg, Vincent Hue, et al. (2021). “Local Time Dependence of Jupiter’s Polar Auroral Emissions Observed by Juno UVS". en. In: *Journal of Geophysical Research: Planets* 126.12, e2021JE006954. DOI: 10.1029/2021JE006954.

Grodent, D., J. T. Clarke, J. Kim, J. H. Waite, et al. (2003a). "Jupiter's main auroral oval observed with HST-STIS". en. In: *Journal of Geophysical Research: Space Physics* 108.A11. DOI: 10.1029/2003JA009921.

Grodent, D., J. T. Clarke, J. H. Waite Jr., S. W. H. Cowley, et al. (2003b). "Jupiter's polar auroral emissions". en. In: *Journal of Geophysical Research: Space Physics* 108.A10. DOI: 10.1029/2003JA010017.

Grodent, D., J.-C. Gérard, J. T. Clarke, G. R. Gladstone, et al. (2004). "A possible auroral signature of a magnetotail reconnection process on Jupiter". en. In: *Journal of Geophysical Research: Space Physics* 109.A5. DOI: 10.1029/2003JA010341.

Grodent, Denis (2015). "A Brief Review of Ultraviolet Auroral Emissions on Giant Planets". en. In: *Space Science Reviews* 187.1-4, pp. 23–50. DOI: 10.1007/s11214-014-0052-8.

Grodent, Denis, B. Bonfond, Z. Yao, J.-C. Gérard, et al. (2018). "Jupiter's Aurora Observed With HST During Juno Orbits 3 to 7". en. In: *Journal of Geophysical Research: Space Physics* 123.5, pp. 3299–3319. DOI: 10.1002/2017JA025046.

Grodent, Denis, Bertrand Bonfond, Jean-Claude Gérard, Aikaterini Radioti, et al. (2008). "Auroral evidence of a localized magnetic anomaly in Jupiter's northern hemisphere". en. In: *Journal of Geophysical Research: Space Physics* 113.A9. DOI: 10.1029/2008JA013185.

Grodent, Denis, J. Hunter Waite Jr., and Jean-Claude Gérard (2001). "A self-consistent model of the Jovian auroral thermal structure". en. In: *Journal of Geophysical Research: Space Physics* 106.A7, pp. 12933–12952. DOI: 10.1029/2000JA900129.

Guo, R. L., Z. H. Yao, D. Grodent, B. Bonfond, et al. (2021). "Jupiter's Double-Arc Aurora as a Signature of Magnetic Reconnection: Simultaneous Observations

From HST and Juno". en. In: *Geophysical Research Letters* 48.14, e2021GL093964. DOI: 10.1029/2021GL093964.

Gustin, J., B. Bonfond, D. Grodent, and J.-C. Gérard (2012). "Conversion from HST ACS and STIS auroral counts into brightness, precipitated power, and radiated power for H2 giant planets". en. In: *Journal of Geophysical Research: Space Physics* 117.A7. DOI: https://doi.org/10.1029/2012JA017607.

Gustin, J., J.-C. Gérard, D. Grodent, S. W. H. Cowley, et al. (2004). "Energy-flux relationship in the FUV Jovian aurora deduced from HST-STIS spectral observations". en. In: *Journal of Geophysical Research: Space Physics* 109.A10. DOI: 10.1029/2003JA010365.

Haewsantati, K., B. Bonfond, S. Wannawichian, G. R. Gladstone, et al. (2021). "Morphology of Jupiter's Polar Auroral Bright Spot Emissions via Juno-UVS Observations". en. In: *Journal of Geophysical Research: Space Physics* 126.2, e2020JA028586. DOI: 10.1029/2020JA028586.

Haewsantati, K., B. Bonfond, S. Wannawichian, G. R. Gladstone, et al. (2023). "Juno's Multi-Instruments Observations During the Flybys of Auroral Bright Spots in Jupiter's Polar Aurorae". en. In: *Journal of Geophysical Research: Space Physics* 128.8, e2023JA031396. DOI: 10.1029/2023JA031396.

Haggerty, D. K., B. H. Mauk, C. P. Paranicas, G. Clark, et al. (2019). "Jovian Injections Observed at High Latitude". en. In: *Geophysical Research Letters* 46.16, pp. 9397–9404. DOI: 10.1029/2019GL083442.

Hall, D. T., P. D. Feldman, M. A. McGrath, and D. F. Strobel (1998). "The Far-Ultraviolet Oxygen Airglow of Europa and Ganymede". en. In: *The Astrophysical Journal* 499.1, pp. 475–481. DOI: 10.1086/305604.

Hallinan, G, S P Littlefair, G Cotter, S Bourke, et al. (2015). "Magnetospherically Driven Optical and Radio Aurorae at the End of the Main Sequence". en. In.

Hansen, C. J., D. E. Shemansky, L. W. Esposito, A. I. F. Stewart, et al. (2011). "The composition and structure of the Enceladus plume". en. In: *Geophysical Research Letters* 38.11. DOI: 10.1029/2011GL047415.

Hattori, Koichi, Masaru Hongo, and Xu-Guang Huang (2022). "New Developments in Relativistic Magnetohydrodynamics". en. In: *Symmetry* 14.9, p. 1851. DOI: 10.3390/sym14091851.

Hess, S. L. G., B. Bonfond, P. Zarka, and D. Grodent (2011). "Model of the Jovian magnetic field topology constrained by the Io auroral emissions". en. In: *Journal of Geophysical Research: Space Physics* 116.A5. DOI: 10.1029/2010JA016262.

Hess, S. L. G., P. Delamere, V. Dols, B. Bonfond, et al. (2010). "Power transmission and particle acceleration along the Io flux tube". en. In: *Journal of Geophysical Research: Space Physics* 115.A6. DOI: 10.1029/2009JA014928.

Hill, T. W. (1983). "Longitudinal asymmetry of the Io plasma torus". en. In: *Geophysical Research Letters* 10.10, pp. 969–972. DOI: 10.1029/GL010i010p00969.

— (2001). "The Jovian auroral oval". en. In: *Journal of Geophysical Research: Space Physics* 106.A5, pp. 8101–8107. DOI: 10.1029/2000JA000302.

Hill, T.w. (1979). "Inertial limit on corotation". en. In: *Journal of Geophysical Research: Space Physics* 84.A11, pp. 6554–6558. DOI: 10.1029/JA084iA11p06554.

Hospodarsky, G. B., W. S. Kurth, S. J. Bolton, F. Allegrini, et al. (2017). "Jovian bow shock and magnetopause encounters by the Juno spacecraft". en. In: *Geophysical Research Letters* 44.10, pp. 4506–4512. DOI: 10.1002/2017GL073177.

Huang, Chao-Song (2002). "Evidence of periodic (2–3 hour) near-tail magnetic reconnection and plasmoid formation: Geotail observations". en. In: *Geophysical Research Letters* 29.24, pp. 42–1–42–4. DOI: 10.1029/2002GL016162.

Hue, V., G. R. Gladstone, C. K. Louis, T. K. Greathouse, et al. (2023). "The Io, Europa, and Ganymede Auroral Footprints at Jupiter in the Ultraviolet: Positions and Equatorial Lead Angles". en. In: *Journal of Geophysical Research: Space Physics* 128.5, e2023JA031363. DOI: 10.1029/2023JA031363.

Hue, V., T. K. Greathouse, G. R. Gladstone, B. Bonfond, et al. (2021). "Detection and Characterization of Circular Expanding UV-Emissions Observed in Jupiter's Polar Auroral Regions". en. In: *Journal of Geophysical Research: Space Physics* 126.3, e2020JA028971. DOI: https://doi.org/10.1029/2020JA028971.

Hueso, R., A. Sánchez-Lavega, G. Piccioni, P. Drossart, et al. (2008). "Morphology and dynamics of Venus oxygen airglow from Venus Express/Visible and Infrared Thermal Imaging Spectrometer observations". en. In: *Journal of Geophysical Research: Planets* 113.E5. DOI: 10.1029/2008JE003081.

Hwang, K.-J., M. L. Goldstein, E. Lee, and J. S. Pickett (2011). "Cluster observations of multiple dipolarization fronts". en. In: *Journal of Geophysical Research: Space Physics* 116.A5. DOI: 10.1029/2010JA015742.

Ingersoll, Andrew P. and Shawn P. Ewald (2011). "Total particulate mass in Enceladus plumes and mass of Saturn's E ring inferred from Cassini ISS images". In: *Icarus* 216.2, pp. 492–506. DOI: 10.1016/j.icarus.2011.09.018.

Ingersoll, Andrew P., Ashwin R. Vasavada, Blane Little, Clifford D. Anger, et al. (1998). "Imaging Jupiter's Aurora at Visible Wavelengths". en. In: *Icarus* 135.1, pp. 251–264. DOI: 10.1006/icar.1998.5971.

Jackman, C. M., M. F. Thomsen, D. G. Mitchell, N. Sergis, et al. (2015). "Field dipolarization in Saturn's magnetotail with planetward ion flows and energetic particle flow bursts: Evidence of quasi-steady reconnection". en. In: *Journal of Geophysical Research: Space Physics* 120.5, pp. 3603–3617. DOI: 10.1002/2015JA020995.

Jackman, Caitriona M, Nicholas Achilleos, Stanley W. H. Cowley, and Emma J. Bunce (2013). "Auroral counterpart of magnetic field dipolarizations in Saturn's tail". en. In: *Planetary and Space Science*, p. 9.

James, M. K., G. Provan, A. Kamran, R. J. Wilson, et al. (2023). *JupiterMag*.

Jasinski, Jamie M., Christopher S. Arridge, Andrew J. Coates, Geraint H. Jones, et al. (2016). "Cassini plasma observations of Saturn's magnetospheric cusp". en. In: *Journal of Geophysical Research: Space Physics* 121.12, pp. 12, 047–12, 067. DOI: 10.1002/2016JA023310.

Johnson, R. E., H. Melin, T. S. Stallard, C. Tao, et al. (2018). "Mapping H3+ Temperatures in Jupiter's Northern Auroral Ionosphere Using VLT-CRIRES".

en. In: *Journal of Geophysical Research: Space Physics* 123.7, pp. 5990–6008. DOI: 10.1029/2018JA025511.

Johnson, R. E. and D. F. Strobel (1982). “Charge exchange in the Io torus and exosphere”. en. In: *Journal of Geophysical Research: Space Physics* 87.A12, pp. 10385–10393. DOI: 10.1029/JA087iA12p10385.

Joy, S. P., M. G. Kivelson, R. J. Walker, K. K. Khurana, et al. (2002). “Probabilistic models of the Jovian magnetopause and bow shock locations”. en. In: *Journal of Geophysical Research: Space Physics* 107.A10, SMP 17–1–SMP 17–17. DOI: 10.1029/2001JA009146.

Jurac, S. and J. D. Richardson (2005). “A self-consistent model of plasma and neutrals at Saturn: Neutral cloud morphology”. en. In: *Journal of Geophysical Research: Space Physics* 110.A9. DOI: 10.1029/2004JA010635.

Kamran, A., E. J. Bunce, S. W. H. Cowley, M. K. James, et al. (2022). “Auroral Field-Aligned Current Signatures in Jupiter’s Magnetosphere: Juno Magnetic Field Observations and Physical Modeling”. en. PhD thesis.

Kane, M., Bh Mauk, Ep Keath, and Sm Krimigis (1995). “Hot Ions in Jupiters Magnetodisc - a Model for Voyager-2 Low-Energy Charged-Particle Measurements”. English. In: *JOURNAL OF GEOPHYSICAL RESEARCH-SPACE PHYSICS* 100.A10, pp. 19473–19486. DOI: 10.1029/95JA00793.

Kasahara, S., E. A. Kronberg, T. Kimura, C. Tao, et al. (2013). “Asymmetric distribution of reconnection jet fronts in the Jovian nightside magnetosphere”. en. In: *Journal of Geophysical Research: Space Physics* 118.1, pp. 375–384. DOI: 10.1029/2012JA018130.

Kasahara, S., E. A. Kronberg, N. Krupp, T. Kimura, et al. (2011). “Magnetic reconnection in the Jovian tail: X-line evolution and consequent plasma sheet structures”. en. In: *Journal of Geophysical Research: Space Physics* 116.A11. DOI: 10.1029/2011JA016892.

Khurana, Krishan K, Margaret G Kivelson, Vytenis M Vasyliunas, Norbert Krupp, et al. (2004). “The Configuration of Jupiter’s Magnetosphere”. en. In.

Khurana, Krishan K. (1992). "A generalized hinged-magnetodisc model of Jupiter's nightside current sheet". en. In: *Journal of Geophysical Research: Space Physics* 97.A5, pp. 6269–6276. DOI: 10.1029/92JA00169.

— (2001). "Influence of solar wind on Jupiter's magnetosphere deduced from currents in the equatorial plane". en. In: *Journal of Geophysical Research: Space Physics* 106.A11, pp. 25999–26016. DOI: 10.1029/2000JA000352.

Khurana, Krishan K. and Hannes K. Schwarzl (2005). "Global structure of Jupiter's magnetospheric current sheet". en. In: *Journal of Geophysical Research: Space Physics* 110.A7. DOI: 10.1029/2004JA010757.

Kimura, T., S. V. Badman, C. Tao, K. Yoshioka, et al. (2015). "Transient internally driven aurora at Jupiter discovered by Hisaki and the Hubble Space Telescope". en. In: *Geophysical Research Letters* 42.6, pp. 1662–1668. DOI: 10.1002/2015GL063272.

Kimura, T., J. D. Nichols, R. L. Gray, C. Tao, et al. (2017). "Transient brightening of Jupiter's aurora observed by the Hisaki satellite and Hubble Space Telescope during approach phase of the Juno spacecraft". en. In: *Geophysical Research Letters* 44.10, pp. 4523–4531. DOI: 10.1002/2017GL072912.

Kinrade, J., A. Bader, S. V. Badman, C. Paranicas, et al. (2021). "The Statistical Morphology of Saturn's Equatorial Energetic Neutral Atom Emission". en. In: *Geophysical Research Letters* 48.11, e2020GL091595. DOI: 10.1029/2020GL091595.

Kivelson, M. G. and D. J. Southwood (2005). "Dynamical consequences of two modes of centrifugal instability in Jupiter's outer magnetosphere". en. In: *Journal of Geophysical Research: Space Physics* 110.A12. DOI: 10.1029/2005JA011176.

Kivelson, Margaret G (2003). "Moon–magnetosphere interactions: a tutorial". en. In: *Advances in Space Research*. DOI: 10.1016/j.asr.2003.08.042.

Kivelson, Margaret G. and Krishan K. Khurana (2002). "Properties of the magnetic field in the Jovian magnetotail". en. In: *Journal of Geophysical Research: Space Physics* 107.A8, SMP 23–1–SMP 23–9. DOI: 10.1029/2001JA000249.

Kivelson, Margaret G., Krishan Khurana, Christopher T. Russell, and Raymond J. Walker (1997). “Intermittent short-duration magnetic field anomalies in the Io torus: Evidence for plasma interchange?” In.

Kivelson, Margaret G. and Christopher T. Russell (1995). *Introduction to Space Physics*. DOI: 10.1017/9781139878296.

Knight, Stephen (1973). “Parallel electric fields”. In: *Planetary and Space Science* 21.5, pp. 741–750. DOI: 10.1016/0032-0633(73)90093-7.

Kollmann, P., G. Clark, C. Paranicas, B. Mauk, et al. (2021). “Jupiter’s Ion Radiation Belts Inward of Europa’s Orbit”. en. In: *Journal of Geophysical Research: Space Physics* 126.4, e2020JA028925. DOI: 10.1029/2020JA028925.

Kronberg, E. A., S. Kasahara, N. Krupp, and J. Woch (2012). “Field-aligned beams and reconnection in the jovian magnetotail”. In: *Icarus* 217.1, pp. 55–65. DOI: 10.1016/j.icarus.2011.10.011.

Kronberg, E. A., J. Woch, N. Krupp, A. Lagg, et al. (2005). “Mass release at Jupiter: Substorm-like processes in the Jovian magnetotail”. en. In: *Journal of Geophysical Research: Space Physics* 110.A3. DOI: 10.1029/2004JA010777.

Kronberg, E. A., J. Woch, N. Krupp, A. Lagg, et al. (2008). “Comparison of periodic substorms at Jupiter and Earth”. en. In: *Journal of Geophysical Research: Space Physics* 113.A4. DOI: 10.1029/2007JA012880.

Krupp, N, V M Vasyliunas, J Woch, A Lagg, et al. (2004). “Dynamics of the Jovian Magnetosphere”. en. In.

Krupp, N., E. Keppler, R. Seidel, J. Woch, et al. (1997). “Field-aligned particle streaming in the duskside high latitude Jovian magnetosphere”. en. In: *Advances in Space Research* 20.2, pp. 225–228. DOI: 10.1016/S0273-1177(97)00538-3.

Krupp, N., A. Lagg, S. Livi, B. Wilken, et al. (2001). “Global flows of energetic ions in Jupiter’s equatorial plane: First-order approximation”. en. In: *Journal of Geophysical Research: Space Physics* 106.A11, pp. 26017–26032. DOI: 10.1029/2000JA900138.

Krupp, Norbert, Elena Kronberg, and Aikaterini Radioti (2015). "Jupiter's Magnetotail". en. In: pp. 85–98. DOI: 10.1002/9781118842324.ch5.

Kulsrud, Russell M. (2001). "Magnetic reconnection: Sweet-Parker versus Petschek". In: *Earth, Planets and Space* 53.6, pp. 417–422. DOI: 10.1186/BF03353251.

Kurth, W. S., G. B. Hospodarsky, D. L. Kirchner, B. T. Mokrzycki, et al. (2017). "The Juno Waves Investigation". en. In: *Space Science Reviews* 213.1, pp. 347–392. DOI: 10.1007/s11214-017-0396-y.

Lam, Hoanh An, Nicholas Achilleos, Steven Miller, Jonathan Tennyson, et al. (1997). "A Baseline Spectroscopic Study of the Infrared Auroras of Jupiter". en. In: *Icarus* 127.2, pp. 379–393. DOI: 10.1006/icar.1997.5698.

Lamy, L. (2020). "Auroral emissions from Uranus and Neptune". en. In: *Philosophical Transactions of the Royal Society A: Mathematical, Physical and Engineering Sciences* 378.2187, p. 20190481. DOI: 10.1098/rsta.2019.0481.

Lamy, L., R. Prangé, K. C. Hansen, C. Tao, et al. (2017). "The aurorae of Uranus past equinox". en. In: *Journal of Geophysical Research: Space Physics* 122.4, pp. 3997–4008. DOI: 10.1002/2017JA023918.

Lee, L. C. and K. H. Lee (2020). "Fluid and kinetic aspects of magnetic reconnection and some related magnetospheric phenomena". en. In: *Reviews of Modern Plasma Physics* 4.1, p. 9. DOI: 10.1007/s41614-020-00045-7.

Li, W., R. M. Thorne, Q. Ma, X.-J. Zhang, et al. (2017). "Understanding the Origin of Jupiter's Diffuse Aurora Using Juno's First Perijove Observations". en. In: *Geophysical Research Letters* 44.20, pp. 10, 162–10, 170. DOI: 10.1002/2017GL075545.

Lillis, Robert J., Justin Deighan, Krishnaprasad Chirakkil, Sonal Jain, et al. (2024). "Sinuous Aurora at Mars: A Link to the Tail Current Sheet?" en. In: *Journal of Geophysical Research: Space Physics* 129.6, e2024JA032477. DOI: 10.1029/2024JA032477.

Lindsay, S.T., M.K. James, E.J. Bunce, S.M. Imber, et al. (2016). "MESSENGER X-ray observations of magnetosphere–surface interaction on the nightside of Mercury". en. In: *Planetary and Space Science* 125, pp. 72–79. DOI: 10.1016/j.pss.2016.03.005.

Ling, Samuel J., Jeff Sanny, William Moebs, and Daryl Janzen (2018). *Introduction to Electricity, Magnetism, and Circuits*. en-ca.

Livengood, T. A. and H. W. Moos (1990). "Jupiter's north and south polar aurorae with IUE data". en. In: *Geophysical Research Letters* 17.12, pp. 2265–2268. DOI: 10.1029/GL017i012p02265.

Lorch, C. T. S., L. C. Ray, C. S. Arridge, K. K. Khurana, et al. (2020). "Local Time Asymmetries in Jupiter's Magnetodisc Currents". en. In: *Journal of Geophysical Research: Space Physics* 125.2. DOI: 10.1029/2019JA027455.

Louarn, Philippe, Nicolas Andre, Caitriona M. Jackman, Satoshi Kasahara, et al. (2015). "Magnetic Reconnection and Associated Transient Phenomena Within the Magnetospheres of Jupiter and Saturn". en. In: *Space Science Reviews* 187.1-4, pp. 181–227. DOI: 10.1007/s11214-014-0047-5.

Marzok, A., S. Schlegel, J. Saur, L. Roth, et al. (2022). "Mapping the Brightness of Ganymede's Ultraviolet Aurora Using Hubble Space Telescope Observations". en. In: *Journal of Geophysical Research: Planets* 127.6, e2022JE007256. DOI: 10.1029/2022JE007256.

Masters, A., W. R. Dunn, T. S. Stallard, H. Manners, et al. (2021). "Magnetic Reconnection Near the Planet as a Possible Driver of Jupiter's Mysterious Polar Auroras". en. In: *Journal of Geophysical Research: Space Physics* 126.8, e2021JA029544. DOI: 10.1029/2021JA029544.

Mauk, B., D. Hamilton, T. Hill, George Hospodarsky, et al. (2009). "Fundamental Plasma Processes in Saturn's Magnetosphere". In: *Saturn from Cassini-Huygens, 281-331 (2009)*. DOI: 10.1007/978-1-4020-9217-6_11.

Mauk, B. H., G. Clark, G. R. Gladstone, S. Kotsiaros, et al. (2020). "Energetic Particles and Acceleration Regions Over Jupiter's Polar Cap and Main Aurora: A Broad Overview". en. In: *Journal of Geophysical Research: Space Physics* 125.3. DOI: 10.1029/2019JA027699.

Mauk, B. H., J. T. Clarke, D. Grodent, J. H. Waite, et al. (2002). "Transient aurora on Jupiter from injections of magnetospheric electrons". en. In: *Nature* 415.6875, pp. 1003–1005. DOI: 10.1038/4151003a.

Mauk, B. H., I. J. Cohen, D. K. Haggerty, G. B. Hospodarsky, et al. (2019). "Investigation of Mass-/Charge-Dependent Escape of Energetic Ions Across the Magnetopauses of Earth and Jupiter". en. In: *Journal of Geophysical Research: Space Physics* 124.7, pp. 5539–5567. DOI: 10.1029/2019JA026626.

Mauk, B. H., D. K. Haggerty, S. E. Jaskulek, C. E. Schlemm, et al. (2017a). "The Jupiter Energetic Particle Detector Instrument (JEDI) Investigation for the Juno Mission". en. In: *Space Science Reviews* 213.1-4, pp. 289–346. DOI: 10.1007/s11214-013-0025-3.

Mauk, B. H., D. K. Haggerty, C. Paranicas, G. Clark, et al. (2017b). "Discrete and broadband electron acceleration in Jupiter's powerful aurora". en. In: *Nature* 549.7670, pp. 66–69. DOI: 10.1038/nature23648.

Mauk, B. H., D. K. Haggerty, C. Paranicas, G. Clark, et al. (2017c). "Juno observations of energetic charged particles over Jupiter's polar regions: Analysis of monodirectional and bidirectional electron beams". en. In: *Geophysical Research Letters* 44.10, pp. 4410–4418. DOI: 10.1002/2016GL072286.

Mauk, B. H., D. K. Haggerty, C. Paranicas, G. Clark, et al. (2018). "Diverse Electron and Ion Acceleration Characteristics Observed Over Jupiter's Main Aurora". en. In: *Geophysical Research Letters* 45.3, pp. 1277–1285. DOI: 10.1002/2017GL076901.

Mauk, B. H., D. J. Williams, R. W. McEntire, K. K. Khurana, et al. (1999). "Stormlike dynamics of Jupiter's inner and middle magnetosphere". en. In: *Journal of Geophysical Research: Space Physics* 104.A10, pp. 22759–22778. DOI: 10.1029/1999JA900097.

McComas, D. J., N. Alexander, F. Allegrini, F. Bagenal, et al. (2013). "The Jovian Auroral Distributions Experiment (JADE) on the Juno Mission to Jupiter". en.

In: *Space Science Reviews* 213.1-4, pp. 547–643. DOI: 10.1007/s11214-013-9990-9.

McComas, D. J., F. Allegrini, F. Bagenal, F. Crary, et al. (2007). "Diverse Plasma Populations and Structures in Jupiter's Magnetotail". EN. In: *Science*. DOI: 10.1126/science.1147393.

McEntee, Seán (2021). *SeanMcEntee/CXO_and_GOES_analyses: Release of alternative go_chandra and new PI filtering method for analysing Jupiter's X-rays using Chandra HRC-I*. DOI: 10.5281/zenodo.5657142.

Melin, Henrik, L. N. Fletcher, T. S. Stallard, S. Miller, et al. (2019). "The H3+ ionosphere of Uranus: decades-long cooling and local-time morphology". In: *Philosophical transactions. Series A, Mathematical, physical, and engineering sciences* 377.2154, p. 20180408. DOI: 10.1098/rsta.2018.0408.

Milan, S. E. (2013). "Modeling Birkeland currents in the expanding/contracting polar cap paradigm". en. In: *Journal of Geophysical Research: Space Physics* 118.9, pp. 5532–5542. DOI: 10.1002/jgra.50393.

Miller, Steve (2021). "Planetary Aurorae". en. In: DOI: 10.1093/acrefore/9780190647926.013.228.

Mitchell, D. G., P. C. Brandt, J. F. Carbary, W. S. Kurth, et al. (2015). "Injection, Interchange, and Reconnection". en. In: pp. 327–343. DOI: 10.1002/9781118842324.ch19.

Moirano, Alessandro, Alessandro Mura, Alberto Adriani, Vincent Dols, et al. (2021). "Morphology of the Auroral Tail of Io, Europa, and Ganymede From JIRAM L-Band Imager". en. In: *Journal of Geophysical Research: Space Physics* 126.9, e2021JA029450. DOI: 10.1029/2021JA029450.

Moore, K. M., L.K. Yadav, and L. Kulowksi (2018). "A complex dynamo inferred from the hemispheric dichotomy of Jupiter's magnetic field". In: DOI: https://doi.org/10.1038/s41586-018-0468-5.

Muñoz Jr, J. R., F. Allegrini, R. W. Ebert, R. J. Wilson, et al. (2022). "A Survey of Electron Conics at Jupiter Utilizing the JADE-E Data During Science Orbits 01, 03-30". en. In: *Journal of Geophysical Research: Space Physics* 127.10, e2022JA030418. DOI: 10.1029/2022JA030418.

Mura, A., A. Adriani, F. Altieri, J. E. P. Connerney, et al. (2017). "Infrared observations of Jovian aurora from Juno's first orbits: Main oval and satellite footprints". en. In: *Geophysical Research Letters* 44.11, pp. 5308–5316. DOI: 10.1002/2017GL072954.

Nakamura, R., W. Baumjohann, B. Klecker, Y. Bogdanova, et al. (2002). "Motion of the dipolarization front during a flow burst event observed by Cluster". en. In: *Geophysical Research Letters* 29.20. DOI: 10.1029/2002GL015763.

Nakamura, R., W. Baumjohann, R. Schödel, M. Brittnacher, et al. (2001). "Earthward flow bursts, auroral streamers, and small expansions". en. In: *Journal of Geophysical Research: Space Physics* 106.A6, pp. 10791–10802. DOI: 10.1029/2000JA000306.

Nichols, J. D., N. Achilleos, and S. W. H. Cowley (2015). "A model of force balance in Jupiter's magnetodisc including hot plasma pressure anisotropy". en. In: *Journal of Geophysical Research: Space Physics* 120.12, pp. 10, 185–10, 206. DOI: 10.1002/2015JA021807.

Nichols, J. D., F. Allegrini, F. Bagenal, B. Bonfond, et al. (2023). "Jovian Magnetospheric Injections Observed by the Hubble Space Telescope and Juno". en. In: *Geophysical Research Letters* 50.20, e2023GL105549. DOI: 10.1029/2023GL105549.

Nichols, J. D., S. V. Badman, F. Bagenal, S. J. Bolton, et al. (2017). "Response of Jupiter's auroras to conditions in the interplanetary medium as measured by the Hubble Space Telescope and Juno: JUPITER'S AURORAS DURING JUNO APPROACH". en. In: *Geophysical Research Letters* 44.15, pp. 7643–7652. DOI: 10.1002/2017GL073029.

Nichols, J. D., E. J. Bunce, J. T. Clarke, S. W. H. Cowley, et al. (2007). "Response of Jupiter's UV auroras to interplanetary conditions as observed by the Hubble

Space Telescope during the Cassini flyby campaign". en. In: *Journal of Geophysical Research: Space Physics* 112.A2. DOI: 10.1029/2006JA012005.

Nichols, J. D., J. T. Clarke, J. C. Gérard, D. Grodent, et al. (2009). "Variation of different components of Jupiter's auroral emission: JUPITER'S AURORAL COMPONENTS". en. In: *Journal of Geophysical Research: Space Physics* 114.A6, n/a–n/a. DOI: 10.1029/2009JA014051.

Nichols, J. D. and S. W. H. Cowley (2022). "Relation of Jupiter's Dawnside Main Emission Intensity to Magnetospheric Currents During the Juno Mission". en. In: *Journal of Geophysical Research: Space Physics* 127.1, e2021JA030040. DOI: 10.1029/2021JA030040.

Nishida, A. (1983). "Reconnection in the Jovian magnetosphere". en. In: *Geophysical Research Letters* 10.6, pp. 451–454. DOI: 10.1029/GL010i006p00451.

Nulsen, S., R. Kraft, G. Germain, W. Dunn, et al. (2020). "X-Ray Emission from Jupiter's Galilean Moons: A Tool for Determining Their Surface Composition and Particle Environment". en. In: *The Astrophysical Journal* 895.2, p. 79. DOI: 10.3847/1538-4357/ab8cbc.

Øieroset, M., T. D. Phan, M. Fujimoto, R. P. Lin, et al. (2001). "In situ detection of collisionless reconnection in the Earth's magnetotail". en. In: *Nature* 412.6845, pp. 414–417. DOI: 10.1038/35086520.

Olson, Peter and Ulrich R. Christensen (2006). "Dipole moment scaling for convection-driven planetary dynamos". en. In: *Earth and Planetary Science Letters* 250.3-4, pp. 561–571. DOI: 10.1016/j.epsl.2006.08.008.

Pallier, Laurent and Renée Prangé (2001). "More about the structure of the high latitude Jovian aurorae". en. In: *Planetary and Space Science* 49.10-11, pp. 1159–1173. DOI: 10.1016/S0032-0633(01)00023-X.

— (2004). "Detection of the southern counterpart of the Jovian northern polar cusp: Shared properties". en. In: *Geophysical Research Letters* 31.6. DOI: 10.1029/2003GL018041.

Palmaerts, B., D. Grodent, B. Bonfond, Z.H. Yao, et al. (2024). "Overview of a large observing campaign of Jupiter's aurora with the Hubble Space Telescope combined with Juno-UVS data". en. In: *Icarus* 408, p. 115815. DOI: 10.1016/j.icarus.2023.115815.

Palmaerts, B., A. Radioti, D. Grodent, E. Chané, et al. (2014). "Transient small-scale structure in the main auroral emission at Jupiter". en. In: *Journal of Geophysical Research: Space Physics* 119.12, pp. 9931–9938. DOI: 10.1002/2014JA020688.

Panov, E. V., W. Baumjohann, R. Nakamura, P. L. Pritchett, et al. (2019). "Ionospheric Footprints of Detached Magnetotail Interchange Heads". en. In: *Geophysical Research Letters* 46.13, pp. 7237–7247. DOI: 10.1029/2019GL083070.

Panov, E. V., V. A. Sergeev, P. L. Pritchett, F. V. Coroniti, et al. (2012). "Observations of kinetic ballooning/interchange instability signatures in the magnetotail". en. In: *Geophysical Research Letters* 39.8. DOI: 10.1029/2012GL051668.

Paranicas, C., B. H. Mauk, D. K. Haggerty, G. Clark, et al. (2018). "Intervals of Intense Energetic Electron Beams Over Jupiter's Poles". en. In: *Journal of Geophysical Research: Space Physics* 123.3, pp. 1989–1999. DOI: 10.1002/2017JA025106.

Paschmann, G., B. U. Ö Sonnerup, I. Papamastorakis, N. Sckopke, et al. (1979). "Plasma acceleration at the Earth's magnetopause: evidence for reconnection". en. In: *Nature* 282.5736, pp. 243–246. DOI: 10.1038/282243a0.

Paschmann, Götz, Stein Haaland, and Rudolf Treumann (2002). "In Situ Measurements in the Auroral Plasma". en. In: pp. 93–208. DOI: 10.1007/978-94-007-1086-3_4.

Pater, Imke De and David E Dunn (2003). "VLA observations of Jupiter's synchrotron radiation at 15 and 22 GHz". en. In: *Icarus* 163.2, pp. 449–455. DOI: 10.1016/S0019-1035(03)00068-X.

Provan, G., S. W. H. Cowley, and J. D. Nichols (2024). "Juno Observations of Large-Scale Azimuthal Fields in Jupiter's Nightside Magnetosphere and Related Radial Currents". en. In: *Journal of Geophysical Research: Space Physics* 129.10, e2024JA032677. DOI: 10.1029/2024JA032677.

Provan, G., R. J. Wilson, M. F. Vogt, A. Kamran, et al. (2023). *con2020*. DOI: 10.5281/zenodo.7589982.

Radioti, A., J.-C. Gérard, D. Grodent, B. Bonfond, et al. (2008a). "Discontinuity in Jupiter's main auroral oval". en. In: *Journal of Geophysical Research: Space Physics* 113.A1. DOI: 10.1029/2007JA012610.

Radioti, A., D. Grodent, J.-C. Gérard, B. Bonfond, et al. (2008b). "Auroral polar dawn spots: Signatures of internally driven reconnection processes at Jupiter's magnetotail". en. In: *Geophysical Research Letters* 35.3. DOI: 10.1029/2007GL032460.

Radioti, A., A. T. Tomás, D. Grodent, J.-C. Gérard, et al. (2009). "Equatorward diffuse auroral emissions at Jupiter: Simultaneous HST and Galileo observations". en. In: *Geophysical Research Letters* 36.7. DOI: 10.1029/2009GL037857.

Radioti, Aikaterini (2006). *Energetic ion composition and acceleration mechanisms in the magnetosphere of Jupiter*. de.

Ray, L. C., N. A. Achilleos, M. F. Vogt, and J. N. Yates (2014). "Local time variations in Jupiter's magnetosphere-ionosphere coupling system". en. In: *Journal of Geophysical Research: Space Physics* 119.6, pp. 4740–4751. DOI: 10.1002/2014JA019941.

Ray, L. C., Y.-J. Su, R. E. Ergun, P. A. Delamere, et al. (2009). "Current-voltage relation of a centrifugally confined plasma". en. In: *Journal of Geophysical Research: Space Physics* 114.A4. DOI: 10.1029/2008JA013969.

Richardson, John D., George L. Siscoe, F. Bagenal, and James D. Sullivan (1980). "Time dependent plasma injection by Io". en. In: *Geophysical Research Letters* 7.1, pp. 37–40. DOI: 10.1029/GL007i001p00037.

Roth, L, A Blöcker, K de Kleer, D Goldstein, et al. (2024). "Mass supply from Io to Jupiter's magnetosphere". en. In.

Runov, A., V. Angelopoulos, M. I. Sitnov, V. A. Sergeev, et al. (2009). "THEMIS observations of an earthward-propagating dipolarization front". en. In: *Geophysical Research Letters* 36.14. DOI: 10.1029/2009GL038980.

Rutala, M. J., J. T. Clarke, J. D. Mullins, and J. D. Nichols (2022). "Illuminating the Motions of Jupiter's Auroral Dawn Storms". en. In: *Journal of Geophysical Research: Space Physics* 127.6, e2022JA030448. DOI: 10.1029/2022JA030448.

Salveter, A., J. Saur, G. Clark, and B. H. Mauk (2022). "Jovian Auroral Electron Precipitation Budget—A Statistical Analysis of Diffuse, Mono-Energetic, and Broadband Auroral Electron Distributions". en. In: *Journal of Geophysical Research: Space Physics* 127.8, e2021JA030224. DOI: 10.1029/2021JA030224.

Saur, Joachim, Stefan Duling, Alexandre Wennmacher, Clarissa Willmes, et al. (2022). "Alternating North-South Brightness Ratio of Ganymede's Auroral Ovals: Hubble Space Telescope Observations Around the Juno PJ34 Flyby". en. In: *Geophysical Research Letters* 49.23, e2022GL098600. DOI: 10.1029/2022GL098600.

Saur, Joachim, Sascha Janser, Anne Schreiner, George Clark, et al. (2018). "Wave-Particle Interaction of Alfvén Waves in Jupiter's Magnetosphere: Auroral and Magnetospheric Particle Acceleration". en. In: *Journal of Geophysical Research: Space Physics* 123.11, pp. 9560–9573. DOI: 10.1029/2018JA025948.

Schneider, N. M., J. Deighan, S. K. Jain, and A. Stiepen (2015). "Discovery of diffuse aurora on Mars". en. In: *Science* 350.6261. DOI: 10.1126/science.aad0313.

Sitnov (2009). "Dipolarization fronts as a signature of transient reconnection in the magnetotail". In: *Journal of Geophysical Research.*

Slanger, T.G., D.L. Huestis, P.C. Cosby, N.J. Chanover, et al. (2006). "The Venus nightglow: Ground-based observations and chemical mechanisms". en. In: *Icarus* 182.1, pp. 1–9. DOI: 10.1016/j.icarus.2005.12.007.

Smith, A. W., C. M. Jackman, and M. F. Thomsen (2016). "Magnetic reconnection in Saturn's magnetotail: A comprehensive magnetic field survey". en. In: *Journal of Geophysical Research: Space Physics* 121.4, pp. 2984–3005. DOI: 10.1002/2015JA022005.

Smith, H. T., R. E. Johnson, M. E. Perry, D. G. Mitchell, et al. (2010). "Enceladus plume variability and the neutral gas densities in Saturn's magnetosphere". en.

In: *Journal of Geophysical Research: Space Physics* 115.A10. DOI: 10.1029/2009JA015184.

Smoluchowski, R. (1971). "Metallic Interiors and Magnetic Fields of Jupiter and Saturn". en. In: *The Astrophysical Journal* 166, p. 435. DOI: 10.1086/150971.

Southwood, D. J. and E. Chané (2016). "High-latitude circulation in giant planet magnetospheres". en. In: *Journal of Geophysical Research: Space Physics* 121.6, pp. 5394–5403. DOI: 10.1002/2015JA022310.

Southwood, D. J. and M. G. Kivelson (2001). "A new perspective concerning the influence of the solar wind on the Jovian magnetosphere". en. In: *Journal of Geophysical Research: Space Physics* 106.A4, pp. 6123–6130. DOI: 10.1029/2000JA000236.

Southwood, David J. and Margaret G. Kivelson (1989). "Magnetospheric interchange motions". en. In: *Journal of Geophysical Research: Space Physics* 94.A1, pp. 299–308. DOI: 10.1029/JA094iA01p00299.

Spencer, J, S Stern, Andrew Cheng, H Weaver, et al. (2007). "Io Volcanism Seen by New Horizons: A Major Eruption of the Tvashtar Volcano". In: *Science (New York, N.Y.)* 318, pp. 240–3. DOI: 10.1126/science.1147621.

Stallard, T. S., S. Miller, S. W. H. Cowley, and E. J. Bunce (2003). "Jupiter's polar ionospheric flows: Measured intensity and velocity variations poleward of the main auroral oval". English. In: *GEOPHYSICAL RESEARCH LETTERS* 30.5, p. 1221. DOI: 10.1029/2002GL016031.

Stix, Michael (2002). *The Sun.* Astronomy and Astrophysics Library. DOI: 10.1007/978-3-642-56042-2.

Sundberg, Torbjörn, James A. Slavin, Scott A. Boardsen, Brian J. Anderson, et al. (2012). "MESSENGER observations of dipolarization events in Mercury's magnetotail". en. In: *Journal of Geophysical Research: Space Physics* 117.A12. DOI: 10.1029/2012JA017756.

Tao, Chihiro, Ryuho Kataoka, Hiroshi Fukunishi, Yukihiro Takahashi, et al. (2005). "Magnetic field variations in the Jovian magnetotail induced by solar wind dynamic pressure enhancements". en. In: *Journal of Geophysical Research: Space Physics* 110.A11. DOI: 10.1029/2004JA010959.

Thomas, Emma M., Henrik Melin, Tom S. Stallard, Mohammad N. Chowdhury, et al. (2023). "Detection of the infrared aurora at Uranus with Keck-NIRSPEC". en. In: *Nature Astronomy* 7.12, pp. 1473–1480. DOI: 10.1038/s41550-023-02096-5.

Thomas, Nicolas (1992). "Optical observations of Io's neutral clouds and plasma torus". en. In: *Surveys in Geophysics* 13.2, pp. 91–164. DOI: 10.1007/BF01903525.

Tomás, A. T., J. Woch, N. Krupp, A. Lagg, et al. (2004a). "Energetic electrons in the inner part of the Jovian magnetosphere and their relation to auroral emissions". en. In: *Journal of Geophysical Research: Space Physics* 109.A6. DOI: 10.1029/2004JA010405.

Tomás, Woch, Krupp, and Lagg (2004b). "Changes of the energetic particles characteristics in the inner part of the Jovian magnetosphere: a topological study". en. In: DOI: 10.1016/j.pss.2003.06.011.

Vasavada, Ashwin R., Antonin H. Bouchez, Andrew P. Ingersoll, Blane Little, et al. (1999). "Jupiter's visible aurora and Io footprint". en. In: *Journal of Geophysical Research: Planets* 104.E11, pp. 27133–27142. DOI: 10.1029/1999JE001055.

Vasyliunas, Vytenis M. (1975). "Theoretical models of magnetic field line merging". en. In: *Reviews of Geophysics* 13.1, pp. 303–336. DOI: 10.1029/RG013i001p00303.

— (1983). "Plasma distribution and flow". In: Cambridge Planetary Science Old, pp. 395–453. DOI: 10.1017/CBO9780511564574.013.

Vincent, M (2000). "Mapping Jupiter's Latitudinal Bands and Great Red Spot Using HST/WFPC2 Far-Ultraviolet Imaging". en. In: *Icarus* 143.2, pp. 189–204. DOI: 10.1006/icar.1999.6232.

Vogt, Marissa F., John E.P. Connerney, Gina A. DiBraccio, Rob J. Wilson, et al. (2020). "Magnetotail Reconnection at Jupiter: A Survey of Juno Magnetic Field Observations". en. In: *Journal of Geophysical Research: Space Physics* 125.3, e2019JA027486. DOI: 10.1029/2019JA027486.

Vogt, Marissa F., Caitriona M. Jackman, James A. Slavin, Emma J. Bunce, et al. (2014). "Structure and statistical properties of plasmoids in Jupiter's magnetotail". en. In: *Journal of Geophysical Research: Space Physics* 119.2, pp. 821–843. DOI: 10.1002/2013JA019393.

Vogt, Marissa F., Margaret G. Kivelson, Krishan K. Khurana, Steven P. Joy, et al. (2010). "Reconnection and flows in the Jovian magnetotail as inferred from magnetometer observations". en. In: *Journal of Geophysical Research: Space Physics* 115.A6. DOI: 10.1029/2009JA015098.

Vogt, Marissa F., Margaret G. Kivelson, Krishan K. Khurana, Raymond J. Walker, et al. (2011). "Improved mapping of Jupiter's auroral features to magnetospheric sources". en. In: *Journal of Geophysical Research: Space Physics* 116.A3. DOI: 10.1029/2010JA016148.

Vogt, Marissa F., Matthew Rutala, Bertrand Bonfond, John T. Clarke, et al. (2022). "Variability of Jupiter's Main Auroral Emission and Satellite Footprints Observed With HST During the Galileo Era". en. In: *Journal of Geophysical Research: Space Physics* 127.2, e2021JA030011. DOI: 10.1029/2021JA030011.

Waite, J. H., G. R. Gladstone, W. S. Lewis, R. Goldstein, et al. (2001). "An auroral flare at Jupiter". en. In: *Nature* 410.6830, pp. 787–789. DOI: 10.1038/35071018.

Waite Jr., J. H., F. Bagenal, F. Seward, C. Na, et al. (1994). "ROSAT observations of the Jupiter aurora". en. In: *Journal of Geophysical Research: Space Physics* 99.A8, pp. 14799–14809. DOI: 10.1029/94JA01005.

Waite Jr., J. H., D. C. Boice, K. C. Hurley, S. A. Stern, et al. (1992). "Jovian Bremsstrahlung X rays: A Ulysses prediction". en. In: *Geophysical Research Letters* 19.2, pp. 83–86. DOI: 10.1029/92GL00052.

Walker, Raymond J. and Christopher T. Russell (1985). "Flux transfer events at the Jovian magnetopause". en. In: *Journal of Geophysical Research: Space Physics* 90.A8, pp. 7397–7404. DOI: 10.1029/JA090iA08p07397.

Walsh, J R, P Goudfrooij, and E Malumuth (2001). "STIS Geometric Distortion - SMOV3A tests for CCD, NUV- MAMA and FUV-MAMA". en. In.

Weigt, D. M., C. M. Jackman, W. R. Dunn, G. R. Gladstone, et al. (2020). "Chandra Observations of Jupiter's X-ray Auroral Emission During Juno Apojove 2017". en. In: *Journal of Geophysical Research: Planets* 125.4, e2019JE006262. DOI: 10.1029/2019JE006262.

Weigt, D. M., C. M. Jackman, D. Moral Pombo, S. V. Badman, et al. (2023). "Identifying the Variety of Jovian X-Ray Auroral Structures: Tying the Morphology of X-Ray Emissions to Associated Magnetospheric Dynamics". en. In: *Journal of Geophysical Research: Space Physics* 128.11. DOI: 10.1029/2023JA031656.

Weigt, D. M., C. M. Jackman, M. F. Vogt, H. Manners, et al. (2021). "Characteristics of Jupiter's X-Ray Auroral Hot Spot Emissions Using Chandra". en. In: *Journal of Geophysical Research: Space Physics* 126.9, e2021JA029243. DOI: 10.1029/2021JA029243.

Went, D. R., M. G. Kivelson, N. Achilleos, C. S. Arridge, et al. (2011). "Outer magnetospheric structure: Jupiter and Saturn compared". en. In: *Journal of Geophysical Research: Space Physics* 116.A4. DOI: 10.1029/2010JA016045.

West, Robert A., Erich Karkoschka, A. James Friedson, Mark Seymour, et al. (1995). "Impact Debris Particles in Jupiter's Stratosphere". en. In: *Science* 267.5202, pp. 1296–1301. DOI: 10.1126/science.7871426.

Wibisono, A. D., G. Branduardi-Raymont, W. R. Dunn, T. Kimura, et al. (2021). "Jupiter's X-ray aurora during UV dawn storms and injections as observed by XMM-Newton, Hubble, and Hisaki". In: *Monthly Notices of the Royal Astronomical Society* 507.1, pp. 1216–1228. DOI: 10.1093/mnras/stab2218.

Wilkes, Belinda J., Raffaele D'Abrusco, and Rafael Martínez-Galarza (2019). "Chandra X-ray Observatory Overview". en. In: DOI: 10.1088/2514-3433/ab43dcch2.

Wilson, R. J., M. F. Vogt, G. Provan, A. Kamran, et al. (2023). "Internal and External Jovian Magnetic Fields: Community Code to Serve the Magnetospheres of the Outer Planets Community". en. In: *Space Science Reviews* 219.1, p. 15. DOI: 10.1007/s11214-023-00961-3.

Woodfield, E. E., R. B. Horne, S. A. Glauert, J. D. Menietti, et al. (2013). "Electron acceleration at Jupiter: input from cyclotron-resonant interaction with whistler-mode chorus waves". English. In: *Annales Geophysicae* 31.10, pp. 1619–1630. DOI: 10.5194/angeo-31-1619-2013.

— (2014). "The origin of Jupiter's outer radiation belt". en. In: *Journal of Geophysical Research: Space Physics* 119.5, pp. 3490–3502. DOI: 10.1002/2014JA019891.

Woodgate, B. E., R. A. Kimble, C. W. Bowers, S. Kraemer, et al. (1998). "The Space Telescope Imaging Spectrograph Design". en. In: *Publications of the Astronomical Society of the Pacific* 110.752, pp. 1183–1204. DOI: 10.1086/316243.

Xu, S. B., S. Y. Huang, Z. G. Yuan, X. H. Deng, et al. (2021). "Global Spatial Distribution of Dipolarization Fronts in the Saturn's Magnetosphere: Cassini Observations". en. In: *Geophysical Research Letters* 48.17, e2021GL092701. DOI: 10.1029/2021GL092701.

Xu, S. B., S. Y. Huang, Z. G. Yuan, K. Jiang, et al. (2022). "Successive Dipolarization Fronts With a Stepwise Electron Acceleration During a Substorm in Saturn's Magnetotail". en. In: *Geophysical Research Letters* 49.5, e2021GL097227. DOI: 10.1029/2021GL097227.

Xu, Y., C. S. Arridge, Z. H. Yao, B. Zhang, et al. (2024). "In situ evidence of the magnetospheric cusp of Jupiter from Juno spacecraft measurements". en. In: *Nature Communications* 15.1, p. 6062. DOI: 10.1038/s41467-024-50449-z.

Yao, Z. H., B. Bonfond, G. Clark, D. Grodent, et al. (2020). "Reconnection- and Dipolarization-Driven Auroral Dawn Storms and Injections". en. In: *Journal of Geophysical Research: Space Physics* 125.8, e2019JA027663. DOI: 10.1029/2019JA027663.

Yao, Z. H., B. Bonfond, D. Grodent, E. Chané, et al. (2022). "On the Relation Between Auroral Morphologies and Compression Conditions of Jupiter's Magnetopause: Observations From Juno and the Hubble Space Telescope". en. In: *Journal of Geophysical Research: Space Physics* 127.10, e2021JA029894. DOI: 10.1029/2021JA029894.

Yao, Z. H., W. R. Dunn, E. E. Woodfield, and G. B. Clark (2021). "Revealing the source of Jupiter's x-ray auroral flares". In: DOI: 10.1126/sciadv.abf0851.

Yao, Z. H., D. Grodent, W. S. Kurth, G. Clark, et al. (2019). "On the Relation Between Jovian Aurorae and the Loading/Unloading of the Magnetic Flux: Simultaneous Measurements From Juno, Hubble Space Telescope, and Hisaki". en. In: *Geophysical Research Letters* 46.21, pp. 11632–11641. DOI: 10.1029/2019GL084201.

Yoneda, M., H. Nozawa, H. Misawa, M. Kagitani, et al. (2010). "Jupiter's magnetospheric change by Io's volcanoes". en. In: *Geophysical Research Letters* 37.11. DOI: 10.1029/2010GL043656.

Yoshikawa, Ichiro, Fumiharu Suzuki, Reina Hikida, Kazuo Yoshioka, et al. (2017). "Volcanic activity on Io and its influence on the dynamics of the Jovian magnetosphere observed by EXCEED/Hisaki in 2015". en. In: *Earth, Planets and Space* 69.1, p. 110. DOI: 10.1186/s40623-017-0700-9.

Zhang, Binzheng, Peter A. Delamere, Zhonghua Yao, Bertrand Bonfond, et al. (2021). "How Jupiter's unusual magnetospheric topology structures its aurora". en. In: *Science Advances* 7.15, eabd1204. DOI: 10.1126/sciadv.abd1204.

Zhang, T. L., Q. M. Lu, W. Baumjohann, C. T. Russell, et al. (2012). "Magnetic Reconnection in the Near Venusian Magnetotail". en. In: *Science* 336.6081, pp. 567–570. DOI: 10.1126/science.1217013.